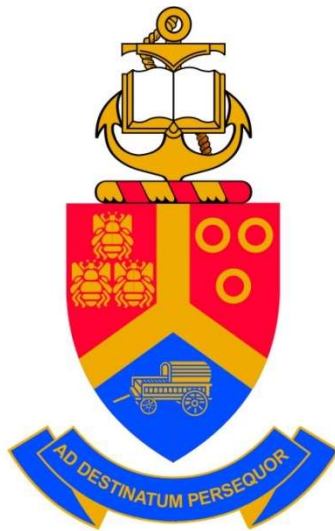


***Ab initio* study of the beryllium-sulphur and beryllium-nitrogen co-doped graphene for nanoelectronic and optoelectronic devices**

by

**Okikiola Olaniyan**



A thesis submitted in partial fulfillment of the requirements for the degree of

**DOCTOR OF PHILOSOPHY (PhD.) IN PHYSICS**

Faculty of Natural and Agricultural Sciences

University of Pretoria

Hatfield Pretoria

August 2018

Supervisor/promoter: **Prof. N. I. Manyala**

## Declaration

I, Okikiola Olaniyan, hereby declare that the matter embodied in this thesis entitled “*Ab initio study of the beryllium-sulphur and beryllium-nitrogen co-doped graphene for nanoelectronic and optoelectronic devices*” is the result of the investigations carried out by me under the supervision of Prof. N. Manyala, in the Physics department at the University of Pretoria South Africa and that it has not been submitted elsewhere for the award of any degree or diploma. In keeping with the general practice of reporting scientific observations, due acknowledgment has been made whenever the work described is based on the findings of other investigators.

Signature.....

Date.....

## Abstract

Silicon and indium tin oxide (ITO) are the active components of the modern day devices. ITO is the most used transparent conducting material (TC) in smartphones and other touch panel devices, because the required properties of TCs such as low sheet resistance, high optical transparency, and stability found in ITO are difficult to match by other materials. However, due to its limited geographical availability, susceptibility to conductivity degradation, rising price and limited flexibility, which does not favour the demand for flexible devices, there is a need for an ideal replacement for ITO and likewise for silicon. Silicon has been the base material in microelectronics for over 49 years. However, as a result of the rising demand for miniaturized flexible devices further scaling of silicon for use in the active developing field of nanoelectronics might lead to performance restriction due to overheating and current leakage through the gate.

Graphene has a stable structure, high charge carrier mobility, good thermal conductivity, high optical transparency, and high tensile strength of 130.5 GPa. In fact, it is the strongest material ever to be tested. Due to these fascinating properties, graphene has been proposed as a potential replacement for silicon and ITO for use in nanoelectronic and optoelectronic devices. However, despite these outstanding properties, it has no band-gap which makes it unsuitable for a direct integration in nanoelectronic devices. Aside from these limitations, graphene also has high sheet resistance and lower conductivity compared to ITO. These drawbacks likewise limit its application as a TC.

Substitutional doping of graphene with heteroatoms has been extensively reported as a facile approach for tailoring the properties in order to increase its applicability range to the field of nanoelectronics and optoelectronics. Despite the gigantic stride that has been achieved through first-principles calculations in predicting nanomaterials that satisfy the aforementioned

applications, synthesizing experimentally such heteroatom-doped graphene with the required specifications remains a contending issue. As a result, other heteroatom-doped graphene are being explored to determine if they would be amenable for synthesis experimentally.

In this study, for the first time, *ab initio* calculations within the framework of density functional theory were performed to study the vibrational, electronic structure, structural and optical properties of beryllium/nitrogen (Be-N) and beryllium/sulphur (Be-S) co-doped graphene. It is observed that Be-S co-doped graphene is thermodynamically stable, has no metallic character and the band-gap can be tuned from zero to 0.7 eV by increasing the impurity concentration. A minimum band-gap of 0.4 eV is required for ON/OFF ratio in a transistor with graphene platform. Thus, the calculated value of the band-gap of Be-S co-doped graphene meets this specification. In addition, Be-N co-doped graphene was found to be also thermodynamically stable due to the absence of negative frequencies in the phonon dispersion. Interestingly, it exhibits both metallic and semiconducting character, and the band-gap can be tuned from zero up to 1.88 eV depending on the impurity concentration of the system. The presence of metallic character implies that the system is highly conductive as compared to pristine graphene. Moreover, the analysis of the optical spectrum shows that the system is transparent within the optical frequency of 7.0-10 eV for the parallel polarisation of the electromagnetic field irrespective of the impurity concentration. Thus, the interesting properties of Be-N co-doped graphene make it an alternative proposition as a replacement for ITO. However further research is needed to determine the work-function of this material to know if the application as a transparent electrode material in a photovoltaic is imminent. This study contributes to the on-going research of finding alternative nanomaterials to replace silicon and ITO for use in the field of nanoelectronics and optoelectronics respectively.

## **Dedication**

This thesis is dedicated to God almighty, and my sister, Mrs. C.E. Aiyedogbon. Thank you for your guidance, care, financial and moral support through all my degrees.

## Acknowledgements

I would like to acknowledge the people who in one way or the other contributed significantly to the success of this study.

First on this list is my supervisor, Prof. N. Manyala. I am grateful for his support, invaluable suggestion, constructive criticism, advice, and discussion in the course of this Ph.D. study.

My gratitude goes to the head of the department of physics, Prof. C. Theron for giving me jobs to supplement my finances especially during the first year of my study when I had a limited support. He also made available part of the resources that were used for this Ph.D. study.

Dr. A. Bello and Dr. B. Mutuma made themselves selflessly available to proofread the thesis and offered constructive comments on how to improve the write-up. Dr. J.K Dangbegnon was also very helpful. He read through some of the manuscripts, before they were published, and gave positive criticism which helped to reshape the study. As a result, I would like to thank them for their support.

I wish to thank Dr. E. Igumbor and Dr. R.E. Mapasha for introducing me to the practical Density Functional Theory (DFT) calculation which was the tool employed to obtain all the results in this thesis.

My sincere gratitude goes to Dr. N. Kunjuzwa for her kindness, support, care, and valuable friendship. This study has been interesting and memorable with you.

I am also thankful to Dr. J. Pretorius for giving me technical support and computer nodes to run all the calculations in this thesis without which this study would not have been successful.

The carbon technology research group members such as Dr. J. Madito, Dr. D.Y. Momodu, Dr. A.A Khaleed, Dr. F.O. Ochai-Ejeh, Dr. K. Oyedotun, Mrs. N. M. Ndiaye, Miss N. F. Sylla, and others, have been helpful, supportive, and inspiring. I am grateful to them for their encouragement and the useful discussion we had during this study.

Last but not the least, are my sister (mother) and family members. This study would not have been possible without their encouragement, moral support, prayers, unconditional love, and guidance. I would also like to express my appreciation to Dr. V. Sumanu for her encouragement, prayers, and care in the course of this study.

# Table of Contents

<b>List of figures</b> .....	xi
<b>List of Tables</b> .....	xiii
Chapter 1.....	1
<b>Introduction</b> .....	1
1.1 Background and motivation.....	1
1.2 Aims and objectives.....	4
1.3 Thesis outline.....	6
<b>References</b> .....	7
Chapter 2.....	10
<b>Literature Review</b> .....	10
2.1 Background of carbon material.....	10
2.2 Hybridization in carbon.....	11
2.2.1 Diamond— $sp^3$ hybridization.....	11
2.2.2 Graphene and graphite— $sp^2$ hybridization.....	12
2.3 Graphene.....	13
2.3.1 The graphene structure.....	13
2.3.2 The electronic properties of graphene.....	15
2.3.3 The electronic density of state (DOS) of graphene.....	17
2.3.4 The vibrational properties of graphene.....	18
2.3.5 The optical properties of graphene.....	22
2.4 Band-gap modification in graphene.....	28
2.5 The review of first-principles studies on graphene.....	30
<b>References</b> .....	35
Chapter 3.....	43
<b>Theoretical background</b> .....	43
3.1 The electronic structure calculations.....	44
3.1.1 Adiabatic or Born-Oppenheimer approximation [1].....	46
3.1.2 The variational principle.....	47
3.1.3 The Hartree approximation.....	48
3.1.4 The Hartree-Fock (HF) approximation.....	49



3.1.5	Density functional theory.....	51
3.1.6	Hohenberg-Kohn theorem .....	51
3.1.7	Kohn-Sham scheme .....	54
3.1.8	Kohn-Sham variational equations.....	56
3.2	The exchange-correlation energy .....	57
3.2.1	Local density approximation (LDA).....	58
3.2.2	The generalized gradient approximation (GGA) .....	59
3.2.3	The hybrid functionals .....	61
3.3	The electron-ion interaction .....	63
3.3.1	Pseudopotential method.....	64
3.4	Formalism of Kohn-Sham equation in momentum space.....	71
3.4.1	Energy cut-off.....	71
3.4.2	Brillouin zone sampling.....	72
3.4.3	Hellmann-Feynman forces.....	74
3.4.4	Self-Consistent iterative procedure.....	75
3.5	Geometry optimization.....	77
3.6	Computational code.....	77
	<b>References</b> .....	80
Chapter 4	.....	84
4.1	Introduction .....	84
4.2	Test of convergence .....	85
4.2.1	Test of convergence with respect to cut-off energy (Ecut).....	85
4.2.2	Test of convergence with respect to k-points mesh .....	87
4.2.3	Validation of the structural properties of graphene .....	88
4.3	Exploring the stability and electronic structure of beryllium and sulphur co-doped graphene: a first principles study .....	90
4.3.1	Introduction.....	90
4.3.2	Results and discussions.....	92
4.3.3	Concluding remarks .....	104
	<b>References</b> .....	105
4.4	A systematic study of the stability, electronic and optical properties of beryllium and nitrogen co-doped graphene.....	106
4.4.1	Introduction.....	106

4.4.2	Results and discussions.....	107
4.4.3	Concluding remarks.....	131
	<b>References</b> .....	132
4.5	Ab-initio study of the optical properties of beryllium-sulphur co-doped graphene.....	133
4.5.1	Introduction.....	133
4.5.2	Results and discussions.....	133
4.5.3	Concluding remarks.....	155
Chapter 5	.....	156
	<b>Concluding Remarks and Recommendations</b> .....	156
5.1	Conclusions.....	156
5.1.1	Dynamic stability of Be, N, and S doped graphene.....	156
5.1.2	Electronic structure of Be, N, and S doped graphene.....	157
5.1.3	Optical properties of Be, N, and S doped graphene.....	158
5.1.4	Applications.....	159
5.2	Recommendations.....	159
5.2.1	Methodology.....	159
5.2.2	Functionalization of graphene.....	160
5.2.3	Effect of Van der Waals on doped monolayer graphene.....	160
	<b>References</b> .....	162

# List of figures

FIGURE 1.1 THE UNIT CELL OF GRAPHENE HAS TWO CARBON ATOMS. THE TWO NON-EQUIVALENT SITES ARE DENOTED BY  $\alpha$  AND  $\beta$  WHERE  $\mathbf{a}$  AND  $\mathbf{b}$  DENOTE THE PRIMITIVE UNIT VECTORS-----2

FIGURE 2.1 (A) TETRAHEDRON  $sp^3$  HYBRIDIZATION OF CARBON ATOMS (B) THE UNIT CELL OF CARBON WITH THE DIAMOND STRUCTURE. ----- 12

FIGURE 2.2 (A)  $sp^2$  HYBRIDIZATION OF CARBON ATOMS (B) THE UNIT CELL OF GRAPHITE WITH ABA STACKING. --- 13

FIGURE 2.3 HONEYCOMB LATTICE OF GRAPHENE WITH  $\alpha$  and  $\beta$  SUBLATTICES WHERE  $\mathbf{a}_1$  AND  $\mathbf{a}_2$  ARE THE PRIMITIVE UNIT VECTORS OF THE SYSTEM. ----- 14

FIGURE 2.4 RECIPROCAL LATTICE OF GRAPHENE IN TWO DIMENSION WHERE  $\mathbf{a}_1^*$  AND  $\mathbf{a}_2^*$  ARE THE PRIMITIVE VECTORS. THE SHADED REGION DENOTES THE FIRST BZ WITH  $\Gamma$  CENTER AND OTHER UNIQUE HIGH SYMMETRY POINTS, KS AND MS. ----- 15

FIGURE 2.5 (A) 3D BANDSTRUCTURE OF GRAPHENE WITH ONE OF THE DIRAC POINTS BLOWN OUT OF PROPORTION. ADAPTED WITH THE PERMISSION FROM NETO [10].----- 16

FIGURE 2.6 THE DENSITY OF STATES (DOS),  $\rho$ , OF A MONOLAYER GRAPHENE SYSTEM AT DIFFERENT ENERGIES, E. REPRODUCED WITH THE PERMISSION FROM NETO [10].----- 18

FIGURE 2.7 THE CALCULATED PHONON CURVE OF PURE GRAPHENE (SOLID LINES) REF.[32], (THEORETICAL) (DASHED LINES) REF.[33] AND (RED SQUARES) (EXPERIMENTAL CURVE) REF.[34]. REPRODUCED WITH THE PERMISSION FROM MANN [32]. ----- 21

FIGURE 2.8 (A). THEORETICAL AND EXPERIMENTAL PERPENDICULAR DIELECTRIC FUNCTIONS ( $\epsilon_2 \perp$ ). THE SOLID LINE (REF.[59]) IS FROM THEORETICAL DATA, WHILE THE DOTTED (REF.[60]) AND THE DASHED (REF.[61]) LINES ARE FROM EXPERIMENTS. (B) THE THEORETICAL AND EXPERIMENTAL PARALLEL DIELECTRIC FUNCTIONS ( $\epsilon_2 \parallel$ ) OF GRAPHITE. THE SOLID LINE IS THE THEORETICAL  $\epsilon_2 \parallel$ , THE DOTTED AND THE DASHED LINES ARE THE EXPERIMENTAL VALUES OBTAINED FROM OPTICAL MEASUREMENT (REF.[62]) AND THE ELECTRON ENERGY LOSS SPECTRA (REF.[61]) RESPECTIVELY. REPRODUCED WITH THE PERMISSION FROM DANIEL [61] ----- 25

FIGURE 3.1 THE BLUE DASHED LINES SHOW A SCHEMATIC ILLUSTRATION OF ALL-ELECTRON POTENTIAL  $V \sim Z/r$  WITH THE CORRESPONDING VALENCE WAVE FUNCTION  $\Psi_V \sim z/r$  WHILE THE RED SOLID LINES REPRESENT THE PSEUDOPOTENTIAL  $V_{pseudo}$  AND THE CORRESPONDING PSEUDO  $\Psi_{pseudo}$ . REPRODUCED WITH PERMISSION FROM SCHWERDTFEGER [42].----- 65

FIGURE 3.2 A FLOW CHART ILLUSTRATING THE SELF-CONSISTENT FIELD (SCF) CALCULATION OF THE DFT----- 76

FIGURE 4.1 THE CONVERGENCE OF THE CALCULATED TOTAL ENERGIES OF THE UNIT CELL OF GRAPHENE AGAINST THE CUT-OFF ENERGIES. ----- 86

FIGURE 4.2 THE CALCULATED TOTAL ENERGY OF 2X2 SUPERCELL OF GRAPHENE AS A FUNCTION OF K-POINTS. --- 88

FIGURE 4.3 THE TOTAL ENERGY VS LATTICE PARAMETER OF GRAPHENE. THE RED FILLED SYMBOLS SHOW THE NUMERICALLY COMPUTED DATA POINTS WHILE THE BLACK CURVE SHOWS A POLYNOMIAL FIT OF THE DFT DATA. ----- 89

FIGURE 4.4 THE TOTAL ENERGY VS INTERLAYER SPACING BETWEEN TWO LAYERS OF GRAPHENE. ----- 90

FIGURE 4.5 THE DIFFERENT DOPING CONFIGURATIONS OF BE-S CO-DOPED MONO LAYER GRAPHENE ADOPTED IN THE STUDY. SITES A1, B1, C2, ETC. ARE THE SAME SUBLATTICES OCCUPIED BY BE-ATOM (BLUE COLOUR) WHILE SITE O IS A FIXED POSITION OCCUPIED BY S-ATOM (YELLOW COLOUR). ONLY A PAIR OF BE AND S IS CONSIDERED AT A TIME IN EACH RUN. ----- 92

## List of Tables

TABLE 3.1 THE CALCULATED AND EXPERIMENTAL BAND-GAPS OF SOME SELECTED MATERIALS ----- 63

## Abbreviations Used in the Thesis

2D – two dimensional

Al – aluminum

Al<sub>2</sub>O<sub>3</sub> – aluminum (III) oxide

As – arsenic

B – boron

BG – B-doped graphene

BSG – B-S co-doped graphene

Be – beryllium

BeNG – Be-N co-doped graphene

BeSG – Be-S co-doped graphene

BLYP – Becke-Lee-Yang-Parr

B3LYP – 3 parameter

BN – boron nitride

BSE – Bethe-Salpeter equation

BZ – Brillouin zone

C – carbon

Cd – cadmium

CNT – carbon nanotube

CNT – carbon nanotubes

DFPT – density-functional perturbation theory

DFT – density-functional theory

DOS – density of states

*E* – external electric field

*E<sub>cut</sub>* – energy cut-off

EELS – electron loss spectroscopy

*E<sub>f</sub>* – formation energy

EM – electromagnetic  
 $E_{XC}$  – exchange-correlation energy  
F – fluorine  
fcc – face-centered cubic  
Fe – iron  
FE – formation energy  
FET – field effect transistor  
Ga – gallium  
Ge – germanium  
GGA – generalized gradient approximation  
GIC – graphite intercalation compounds  
 $GW$  – Green's function ( $G$ ) times screened interaction ( $W$ ) approximation to the 1-electron self-energy  
H – hydrogen  
 $H_2O$  – water  
h-BN – hexanol boron nitride  
HF – Hartree-Fock  
HK – Hohenberg-Kohn  
HREELS – high resolution electron-energy-loss spectroscopy  
HSE06 – Heyd, Scuseria, and Ernzerhof 2006 hybrid functional  
IBZ – irreducible Brillouin zone  
In – indium  
IR – infrared  
ITO – indium tin oxide  
IXS – inelastic x-ray scattering  
LA – longitudinal acoustic  
LCD – liquid crystal display  
LDA – local density approximation  
LFE – local field effect

LO – longitudinal optical  
LR – long-range  
LSDA – local spin density approximation  
N – nitrogen  
4NNFC – fourth nearest-neighbor force constant  
NG – nitrogen-doped graphene  
NO – nitrogen dioxide  
O – oxygen  
OER – oxygen evolution reaction  
OLED – organic light emitting diode  
ORR – oxygen reduction reactions  
P – phosphorus  
PAW – projected augmented wave  
Pb – lead  
PBE – Perdew-Burke-Ernzerhof  
PDOS – partial density of states  
PW91 – Perdew-Wang 1991  
RIXS – resonant inelastic X-ray scattering  
RPA – random-phase approximation  
S – sulphur  
Sb – antimony  
scf – self-consistent field  
SCF – self-consistent field  
Se – selenium  
SG – sulphur-doped graphene  
Sn – tin  
Si – silicon  
SiC – silicon carbide



SiO<sub>2</sub> – silicon (VI) oxide  
SNG – sulphur-nitrogen-graphene  
SR – short-range  
STM – scanning tunneling microscopy  
SWCNT – single-walled carbon nanotube  
TA – transverse acoustic  
TC – transparent conductor  
TCs – transparent conductors  
TCNE – tetracyanoethylene  
Te – tellurium  
TO – transverse optical  
USPP – ultrasoft pseudopotential  
UV – ultraviolet  
VASP – Vienna Ab initio Simulation Package  
w.r.t. – with respect to  
XAS – X-ray absorption spectroscopy  
XES – X-ray emission spectroscopy  
ZA – out-of-plane acoustic  
ZO – out-of-plane optical  
Zn – zinc

## Articles

- 1) E. Igumbor, O. Olaniyan, R.E. Mapasha, H.T. Danga, E. Omotoso, and W.E. Meyer, “Induced defect levels of P and Al vacancy-complexes in 4H-SiC: A hybrid functional study”, *J. Mater. Sci. Semicond. Proc.* **89**, 77 (2019).
- 2) O. Olaniyan, R.E. Mapasha, M.J. Madito, A.A. Khaleed, E. Igumbor, N.I. Manyala, “A systematic study of the stability, electronic and optical properties of beryllium and nitrogen co-doped graphene”, *Carbon* **129**, 207 (2018).
- 3) F. Ochai-Ejeh, M.J. Madito, K. Makgopa, M.N. Rantho, O. Olaniyan, and N. Manyala, “Electrochemical performance of hybrid supercapacitor device based on birnessite-type manganese oxide decorated on uncapped carbon nanotubes and porous activated carbon nanostructures”, *Electrochem. Acta*, **289**, 363 (2018).
- 4) E. Igumbor, O. Olaniyan, R.E. Mapasha, H.T. Danga, E. Omotoso, and W.E. Meyer, “Electrically active induced energy levels and metastability of B and N vacancy-complexes in 4H-SiC”, *J. Phys. Cond. Matt.* **30**, 185702 (2018).
- 5) A.A. Khaleed, A. Bello, J.K. Dangbegnon, M.J. Madito, O. Olaniyan, F. Barzegar, K. Makgopa, K.O. Oyedotun, B.W. Mwakikunga, S.C. Ray, and N.I. Manyala, “Solvothermal synthesis of surfactant free spherical nickel hydroxide/graphene oxide composite for supercapacitor application”, *J. Alloys Compounds* **721**, 80 (2017).
- 6) A.A. Khaleed, A. Bello, J.K. Dangbegnon, D.Y. Momodu, M.J. Madito, F.U. Ugbo, A.A. Akande, B.P. Dhonge, F. Barzegar, O. Olaniyan, B.W. Mwakikunga, and N. Manyala, *J. Alloys Compounds* **694**, 155 (2017).
- 7) D. Momodu, M. Madito, F. Barzegar, A. Bello, A. Khaleed, O. Olaniyan, J. Dangbegnon, and N. Manyala, “Activated carbon derived from tree bark biomass with promising material properties for supercapacitors”, *J. Solid State Electrochem.* **21**, 589 (2017).
- 8) F.O. Ochai-Ejeh, M.J. Madito, D.Y. Momodu, A.A. Khaleed, O. Olaniyan, and N. Manyala, “High performance hybrid supercapacitor device based on cobalt manganese layered double hydroxide and activated carbon derived from cork (*Quercus Suber*)”, *Electrochem. Acta* **252**, 41 (2017).
- 9) A.A. Khaleed, A. Bello, J.K. Dangbegnon, F.U. Ugbo, F. Barzegar, D.Y. Momodu, M.J. Madito, T.M. Masikhwa, O. Olaniyan, and N. Manyala, “A facile hydrothermal reflux synthesis of Ni(OH)<sub>2</sub>/GF electrode for supercapacitor application”, *J. Mater. Sci.* **51**, 6041 (2016).
- 10) O. Olaniyan, R.E. Mapasha, D.Y. Momodu, M.J. Madito, A.A. Khaleed, F.U. Ugbo, A. Bello, F. Barzegar, K.O. Oyedotun, N.I. Manyala, “Exploring the stability and electronic structure of beryllium and Sulphur co-doped graphene: a first principles study”, *Carbon* **6**, 88392 (2016).

# Chapter 1

## Introduction

### 1.1 Background and motivation

The discovery of graphene and the realization of its remarkable properties have sparked intense research interest in the field of nanoelectronics and optoelectronics as it has been lauded as a promising replacement for both silicon (Si) and indium tin oxide (ITO) in future flexible nanoscale devices. Graphene is a two dimensional (2D) hexagonal sheet of  $sp^2$  hybridized carbon atoms. The two carbon atoms ( $\alpha$  and  $\beta$ ) of the unit cell are in non-equivalent positions forming two interpenetrating triangular sublattices as shown in Figure 1.1 The unit cell of graphene has two carbon atoms. The two non-equivalent sites are denoted by  $\alpha$  and  $\beta$  where  $\vec{a}$  and  $\vec{b}$  denote the primitive unit vectors. It is well-known to be the basic and integral part of other graphitic carbon materials such as carbon nanotubes, fullerenes (buckyball) and graphite [1]–[4]. Graphene’s existence was predicted theoretically by P.R. Wallace in 1947 [1]. However, it was considered to be unstable due to the thermal fluctuations [3], [5], in what was popularly known as the Landau-Peierls arguments. Interestingly, in 2004, Novoselov *et al.*[6] isolated graphene from ordered pyrolytic graphite through micromechanical exfoliation (often referred to as the scotch-tape method). Ever since the isolation, the material has gained widespread attention among researchers due to its exceptional properties. That is, it is known to be stable [7], mechanically strong [8], have a high charge carrier mobility [4], [9]–[12], excellent thermal conductivity [13], [14], together with the outstanding electrical [1] and optical characteristics [8], [9], [15], [16].

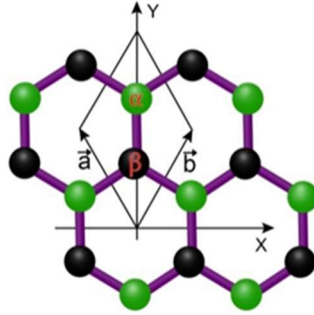


**Figure 1.1** The unit cell of graphene has two carbon atoms. The two non-equivalent sites are denoted by  $\alpha$  and  $\beta$  where  $\vec{a}$  and  $\vec{b}$  denote the primitive unit vectors

Flexible and stretchable electronic components are more useful than the rigid ones and are sought after for device applications (such as displays, solar cells, light emitters, and touch panels). In optoelectronic devices, transparent conductors (TCs) are the active components and are typically made from ITO simply because of its relatively low sheet resistance and optical transparency. However, ITO is limited in supply, expensive, and suffers from poor mechanical strength which compromises the rising demand for flexible nanoscale devices. Due to the poor mechanical properties, when bent or stretched, the material tends to crack leading to the degradation of the electrical properties. As a result of these drawbacks, there is a need for an alternative to ITO and similarly Si for use in the future nanoscale devices. For Si, which is often used in conjunction with ITO in some devices, the technology is at the critical stage and further scaling of the component might lead to overheating and consequently performance restriction. Due to the extraordinary properties, graphene has emerged as an ideal material to overcome the limitations suffered by both Si and ITO. However, graphene has a relatively high sheet resistance as compared to ITO [17], and this shortcoming limits its application as a TC material. The 2D

material also has no band-gap which makes it difficult for a direct integration in nanoelectronic devices.

There are different approaches (superstructure fabrication, functionalization, application of electric field, deposition of graphene on a substrate, heteroatom doping ) [18]–[20] that could be employed to open up an electronic energy gap in graphene. Out of these approaches, doping of graphene with heteroatoms is often the preferred technique because impurities are the major scatterers that control the intrinsic electronic and transport properties of crystals. As such, this method, which is also known as chemical doping, could be used to create a sizeable band-gap in graphene (by symmetry breaking) while reducing the sheet resistance as a result of the increase in the carrier concentration. Heteroatoms doping of graphene means an act of replacing the carbon atoms of graphene with any elements in the periodic table, apart from the carbon, hydrogen, and elements with filled valence shells. Although nitrogen (N) and boron (B) atom are the natural substitutes for the carbon atoms of graphene as a result of the size of their atomic radii, which are almost equal to that of a carbon atom, other light elements such as beryllium (Be) and sulphur (S) are being investigated to tailor the properties of graphene. While light elements like N [21], [22], B [21], [23], Be [23], etc. have been studied from the first-principles to tailor the properties of graphene, this research area is far from being exhausted. Since the electronic and optical properties of graphene could be altered by the type and amount of the heteroatoms present in the matrix, a new study could be directed at investigating the effect of the above named heteroatoms co-doping (i.e. using a pair of dissimilar atoms simultaneously) of graphene on the stability, electronic and optical properties of the system. For example, the electronic and optical properties of systems like Be-S and Be-N co-doped graphene have rarely been studied.

In this thesis, for the first time, *ab initio* calculations within the framework of density functional theory (DFT), as implemented in Vienna *ab initio* Simulation Package (VASP) [24], [25], were performed to study the vibrational, electronic, structural and optical properties of Be-N and Be-S co-doped graphene for potential applications in nanoelectronic and optoelectronic devices. Moreover, the isomerization and the impurity concentration effects on the aforementioned properties of the systems were taken into consideration. The method that replaces the chemical inert core of electrons with pseudopotentials was employed for the calculations. Frequently used pseudopotentials are the ultrasoft [26], the norm-conserving [27] and the projector-augmented wave (PAW) [28] pseudopotentials. The latter, which was introduced by Blöchl and the most popular, was used in this study. The use of DFT involves the specification of an exchange-correlation functional in order to compute the ground state energy of the system. These functionals could be classified as the local density approximation (LDA) [29], generalised gradient approximation (GGA) (e.g. Perdew, Burke and Ernzerhof (PBE)) [30], and range-separated hybrid functionals (e.g. Heyd, Scuseria, and Ernzerhof (HSE)) [31] to name but a few. The two exchange-correlation functionals that were used in this study are the GGA and HSE. While the GGA usually gives an acceptable result for the lattice constant of semiconductors, it often underestimates the band-gaps [32]. In contrast, HSE usually gives accurate results of the band-gap of semiconductors [32]. For the optical properties of the systems, the linear dielectric response was calculated using first-order time-dependent perturbation theory within the dipole approximation [33].

## **1.2 Aims and objectives**

The aim of this study is to explore the stability, electronic and optical properties of pristine and Be-S and Be-N co-doped graphene from the first-principles within the framework of density

functional theory for prospective applications in nanoelectronic and optoelectronic devices. In order to achieve this aim, the research will be conducted to attain the following objectives:

1. A test of convergence will be performed with respect to the kinetic energy cut-off to determine the accurate Kohn-Sham orbitals in the plane wave basis.
2. Calculation of the right k-points for the Brillouin zone sampling of all the systems will also be performed.
3. Structural optimisation of the systems will be performed in order to get the right equilibrium lattice constant and bond length to be used in the rest of the calculations.
4. The defect formation energy of the doped graphene will be investigated to understand how the impurities in the system prefer to co-exist.
5. Phonon calculation at 0 K will be performed to assess if the heteroatom-doped graphene at different impurity concentration are dynamically stable.
6. The electronic properties, such as total densities of state and band structures of the systems will be calculated in order to determine their electrical conductivities.
7. The dielectric response in the long wavelength limit of all the systems of study will be calculated in order to analyze their corresponding optical properties.
8. All the results of this study, where necessary, will be compared with the data from the literature for the purpose of validation.

### 1.3 Thesis outline

This thesis is sectioned into five chapters as follows:

Chapter 1 gives the motivation of the study, aims, and objectives of the thesis.

Chapter 2 presents a brief technical background on the structural, electronic and optical properties of graphene along with the relevant past studies in the literature.

Chapter 3 provides a brief overview of the theoretical background of density functional theory along with the implementation that is relevant to this thesis.

Chapter 4 contains the results and discussion of the study.

4.2. The tests of convergence with respect to k-point and energy cut-off were discussed.

4.3. The stability and electronic structures of beryllium and sulphur co-doped graphene are discussed.

4.4. The dynamic stability, electronic and optical properties of beryllium and nitrogen co-doped graphene are presented.

4.5. The lattice dynamics and optical properties of beryllium and sulphur co-doped graphene are reported.

Chapter 5 gives general concluding remarks and future prospects that might emanate from the study.



## References

- [1] P. R. Wallace, “The Band Theory of Graphite,” *Phys. Rev.*, vol. 71, no. 9, pp. 622–634, May 1947.
- [2] R. Saito, G. Dresselhaus, and M. Dresselhaus, "*Physical properties of carbon nanotubes*". 1998.
- [3] A. K. Geim and K. S. Novoselov, “The rise of graphene,” *Nat. Mater.*, vol. 6, no. 3, pp. 183–191, Mar. 2007.
- [4] A. H. C. Neto, F. Guinea, N. M. R. Peres, A. H. Castro Neto, N. M. R. Peres, K. S. Novoselov, A. K. Geim, A. H. C. Neto, F. Guinea, N. M. R. Peres, K. S. Novoselov, and A. K. Geim, “The electronic properties of graphene,” *Rev. Mod. Phys.*, vol. 81, no. 1, pp. 109–162, Jan. 2009.
- [5] J. C. Meyer, A. K. Geim, M. I. Katsnelson, K. S. Novoselov, T. J. Booth, and S. Roth, “The structure of suspended graphene sheets,” *nature.com*, vol. 446, no. March, 2007.
- [6] K. S. Novoselov, A. K. Geim, S. V. Morozov, D. Jiang, Y. Zhang, S. V. Dubonos, I. V. Grigorieva, and A. A. Firsov, “Electric field in atomically thin carbon films,” *Science*, vol. 306, no. 5696, pp. 666–669, Oct. 2004.
- [7] N. Savage, “Materials science: Super carbon,” *Nature*, vol. 483, no. 7389, pp. S30–S31, Mar. 2012.
- [8] A. H. C. Neto and K. Novoselov, “New directions in science and technology: Two-dimensional crystals,” *Reports Prog. Phys.*, vol. 74, no. 8, p. 082501, Aug. 2011.
- [9] K. S. Novoselov, A. K. Geim, S. V. Morozov, D. Jiang, M. I. Katsnelson, I. V. Grigorieva, S. V. Dubonos, and A. A. Firsov, “Two-dimensional gas of massless Dirac fermions in graphene,” *Nature*, vol. 438, no. 7065, pp. 197–200, Nov. 2005.
- [10] J. Chen, C. Jang, S. Xiao, M. Ishigami, and M. S. Fuhrer, “Intrinsic and Extrinsic Performance Limits of Graphene Devices on SiO<sub>2</sub>,” *Nat. Nanotechnol.*, vol. 3, no. 4, pp. 206–209, Apr. 2007.
- [11] S. V. Morozov, K. S. Novoselov, M. I. Katsnelson, F. Schedin, D. C. Elias, J. A. Jaszczak, and A. K. Geim, “Giant intrinsic carrier mobilities in graphene and its bilayer,” *Phys. Rev. Lett.*, vol. 100, no. 1, p. 016602, Jan. 2008.
- [12] D. A. Siegel, C. Park, C. Hwang, J. Deslippe, A. V. Fedorov, S. G. Louie, and A. Lanzara, “Many-body interactions in quasi-freestanding graphene,” *Proc. Natl. Acad. Sci.*, vol. 108, no. 28, pp. 11365–11369, Jul. 2011.
- [13] A. A. A. Balandin, S. Ghosh, W. Bao, I. Calizo, D. Teweldebrhan, F. Miao, and C. N. Lau, “Superior thermal conductivity of single-layer graphene,” *Nano Lett.*, vol. 8, no. 3, pp. 902–907, Mar. 2008.
- [14] M. E. Pumarol, M. C. Rosamond, P. Tovee, M. C. Petty, D. A. Zeze, V. Falko, and O. V. Kolosov, “Direct Nanoscale Imaging of Ballistic and Diffusive Thermal Transport in

- Graphene Nanostructures,” *Nano Lett.*, vol. 12, no. 6, pp. 2906–2911, Jun. 2012.
- [15] S. Chen, Q. Wu, C. Mishra, J. Kang, H. Zhang, K. Cho, W. Cai, A. A. Balandin, and R. S. Ruoff, “Thermal conductivity of isotopically modified graphene,” *Nat. Mater.*, vol. 11, no. 3, pp. 203–207, Mar. 2012.
- [16] J. Rafiee, X. Mi, H. Gullapalli, A. V. Thomas, F. Yavari, Y. Shi, P. M. Ajayan, and N. A. Koratkar, “Wetting transparency of graphene,” *Nat. Mater.*, vol. 11, no. 3, pp. 217–222, Mar. 2012.
- [17] M. F. Craciun, T. H. Bointon, and S. Russo, “Is graphene a good transparent electrode for photovoltaics and display applications,” *IET Circuits, Devices Syst.*, vol. 9, no. 6, pp. 403–412, Nov. 2015.
- [18] L. L. Zhang, X. Zhao, H. Ji, M. D. Stoller, L. Lai, S. Murali, S. McDonnell, B. Cleveger, R. M. Wallace, and R. S. Ruoff, “Nitrogen doping of graphene and its effect on quantum capacitance, and a new insight on the enhanced capacitance of N-doped carbon,” *Energy Environ. Sci.*, vol. 5, no. 11, p. 9618, Oct. 2012.
- [19] E. Cruz-Silva, Z. M. Barnett, B. G. Sumpter, and V. Meunier, “Structural, magnetic, and transport properties of substitutionally doped graphene nanoribbons from first principles,” *Phys. Rev. B*, vol. 83, no. 15, p. 155445, Apr. 2011.
- [20] P. Shemella and S. K. S. Nayak, “Electronic structure and band-gap modulation of graphene via substrate surface chemistry,” *Appl. Phys. Lett.*, vol. 94, no. 3, p. 032101, Jan. 2009.
- [21] P. Nath, D. Sanyal, and D. Jana, “Semi-metallic to semiconducting transition in graphene nanosheet with site specific co-doping of boron and nitrogen,” *Phys. E: Low-Dimensional Syst. Nanostructures*, vol. 56, pp. 64–68, 2014.
- [22] P. Nath, S. Chowdhury, D. Sanyal, and D. Jana, “Ab-initio calculation of electronic and optical properties of nitrogen and boron doped graphene nanosheet,” *Carbon N. Y.*, vol. 73, pp. 275–282, 2014.
- [23] A. Hussain, S. Ullah, and M. Farhan, “Fine tuning of band-gap of graphene by atomic and molecular doping: A density functional theory study,” *RSC Adv.*, vol. 6, pp. 55990–56003, 2016.
- [24] G. Kresse and J. Hafner, “Ab initio molecular-dynamics simulation of the liquid-metal–amorphous-semiconductor transition in germanium,” *Phys. Rev. B*, vol. 49, no. 20, pp. 14251–14269, May 1994.
- [25] G. Kresse and J. Furthmüller, “Efficiency of ab-initio total energy calculations for metals and semiconductors using a plane-wave basis set,” *Comput. Mater. Sci.*, vol. 6, no. 1, pp. 15–50, Jul. 1996.
- [26] G. Kresse and D. Joubert, “From ultrasoft pseudopotentials to the projector augmented-wave method,” *Phys. Rev. B*, vol. 59, no. 3, pp. 1758–1775, Jan. 1999.
- [27] D. R. Hamann, “Generalized norm-conserving pseudopotentials,” *Phys. Rev. B*, vol. 40, no. 5, pp. 2980–2987, Nov. 1989.

- [28] P. E. Blöchl, “Projector augmented-wave method,” *Phys. Rev. B*, vol. 50, no. 24, pp. 17953–17979, Dec. 1994.
- [29] W. Kohn and L. J. Sham, “Self-consistent equations including exchange and correlation effects,” *Phys. Rev.*, vol. 140, no. 4A, pp. A1133–15 Nov. 1965.
- [30] J. P. Perdew, K. Burke, and M. Ernzerhof, “Generalized Gradient Approximation Made Simple,” *Phys. Rev. Lett.*, vol. 77, no. 18, pp. 3865–3868, Oct. 1996.
- [31] A. V. Krukau, O. A. Vydrov, A. F. Izmaylov, and G. E. Scuseria, “Influence of the exchange screening parameter on the performance of screened hybrid functionals,” *J. Chem. Phys.*, vol. 125, no. 22, p. 224106, Dec. 2006.
- [32] V. Barone, O. Hod, J. E. Peralta, and G. E. Scuseria, “Accurate prediction of the electronic properties of low-dimensional graphene derivatives using a screened hybrid density functional,” *Acc. Chem. Res.*, vol. 44, no. 4, pp. 269–279, Apr. 2011.
- [33] M. Gajdoš, K. Hummer, G. Kresse, J. Furthmüller, and F. Bechstedt, “Linear optical properties in the projector-augmented wave methodology,” *Phys. Rev.*, vol. 73, no. 4, pp. 045112, Jan. 2006.

## Chapter 2

### Literature Review

This chapter presents a brief technical background on the structural, electronic and optical properties of graphene along with the relevant past studies in the literature.

#### 2.1 Background of carbon material

Discovered through exploration earlier as charcoal, carbon was famously named by A.L. Lavoisier in 1789 [1] and is commonly found in nature. It occupies the group IV of period III of the periodic table. The atom is made up of 6 protons, 6 electrons, and “A” neutrons which can assume any of 6, 7 and 8 value to form the isotopes  $^{12}\text{C}$ ,  $^{13}\text{C}$ , and  $^{14}\text{C}$ , respectively. While the first two isotopes are stable,  $^{12}\text{C}$  with a nuclear spin  $I=0$  is the most abundant with 99% occurrence among the carbon isotopes in nature.  $^{13}\text{C}$ , with a nuclear spin  $I=1/2$ , is the next with 1% of all carbon atoms.  $^{14}\text{C}$  rarely occurs; nevertheless, it is vital for archaeological dating to estimate the biological activity of organic materials. In general, carbon has many allotropes such as graphite, diamond, fullerene, carbon nanotubes (CNTs), and graphene. Thermodynamically, all the allotropes formed by carbon are stable and the carbon can react under a high temperature with oxygen to form carbon dioxide [2].

In the ground state, the configuration of the 6 electrons is given as  $1s^2 2s^2 2p^2$ . The inner shell (1s) is occupied by two electrons and does not take part in chemical reactions. The remaining 4 electrons occupy 2s and 2p orbitals. Since the energy of the 2p orbitals ( $p_x$ ,  $p_y$ , and  $p_z$ ) is 4 eV higher than 2s, the 2p orbital is filled with the last two electrons after 2 s. However, it is energetically more favourable to promote one electron from 2s to  $2p_z$ , in order to be able to form covalent bonds with other atoms such as H, O, C and etc. The energy gained from such covalent

bond is higher than 4 eV that must be overcome in the electronic excitation. In the excited state, four equivalent quantum orbitals  $2s$ ,  $2p_x$ ,  $2p_y$  and  $2p_z$  are formed. The superposition of the state  $|2s\rangle$  with  $n$   $|2p_j\rangle$  states is termed  $sp^n$  hybridization. Where  $n=1, 2$  or  $3$  and  $j=x, y$ , or  $z$ .

## 2.2 Hybridization in carbon

### 2.2.1 Diamond— $sp^3$ hybridization

The superposition of  $2s$  and all the three  $2p$  orbitals form  $sp^3$  hybridization. An example of this hybridization is diamond and the carbon atoms are bonded together to form a tetrahedron (see Figure 2.1 (a)). The crystal lattice contains two interpenetrating face-centred-cubic (fcc) lattices with a lattice constant of 0.357 nm as shown in Figure 2.1 (b). Diamond is one of the hardest natural materials ever observed because all the bonds are  $\sigma$ -bonds. It is reported to have a high bulk modulus of 443 GPa [3] and Young's modulus of 1050 GPa [4], [5]. Due to the fact that all the valence electrons are employed in the formation of  $\sigma$ -bonds, diamond is an insulator with a large band-gap of 5.47 eV [6]. As a result, the thermal conductivity is within 1000–2200  $W.m^{-1}.K^{-1}$  [7]. The applications involving the use of diamond tends to explore the hardness and the low electrical conductivity of the material. For instance, in most industrial applications, it is used for drilling, cutting, polishing, grinding, etc.

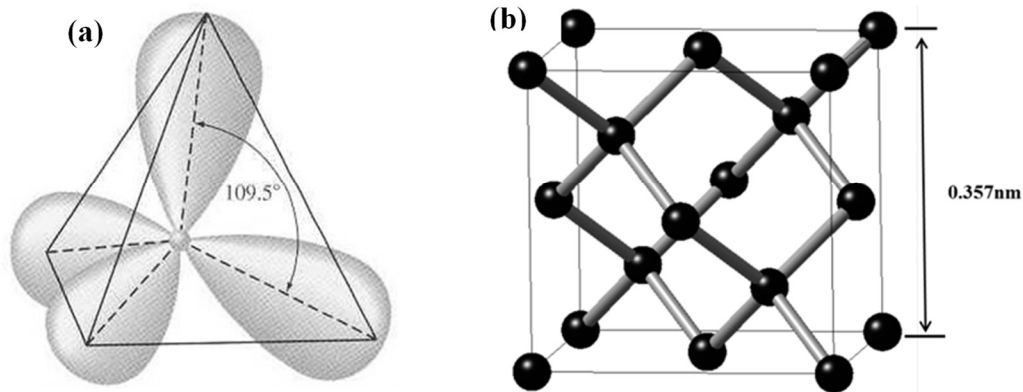


**Figure 2.1** (a) Tetrahedron  $sp^3$  hybridization of carbon atoms (b) the unit cell of carbon with the diamond structure.

### 2.2.2 Graphene and graphite— $sp^2$ hybridization

The superposition of the  $2s$  and the two of  $2p$  orbitals ( $|2p_x\rangle$  and  $|2p_y\rangle$  states) would result in the formation of planar  $sp^2$  hybridization (Figure 2.2 (a)). While these orbitals are aligned in the  $xy$ -plane with  $120^\circ$  mutual angles between them, the  $2p_z$  hybridized orbital is oriented perpendicular to the plane. A noticeable example of this hybridization is graphene, a layer of graphite (Figure 2.2 (b)). Multiple layers of graphene would form graphite when they are stacked together with the ABAB... sequence (see Figure 2.2 (b)). All the layers of graphite are loosely bounded via the weak Van der Waals force which accounts for the softness of graphite. The delocalized electron from each of the carbon atom forms a  $\pi$ -electron cloud which makes graphite an electrical conductor. The bond length between the carbon atoms is  $1.42 \text{ \AA}$  and the interlayer distance is  $3.34 \text{ \AA}$  [8]. It is anisotropic [9] due to the in-plane metallic bonding, has good electrical and thermal conductivity along the plane of the layers. However, it is a poor electrical and thermal conductor along the perpendicular to the plane of the layers due to the presence of the weak Van

der Waals forces. Unlike diamond, graphite electrical conductivity enables it to be useful as electrochemical electrodes and electric brushes.

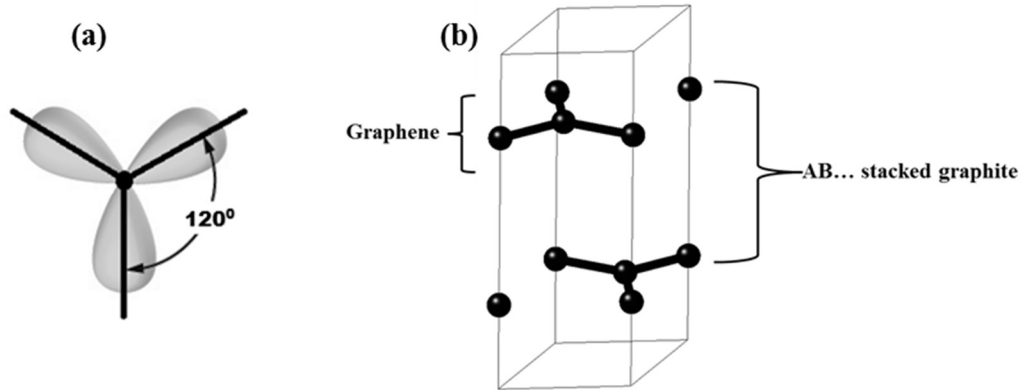


**Figure 2.2** (a)  $sp^2$  hybridization of carbon atoms (b) the unit cell of graphite with ABA stacking.

## 2.3 Graphene

### 2.3.1 The graphene structure

As mentioned earlier, the carbon atoms in graphene formed honeycomb lattice due to  $sp^2$  hybridization. The honeycomb is not a Bravais lattice due to the non-equivalent neighboring lattice sites. Graphene has two sublattices,  $\alpha$ , and  $\beta$ . Figure 2.3 shows that any site on the A sublattice has three nearest neighbors (nn) in the direction of the north-west, north-east, and south, while south-east, south-west, and north are the directions of the nn of a site on the sublattice B.

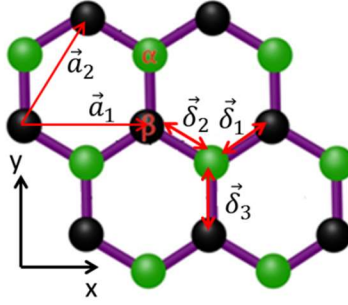


**Figure 2.3** Honeycomb lattice of graphene with  $\alpha$  and  $\beta$  sublattices where  $\vec{a}_1$  and  $\vec{a}_2$  are the primitive unit vectors of the system.

However,  $\alpha$  and  $\beta$  are triangular [10], [11] Bravais lattices, as such the honeycomb lattice could be described as a triangular Bravais lattice with two atoms per unit cell. The shortest distance between any two closest carbon atoms is 0.142 nm. The three vectors ( $\vec{\delta}_1$ ,  $\vec{\delta}_2$ , and  $\vec{\delta}_3$ ) connecting any site on the sublattice  $\alpha$  with the nn on the sublattice  $\beta$  are given by equation (2.1):

$$\vec{\delta}_1 = \frac{a}{2}(\sqrt{3}\hat{e}_x + \hat{e}_y), \quad \vec{\delta}_2 = \frac{a}{2}(-\sqrt{3}\hat{e}_x + \hat{e}_y), \quad \vec{\delta}_3 = -a\hat{e}_y \quad (2.1)$$

while the primitive vectors for the triangular Bravais lattice is expressed using equation (2.2)

$$\vec{a}_1 = \sqrt{3}a\hat{e}_x; \quad \vec{a}_2 = \frac{\sqrt{3}a}{2}(\hat{e}_x + \sqrt{3}\hat{e}_y) \quad (2.2)$$

The average carbon-carbon distance is denoted by “a” in both equation (2.1) and (2.2) and it is about 1.42 Å. The modulus of the primitive vectors yields the lattice constant,  $|\vec{a}_1| = |\vec{a}_2| = 2.46$  Å while the area of the unit cell  $A_{\text{ucel}} = \frac{3}{2}\sqrt{3} a^2 = 0.051 \text{ nm}^2$ . The density of the carbon atoms is, thus,  $n_c = \frac{2}{A_{\text{ucel}}} = 39 \text{ nm}^{-2}$ . This number is equal to the  $\pi$ -electron density in graphene since there is one  $\pi$ -electron per carbon atom in graphene.

The reciprocal lattice of graphene, which is defined in relation to the triangular Bravais lattice, is shown in Figure 2.4. It is spanned by the vectors in equation (2.3):



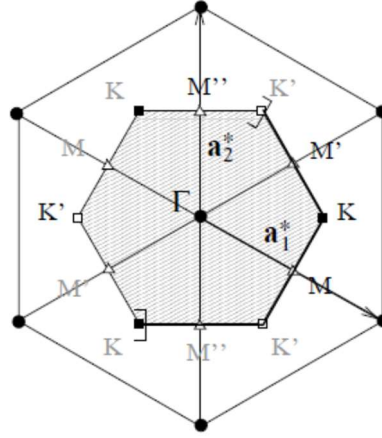


**Figure 2.4** Reciprocal lattice of graphene in two dimension where  $\vec{a}_1^*$  and  $\vec{a}_2^*$  are the primitive vectors. The shaded region denotes the first BZ with  $\Gamma$  center and other unique high symmetry points, Ks and Ms.

$$\vec{a}_1^* = \frac{2\pi}{\sqrt{3}a} \left( \hat{e}_x - \frac{\hat{e}_y}{\sqrt{3}} \right) \text{ and } \vec{a}_2^* = \frac{4\pi}{3a} \hat{e}_y \quad (2.3)$$

where  $\vec{a}_1^*$  and  $\vec{a}_2^*$  are the reciprocal lattice vectors. The shaded part, indicates the first Brillouin zone (BZ) as shown in Fig 2.4, showing a set of non-equivalent points in the reciprocal space. At the centre of the BZ, which is designated as the  $\Gamma$  point, the long wavelength excitations are found within the vicinity. Other points such as Ms, and Ks are other high-symmetry K-points of which K and  $K'$  are represented as:

$$\pm \vec{K} = \pm \frac{4\pi}{3\sqrt{3}a} \hat{e}_x \quad (2.4)$$

### 2.3.2 The electronic properties of graphene

The touching of the valence and conduction bands at the Dirac points makes graphene a zero-gap semiconductor (see Figure 2.5). The Dirac points are points on the edge of the Brillouin zone in the momentum space. There are three pairs of Dirac points. With symmetry, the points could be reduced to a pair of independent K and  $K'$  point. In the low energies region, which is essential in the electron transport, the bands have a linear dispersion relation and the band structure

could be regarded as two cones touching at the Dirac point (see Figure 2.5). The electrons within 1 eV of the Dirac energy possess a linear dispersion relation. This linear dispersion relation is well-expressed by the Dirac equation for massless fermions.

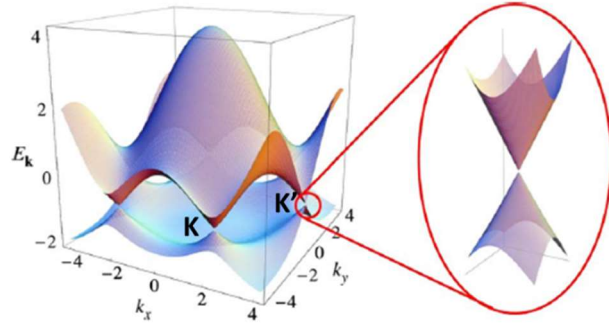


**Figure 2.5** (a) 3D bandstructure of graphene with one of the Dirac points blown out of proportion. Adapted with the permission from Neto [10].

This implies that the effective mass of the charge carriers in this energy region is zero. Generally, the dispersion relation around the K points is expressed as:

$$E_{\pm}(k) \approx \pm \hbar v_f |k - K| \quad (2.5)$$

Equation (2.5) is related to the spectrum of the Dirac Hamiltonian for low-energy Dirac particle and it is expressed as follows:

$$\mathcal{H}_K = \hbar v_F \begin{pmatrix} 0 & k_x - ik_y \\ k_x + ik_y & 0 \end{pmatrix} = \hbar v_F \vec{\sigma} \cdot \vec{k} \quad (2.6)$$

Equation (2.6) is simply the tight binding result [12] expanded in the vicinity of K while the corresponding equation close to point K' is given by equation (2.7).

$$\mathcal{H}_{K'} = \hbar v_F \vec{\sigma}^* \cdot \vec{k} \quad (2.7)$$

where  $\vec{\sigma}$  is the Pauli matrices in two dimensions, \* represents the complex conjugate,  $v_F \approx 10^6$  m/s (which is 1/300<sup>th</sup> of the light in the vacuum) is the Fermi velocity, and  $\vec{k}$  is the wavevector. In graphene, the charge particles act like relativistic particles with the speed given by the Fermi velocity. This unique behaviour accounts, in part, for the huge research interest in graphene.

### 2.3.3 The electronic density of state (DOS) of graphene

The electronic density of states (DOS) could be used to characterise the electrical conductivity of graphene. The theoretical DOS of graphene is shown in Figure 2.6 and the features of the graph reaffirm the semi-metallic behaviour of the system. Due to the touching of the valence and conduction bands, the DOS of the system has a zero band-gap. This feature is in sharp contrast to what is obtainable in diamond, another allotrope of carbon known to have a wide band-gap of 5.47 eV [6].

The theoretical DOS per unit cell ( $\rho(E)$ ) of graphene can be derived through equation (2.8):

$$\rho(E) = \frac{1}{A_c} \frac{dN}{dE} = \frac{1}{A} \frac{dN}{dk} \frac{dk}{dE} \quad (2.8)$$

where  $A_c$  is the area of the unit cell; N which is the number of states, for a two-dimensional material, can be expressed by equation (2.9):

$$N = \frac{A_c k^2}{2\pi} \rightarrow \frac{dN}{dk} = \frac{A_c k}{\pi} \quad (2.9)$$

Thus, the DOS per unit cell ( $\rho(E)$ ) of graphene in the vicinity of a Dirac point is given by equation (2.10), and is obtained by combining equation (2.5), (2.8) and (2.9) together.

$$\rho(E) = \frac{2}{\pi h^2} \frac{|E|}{v_F^2} \quad (2.10)$$

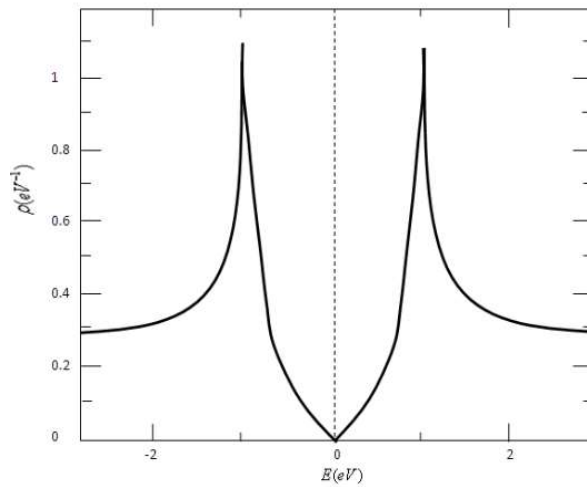


**Figure 2.6** The density of states (DOS),  $\rho$ , of a monolayer graphene system at different energies,  $E$ . Reproduced with the permission from Neto [10].

### 2.3.4 The vibrational properties of graphene

The vibrational properties of graphene are important in understanding the high thermal conductivity of the system. Moreover, they are also responsible for other attributes of graphene such as the structural stability via the absence of imaginary modes, optical properties through phonon-phonon scattering (as in the case of Raman scattering) and the electronic properties through electron-phonon scattering.

The vibrational properties of graphene could be understood with the aid of the phonon dispersion relation. Some experimental methods have been employed to measure the phonon dispersions of graphite as well as graphene, for example, electron loss spectroscopy (EELS) [13], inelastic neutron scattering [14], high-resolution electron-energy-loss spectroscopy (HREELS) [15], and inelastic x-ray scattering (IXS) [16], [17]. However, the measurements made with these spectroscopies require a large amount of quality samples and are restricted to specific directions

or phonon modes. Some of these aforementioned methods have been used to carry out phonon studies of graphite. Recently, using IXS Mohr et al.[16] reported optical and acoustic phonon modes measurements of graphite along  $\Gamma$ -K-M- $\Gamma$  directions. The measurements were found to be very close. The G band in the layers of graphene has been measured through Raman scattering [18]–[21]. It was reported that as the number of layers of graphene changes, the intensity and position of second order D and the first order G band of Raman spectra change as well [18], [19]. Theoretically, Grüneis et al.[22] reported the phonon dispersions of graphite employing the fourth nearest-neighbor force constant (4NNFC) technique. However, as a result of the Kohn anomaly at  $\Gamma$  and K point, it has been argued that it is not possible to get the right phonon dispersions near  $\Gamma$  and K using the force constant method [23]. Dubay and Kresse [24] investigated phonon dispersion calculations of graphite using density functional theory (DFT) within the framework of local density approximation (LDA). Their results are consistent with the phonon measurements by HREELS. Wirtz and Rubio [25] performed phonon dispersion calculations of graphite using the generalized gradient approximation (GGA) and LDA, the results obtained are in good agreement with the vast majority of the experimental data points plotted together. Mounet and Marzari [26], at the level of GGA-PBE, reported a comprehensive calculation of the phonon dispersion of graphite and graphene.

Linear-response [27] and the direct approach [28], [29] are the two implementations widely used for the first-principles computation of lattice dynamics. With the linear-response approach, the dynamical matrix is evaluated at a predefined coarse grid in the BZ via the density functional perturbation theory [27], [30], [31]. To obtain the interatomic force constant on the corresponding real space grid, the backward Fourier transform of the computed dynamical matrix at the coarse wave- vector grid is used. However, with the direct approach, the force constants are

first calculated through a predefined reference supercell of the unit cell. The direct approach, in the literature, is also known as the frozen-phonon approach, the small-displacement method or the supercell method. In order to obtain phonon frequencies of a given crystal, the ground state energy, expressed as a function of the atom positions, could be expanded within harmonic approximation as:

$$\begin{aligned}
E(\dots \vec{r}(l, k) \dots \vec{r}(l', k') \dots) \\
= E_o + \frac{1}{2} \sum_{l, k, l', k'} \Phi(l, k; l', k') U(l, k) U(l', k') + O(U^3) \quad (2.11)
\end{aligned}$$

where  $\vec{r}(l, k)$  is the position of  $l$ -th atom in the  $k$ -th unit cell;  $E_o$  is the equilibrium energy and  $U$  is the displacement of any of the system. The elements of the interatomic force constants  $\Phi_{\alpha\beta}$  matrix are expressed as:

$$\phi_{\alpha, \beta}(l, k; l', k') = \frac{\partial^2 E}{\partial r_{\alpha}(l, k) \partial r_{\beta}(l', k')} \quad (2.12)$$

where the Cartesian indices are denoted by  $\alpha$  and  $\beta$ . In the finite displacement method, equation (2.12) could be further expressed as:

$$\phi_{\alpha, \beta}(l, k; l', k') = \frac{F_{\beta}(l', k'; \Delta r_{\alpha}(l, k)) - F_{\beta}(l', k')}{\Delta r_{\alpha}(l, k)} \quad (2.13)$$

where  $F_{\beta}(l, k)$  is the force in the direction of  $\beta$  on the atom  $(l, k)$ , and the finite displacement is represented as  $\Delta r_{\alpha}$ . With equation (2.13) the interatomic constants  $\phi_{\alpha, \beta}$ , and the dynamical matrix can be calculated. Thus, for a given wave vector  $\mathbf{q}$  and mode  $\mathbf{i}$ , the phonon frequency  $\omega_{\mathbf{qi}}$  can be obtained by diagonalizing the dynamical matrix.

The phonon dispersion curves ref.[32] of a unit cell of graphene computed using the direct approach, from first principles at the level of GGA-PBE, is shown in Figure 2.7, which is displayed

along with a theoretical ref.[33] and experimental ref.[34] curve. The two atoms in the unit cell of graphene correspond to six allowed modes. The ZA (acoustic) and ZO (optical) are the out-of-plane vibrations while the in-plane vibrations correspond to transverse acoustic (TA), transverse optical (TO), longitudinal acoustic (LA), and longitudinal optical (LO).

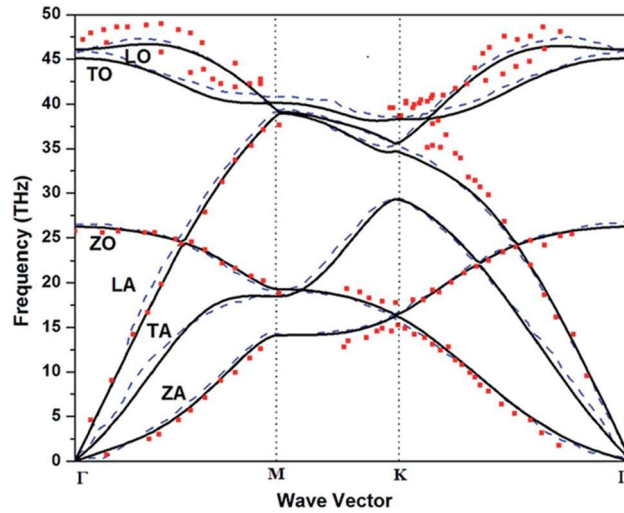


**Figure 2.7** The calculated phonon curve of pure graphene (solid lines) ref.[32], (theoretical) (dashed lines) ref.[33] and (red squares) (experimental curve) ref.[34]. Reproduced with the permission from Mann [32].

The main feature of Figure 2.7 is the existence ZA mode also known as flexural mode [35] which is the least frequency and the easiest to excite. The mode, which is only derivable from 2D systems, originated from the surface interactions and it is quadratic in the vicinity of  $\Gamma$  point. This quadratic nature of ZA mode around the  $\Gamma$  point in Figure 2.7 is in contrast with the linear dispersion obtained using the atomic potentials containing three parameters [36]. Interestingly, the experimental curves (red) tend to be in agreement with the quadratic behavior at the  $\Gamma$  point.

One of the consequences of the graphene phonon dispersion relation is the high value of the in-plane sound velocity,  $c_{ph} \approx 20$  km/s [36] leading to high thermal conductivities. The thermal conductivity  $\kappa$ , from the kinetic theory of gases, is given by equation (2.14):

$$\kappa \sim c_{ph} C_v(T) \lambda \quad (2.14)$$

where  $C_v(T)$  denotes the specific heat per unit volume, and the phonon free mean path is represented by  $\lambda$ .  $c_{ph}$  of graphene is very high, consequently, a high thermal conductivity is expected. This is indeed the case, as obtained in experiments at almost room temperature gives  $\kappa \approx 3080\text{--}5150$  W/mK and a phonon free mean path of  $\lambda=775$  nm for a given set of graphene flakes [37], [38]. In recent experimental reports, smaller values between 600 and 3000 W/mK [39]–[41] of free-standing graphene have been reported. However, these values are among the highest ever measured from any material till date. Thus, the results of the thermal conductivities of graphene indicate that the material is a potential candidate for applications in nano or even microelectronic devices. Since a high thermal conductivity enhances the diffusion of heat away easily from the devices.

### 2.3.5 The optical properties of graphene

The research on graphene has shown that the material exhibits unique optical properties [42] which can be ascribed to the linear dispersion of the band structure, zero band-gap and the strong interactions of the Dirac Fermions with light [43], and high speed operation [44] along with gate variable conductivity [45]. These properties are very useful for addressing the future needs of the electro-optic modulators. The growing interest of graphene in photonics and optoelectronics could also be attributed to the potential application of the material in solar cells, light-emitting devices, touch panel, photo-detectors, ultrafast lasers, etc.



Due to the optical transparency, graphene has emerged as a potential transparent coating material. The absorption in graphene covers a wide spectra range which is contributed by intraband and interband transitions. From the visible to near infrared region, the absorption is modeled by interband transitions which is frequency independent and described by the fine structure constant [43], [46]. In the far infrared region, the optical response arises from the intraband transitions or free carrier absorption [47]. Due to the momentum mismatch, direct optical absorption is not possible via intraband transition. In order for momentum to be conserved, photon scattering eventuates and accompanied by population inversion of the free carriers in the vicinity of the K-point. For light polarization that is parallel or perpendicular to the plane of the sheet, the optical absorption of graphene is anisotropic. In graphene, the conductivity due to free carriers' absorption portrays Drude like frequency dependence [48]. As compared to graphite, it has been reported experimentally that the optical energy loss spectrum of graphene exhibit a redshift,  $\pi+\sigma$  electron plasmon and disappearance of bulk plasmon [49], [50]. This optical characteristic can be used to differentiate graphene from graphite. For example, Eberlein et al. [51] revealed that  $\pi$  and  $\pi+\sigma$  surface plasmon modes in free suspended graphene occur at 4.7 and 14.6 eV respectively, whereas in bulk graphite, the modes are found at 7 and 25 eV. The observed redshift is noted to decrease as the number of layers of the system reduces.

The origins of the different peaks in the optical spectrum of graphene or the heteroatom doped graphene could be explained by taking into consideration many-body effects such as electron-electron (e-e) and electron-hole interactions. Bethe-Salpeter equations [52] coupled with Green's function (GW) [53] could easily be used to address these many-body effects. Taking into account the computational cost of this method, the self-energy correction and excitonic effects almost cancel out as demonstrated in the calculations of the absorption spectra graphene layers

using GW-RPA and GW-BSE [54]–[56]. Likewise, GW calculations sometimes give optical modes of two-dimensional materials that cannot be measured within the context of an experiment [55], [57]. Hence, it is assumed that the optical properties of graphene and the modified form could be studied within the context of the independent particles approximation of the complex dielectric function[56].

Generally, the optical properties of a system could be calculated with the frequency dependent complex dielectric function  $\varepsilon(\omega)$  (see equation(2.15)); where  $\varepsilon_2$  denotes the imaginary component which can be computed using first-order time-dependent perturbation theory in the framework of simple dipole approximation. The Local Field Effects (LFE), which is the changes in the periodic part of the potential, can be included within random phase approximation (RPA).

$$\varepsilon(\omega) = \varepsilon_1(\omega) + i\varepsilon_2(\omega) \quad (2.15)$$

In the limit of long wavelength,  $\varepsilon_2$  could be expressed as:

$$\varepsilon_2(q \rightarrow 0, \omega) = \frac{2e^2\pi}{V\varepsilon_0} \sum_{c,v,k} |\langle \psi_k^c | \vec{u} \cdot \vec{r} | \psi_k^v \rangle|^2 \delta(E_k^c - E_k^v - \omega) \quad (2.16)$$

where ‘c’ and ‘v’ denote the band indices which correspond to the conduction and the valence bands; V,  $\varepsilon_0$ , and  $\omega$  (in eV) are the volume of the unit cell, free space permittivity and a certain frequency of the incident electromagnetic wave (EM) respectively;  $\vec{u}$  and  $\vec{r}$  represent the polarization vector of the incident EM field and the position vector. The eigenfunctions of the valence (v) and conduction (c) band of the systems at a k-point are represented by  $\psi_k^v$  and  $\psi_k^c$  respectively while the  $E_k^c$  and  $E_k^v$  correspond to the eigenvalues. The  $\varepsilon_1$  (see equation (2.17)), which is the real part of the frequency dependent dielectric function, can be calculated from  $\varepsilon_2$  using the Kramers-Krönig transformation:

$$\epsilon_1(\omega) = \Re[\epsilon(q \rightarrow 0, \omega)] = 1 + \frac{2}{\pi} P \int_0^{\infty} \frac{d\omega' \epsilon_2(\omega') \omega'}{\omega'^2 - \omega^2 + i\eta} \quad (2.17)$$

where P represents the Cauchy principal value. The technique is reported in Ref.[58]. It is worth mentioning that  $\epsilon_1$  and  $\epsilon_2$  could have two independent components which correspond to the two polarizations of the electric field vectors with respect to the plane of the given systems. The two polarizations could be termed parallel (i.e. the polarized vector is along the plane of the system) and perpendicular (i.e., the polarized field vector is out of the plane of the system) polarization. The Drude term is associated with the intraband transitions which are prevalent at low photon energies. It is worth stating that equation (2.16) has no Drude component. As a result, only interband transitions above 1.0 eV can be analyzed effectively with the expression.

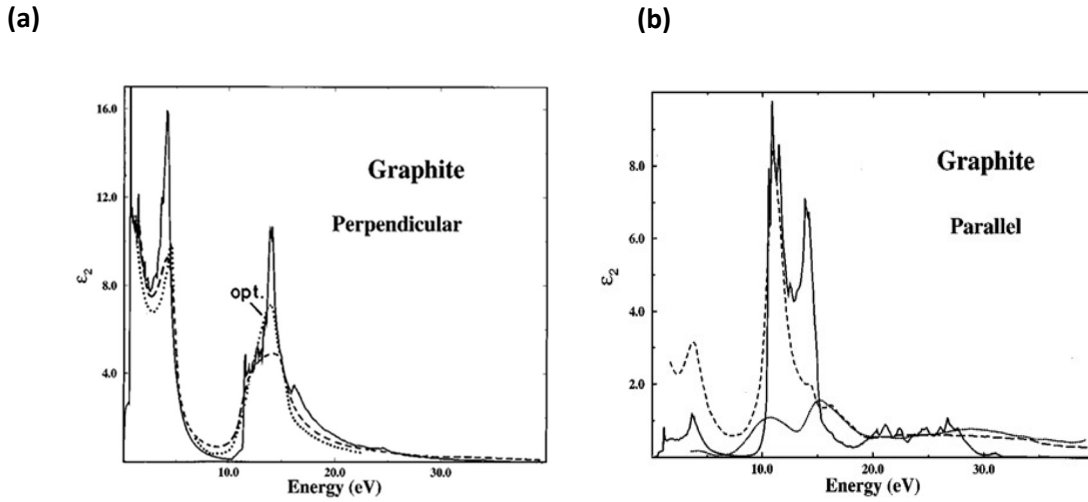


**Figure 2.8** (a). Theoretical and experimental perpendicular dielectric functions ( $\epsilon_2^\perp$ ). The solid line (Ref.[59]) is from theoretical data, while the dotted (Ref.[60]) and the dashed (Ref.[61]) lines are from experiments. (b) The theoretical and experimental parallel dielectric functions ( $\epsilon_2^\parallel$ ) of graphite. The solid line is the theoretical  $\epsilon_2^\parallel$ , the dotted and the dashed lines are the experimental values obtained from optical measurement (Ref.[62]) and the electron energy loss spectra (Ref.[61]) respectively. Reproduced with the permission from Daniel [61]

The anisotropic dielectric spectra of graphite are depicted in Figure 2.8 (a) and (b). The two figures compared theoretical and experimental curves of the imaginary part of both the parallel and perpendicular dielectric function. In Figure 2.8 (a) and (b), the experimental data were obtained from [61]. The features of the spectra could be properly analyzed in terms of the major peaks. The theoretical spectrum in Figure 2.8 (a) has two major peaks at  $\sim 4$  ,  $\sim 15$  eV and a minimum in the vicinity of  $\sim 9$  eV. The positions of these peaks are in accordance with the corresponding experimentally observed peaks in Figure 2.8 (a). The agreement between the theory and the experiment demonstrates the reliability of the theoretical approach employed for the calculations. As regard to Figure 2.8 (b), the calculated spectrum has two dominant peaks at  $\sim 4$  eV and a larger peak with two spikes at  $\sim 11-14$  eV. It is worth pointing out there are inconsistencies between the theory and the experiments. However, the theory agreed with the experiment within the photon energy interval of 11–14 eV. The experimental data were obtained from the electron-energy-loss spectra (the dashed line) and the optical measurement (the dotted line). It can be seen that the two measurements are not consistent. The inconsistency between the two measurements could be associated with an imperfection in the graphene samples that were used in the experiments. This imperfection might have occurred as a result of a substrate effect. Thus, the discrepancy between the theoretical and the experimental results could be associated with the imperfection in the graphene sample used in the experiments.

The origin of the observed peaks of the dielectric functions of graphite could be explained on the account of the interband transitions in monolayer graphite or graphene. This is because the atomic layers in graphite interact weakly. As a result, explaining the optical transition in terms of that of graphene is a good approximation. Monolayer graphene has reflection symmetry on the plane and consequently the following restrictions apply to the matrix elements associated with the

momentum operators: with respect to the momentum on the plane  $p_x$ ,  $\pi \rightarrow \pi^*$  or  $\sigma \rightarrow \sigma^*$  are the only allowed transitions; while for  $p_z$ , the allowed transitions are  $\pi \rightarrow \sigma^*$  or  $\sigma \rightarrow \pi^*$ . These conditions help to identify the different peaks of the dielectric function of graphite. Thus, in Figure 2.8 (a) the observed peak within 0–5 eV is due to  $\pi \rightarrow \pi^*$  interband transitions, while the feature at ~14 eV can be attributed to  $\sigma \rightarrow \sigma^*$  transitions. In the case of Figure 2.8 (b), the peak around 4 eV arises from  $\pi \rightarrow \pi^*$  whereas the  $\pi \rightarrow \sigma^*$  transitions give rise to the observed feature at 14 eV.

With equations (2.16) and (2.17), other optical parameters of materials such as refractive index  $\tilde{n}(\omega)$ , reflectivity  $R(\omega)$ , absorptivity  $\alpha(\omega)$  and electron energy loss function  $L(\omega)$  can be computed:

$$n(\omega) = \left( \frac{\sqrt{\varepsilon_1^2 + \varepsilon_2^2} + \varepsilon_1}{2} \right)^{\frac{1}{2}} \quad (2.18)$$

$$k(\omega) = \left( \frac{\sqrt{\varepsilon_1^2 + \varepsilon_2^2} - \varepsilon_1}{2} \right)^{\frac{1}{2}} \quad (2.19)$$

where  $n(\omega)$  and  $k(\omega)$  are the real and imaginary part of the complex refractive index, respectively.

The indices are related as  $\tilde{n} = n(\omega) + ik(\omega)$ . The reflectivity  $R(\omega)$  spectrum of a system can be computed using equations (2.18) and (2.19) such that,

$$R(\omega) = \frac{(n - 1)^2 + k^2}{(n + 1)^2 + k^2} \quad (2.20).$$

The absorptivity  $\alpha(\omega)$  of the system can be calculated using equation (2.19) to give:

$$\alpha(\omega) = \frac{2k\omega}{c\hbar} \quad (2.21).$$

In equation (2.21), “c” denotes the speed of light in vacuum, while the rest of the parameters maintain the same descriptions as stated previously.

$$L(\omega) = \frac{\varepsilon_2}{\varepsilon_1^2 + \varepsilon_2^2} \quad (2.22)$$

The electron energy loss function  $L(\omega)$  is a measure of the collective excitation of a given system and it could be expressed using equation (2.22).

## 2.4 Band-gap modification in graphene

Graphene is a semimetal with high carrier mobility, excellent optical transparency, and high mechanical strength. As a result of the excellent properties, graphene has been touted as a potential material for both nanoelectronic and optoelectronic applications. However, due to the absence of a band-gap in graphene, the material cannot be employed directly as a platform for a device application. Interestingly, techniques such as super-structural fabrications, chemical doping, application of the electric field and graphene deposition on epitaxial substrates have been identified to create a sizeable band-gap in graphene. These different band-gap inductive techniques are discussed in detail in the following paragraphs.

The superstructure fabrication such as graphene quantum-dots [63], [64], nanoribbons [65], [66] or nanomeshes [67] induces a band-gap in the material through quantum confinement. However, fabricating such structures dimensionwise still poses an enormous challenge. That is designing superstructures with uniform width and edges less than 10 nm is still difficult to achieve with a top-down method like etching and lithography [68]. Homogenous structures could be obtained easily with a bottom-up approach [69], yet peeling off patterned ribbons remains a contending procedure.

Another approach that can be used to induce a band-gap in graphene is by depositing it on epitaxial substrates such as SiC [70], Al<sub>2</sub>O<sub>3</sub> [71], etc. Notwithstanding the contentious issue of controlling the morphology and the surface energies of the material, the energy gap induced by this technique is not tuneable [72]. However, to achieve a tuneable band-gap, the application of an electric field could be a viable option. Through the breaking of the material inversion symmetry, an applied perpendicular electric field to the plane of AB-stacked bilayer graphene can create a band-gap tuneable up to 0.25 eV in the system. With this technique, the carrier mobility of the system is not noticeably affected. In spite of the robustness of the technique for AB-stacked bilayer graphene, the application of an electric field does not directly lead to a band-gap opening in monolayer graphene [72]. This is because the application of an electric field does not affect the inherent symmetry of graphene sublattices.

Furthermore, unlike the electric field approach which is more effective with respect to multiple layers of graphene, heteroatoms doping is the most feasible technique of inducing semiconducting character in monolayer graphene [73]. B and N atoms are considered as the ideal dopants for substitutional doping in graphene due to their atomic sizes which are almost equal to that of carbon (C). Interestingly, the doping of graphene with N atom leads to n-type semiconductor (due to the electron rich character of the dopant compared to C) while doping with B atoms results to a doped system with p-type character. As compared to either N-N or B-B, due to the comparable bond length of B-N to C-C, B-N is the natural replacement for C-C of graphene. It is worth mentioning that this method of substitution doping came into the limelight shortly after the isolation of monolayer graphene in 2004, and thereafter the method has widely been reported in the literature [74]–[76].

## 2.5 The review of first-principles studies on graphene

Graphene has attracted a lot of attention due to its fascinating properties. Nevertheless, some of the properties need to be tailored to meet the specifications of certain applications. Substituting heteroatoms for some carbon atoms of graphene would cause structural and the electronic changes leading to alteration of the thermal, charge transport, band-gap, Fermi level, optical and magnetic properties of the system. Depending on the chemical nature of the dopants and the configuration, a new or an improved property might arise and could be of benefit for certain applications. A good understanding of how the properties of graphene can be tuned is important for researchers in order to further extend the range of applications. Consequently, recently reports aimed at tailoring the properties of these systems via doping are hereby reviewed:

Boron (B), a group III element and the nearest neighbor to carbon, is suitable for doping of graphene. The in-plane substitution of B in graphene is the most stable with respect to the out-of-plane conformation [73]. B substitution in graphene leads to  $sp^2$  hybridization, while charge polarization exists between neighboring C and B atoms. The structural parameters are slightly changed since C–C (1.42 Å) is less than B–C (1.50 Å) bond length in graphene [73], [77], [78]. In spite of the long bond length compared to C–C, the strong B–C bond ensures that B-doped graphene has excellent mechanical properties [79]. Meanwhile, B-doping reduces the thermal conductivity of graphene. In fact, 0.75% of B in graphene can lead to a 60% reduction of the thermal conductivity [79]. B is electron-deficient compared to C, as such it induces p-type conductivity in graphene accompanied by a downshift of the Fermi level away from the Dirac point. Scanning tunneling microscopy (STM) and simulations have shown that B-doping leads to density of states above the Fermi level due to the hole-doping effect [77], [80]. A band-gap of 0.14 eV can be induced in graphene by a B atom replacing a C atom of graphene with 50 atoms



[73], [81]. The symmetry breaking in graphene is considered to be the cause of the band-gap opening. The size of the band-gap depends on the amount of the impurity and the number of layers of graphene [73], [82]. A theoretical study has shown that the remarkable transport properties of graphene are retained even at a high B-doping concentration [83].

N, a group IV element, is close to C in the periodic table. As compared to C, N is electron-rich and this makes N-doped graphene quite different from B-doped graphene. There is three main N bonding configuration that exists, i.e., quaternary, pyrrolic and pyridinic. C–N (1.41 Å) and C–C bond (1.42 Å) have almost an equal bond length, as a result, pyridinic and graphitic N exert a negligible effect of the structural parameters of graphene. However,  $sp^3$  hybridized pyrrolic N changes the structural parameters of graphene [84][30]. Graphitic and pyridinic N bonding conformations are the most stable with respect to Stone-Wale and vacancy defects, while pyridinic dominate in the presence of monovacancy [85], [86]. N is more electronegative than C, as a result, forms polarization in graphene, thus changing the electronic, magnetic and optical properties of graphene [87]. Doping graphene with N transforms it from semimetal to semiconductor [88], [89] depending on the doping configurations. For graphitic N, the three of the five valence electrons form  $\sigma$ -bonds with the adjacent carbon atoms, one is involved in a  $\pi$ -bond formation, and the last electron is partially involved in  $\pi^*$  state of the conduction band. Liu et al. showed graphitic N to be n-type with the carrier mobility of 200-450  $cm^2$  [89]. The report of Usachov et al. shows that with 0.4 % doping of graphitic N a bandgap opening of  $\sim 0.3$  eV and charge-carrier concentration of  $\sim 8 \times 10^{12} cm^{-2}$  are induced in the system [90]. However, Sodi et al. theoretically demonstrate that edge-functional groups exert a negligible effect on the band structure of graphene [91]. Ouerghi et al., as shown that only 0.6% graphitic N-doping results in large carrier concentrations of  $2.6 \times 10^{13} cm^{-2}$  (4 times higher than that of pristine graphene), whereas pyridinic and pyrrolic

N exert little effect [92]. N doping can also be used to tailor the optical properties of graphene. Chiou et al. reported the effect of N-doping on the photoluminescence characteristic of graphene nanoflakes [93]. When excited, the electron of N-doped graphene would transfer energy to the  $\pi^*$  state of the nano-cluster. Thus, a large amount of energy would be released when electrons drop from the  $\pi^*$  state back to the  $\pi$  state, leading to high spectrum intensity.

Group VI elements are called the oxygen family, of which, oxygen is the most electronegative. Substitutional doping of graphene with O is rare because of the large size of the atom and its strong electronegativity. S has a similar doping configuration as O [94]. The bond length (1.78 Å) is about 25% greater than that the C–C bond length [95]. As a result, a carbon nanostructure with a given curvature favors S substitution that flat graphene. A theoretical report has shown that S-doping of graphene occurs mainly in two stages: the formation of defect sites and the rupture of S=S bond. Depending on the amount of the impurity, the S-doped graphene can form a small-band-gap semiconductor or metallic material [96].

Group VII is known as the halogens and has higher reactivity than group III-VI elements. Halogen-doping changes the  $sp^2$  hybridization of the carbon network of graphene to  $sp^3$  bonding. This leads to the distortion of the structure of graphene, and changes in the electronic structures. One of the most reactive elements is fluorine (F). The F–C bond in graphene is strong and protrude out of the basal plane [97]. The F atom stretches the C–C bond length to 1.57 Å [98]. Ab initio calculations suggest that due to the high affinity of F to C, a negative chemisorption energy of F on graphene is obtained even if the whole plane is covered with F atoms to form fluorographene [99]. Fluorographene has excellent mechanical strength, high thermodynamic stability, and outstanding chemical inertness [96], [99]. F-doped graphene can be used as a semiconductor with a tunable band-gap through F coverage [100]. one-sided doped graphene, 25% coverage, is

optically transparent with a large band-gap of 2.93 eV and excessive six order of increase in the resistance with respect to graphene [101].

Graphene hydrogenation through  $sp^3$  hybridization can transform it into a wide-gap semiconductor [102], [103]. Quite a lot of studies have been performed on the structural, electronic and magnetic properties of fully and partially hydrogenated graphene [104]–[106]. However, the practical application is limited due to the slight difference in the electronegativity between C and H. The C–H bond is not non-polar, and thus non-reactive.

The doping of graphene with metallic atoms has rarely been done experimentally. This might be because the binding energy between the metallic impurity and graphene is lower than the cohesive energy. As such, they tend to aggregate into clusters instead of doping graphene uniformly on the surface [107]. This could explain the rarity of experimentally synthesized Be-doped graphene. Although, Ullah et al.[68]reported the structural and electronic properties of Be-doped graphene via first principles, experimental reports of such system is scarce. Meanwhile, metal atoms with large molecular radii can form a large local curvature suitable for chemisorption of small molecules (e.g.  $H_2O$ ,  $O_2$ ,  $NO$ ) from the atmosphere, thereby limiting the application of such doped graphene [108], [109].

Doping graphene with heteroatoms modify the physical properties. These properties depend on the impurity concentration, doping sites and the chemical nature of the foreign atoms. Thus, substituting multiple species of foreign atoms in graphene, the technique that is termed co-doping, provides countless possibilities of introducing different chemical species in graphene thereby leading to emergence of new properties or formation of synergistic effects. B and N have almost equal atomic size and cause opposite doping effects on graphene when used as co-dopants. B-N co-doped graphene has a boron nitride domain as a result of the phase separation between C

and BN [110]–[114]. The existence of the domain can be ascribed to the higher binding energy of B-N and C-C than N-C and B-C bonds. The strong charge Polarization between B and N [112], [115] leads to active surface chemistry. The thermal stability of B-N co-doped graphene is less than N-doped graphene but greater than B-doped graphene [116].

As earlier stated, Be-doped graphene might not be stable at room temperature, while S-doped graphene can either exist as a metal or semiconductor (with a narrow band-gap) depending on the impurity concentration. A study designed to extend the properties of Be-doped and S-doped graphene by co-doping is worth investigating. For example, a report on the structural, electronic and optical properties of BeN and BeS co-doped graphene is scarce.

## References

- [1] M. E. Galvez and J. Gaillardet, “Historical constraints on the origins of the carbon cycle concept,” *Comptes Rendus Geosci.*, vol. 344, no. 11–12, pp. 549–567, Nov. 2012.
- [2] D. M. Haaland, “Graphite-liquid-vapor triple point pressure and the density of liquid carbon,” *Carbon*, vol. 14, no. 6, pp. 357–361, 1976.
- [3] H. Cynn, J. E. Klepeis, C. S. Yoo, and D. A. Young, “Osmium has the Lowest Experimentally Determined Compressibility,” *Phys. Rev. Lett.*, vol. 88, no. 13, p. 4, 2002.
- [4] N. Savvides and T. J. Bell, “Hardness and elastic modulus of diamond and diamond-like carbon films,” *Thin Solid Films*, vol. 228, no. 1–2, pp. 289–292, May 1993.
- [5] A. H. C. Neto and K. Novoselov, “New directions in science and technology: Two-dimensional crystals,” *Reports Prog. Phys.*, vol. 74, no. 8, p. 082501, Aug. 2011.
- [6] C. J. H. Wort and R. S. Balmer, “Diamond as an electronic material,” *Mater. Today*, vol. 11, no. 1–2, pp. 22–28, Jan. 2008.
- [7] S. V. Kidalov and F. M. Shakhov, “Thermal conductivity of diamond composites,” *Materials (Basel)*, vol. 2, no. 4, pp. 2467–2495, Dec. 2009.
- [8] F. Tuinstra and J. L. Koenig, “Raman Spectrum of Graphite,” *J. Chem. Phys.*, vol. 53, no. 3, pp. 1126–1130, 1970.
- [9] D. D. L. Chung, “Review graphite,” *J. Mater. Sci.*, vol. 37, no. 8, pp. 1475–1489, 2002.
- [10] A. H. C. Neto et al., “The electronic properties of graphene,” *Rev. Mod. Phys.*, vol. 81, no. 1, pp. 109–162, Jan. 2009.
- [11] D. R. Cooper et al., “Experimental review of graphene,” *ISRN Condens. Matter Phys.*, vol. 2012, pp. 1–56, 2011.
- [12] P. R. Wallace, “The Band Theory of Graphite,” *Phys. Rev.*, vol. 71, no. 9, pp. 622–634, May 1947.
- [13] C. Oshima, T. Aizawa, R. Souda, Y. Ishizawa, and Y. Sumiyoshi, “Surface phonon dispersion curves of graphite (0001) over the entire energy region,” *Solid State Commun.*, vol. 65, no. 12, pp. 1601–1604, 1988.
- [14] R. Nicklow, N. Wakabayashi, and H. G. Smith, “Lattice dynamics of pyrolytic graphite,” *Phys. Rev. B*, vol. 5, no. 12, pp. 4951–4962, Jun. 1972.
- [15] S. Siebentritt, R. Poes, K. Rieder, and A. Shikin, “Surface phonon dispersion in graphite and in a lanthanum graphite intercalation compound,” *Phys. Rev. B*, 1997.
- [16] M. Mohr, J. Maultzsch, E. Dobardžić, and S. Reich, “Phonon dispersion of graphite by inelastic x-ray scattering,” *Phys. Rev. B*, 2007.
- [17] J. Maultzsch, S. Reich, C. Thomsen, H. Requardt, and P. Ordejón, “Phonon Dispersion in Graphite,” *Phys. Rev. Lett.*, vol. 92, no. 7, p. 075501, Feb. 2004.

- [18] D. Graf et al. “Spatially resolved Raman spectroscopy of single-and few-layer graphene,” *nano Lett.*, vol. 7, no. 2, pp. 238-242 Jan., 2007.
- [19] A. C. Ferrari et al., “Raman Spectrum of Graphene and Graphene Layers,” *Phys. Rev. Lett.*, vol. 97, no. 18, p. 187401, Oct. 2006.
- [20] A. Gupta, G. Chen, P. Joshi, and S. Tadigadapa “Raman scattering from high-frequency phonons in supported n-graphene layer films,” *Nano Lett.*, vol. 6, no. 12 pp. 2667-2673, Nov. 2006.
- [21] J. Yan, Y. Zhang, P. Kim, and A. Pinczuk, “Electric field effect tuning of electron-phonon coupling in graphene,” *Phys. Rev. Lett.*, vol. 98, no. 16, 2007.
- [22] A. Grüneis et al., “Determination of two-dimensional phonon dispersion relation of graphite by Raman spectroscopy,” *Phys. Rev. B*, vol. 65, no. 15, pp. 1554051–1554057, Mar. 2002.
- [23] S. Piscanec, M. Lazzeri, F. Mauri, A. C. Ferrari, and J. Robertson, “Kohn anomalies and electron-phonon interactions in graphite,” *Phys. Rev. Lett.*, vol. 93, no. 18, p. 185503, Oct. 2004.
- [24] O. Dubay and G. Kresse, “Accurate density functional calculations for the phonon dispersion relations of graphite layer and carbon nanotubes,” *Phys. Rev. B - Condens. Matter Mater. Phys.*, vol. 67, no. 3, 2003.
- [25] L. Wirtz and A. Rubio, “The phonon dispersion of graphite revisited,” *Solid State Commun.*, vol. 131, no. 3-4, pp. 141-152, Jul., 2004.
- [26] N. Mounet and N. Marzari, “First-principles determination of the structural, vibrational and thermodynamic properties of diamond, graphite, and derivatives,” *Phys. Rev. B - Condens. Matter Mater. Phys.*, vol. 71, no. 20, pp. 1–14, May 2005.
- [27] S. Baroni, S. De Gironcoli, A. Dal Corso, and P. Giannozzi, “Phonons and related crystal properties from density-functional perturbation theory,” *Rev. Mod. Phys.*, vol. 73, no. 2, pp. 515–562, 2001.
- [28] K. Parlinski, Z. Q. Li, and Y. Kawazoe, “First-Principles Determination of the Soft Mode in Cubic ZrO<sub>2</sub>,” *Phys. Rev. Lett.*, vol. 78, no. 5, pp. 186802, 1997.
- [29] A. Togo, F. Oba, and I. Tanaka, “First-principles calculations of the ferroelastic transition between rutile-type and CaCl<sub>2</sub>-type SiO<sub>2</sub> at high pressures,” *Phys. Rev. B - Condens. Matter Mater. Phys.*, vol. 78, no. 13, p. 134106, Oct. 2008.
- [30] Y. Wang, S. Shang, H. Fang, Z. Liu, L. Chen. *Materials*, and undefined 2016, “First-principles calculations of lattice dynamics and thermal properties of polar solids,” *nature.com*, vol. 2, no. 1, pp. 16006, Nov. 2016.
- [31] X. Gonze and C. Lee, “Dynamical matrices, Born effective charges, dielectric permittivity tensors, and interatomic force constants from density-functional perturbation theory.” *phys. Rev. B - Condens. Matter Mater. Phys.*, vol. 55, no. 116, p. 10355, Apr. 1997.
- [32] S. Mann, P. Rani, R. Kumar, G. S. Dubey, and V. K. Jindal, “Thermodynamic properties of pure and doped (B, N) graphene,” *RSC Adv.*, vol. 6, no. 15, pp. 12158–12168, 2016.

- [33] H. Zhang, G. Lee, and K. Cho, “Thermal transport in graphene and effects of vacancy defects,” *Phys. Rev. B - Condens. Matter Mater. Phys.*, vol. 84, no. 11, p. 115460, Sep. 2011.
- [34] H. Yanagisawa et al., “Analysis of phonons in graphene sheets by means of HREELS measurement and ab initio calculation,” *Surf. Interface Anal.*, vol. 37, no. 2, pp. 133–136, 2005.
- [35] J. W. Jiang, B. S. Wang, J. S. Wang, and H. S. Park, “A review on the flexural mode of graphene: Lattice dynamics, thermal conduction, thermal expansion, elasticity and nanomechanical resonance,” *J. Phys. Condens. Matter*, vol. 27, no. 8, p. 083001, Mar. 2015.
- [36] V. Adamyan and V. Zavalniuk, “Phonons in graphene with point defects,” *J. Phys. Condens. Matter*, vol. 23, no. 1, p. 015402, Jan. 2011.
- [37] A. A. Balandin et al., “Superior thermal conductivity of single-layer graphene,” *Nano Lett.*, vol. 8, no. 3, pp. 902–907, Mar. 2008.
- [38] S. Ghosh et al., “Extremely high thermal conductivity of graphene : Prospects for thermal management applications in nanoelectronic circuits Extremely high thermal conductivity of graphene : Prospects for thermal management applications in nanoelectronic circuits,” *Appl. Phys. Lett.*, vol. 151911, no. 15, pp. 92–95, 2008.
- [39] S. Chen et al., “Raman measurements of thermal transport in suspended monolayer graphene of variable sizes in vacuum and gaseous environments,” *ACS Nano*, vol. 5, no. 1, pp. 321–328, Jan. 2011.
- [40] C. Faugeras, B. Faugeras, M. Orlita, M. Potemski, R. R. Nair, and A. K. Geim, “Thermal conductivity of graphene in corbino membrane geometry,” *ACS Nano*, vol. 4, no. 4, pp. 1889–1892, Apr. 2010.
- [41] J. U. Lee, D. Yoon, H. Kim, S. W. Lee, and H. Cheong, “Thermal conductivity of suspended pristine graphene measured by Raman spectroscopy,” *Phys. Rev. B - Condens. Matter Mater. Phys.*, vol. 83, no. 8, p. 081419, Feb. 2011.
- [42] F. Bonaccorso, Z. Sun, T. Hasan, and A. C. Ferrari, “Graphene photonics and optoelectronics,” *Nat. Photonics*, vol. 4, no. 9, pp. 611–622, 2010.
- [43] R. R. Nair et al., “Fine structure constant defines visual transparency of graphene.,” *Science*, vol. 320, no. 5881, p. 1308, Jun. 2008.
- [44] F. Xia, T. Mueller, Y. Lin, A. Valdes-Garcia, and P. Avouris, “Ultrafast graphene photodetector,” *Nat. Nanotechnol.*, vol. 4, no. 12, pp. 839–843, Dec. 2009.
- [45] F. Wang et al., “Gate-variable optical transitions in graphene.,” *Science*, vol. 320, no. 5873, pp. 206–209, 2008.
- [46] K. F. Mak, M. Y. Sfeir, Y. Wu, C. H. Lui, J. A. Misewich, and T. F. Heinz, “Measurement of the optical conductivity of graphene,” *Phys. Rev. Lett.*, vol. 101, no. 19, p. 196405, Nov. 2008.
- [47] I. Gierz et al., “Snapshots of non-equilibrium Dirac carrier distributions in graphene,” *Nat.*

- Mater., vol. 12, no. 12, pp. 1119–1124, Dec. 2013.
- [48] J. Horng et al., “Drude conductivity of Dirac fermions in graphene,” *Phys. Rev. B - Condens. Matter Mater. Phys.*, vol. 83, no. 16, p. 165113, Apr. 2011.
- [49] L. A. Falkovsky, “Optical properties of graphene,” *J. Phys. Conf. Ser.*, vol. 129, no. 1, p. 012004, Oct. 2008.
- [50] J. L. Cheng, C. Salazar, and J. E. Sipe, “Optical properties of functionalized graphene,” *Phys. Rev. B*, vol. 88, no. 4, p. 045438, Jul. 2013.
- [51] T. Eberlein et al., “Plasmon spectroscopy of free-standing graphene films,” *Phys. Rev. B - Condens. Matter Mater. Phys.*, vol. 77, no. 23, pp. 1–4, 2008.
- [52] G. Onida, L. Reining, and A. Rubio, “Electronic excitations: Density-functional versus many-body Green’s-function approaches,” *Rev. Mod. Phys.*, vol. 74, no. 2, pp. 601–659, Jun. 2002.
- [53] F. Aryasetiawan and O. Gunnarsson, “The GW method,” *Reports Prog. Phys.*, vol. 61, no. 3, pp. 237–312, Mar. 1998.
- [54] L. Yang, J. Deslippe, C.-H. H. Park, M. L. Cohen, and S. G. Louie, “Excitonic Effects on the Optical Response of Graphene and Bilayer Graphene,” *Phys. Rev. Lett.*, vol. 103, no. 18, p. 186802, 2009.
- [55] F. Karlický and M. Otyepka, “Band gaps and optical spectra of chlorographene, fluorographene and graphane from G0W0, GW0 and GW calculations on top of PBE and HSE06 orbitals,” *J. Chem. Theory Comput.*, vol. 9, no. 9, pp. 4155–4164, Sep. 2013.
- [56] K. F. Mak, J. Shan, and T. F. Heinz, “Seeing Many-Body Effects in Single- and Few-Layer Graphene: Observation of Two-Dimensional Saddle-Point Excitons,” *Phys. Rev. Lett.*, vol. 106, no. 4, p. 046401, Jan. 2011.
- [57] C. Ataca, S. C.-T. J. of P. C. C, and undefined 2011, “Functionalization of Single-Layer MoS2 Honeycomb Structures,” *ACS Publ.*
- [58] M. Gajdoš, K. Hummer, G. Kresse, J. Furthmüller, and F. Bechstedt, “Linear optical properties in the projector-augmented wave methodology,” *Phys. Rev. B - Condens. Matter Mater. Phys.*, vol. 73, no. 4, pp. 045112, 2006
- [59] H. Belhadj et al., “Optical properties of  $(\text{Pb}_{1-x}\text{Mn}_x\text{S})_{1-y}\text{Fe}_y$  materials from first-principles calculations,” *Chinese J. Phys.*, vol. 55, no. 3, pp. 1032–1043, Feb. 2017.
- [60] E. A. Taft and H. R. Philipp, “Optical Properties of Graphite,” *Phys. Rev.*, vol. 138, no. 1A, pp. A197–A202, Apr. 1965.
- [61] J. Daniels, C. v Festenberg, H. Raether, and K. Zeppenfeld, “Optical constants of solids by electron spectroscopy,” in *Springer Tracts in Modern Physics, Volume 54*, vol. 54, Springer, Berlin, Heidelberg, 1970, pp. 77–135.
- [62] R. Klucker, M. Skibowski, and W. Steinmann, “Anisotropy in the Optical Transitions from the  $\pi$  and  $\sigma$  Valence Bands of Graphite,” *Phys. Status Solidi*, vol. 65, no. 2, pp. 703–710, Oct. 1974.



- [63] L. Ponomarenko, F. Schedin, and M. Katsnelson, “Chaotic Dirac billiard in graphene quantum dots,” *Science*, vol. 320, no. 5874, pp. 356-358, Apr. 2008.
- [64] B. Trauzettel, D. V. Bulaev, D. Loss, and G. Burkard, “Spin qubits in graphene quantum dots,” *Nat. Phys.*, vol. 3, no. 3, pp. 192–196, Feb. 2007.
- [65] M. Han, B. Özyilmaz, Y. Zhang, and P. Kim, “Energy Band-Gap Engineering of Graphene Nanoribbons,” *Phys. Rev. Lett.*, vol. 98, no. 20, pp. 206805, May 2007.
- [66] X. Li, X. Wang, L. Zhang, S. Lee, and H. Dai, “Chemically derived, ultrasmooth graphene nanoribbon semiconductors,” *Science*, vol. 319, no. 5867, pp. 1229-32, Feb., 2008.
- [67] J. Bai, X. Zhong, S. Jiang, Y. Huang, and X. Duan, “Graphene nanomesh,” *Nat. Nanotechnol.*, vol. 5, no. 3, pp. 190–194, Feb. 2010.
- [68] S. Ullah et al., “Band-gap tuning of graphene by Be doping and Be, B co-doping: a DFT study,” *RSC Adv.*, vol. 5, no. 69, pp. 55762–55773, 2015.
- [69] J. Cai et al., “Atomically precise bottom-up fabrication of graphene nanoribbons,” *Nature*, vol. 466, no. 7305, pp. 470–3, Jul. 2010.
- [70] “Substrate-induced bandgap opening in epitaxial graphene,” *Nat. Mater.*, vol. 6 pp. 770-775 Nov. 2007.
- [71] B. Huang, Q. Xu, and S.-H. Wei, “Theoretical study of corundum as an ideal gate dielectric material for graphene transistors,” *Phys. Rev. B*, vol. 84, no. 15, p. 155406, Oct. 2011.
- [72] R. Quhe et al., “Tunable and sizable band gap of single-layer graphene sandwiched between hexagonal boron nitride,” *NPG Asia Mater.*, vol. 4, no. 2, p. e6, Feb. 2012.
- [73] P. Rani and V. K. Jindal, “Designing band gap of graphene by B and N dopant atoms,” *RSC Adv.*, vol. 3, no. 3, pp. 802–812, Dec. 2013.
- [74] L. Ferrighi, M. I. Trioni, and C. Di Valentin, Boron-Doped, Nitrogen-Doped, and Codoped Graphene on Cu(111) A DFT + vdW Study.pdf, vol. 119, no. 11. 2015, pp. 6056–6064.
- [75] T. Wu, H. Shen, L. Sun, B. Cheng, B. Liu, and J. Shen, “Nitrogen and boron doped monolayer graphene by chemical vapor deposition using polystyrene, urea and boric acid,” *New J. Chem.*, vol. 36, no. 6, p. 1385, 2012.
- [76] S. Sharma, P. Rani, a. S. Verma, and V. K. Jindal, “Structural and electronic properties of sulphur-doped boron nitride nanotubes,” *Solid State Commun.*, vol. 152, no. 9, pp. 802–805, 2012.
- [77] R. H. Miwa, T. B. Martins, and A. Fazzio, “Hydrogen adsorption on boron doped graphene: An ab initio study,” *Nanotechnology*, vol. 19, no. 15, p. 155708, Apr. 2008.
- [78] R. Faccio, L. Fernández-Werner, H. Pardo, C. Goyenola, O. N. Ventura, and A. W. Mombrú, “Electronic and structural distortions in graphene induced by carbon vacancies and boron doping,” *J. Phys. Chem. C*, vol. 114, no. 44, pp. 18961–18971, 2010.
- [79] L. S. Panchakarla et al., “Synthesis, structure, and properties of boron- and nitrogen-doped graphene,” *Adv. Mater.*, vol. 21, no. 46, pp. 4726–4730, 2009.

- [80] B. Zheng, P. Hermet, and L. Henrard, "Scanning tunneling microscopy simulations of nitrogen- and boron-doped graphene and single-walled carbon nanotubes," *ACS Nano*, vol. 4, no. 7, pp. 4165–4173, Jul. 2010.
- [81] Q. Zhu, J. Yu, W. Zhang, H. Dong, and L. Dong, "Solvothermal synthesis of boron-doped graphene and nitrogen-doped graphene and their electrical properties," *J. Renew. Sustain. Energy*, vol. 5, no. 2, p. 021408, Mar. 2013.
- [82] S. Mukherjee and T. P. Kaloni, "Electronic properties of boron- and nitrogen-doped graphene: A first principles study," *J. Nanoparticle Res.*, vol. 14, no. 8, p. 1059, Aug. 2012.
- [83] A. Lherbier, X. Blase, Y. M. Niquet, F. Triozon, and S. Roche, "Charge transport in chemically doped 2D graphene," *Phys. Rev. Lett.*, vol. 101, no. 3, p. 036808, Jul. 2008.
- [84] C. K. Chang et al., "Band gap engineering of chemical vapor deposited graphene by in situ BN doping," *ACS Nano*, vol. 7, no. 2, pp. 1333–1341, Mar. 2013.
- [85] Z. Hou, X. Wang, T. Ikeda, K. Terakura, M. Oshima, and M. Kakimoto, "Electronic structure of N-doped graphene with native point defects," *Phys. Rev. B*, vol. 87, no. 16, p. 165401, Apr. 2013.
- [86] Z. Hou et al., "Interplay between nitrogen dopants and native point defects in graphene," *Phys. Rev. B - Condens. Matter Mater. Phys.*, vol. 85, no. 16, p. 165439, Apr. 2012.
- [87] P. Wu, P. Du, H. Zhang, and C. Cai, "Microscopic effects of the bonding configuration of nitrogen-doped graphene on its reactivity toward hydrogen peroxide reduction reaction," *Phys. Chem. Chem. Phys.*, vol. 15, no. 18, pp. 6920–6928, Apr. 2013.
- [88] A. Lherbier, A. Botello-Mendez, J. C.-N. Letters, and U. 2013, "Electronic and transport properties of unbalanced sublattice N-doping in graphene," *ACS Publ.*, vol. 13, no. 4, pp. 1446–1450, 2013.
- [89] D. Wei, Y. Liu, Y. Wang, H. Zhang, L. Huang, and G. Yu, "Synthesis of n-doped graphene by chemical vapor deposition and its electrical properties," *Nano Lett.*, vol. 9, no. 5, pp. 1752–1758, May 2009.
- [90] D. Usachov et al., "Nitrogen-doped graphene: Efficient growth, structure, and electronic properties," *Nano Lett.*, vol. 11, no. 12, pp. 5401–5407, Dec. 2011.
- [91] F. Cervantes-Sodi, G. Csányi, S. Piscanec, and A. C. Ferrari, "Edge-functionalized and substitutionally doped graphene nanoribbons: Electronic and spin properties," *Phys. Rev. B - Condens. Matter Mater. Phys.*, vol. 77, no. 16, p. 165427, Apr. 2008.
- [92] E. Velez-Fort et al., "Epitaxial graphene on 4H-SiC(0001) grown under nitrogen flux: Evidence of low nitrogen doping and high charge transfer," *ACS Nano*, vol. 6, no. 12, pp. 10893–10900, 2012.
- [93] J. W. Chiou et al., "Nitrogen-functionalized graphene nanoflakes (GNFs:N): Tunable photoluminescence and electronic structures," *J. Phys. Chem. C*, vol. 116, no. 30, pp. 16251–16258, Aug. 2012.
- [94] Z. Yang et al., "Sulfur-doped graphene as an efficient metal-free cathode catalyst for oxygen

- reduction,” *ACS Nano*, vol. 6, no. 1, pp. 205–211, Jan. 2012.
- [95] P. A. Denis, “Band gap opening of monolayer and bilayer graphene doped with aluminium, silicon, phosphorus, and sulfur,” *Chem. Phys. Lett.*, vol. 492, no. 4–6, pp. 251–257, Jun. 2010.
- [96] P. A. Denis, R. Faccio, and A. W. Mombro, “Is it possible to dope single-walled carbon nanotubes and graphene with sulfur?,” *ChemPhysChem*, vol. 10, no. 4, pp. 715–722, 2009.
- [97] J. Wu et al., “Controlled chlorine plasma reaction for noninvasive graphene doping,” *J. Am. Chem. Soc.*, vol. 133, no. 49, pp. 19668–19671, Dec. 2011.
- [98] R. Zbořil et al., “Graphene fluoride: A stable stoichiometric graphene derivative and its chemical conversion to graphene,” *Small*, vol. 6, no. 24, pp. 2885–2891, Dec. 2010.
- [99] M. A. Ribas, A. K. Singh, P. B. Sorokin, and B. I. Yakobson, “Patterning nanoroads and quantum dots on fluorinated graphene,” *Nano Res.*, vol. 4, no. 1, pp. 143–152, Jan. 2011.
- [100] H. Chang et al., “Facile synthesis of wide-bandgap fluorinated graphene semiconductors,” *Chem. - A Eur. J.*, vol. 17, no. 32, pp. 8896–8903, Aug. 2011.
- [101] J. T. Robinson et al., “Properties of fluorinated graphene films,” *Nano Lett.*, vol. 10, no. 8, pp. 3001–3005, Aug. 2010.
- [102] R. Balog et al., “Bandgap opening in graphene induced by patterned hydrogen adsorption,” *Nat. Mater.*, vol. 9, no. 4, pp. 315–319, Apr. 2010.
- [103] E. D.C., N. R.R., M. T.M.G., M. S.V., B. P., and et al., “Control of graphene’s properties by reversible hydrogenation: evidence for graphene,” *Science*, no. 323, p. 610, 2009.
- [104] M. Pumera and C. H. An Wong, “Graphane and hydrogenated graphene,” *Chem. Soc. Rev.*, vol. 42, no. 14, pp. 5987–5995, Jun. 2013.
- [105] S. C. Ray et al., “Graphene supported graphone/graphane bilayer nanostructure material for spintronics,” *Sci. Rep.*, vol. 4, 2014.
- [106] R. Jayasingha, A. Sherehiy, S. Y. Wu, and G. U. Sumanasekera, “In situ study of hydrogenation of graphene and new phases of localization between metal-insulator transitions,” *Nano Lett.*, vol. 13, no. 11, pp. 5098–5105, Nov. 2013.
- [107] Y. Lee, S. Lee, Y. Hwang, and Y. C. Chung, “Modulating magnetic characteristics of Pt embedded graphene by gas adsorption (N<sub>2</sub>, O<sub>2</sub>, NO<sub>2</sub>, SO<sub>2</sub>),” *Appl. Surf. Sci.*, vol. 289, pp. 445–449, Jan. 2014.
- [108] J. Dai, J. Yuan, and P. Giannozzi, “Gas adsorption on graphene doped with B, N, Al, and S: A theoretical study,” *Appl. Phys. Lett.*, vol. 95, no. 23, p. 232105, Dec. 2009.
- [109] Z. M. Ao, J. Yang, S. Li, and Q. Jiang, “Enhancement of CO detection in Al doped graphene,” *Chem. Phys. Lett.*, vol. 461, no. 4–6, pp. 276–279, Aug. 2008.
- [110] H. Nozaki and S. Itoh, “Structural stability of BC<sub>2</sub>N,” *J. Phys. Chem. Solids*, vol. 57, no. 1, pp. 41–49, Jan. 1996.
- [111] S. Bhandary and B. Sanyal, “Graphene-Boron Nitride Composite: A Material with

Advanced Functionalities,” in *Composites and Their Properties*, InTech, 2012.

- [112] P. Rani and V. K. Jindal, “Stability and electronic properties of isomers of B/N co-doped graphene,” *Appl. Nanosci.*, vol. 4, no. 8, pp. 989–996, Nov. 2014.
- [113] B. Muchharla et al., “Tunable electronics in large-area atomic layers of boron-nitrogen-carbon,” *Nano Lett.*, vol. 13, no. 8, pp. 3476–3481, Aug. 2013.
- [114] L. Ci et al., “Atomic layers of hybridized boron nitride and graphene domains,” *Nat. Mater.*, vol. 9, no. 5, pp. 430–435, 2010.
- [115] H. Tachikawa, T. Iyama, and K. Azumi, “Density functional theory study of boron- and nitrogen-atom-doped graphene chips,” *Jpn. J. Appl. Phys.*, vol. 50, no. 1 PART 3, p. 01BJ03, Jan. 2011.
- [116] C. Berger et al., “Ultrathin Epitaxial Graphite: 2D Electron Gas Properties and a Route toward Graphene-based Nanoelectronics,” *J. Phys. Chem. B*, vol. 108, no. 52, pp. 19912–19916, Dec. 2004.

## Chapter 3

### Theoretical background

The results in this thesis are obtained based on the first-principles calculations. This implies there were no empirical data (but the atomic numbers and the positions) employed in the calculation of the electronic structures of the listed systems in this study.

A brief overview of the theoretical approaches and the approximations employed in the modelling of the geometries and the electronic structures of the systems investigated in this study are discussed. The implementation of the theory for the case study presented in the later chapter is also discussed and relevant references are provided for in-depth understanding. For readers who might be interested in learning more about this chapter, the list of the textbooks used in learning this material is hereby provided:

- a) Levine, Ira N. (199). Quantum Chemistry (4 ed.). Englewood Cliffs, New Jersey: Prentice Hall. pp. 455-544. ISBN 0-205-12770-3.
- b) Cramer, Christopher J. (2002). Essentials of Computational Chemistry. Chichester: John Wiley & Sons, Ltd. pp. 153–189. ISBN 0-471-48552-7.
- c) Szabo, A., Ostlund, N. S. (1996). Modern Quantum Chemistry. Mineola, New York: Dover Publishing. ISBN 0-486-69186-1.
- d) Patterson, J., Bailey, B. (2010). Solid-State Physics (2<sup>nd</sup> ed.). Berlin, Heidelberg: Springer Berlin Heidelberg. ISBN 978-3-642-02588-4.

### 3.1 The electronic structure calculations

The properties of a material can be described, in principle, by first constructing the Hamiltonian of the system and then solving the Schrödinger equation. The time-independent Schrödinger equation is given as:

$$\hat{H}\psi_i = E_i\psi_i . \quad (3.23)$$

where  $\hat{H}$ ,  $\psi_i$  and  $E_i$  are the Hamiltonian, eigenfunction and energy, respectively, of the system in a  $i$ th state. In principle, the  $\psi_i$  could be expressed as:

$$\psi_i = \psi_i(\vec{r}_1, \dots, \vec{r}_N, \sigma_1, \dots, \sigma_N : \vec{R}_1, \dots, \vec{R}_M, \delta_1, \dots, \delta_M) . \quad (3.24)$$

where  $\vec{r}$  and  $\sigma$  represent the spatial and spin coordinates of the electrons, respectively.  $\vec{R}$  and  $\delta$  are, in that order, the spatial and spin coordinates of the nuclei.

The Hamiltonian of the system with  $N$  and  $M$  number of electrons and ions, respectively, could be expressed as:

$$\begin{aligned} \hat{H} = & -\frac{\hbar^2}{2m_e} \sum_{i=1}^N \nabla_i^2 - \hbar^2 \sum_{I=1}^M \frac{\nabla_I^2}{2M_I} + \frac{1}{2} \sum_{i \neq j}^N \frac{e^2}{4\pi\epsilon_0 |\vec{r}_i - \vec{r}_j|} \\ & - \sum_{i=1}^N \sum_{I=1}^M \frac{Z_I e^2}{4\pi\epsilon_0 |\vec{r}_i - \vec{R}_I|} + \frac{1}{2} \sum_{I \neq J}^M \frac{Z_I Z_J e^2}{4\pi\epsilon_0 |\vec{R}_I - \vec{R}_J|} . \end{aligned} \quad (3.25)$$

where  $M_I$  is the mass of the  $I$ th nuclei,  $m_e$  and  $e$  are the mass and the charge of the electron respectively.  $Z_I$  is the atomic number on the nucleus at the position  $\vec{R}_I$ . The first and the second term in equation (3.25) denote kinetic energy operators ( $\hat{T}_{elec}$ ) and ( $\hat{T}_{ion}$ ) of the electrons and the ions respectively. The third term is the coulomb interaction between the electrons (also called the

internal potential) ( $\hat{V}_{\text{elec-ele}}$ ) while the fourth term, which is the electron-ion interaction, is the external potential ( $\hat{V}_{\text{ion-elec}}$ ). The last energy term ( $\hat{V}_{\text{ion-i}}$ ) is the coulomb interaction between the ions. The equation (3.25) can be written in a simple form using atomic units (i.e. the Gaussian units with  $\hbar = e = m_e = 1$ ). That is, each energy term in equation (3.25) can now be expressed as follows:

$$1^{\text{st}} \text{ term} \quad \hat{T}_{\text{elec}} = -\frac{1}{2} \sum_{i=1}^N \nabla_i^2 \quad (3.26)$$

$$2^{\text{nd}} \text{ term} \quad \hat{T}_{\text{ion}} = -\frac{1}{2} \sum_{I=1}^M \nabla_I^2 \quad (3.27)$$

$$3^{\text{rd}} \text{ term} \quad \hat{V}_{\text{elec-elec}} = \frac{1}{2} \sum_{i \neq j}^N \frac{1}{|\vec{r}_i - \vec{r}_j|} \quad (3.28)$$

$$4^{\text{th}} \text{ term} \quad \hat{V}_{\text{ion-elec}} = \sum_{i=1}^N \sum_{I=1}^M \frac{Z_i}{|\vec{r}_i - \vec{R}_I|} \quad (3.29)$$

$$5^{\text{th}} \text{ term} \quad \hat{V}_{\text{ion-ion}} = \frac{1}{2} \sum_{I \neq J}^M \frac{Z_I Z_J}{|\vec{R}_I - \vec{R}_J|} \quad (3.30)$$

With the above simplification, equation (3.25) can be written as:

$$\hat{H} = \hat{T}_{\text{elec}} + \hat{T}_{\text{ion}} + \hat{V}_{\text{ion-elec}} + \hat{V}_{\text{elec-elec}} + \hat{V}_{\text{ion-ion}} \quad (3.31)$$

It is worth mentioning that in the above problem, the electrons have been separated into the valence and the core electrons. The core electrons are found in the occupied orbitals and are closer to the nuclei. They can be grouped with the nuclei to form the ion core. Hence, in equation (3.25), ‘I’ and ‘J’ represent the core ions while ‘i’ and ‘j’ denote the valence electrons. Since most of the physical systems of interest are made up of a large number of atoms, solving equation (3.23) would be difficult due to the multi-degree of freedom of the system and the presence of electron-electron interaction. However, to solve the equation, a number of accepted approximations could be applied to simplify the problem. One of the approximations that could be applied to simplify the equation is known as the Born-Oppenheimer approximation.

### 3.1.1 Adiabatic or Born-Oppenheimer approximation [1]

This approximation decouples the nuclei motion from that of the electrons. The ions are considerably heavier than the electrons and as a result move negligibly slower, thus, the ions could be assumed to be stationary while the electrons move in the field. This makes the nuclei kinetic energy term of equation (3.25) to be negligible and their potential energy a constant. However, the ion-ion interaction term is retained because the positions of the nuclei could be varied to minimize the energy of the system. Following this approximation, the Hamiltonian of the system reduces to:

$$\hat{H}_{\text{elec}} = \hat{T}_{\text{elec}} + \hat{V}_{\text{ion-elec}} + \hat{V}_{\text{elec-elec}} \quad (3.32)$$

where  $\hat{H}_{\text{elec}}$  is the electronic Hamiltonian of the system. Thus, for the electron wave function, equation (3.23) becomes:



$$\hat{H}_{\text{elec}}\Psi_{\text{elec}}(\vec{r}_1, \vec{r}_2, \dots) = E_{\text{elec}}\Psi_{\text{elec}}(\vec{r}_1, \vec{r}_2, \dots). \quad (3.33)$$

It is worth noting that the  $\Psi_{\text{elec}}$  depends parametrically on the nuclear coordinates as a consequence of Born-Oppenheimer approximation. Although the spin coordinates have not been indicated explicitly,  $r_i$  is assumed to account for both the position and the spin coordinates of the electrons. The total energy  $E_{\text{tot}}$  for fixed nuclei could be written as the summation of the electronic energy  $E_{\text{elec}}$  and the nuclei  $E_{\text{nucli}}$ , i.e

$$E_{\text{tot}} = E_{\text{elec}} + E_{\text{nucli}}. \quad (3.34)$$

If one considers the motion of the nuclei in an average field of the electrons, then  $E_{\text{tot}}$  of equation (3.34) provides the potential energy for the nuclear motion. Thus,  $E_{\text{tot}}$  constitutes a potential energy surface, and the nuclei in the Born-Oppenheimer approximation move on this surface.

Despite the fact that the number of the degree of freedom in the electronic wave function in equation (3.33) is lower than that of the equation (3.23), it is still difficult to solve. An approximation that could be employed to solve equation (3.33) is the Hartree approximation. Before discussing the Hartree approximation, it is necessary to first discuss the variation principle which is fundamental to the Hartree approximation, and other concepts (such as the Hartree-Fock approximation and the density functional theory) that will be discussed in this chapter.

### 3.1.2 The variational principle

The variational principle, also known as the Rayleigh-Ritz variational principle, expresses how to construct energies with the values equal or greater than the ground-state energy of a many-body system. The principle is an important tool for the derivation of both the Hartree and Hartree-Fock equations. It can also be used with the density functional method to arrive at the Kohn-Sham equations.

Let  $\hat{H}$  be a positive definite Hermitian operator which has a lowest eigenvalue  $E_0$ . Suppose  $|\Psi\rangle$  is a trial wave function (not necessarily normalized) with an adjustable parameter  $\eta$ , then the basic variational principle is given by equation (3.35) :

$$Q(\Psi) = \frac{\langle \Psi | \hat{H} | \Psi \rangle}{\langle \Psi | \Psi \rangle} \geq E_0 . \quad (3.35)$$

$$\frac{\partial Q}{\partial \eta} = 0 \quad (3.36)$$

If the trial wave function  $|\Psi\rangle$  is not the exact wave function, by applying the minimization technique (equation (3.36)),  $Q(\Psi)$  can get as close as possible to  $E_0$ .

### 3.1.3 The Hartree approximation

The Hartree approximation was formulated in 1928 [2]. With this approximation, the many-body wave function  $\psi$  is written as the product of one-electron wave functions:

$$\Psi(\vec{r}_1, \vec{r}_2, \dots, \vec{r}_N) = \psi_1(\vec{r}_1)\psi_2(\vec{r}_2) \dots \psi_N(\vec{r}_N). \quad (3.37)$$

where the wave function  $\psi_i(\vec{r}_i)$ , which are uncorrelated but orthogonal, satisfies the one-electron Schrödinger equation. The position and the spin coordinates are also considered to be part of  $r_i$ .

As a result of the Hartree approximation, the Hamiltonian  $\hat{H}$  of the many-body problem is given as:

$$\hat{H}_H = \hat{T}_e + \hat{V}_H + \hat{V}_{ion} . \quad (3.38)$$

where  $\hat{T}_e = -\frac{1}{2}\nabla^2$  is the single-electron kinetic energy term;  $\hat{V}_{\text{ion}}$  is the coulomb interaction between the electron and the ion;  $\hat{V}_H$  is the Hartree potential and it is expressed as:

$$\mathbf{v}_H(\vec{\mathbf{r}}_i) = \sum_{i \neq j} \int \frac{d\mathbf{r}'_j}{|\vec{\mathbf{r}}_i - \vec{\mathbf{r}}'_j|} \mathbf{n}(\vec{\mathbf{r}}'_j). \quad (3.39)$$

The probability density of the  $j$ th particle  $\mathbf{n}(\vec{\mathbf{r}}'_j)$  in equation (3.39) is defined as:

$$\mathbf{n}(\vec{\mathbf{r}}'_j) = |\Psi(\vec{\mathbf{r}}'_j)|^2. \quad (3.40)$$

Electrons are fermions and as a result must have antisymmetric wave functions with respect to the interchange of any two electrons [3]. However, the Hartree wave function does not take into account that electrons are fermions. The deficiency in the Hartree wave function can be resolved by writing a new wave function as a linear combination of the Hartree products to form a Slater determinant (after John Slater [4]). The new wave function is the basis of the Hartree-Fock approximation.

### 3.1.4 The Hartree-Fock (HF) approximation

The Hartree-Fock (HF) [5] approximation was formulated to correct the failure of the Hartree approximation. The difference in the two approaches is in the trial wave function that is used. With Slater determinant, Hartree-Fock wave functions could be expressed as:

$$\Psi(\vec{\mathbf{r}}_1, \vec{\mathbf{r}}_2, \dots, \vec{\mathbf{r}}_N) = \frac{1}{\sqrt{N!}} \begin{vmatrix} \Phi_1(\vec{\mathbf{r}}_1) & \Phi_2(\vec{\mathbf{r}}_1) & \dots & \Phi_N(\vec{\mathbf{r}}_1) \\ \Phi_1(\vec{\mathbf{r}}_2) & \Phi_2(\vec{\mathbf{r}}_2) & \dots & \Phi_N(\vec{\mathbf{r}}_2) \\ \cdot & \cdot & \dots & \cdot \\ \cdot & \cdot & \dots & \cdot \\ \cdot & \cdot & \dots & \cdot \\ \Phi_1(\vec{\mathbf{r}}_N) & \Phi_2(\vec{\mathbf{r}}_N) & \dots & \Phi_N(\vec{\mathbf{r}}_N) \end{vmatrix}. \quad (3.41)$$

The factor in front of equation (3.41) is the normalization constant, while  $\phi_k(\vec{r}_j) = \phi_k(\vec{r})\sigma_k$  are one particle spin-orbitals and “ $\vec{r}_j$ ” is a vector which defines the position of the electron, and  $\sigma_k$  is the spin state (down or up). For simplicity, equation (3.41) can be written as equation (3.42):

$$\Psi(\vec{r}_1, \vec{r}_2, \dots, \vec{r}_N) = \frac{1}{\sqrt{N!}} \text{Det}[\phi_1(\vec{r}_1), \phi_2(\vec{r}_2), \dots, \phi_N(\vec{r}_N)]. \quad (3.42)$$

where Det denotes a matrix determinant. The determinant can be shown to satisfy the Pauli Exclusion Principle and the required antisymmetry condition. Minimizing the variation functional with respect to the trial wave function of equation (3.42), a new equation, which is the Hartree equation plus an additional term (known as the exchange term) is obtained. The new equation is called the Hartree-Fock equation, and it is expressed as:

$$\epsilon_i \Psi_i = [\hat{T}_e + \hat{V}_H + \hat{V}_{\text{ion}}] \Psi_i - \frac{1}{2} \sum_j \int d^3r' \psi_j^*(\vec{r}') \psi_i(\vec{r}') \frac{1}{|\vec{r} - \vec{r}'|} \psi_j(\vec{r}). \quad (3.43)$$

The exchange term describes the interaction between the electrons of the same spin. It is nonlocal, which as a result, makes Hartree-Fock equation difficult to solve. The Hartree-Fock approximation has been found to give less satisfactory results in some cases. For instance, its description of the properties of homogeneous gas is limited. This inaccuracy is as a result of not taking into account the coulomb repulsion between electrons of the same spin. The HF energy is always greater than the ground state energy. The difference between the exact and HF energy is known as the correlation energy. To overcome this limitation, numerous methods have been formulated. One of these methods is referred to as density functional theory [6], [7].

### 3.1.5 Density functional theory

Thomas in 1927 [8] and Fermi in 1928 [9] were the first to develop a theory of the electronic energy in terms of electron density distribution,  $n(\mathbf{r})$ . Later, Kohn and Hohenberg in 1964 [7][6] gave a rigorous formula of density-functional theory (DFT) which was made practical after one year by Kohn Sham [10]. The central quantity in DFT is the electron density  $n(\vec{r})$ . With the electron density formulation, the many-body problem appears simpler to solve than the wave function approach. Because, rather than contending with the  $3N$  spatial coordinates, as it is the case in many-body wave function, only three spatial coordinates are specified in electron density approach [11].

### 3.1.6 Hohenberg-Kohn theorem

The two Hohenberg and Kohn theorems, which formed the basis of DFT, are stated as follows:

- 1) The first theorem states that the density of the nondegenerate ground state of a system of bound interacting electrons in an external potential is determined up to an arbitrary additive constant [12].

To prove the theorem, the following assumptions will form the premise of the proof:

Suppose  $n(\vec{r})$  is the non-degenerate ground-state density of  $N$  interacting electrons in an external potential  $v_{ext}^{(1)}$  which corresponds to the ground state  $\Psi^{(1)}$  and the energy  $E^{(1)}$ . Let there exist a second external potential  $v_{ext}^{(2)}$ , which differs from the  $v_{ext}^{(1)}$  beyond a constant, with the same ground state density  $n(\vec{r})$  but gives rise to the ground state  $\Psi^{(2)}$ . If  $H^{(1)}$  and  $H^{(2)}$  are the Hamiltonians which correspond to  $\Psi^{(1)}$  and  $\Psi^{(2)}$ , then following variational principle,

$$\mathbf{E}^{(1)} = \langle \Psi^{(1)} | \hat{H}^{(1)} | \Psi^{(1)} \rangle < \langle \Psi^{(2)} | \hat{H}^{(1)} | \Psi^{(2)} \rangle. \quad (3.44)$$

It is worth noting that equation (3.44) holds because a nondegenerate ground state has been assumed.

The last term in equation (3.44) could be rewritten as:

$$\langle \Psi^{(2)} | \hat{H}^{(1)} | \Psi^{(2)} \rangle = \langle \Psi^{(2)} | \hat{H}^{(2)} | \Psi^{(2)} \rangle + \langle \Psi^{(2)} | \hat{H}^{(1)} - \hat{H}^{(2)} | \Psi^{(2)} \rangle \quad (3.45)$$

$$= \mathbf{E}^{(2)} + \int d\vec{r} \left[ \mathbf{v}_{\text{ext}}^{(1)}(\vec{r}) - \mathbf{v}_{\text{ext}}^{(2)}(\vec{r}) \right] \mathbf{n}(\vec{r}). \quad (3.46)$$

Combining equations (3.44 and 3.46), gets

$$\mathbf{E}^{(1)} < \mathbf{E}^{(2)} + \int d\vec{r} \left[ \mathbf{v}_{\text{ext}}^{(1)}(\vec{r}) - \mathbf{v}_{\text{ext}}^{(2)}(\vec{r}) \right] \mathbf{n}(\vec{r}). \quad (3.47)$$

Similarly,

$$\mathbf{E}^{(2)} = \langle \Psi^{(2)} | \hat{H}^{(2)} | \Psi^{(2)} \rangle < \langle \Psi^{(1)} | \hat{H}^{(2)} | \Psi^{(1)} \rangle. \quad (3.48)$$

Following the steps in equations (3.45 and 3.46), equation (3.48) could be written as:

$$\mathbf{E}^{(2)} < \mathbf{E}^{(1)} + \int d\vec{r} \left[ \mathbf{v}_{\text{ext}}^{(2)}(\vec{r}) - \mathbf{v}_{\text{ext}}^{(1)}(\vec{r}) \right] \mathbf{n}(\vec{r}). \quad (3.49)$$

A contradicting result is obtained if equation (3.47) and equation (3.49) are added together, i.e.

$$\mathbf{E}^{(1)} + \mathbf{E}^{(2)} < \mathbf{E}^{(2)} + \mathbf{E}^{(1)}. \quad (3.50)$$

The result of the equation (3.50) shows that no two external potentials differing by more than a constant have the same non-degenerate ground state electron density. For further detail about this proof see Ref.[13]. It is noteworthy to mention that the external potential is not determined in the region of space where density is zero.

- 2) The second theorem states that a universal functional could be defined to determine the energy that is equivalent to a particular charge density and the external potential. Moreover,

the ground state energy of the system is the minimum of this functional, and the density that minimises the functional is the ground state density [6].

The two theorems narrow the task of finding all the physical properties relating to the ground state of a system to just determining the electron density that minimises the energy functional [11]. Following Hohenberg-Kohn theorem, the energy functional could be written as the summation of the kinetic and potential energy arising from the interaction of the electrons with themselves and the external potential, i.e:

$$\mathbf{E}_{\text{HK}}[\mathbf{n}] = \mathbf{T}_{\text{elec}}[\mathbf{n}] + \mathbf{E}_{\text{int}}[\mathbf{n}] + \mathbf{E}_{\text{ext}}[\mathbf{n}] = \mathbf{F}_{\text{HK}}[\mathbf{n}] + \int \mathbf{n}(\vec{r}) v_{\text{ext}} \mathbf{d}(\vec{r}) . \quad (3.51)$$

where  $F_{\text{HK}}$ , which is independent of a given system and known as the Hohenberg-Kohn functional for the kinetic energy and the electron-electron energy interaction, is expressed as:

$$\mathbf{F}_{\text{HK}}[\mathbf{n}] = \mathbf{T}_{\text{elec}}[\mathbf{n}] + \mathbf{E}_{\text{int}}[\mathbf{n}] . \quad (3.52)$$

Applying the minimization principle in line with the constraint search method by Levy and Lieb [14], [15], equation (3.51) becomes:

$$\mathbf{E}_o \leq \mathbf{E}_{\text{HK}}[\mathbf{n}] = \mathbf{F}_{\text{HK}}[\mathbf{n}] + \int \mathbf{n}(\vec{r}) v_{\text{ext}} \mathbf{d}(\vec{r}) . \quad (3.53)$$

$$\mathbf{F}_{\text{HK}}[\mathbf{n}] = \min_{\Psi \rightarrow \mathbf{n}} \langle \Psi | \mathbf{T}_{\text{elec}} + \mathbf{V}_{\text{e-e}} | \Psi \rangle . \quad (3.54)$$

where  $E_o$  represents the ground-state energy of electrons in an external potential  $v_{\text{ext}}(\vec{r})$ . Equation (3.53) reveals that the electron density that minimises the Hohenberg-Kohn functional is the exact ground state density. Equation (3.54) is a Levy-Lieb functional and shows that the prior knowledge of  $v_{\text{ext}}$  is not required. It is a universal functional of the electron density which must not necessarily be v-representable.

### 3.1.7 Kohn-Sham scheme

The Kohn-Sham scheme involves replacing the interacting many-body system with a different auxiliary system that could be solved more easily. In the scheme, it is assumed that the ground state density of the interacting system is equal to that of some predetermined non-interacting system fermions.

For a system of  $N$  independent electrons with each occupying an orbital  $\psi_i$ , which corresponds to eigenvalue  $\epsilon_i$ , the Hamiltonian for one electron system could be written as :

$$\left[ -\frac{1}{2} \nabla^2 + \hat{V}_{\text{eff}}[\mathbf{n}](\vec{r}) \right] \Psi_{\mathbf{k}} = \Psi_{\mathbf{k}} \epsilon_{\mathbf{k}} . \quad (3.55)$$

The equation (3.55) is used to generate the electron density of the auxiliary Kohn-Sham system, i.e.:

$$\mathbf{n}(\vec{r}) = \sum_{\mathbf{k}=1}^N |\Psi_{\mathbf{k}}(\vec{r})|^2 . \quad (3.56)$$

The Hohenberg-Kohn equation for the ground state energy functional can now be re-expressed in terms of the Kohn-Sham scheme as:

$$\mathbf{E}_{\text{KS}}[\mathbf{n}] = \mathbf{T}_s[\mathbf{n}] + \mathbf{E}_{\text{XC}}[\mathbf{n}] + \int_{\Omega} \mathbf{d}^3\mathbf{r} \hat{V}_{\text{ext}}\mathbf{n}(\vec{r}) + \mathbf{E}_{\text{II}} . \quad (3.57)$$

where the independent particle kinetic energy  $\hat{T}_s[n]$  is expressed as:

$$\mathbf{T}_s = -\frac{1}{2} \sum_{\mathbf{k}=1}^N \langle \Psi_{\mathbf{k}} | \nabla^2 | \Psi_{\mathbf{k}} \rangle . \quad (3.58)$$



The kinetic energy  $\hat{T}_s[n]$  is further extended by Kohn and Sham through a universal functional  $F_{KS}[n]$  which also includes the internal and the exchange-correlation energy,  $E_{XC}[n]$ :

$$\mathbf{F}_{KS}[\mathbf{n}] = \mathbf{T}_s[\mathbf{n}] + \int \mathbf{d}^3\mathbf{r}\mathbf{d}^3\mathbf{r}' \frac{\mathbf{n}(\vec{\mathbf{r}})\mathbf{n}(\vec{\mathbf{r}}')}{|\vec{\mathbf{r}} - \vec{\mathbf{r}}'|} + \mathbf{E}_{XC}[\mathbf{n}]. \quad (3.59)$$

The second term in equation (3.59) is the Hartree energy term. By equating  $F_{KS}[n]$  to Hohenberg-Kohn universal functional  $F_{HK}[n]$  expressed in equation (3.52), we have

$$\mathbf{T}_{elec}[\mathbf{n}] + \mathbf{E}_{int}[\mathbf{n}] = \mathbf{T}_s[\mathbf{n}] + \int \mathbf{d}^3\mathbf{r}\mathbf{d}^3\mathbf{r}' \frac{\mathbf{n}(\vec{\mathbf{r}})\mathbf{n}(\vec{\mathbf{r}}')}{|\vec{\mathbf{r}} - \vec{\mathbf{r}}'|} + \mathbf{E}_{XC}[\mathbf{n}]. \quad (3.60)$$

Equation (3.60) can be rewritten in the following form:

$$\mathbf{E}_{XC}[\mathbf{n}] = \mathbf{T}[\mathbf{n}] - \mathbf{T}_s[\mathbf{n}] + \mathbf{E}_{int}[\mathbf{n}] - \int \mathbf{d}^3\mathbf{r}\mathbf{d}^3\mathbf{r}' \frac{\mathbf{n}(\vec{\mathbf{r}})\mathbf{n}(\vec{\mathbf{r}}')}{|\vec{\mathbf{r}} - \vec{\mathbf{r}}'|}. \quad (3.61)$$

Or

$$\mathbf{E}_{XC}[\mathbf{n}] = \mathbf{T}[\mathbf{n}] - \mathbf{T}_s[\mathbf{n}] + \mathbf{E}_{int}[\mathbf{n}] - \mathbf{E}_{Hartree}[\mathbf{n}]. \quad (3.62)$$

Equation (3.62) shows that  $E_{XC}$  is the sum of the difference between the kinetic and the internal energies of the fully interacting body system and that of the auxiliary independent-particle system such that an electron-electron interaction is replaced by the Hartree energy term. If  $E_{XC}$  is known, then the electron density of the many-body system could be determined by solving the Kohn-Sham equations for the independent particles of the auxiliary system.

### 3.1.8 Kohn-Sham variational equations

The solution of the Kohn-Sham independent particles system for the ground state could be seen as the minimization of equation (3.57) with respect to the electron density subject to the orthonormalization conditions, i.e.:

$$\frac{\delta E_{KS}}{\delta \psi_i^*(\vec{r})} = \frac{\delta T_s}{\delta \psi_i^*(\vec{r})} + \left[ \frac{\delta E_{ext}}{\delta n(\vec{r})} + \frac{\delta E_{Hartree}}{\delta n(\vec{r})} + \frac{\delta E_{XC}}{\delta n(\vec{r})} \right] \frac{\delta n(\vec{r})}{\delta \psi_i^*(\vec{r})} = 0. \quad (3.63)$$

where

$$\frac{\delta T_s}{\delta \psi_i^*(\vec{r})} = -\frac{1}{2} \nabla^2 \psi_i(\vec{r}) ; \frac{\delta n(\vec{r})}{\delta \psi_i^*(\vec{r})} = \psi_i(\vec{r}) \quad (3.64)$$

It is important to note that the concept of functional derivatives has been applied to equation (3.63) and equation (3.65). Given a functional  $F[n]$ , the functional derivative  $\delta F[n]$  is expressed as:

$$\delta F[n] = F[n + \delta n] - F[n] = \int \frac{\delta F}{\delta n(\vec{r})} \delta n(\vec{r}) d\vec{r}. \quad (3.65)$$

Subsequently, the form of equation (3.65) should be assumed wherever functional derivatives have appeared in other expressions in this thesis.

Substituting equation (3.65) into equation (3.63), Kohn-Sham Hamiltonian  $H_{KS}$  is obtained:

$$H_{KS}(\vec{r}) = -\frac{1}{2} \nabla^2 + V_S(\vec{r}). \quad (3.66)$$

where

$$V_S = V_{ext}(\vec{r}) + \frac{\delta E_{Hartree}}{\delta n(\vec{r})} + \frac{\delta E_{XC}}{\delta n(\vec{r})} \quad (3.67)$$

Or

$$\mathbf{V}_{\text{eff}} = \mathbf{V}_{\text{ext}}(\vec{\mathbf{r}}) + \mathbf{V}_{\text{Hartree}} + \mathbf{V}_{\text{XC}} \quad (3.68)$$

The equations (3.55) and equation (3.68) are known as Kohn-Sham equations with the total energy  $E_{\text{KS}}$  given by equation (3.57). The equations assume that the independent particle equations and the potential must be determined self-consistently with the calculated electron density. It is worth mentioning that the equations would lead to the exact ground state electron density and energy of an interacting many-body system, if the exact functional  $E_{\text{XC}}$  is known. The meaning and the classes of the exchange-correlation energy are discussed in section 3.2. Meanwhile, the Kohn-Sham theory contains the assumption of noninteracting  $v$ -representability which means that there always exists a noninteracting electrons system with the same ground state density as the interacting system of electrons. However, it has been proven that this is not always the case [16].

### 3.2 The exchange-correlation energy

The second term of equation (3.57) is the exchange-correlation energy and accounts for all the remaining complex electronic contributions to the total energy. It could be expressed as the sum of the exchange  $E_{\text{X}}$  and correlation energy  $E_{\text{C}}$  (see equation (3.69)). Electrons are indistinguishable (fermions) and as a result, obey the Pauli Exclusion Principle.

$$\mathbf{E}_{\text{XC}} = \mathbf{E}_{\text{X}} + \mathbf{E}_{\text{C}} . \quad (3.69)$$

The Pauli principle implies that no two electrons with the same spin can be found at the same point in real space. Consequently, the average Coulomb repulsive energy acting on the electron is reduced. The energy gain in this process is called the exchange energy. However, the additional interaction terms between electrons of antiparallel spin are called the coulomb correlation energy. This is not the full correlation energy. The right definition of the correlation energy is given by

Löwdin [17] as the difference between the exact energy and the Hartree-Fock limit. Although the accuracy of density functional theory depends on the exchange-correlation energy, unfortunately, for practical applications, the exact form of this functional is unknown and still remains under the expanding field of active research. There are many approximations to the exchange-correlation functionals, namely Local Density Approximation (LDA), Generalized Gradient Approximation (GGA), Meta-GGA and Hybrid Functional. In the following section, only LDA, GGA and Hybrid functional are discussed.

### 3.2.1 Local density approximation (LDA)

The earliest and most fundamental approximation to the exchange-correlation energy functional in DFT is LDA. With the LDA, the energy of an electronic system is formulated such that the exchange-correlation energy per electron  $\epsilon_{XC}$  in a specific region in the electron gas is equal to the exchange-correlation energy per electron in a homogeneous electron gas with the same electrons distribution. With respect to this assumption, for a spinless system, the LDA can be expressed as equation (3.70)

$$\mathbf{E}_{XC}^{LDA}[\mathbf{n}] = \int \mathbf{n}(\vec{\mathbf{r}}) \epsilon_{XC}(\mathbf{n}(\vec{\mathbf{r}})) d\vec{\mathbf{r}} . \quad (3.70)$$

The approximation can be extended to spin polarized system. With the incorporation of spin, the LDA is called the Local Spin Density Approximation (LSDA), and it is written as:

$$\mathbf{E}_{XC}^{LSDA}[\mathbf{n}^\uparrow, \mathbf{n}^\downarrow] = \int \mathbf{n}(\vec{\mathbf{r}}) \epsilon_{XC}(\mathbf{n}^\uparrow(\vec{\mathbf{r}}), \mathbf{n}^\downarrow(\vec{\mathbf{r}})) d\mathbf{r} . \quad (3.71)$$

The LSDA could be described as a function of spin up and down densities, but it is often expressed in terms of the total electrons density  $n = n^\uparrow + n^\downarrow$  and the spin polarization  $\xi = \frac{n^\uparrow - n^\downarrow}{n}$ . One of the advantages of LDA (and generally LSDA) is that it is not computationally demanding. The

approximation is fairly accurate in covalent systems and simple metals in which the electron density varies relatively slowly. However, the functional has failed to predict accurately the electronic properties (such as band-gap) of semiconductor materials. For such systems, LDA underestimates their band-gaps. Other drawbacks of LDA include, but not limited to the underestimation of the lattice parameter, overestimation of the cohesive energy and modulus of solids.

### 3.2.2 The generalized gradient approximation (GGA)

Another approximation to the Kohn-Sham functional is the generalized gradient approximation (GGA). In the formulation, GGA goes beyond LDA by comprising not only the electron density at a particular point  $n(\vec{r})$  but also the gradient  $\nabla n(\vec{r})$  in order to account for the spatial variation in the true electron density. The physical intuition behind the GGA is that, in reality, the electron density of a system is not uniform, as a result including information that embraces the variation in the electron density could lead to a functional with the capacity to describe a real material. The expression for the GGA, as an exchange-correlation functional, is shown in equation (3.72):

$$E_{XC}^{GGA}[n] = \int n(\vec{r}) \epsilon_{XC}(n(\vec{r}), \nabla n(\vec{r})) d\mathbf{r}. \quad (3.72)$$

The equation (3.72) is only valid for a non-spin polarized system. However, for a spin-polarized system, the equation can be modified as equation (3.73) to include the forms of the spin densities in the system:

$$E_{XC}^{GGA}[n^\uparrow, n^\downarrow] = \int n(\vec{r}) \epsilon_{XC}(n^\uparrow, n^\downarrow, \nabla n^\uparrow, \nabla n^\downarrow) d\mathbf{r}. \quad (3.73)$$

There are several known forms of GGA functionals, namely, PBE functional as proposed by Perdew-Burke-Ernzerhof [18], Becke exchange [19], PBEsol which is an extension of PBE for Solids [20] and Lee-Yang-Parr (LYP) correlation [19], [21], [22]. Because the GGA functional has more physical quantities than the LDA, it is often assumed that the GGA would lead to more accurate results than the LDA. Although this is often the case, there are known exceptions. The GGA functionals are known to yield more accurate estimate of the total energies [23]–[27] and atomization energies [22] of a standard set of atoms and molecules. The functionals have also been reported to exhibit significant advantages over LDA in the prediction of the right ferromagnetism configurations of BCC iron at the ground state [19]. With the LDA, the calculated lattice constants are usually 2% lower than the corresponding experimental values, whereas the GGA improves upon these results in most cases but often overestimate with respect to the experimental values [21], [28]. Despite the successes that have been reported with LDA and GGA, there are some common pitfalls associated with the use of the two set of functionals in predicting the physical properties of materials. For example, both the LDA and GGA underestimate the band-gap of semiconductors and insulators. In addition, they also fail to accurately describe the weak Van der Waals attraction between layered materials or the adsorption of gases on graphene. This failure might be attributed to the neglect of the long-range nonlocal correlations in LDA and GGA. One of the pragmatic approaches to overcome this limitation has been given by the DFT-D2 method of Grimme [29] which describes Van der Waals interactions through a simple pair-wise force field and it is optimized for several DFT functionals.

### 3.2.3 The hybrid functionals

It is worth mentioning that while the GGA underestimates a Kohn-Sham band-gap, Hartree-Fock (HF) systematically overestimates it [30]. Due to the inaccuracy of GGA and LDA in predicting the band-gap of some materials, notably the underestimation of the band-gaps of semiconductors, hybrid functionals which describe exchange employing a blend of the exact non-local HF exchange ( $E_X^{\text{HF}}$ ) (see equation (3.74) ) and a number of exchange and correlation functionals, have been developed to overcome such limitations:

$$E_X^{\text{HF}} = -\frac{1}{2} \sum_{ij} \int \int \Psi_i^*(r_1) \Psi_j^*(r_2) \frac{1}{r_{12}} \Psi_j(r_1) \Psi_i(r_2) \mathbf{d}r_1 \mathbf{d}r_2. \quad (3.74)$$

where  $r_{12} = |\mathbf{r}_1 - \mathbf{r}_2|$ .

Although there are different types of hybrid functionals in use today, the most common ones are B3LYP (Becke, 3 parameters, Lee-Yang-Par)[31], [32], PBE0 (Perdew-Burke-Ernzerhof) [33], [34], HSE (Heyd-Scuseria-Ernzerhof) [35] and optimally tuned range separated hybrids [36]. B3LYP is formed from the linear combination of  $E_X^{\text{HF}}$ ,  $E_X^{\text{GGA}}$ ,  $E_C^{\text{GGA}}$ ,  $E_X^{\text{LDA}}$  and  $E_C^{\text{LDA}}$  which are the exchange and the correlation functionals corresponding to GGA and LDA as expressed in equation (3.75).

$$E_{\text{XC}}^{\text{B3LYP}} = E_X^{\text{LDA}} + a_0(E_X^{\text{HF}} - E_X^{\text{LDA}}) + a_x(E_X^{\text{GGA}} - E_X^{\text{LDA}}) + E_C^{\text{LDA}} + a_c(E_C^{\text{GGA}} - E_C^{\text{LDA}}). \quad (3.75)$$

where  $a_0 = 0.2$ ,  $a_x = 0.72$ , and  $a_c = 0.81$ .

With the PBE0 functional, it combines the PBE exchange energy ( $E_X^{\text{PBE}}$ ) and of  $E_X^{\text{HF}}$  in a 3 to 1 ratio with the complete PBE correlation energy ( $E_C^{\text{PBE}}$ ) as shown in equation (3.76):

$$\mathbf{E}_{\text{XC}}^{\text{B3LYP}} = \frac{1}{4} \mathbf{E}_{\text{X}}^{\text{HF}} + \frac{3}{4} \mathbf{E}_{\text{X}}^{\text{PBE}} + \mathbf{E}_{\text{C}}^{\text{PBE}} . \quad (3.76)$$

Hybrid functionals usually give fairly accurate predictions of the band-gaps, reliable total energies and geometries of molecules and solids. However, due to the slow decay of HF exchange, such functionals are computationally expensive and thus could be intractable for extended systems [37]. Therefore, short-range functionals, like the screened hybrid functionals HSE03 [35] and HSE06 [38], are proven alternatives to the standard hybrid functionals. This is because the spatial decay of HF exchange interaction is sped up in HSE03 and HSE06 by substituting the  $\frac{1}{r_{12}}$  Coulomb potential with the screened potential as shown in equation (3.77). The exchange energy term is divided into the short range (SR) and long range (LR), and the long range component is ignored but replaced by the PBE LR contribution. The hybrid exchange-correlation energy is thus expressed as equation (3.78).

$$\frac{1}{\mathbf{r}} = \frac{\text{erfc}(\omega\mathbf{r})}{\mathbf{r}} + \frac{\text{erf}(\omega\mathbf{r})}{\mathbf{r}} \quad (3.77)$$

$$\mathbf{E}_{\text{XC}}^{\text{HSE}} = \alpha \mathbf{E}_{\text{X}}^{\text{HF,SR}}(\omega) + (1 - \alpha) \mathbf{E}_{\text{X}}^{\text{PBE,SR}}(\omega) + \mathbf{E}_{\text{X}}^{\text{PBE,LR}}(\omega) + \mathbf{E}_{\text{C}}^{\text{PBE}} \quad (3.78)$$

where  $r = r_{12}$ ;  $\alpha$  is the mixing parameter (often considered as  $\alpha = 0.25$ ) between the short-range HF exchange energy  $\mathbf{E}_{\text{X}}^{\text{HF,SR}}(\omega)$  and PBE energy  $\mathbf{E}_{\text{X}}^{\text{PBE,SR}}(\omega)$ ;  $\omega$  is the adjustable screening parameter that controls the short-range of the interaction;  $\mathbf{E}_{\text{C}}^{\text{PBE}}$  denotes the PBE correlation energy. Setting  $\omega = 0.2 \text{ \AA}^{-1}$  leads to the HSE03 functional, while HSE06 is formed with  $\omega=0.3 \text{ \AA}^{-1}$ . Table 3.1 compares the experimental band-gaps of materials with the calculated values as predicted by the LDA, GGA and HSE hybrid functionals.



**Table 3.1** The calculated and experimental band-gaps of some selected materials

Materials	LDA(eV)	GGA(eV)	HSE(eV)	EXP (eV)
Ar <sup>c</sup>	8.16	8.74	10.34	14.20
C <sup>a</sup>	4.11	4.21	5.42	5.48
Si <sup>b</sup>	0.61	0.61	1.17	1.17
Ge	0.00	0.00	0.80 <sup>c</sup>	0.78 <sup>a</sup>
AlN <sup>c</sup>	4.17	4.18	5.81	6.19
ZnO <sup>c</sup>	0.75	0.80	2.49	3.44
MgSe <sup>b</sup>	-	1.70	2.60	3.60 <sup>d</sup>
MgTe <sup>b</sup>	2.26	2.34	3.01	3.47 <sup>d</sup>
MgO <sup>c</sup>	4.70	4.68	6.67	7.83

<sup>a</sup>Ref.[28], <sup>b</sup>Ref.[23]<sup>c</sup>Ref.[39], <sup>d</sup>Ref.[40], [41]<sup>e</sup>Spin orbit interaction.

From the table, it can be observed that HSE06 functional accurately predicts the electronic band-gaps of all group IV semiconductors. Apart from the acceptable accuracy in the prediction of the band-gaps of semiconductors, the HSE has been used to obtain reliable results of the electronic properties of materials (such as rare earth elements) with highly localized electrons.

### 3.3 The electron-ion interaction

In order to solve the Khon-Sham equation, two important issues have to be considered. First, the electron-ion interaction or the external potential  $V_{\text{ext}}(\mathbf{r})$  must be treated in a special way since the full coulomb potential of such interaction decays too slowly to be efficiently represented by

small number of Fourier components. The second issue is finding the right mathematical expression for the single particle orbitals. To resolve the first issue, the  $V_{\text{ext}}(r)$  could be treated using two common approaches, i.e., either by employing the all-electron [40], [41] or pseudopotential method. Due to the enormous benefit in terms of computational cost, in this study, pseudopotentials approach was adopted for the treatment of the external potential. For the second issue, it can be resolved by employing basis set to represent the single-particle orbitals.

### **3.3.1 Pseudopotential method**

Pseudopotential approach is used to reduce the weight of complexity of the many-body problem of a large system [42]. Conceptually, with pseudopotential, the core electrons are frozen out since they are not involved in chemical bonding and other physical characteristics of the materials [43]. With the core electrons frozen out, the number of the basis set required to describe the valence-electron wave function reduces thereby saving computational cost. Generally, pseudopotentials are formulated to generate the true potential of a nucleus outside the sphere of a given radius ( $r_c$ ), whereas in the sphere, they are made to be smooth as illustrated in Figure 3.1. It is worth stating that pseudopotentials are not unique, as a result, there is freedom to use the one that simplifies calculations and the analysis of the calculated electronic structure of interest.

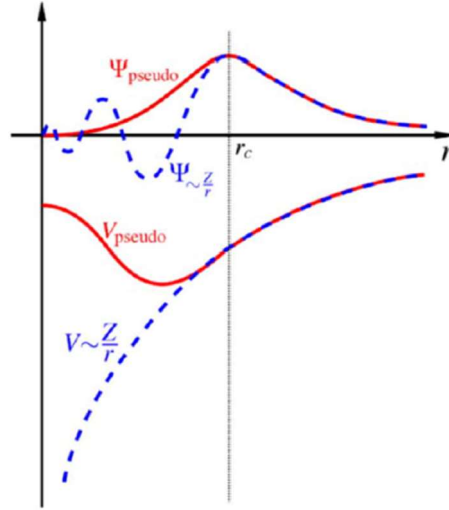


**Figure 3.1** The blue dashed lines show a schematic illustration of all-electron potential  $V \sim \frac{Z}{r}$  with the corresponding valence wave function  $\Psi_{V \sim \frac{Z}{r}}$  while the red solid lines represent the pseudopotential  $V_{pseudo}$  and the corresponding pseudo  $\Psi_{pseudo}$ . Reproduced with permission from Schwerdtfeger [42].

### 3.3.1.1 Non-uniqueness of pseudopotentials

Starting from the single-particle Kohn-Sham equation, the concept of pseudopotential can be developed. Kohn-Sham equation could be expressed as equation (3.79):

$$\mathbf{h}\phi = \epsilon\phi . \quad (3.79)$$

where

$$\begin{aligned} \mathbf{h} &= \mathbf{t}_o[\rho] + \mathbf{v}_{KS}[\rho] \\ &= \mathbf{t}_o[\rho] - \frac{Z_{nucl}}{\mathbf{r}} + \mathbf{v}_H[\rho] + \mathbf{v}_{xc}[\rho] \end{aligned} \quad (3.80)$$

The Hamiltonian of equation (3.80) is the sum of the single particle kinetic energy  $t_o$  and the Kohn-Sham effective potential operator  $v_{KS}$ ; the second term is the Coulomb potential experienced

by the electron at “r” in relation to the nuclear site, and  $Z_{\text{nucl}}$  is the atomic number. To derive the general expression for pseudopotentials, first, the total number of electrons ( $Z_{\text{nucl}}$ ) could be expressed as a sum of the number of core ( $Z_{\text{core}}$ ) and the valence electrons ( $Z$ ), that is:

$$Z_{\text{nucl}} = Z_{\text{core}} + Z . \quad (3.81)$$

Next, the single-particle wave function  $\phi$  could be expanded as:

$$\phi = \psi + \sum_c \alpha_c \psi_c . \quad (3.82)$$

where  $\psi$  represents the smooth part corresponding to valence electron states, the core orbitals are denoted by  $\psi_c$ . The coefficients of expansion  $\alpha_c$  of equation (3.82) can be determined using the following conditions:

$$\langle \psi | \psi_c \rangle = 0 \quad (3.83)$$

$$\alpha_c = \langle \phi | \psi_c \rangle . \quad (3.84)$$

By employing equations (3.82) and (3.84), equation (3.79) can be expressed as:

$$\hat{h}\psi + \sum_c (\epsilon - E_c) \psi_c \langle \psi_c | \psi \rangle = \epsilon \psi . \quad (3.85)$$

where  $E_c$  is the eigenvalue of the core state. Equation (3.85) can be expressed as:

$$(\mathbf{h} + \mathbf{v}_R)\psi = \epsilon \psi . \quad (3.86)$$

where  $\mathbf{v}_R$  represents the repulsive potential operator. Equation (3.86) could further be expressed as

$$(\mathbf{t}_0 + \mathbf{v}^{\text{PS}})\Psi = \epsilon\Psi \quad (3.87)$$

such that

$$\mathbf{v}^{\text{PS}} = \mathbf{v}_A + \mathbf{v}_R = \mathbf{v}_A + \sum_c (\epsilon - \mathbf{E}_c) |\psi_c\rangle\langle\psi_c| \quad (3.88)$$

$\mathbf{v}^{\text{PS}}$  of equation (3.88) is the pseudopotential representing the balance between the attractive potential  $\mathbf{v}_A$  and the repulsive potential  $\mathbf{v}_R$ , first cited by Phillips and Kleinman [44] and later by Antoncik [45]. It is interesting to note that there is no restriction to defining the pseudopotential  $\mathbf{v}^{\text{PS}}$  which depends on how effective the cancellation between the attractive potential of the core and the valence states. The eigenvalues of equation (3.85) remains unchanged by adding any linear combination of the core states to  $|\psi\rangle$ , and the modified  $|\psi\rangle$  will lead to a new pseudopotential. Thus, this explains the non-uniqueness of pseudopotentials. The above features of pseudopotentials have been employed in the development of different types of pseudopotentials. However, only local, nonlocal and the projector-augmented wave pseudopotential have been discussed in this thesis.

### 3.3.1.2 Local and non-local pseudopotentials

The general form of the pseudopotential, expressed as the equation (3.88), is given as:

$$\mathbf{v}^{\text{PS}}(\mathbf{r}) = \sum_{l=0}^{\infty} \sum_{m=-l}^l \mathbf{v}_{\text{ps}}^l |\mathbf{l}m\rangle\langle\mathbf{l}m| = \sum_{l=0}^{\infty} \mathbf{v}_{\text{ps}}^l(\mathbf{r}) \mathbf{P}_l \quad (3.89)$$

where  $l$  is the angular momentum associated with the pseudopotential  $\mathbf{v}_{\text{ps}}^l(\mathbf{r})$ , the operator  $\mathbf{P}_l$  is a projection operator expressed as equation (3.90), and  $|\mathbf{l}m\rangle$  are the spherical harmonics:

$$P_l = \sum_{m=-l}^l |lm\rangle\langle lm|. \quad (3.90)$$

Equation (3.89) implies that when  $v^{PS}$  acts upon an electronic wave function,  $P_l$  picks the  $l^{\text{th}}$  angular momentum component of the wave function which is then multiplied by the local operator  $v_{ps}^l$ . This type of a pseudopotential is called non-local because it responds differently on the different angular component of the wave function. However, if the pseudopotential employs the same potential in every angular momentum channels, it is termed a local pseudopotential. Local pseudopotentials are computationally less expensive as compared to the non-local ones, however, only very few elements can be calculated accurately employing local pseudopotentials. There are different available periodic codes for the implementation of DFT. In the past, there were few comparisons among the different codes. However, this has changed recently such that the results of different periodic codes can now be assessed for comparison [46].

### 3.3.1.3 Projector-augmented wave (PAW) pseudopotentials approach

The specifics of a particular pseudopotential dictate a minimum energy cutoff that should be employed in the calculations involving atoms associated with such pseudopotential. Pseudopotentials that require high energy cutoff energies are termed hard, whereas less computationally expensive pseudopotentials with low cutoff energy are called soft. An example of a hard pseudopotential is norm conservative [47], while ultrasoft pseudopotentials (USPP), developed by Vanderbilt [48], [49], and just as the name implies, are called soft pseudopotentials. USPP is, however, not the only one in the category of plane wave based methods. The projector augmented wave (PAW), first introduced by Blöchl in 1994 [50], some year after USPP, benefits from the underlying all electron treatment, and as a result, it is expected to be more accurate than

USPP. Interestingly, USSP could be obtained from the PAW approach using some simplifying assumptions, as demonstrated by Kresse and Joubert [51]. These authors also investigated an extensive comparison of the USSP, PAW and all electrons calculations for different molecules and extended solids [51]. Their results demonstrate that USPP and the PAW approach give essentially similar results in many cases, and are consistent with the all-electron calculations. However, in the case of magnetic systems, PAW is deemed to be more reliable [52]. The PAW approach is constructed based on the transformation between the all-electron orbitals  $|\psi_n\rangle$  and pseudo orbitals  $|\tilde{\psi}_n\rangle$  as expressed in equation (3.91):

$$|\Psi_n\rangle = |\tilde{\Psi}_n\rangle + \sum_i (|\phi_i\rangle - |\tilde{\phi}_i\rangle) c_i . \quad (3.91)$$

where  $|\phi_i\rangle$  are “true atomic states,  $|\tilde{\phi}_i\rangle$  denotes pseudo waves, and  $c_i$  are the linear coefficients of the pseudo wave function. The advantages of the PAW method are as follows:

- i) There is no need to treat the core electrons. The projector functions are localised in the augmented spheres.
- ii) The pseudo wave function is smooth and has no nodes in the augmented spheres.
- iii) With the PAW method, the all-electron wave functions and electron density can be assessed which could be helpful for orbital-dependent exchange-correlation functionals.

### 3.3.1.4 Basis set

In order to calculate the physical properties of crystals using Kohn-Sham equations with pseudopotentials, it is essential to select a basis set to express the electrons wave functions.

Basically, there are three different ways to express the wave function,  $\phi$ :

- i) Expressing  $\phi$  as a linear combination of plane waves.
- ii) Expressing  $\phi$  as a linear combination of atomic orbitals.
- iii) Expressing  $\phi$  as a linear combination of some i) and ii).

As a result of the simplicity which makes no presumptions about the form of the solution, and the lack of superposition error, the plane wave is one of the most adopted basis sets for the electronic structure calculations. With the plane wave basis set, a single-particle wave function  $\psi_{\mathbf{k}}(\mathbf{r})$  at a point  $\mathbf{r}$  in a crystal could be expressed as:

$$\psi_{\mathbf{j}}(\mathbf{k}, \mathbf{r}) = \frac{1}{\sqrt{N_o \Omega}} + \sum_{\mathbf{G}} A_{\mathbf{j}}(\mathbf{k} + \mathbf{G}) e^{(\mathbf{k} + \mathbf{G}) \cdot \mathbf{r}}. \quad (3.92)$$

where  $N_o$ ,  $\Omega$ ,  $\mathbf{k}$ ,  $\mathbf{j}$ ,  $\mathbf{G}$  and  $A_{\mathbf{j}}(\mathbf{k} + \mathbf{G})$  are the number of unit cells, the volume of the unit cell, the electronic wave vector within the first Brillouin zone, the band index, the reciprocal lattice vector, and the Fourier coefficients, respectively.

While in most ab initio codes electronic wave functions are represented by one of the above listed basis sets, there are few exceptions. For example, Pseudopotential Algorithm for Real-Space Electronic Calculations (PARSEC) solves Kohn-Sham equations using a finite element algorithm [53].



### 3.4 Formalism of Kohn-Sham equation in momentum space

Kohn-Sham equation, employing pseudopotential method with the plane wave basis set, can be expressed in momentum space as equation (3.93):

$$\sum_{\mathbf{G}'} \mathbf{H}_{\mathbf{G},\mathbf{G}'}(\mathbf{k}) \mathbf{A}_j(\mathbf{k} + \mathbf{G}') = \epsilon_j(\mathbf{k}) \mathbf{A}_j(\mathbf{k} + \mathbf{G}) . \quad (3.93)$$

such that

$$\mathbf{H}_{\mathbf{G},\mathbf{G}'}(\mathbf{k}) = \frac{\hbar^2}{2\mathbf{m}} |\mathbf{k} + \mathbf{G}|^2 \delta_{\mathbf{G},\mathbf{G}'} + \mathbf{V}_{\text{ps}}(\mathbf{k} + \mathbf{G}, \mathbf{k} + \mathbf{G}') . \quad (3.94)$$

where  $V_{\text{ps}}$  is the screened pseudopotential. It is pertinent to state that  $V_{\text{ps}}$  is non-local, and the Fourier component can be expressed as:

$$\begin{aligned} \mathbf{V}_{\text{ps}}(\mathbf{k} + \mathbf{G}, \mathbf{k} + \mathbf{G}') \\ = \mathbf{V}_{\text{ps}}^{\text{ion}}(\mathbf{k} + \mathbf{G}, \mathbf{k} + \mathbf{G}') + \mathbf{V}_{\text{xc}}(\mathbf{G} - \mathbf{G}') + \mathbf{V}_{\text{H}}(\mathbf{G} - \mathbf{G}') \end{aligned} \quad (3.95)$$

$$= \mathbf{V}_{\text{ps}}^{\text{ion}}(\mathbf{k} + \mathbf{G}, \mathbf{k} + \mathbf{G}') + \mathbf{V}_{\text{screen}}(\mathbf{G} - \mathbf{G}') . \quad (3.96)$$

$V_{\text{ps}}^{\text{ion}}$  is the Fourier component of the ionic pseudopotential,  $V_{\text{H}}$  and  $V_{\text{xc}}$  are the Fourier components of the Hartree and the exchange-correlation potential, respectively. Thus, to calculate the different properties of solids, using the above equations, all these parameters need to be specified.

#### 3.4.1 Energy cut-off

Equation (3.92) is expressed in terms of a plane wave basis set. According to the equation, evaluating the solution required an infinite number of reciprocal lattice vectors of  $\mathbf{G}$ . The

evaluation of such an expression is impractical. However, the plane wave expansion could be truncated to include only solutions with kinetic energy ( $E$ ) less than some value, also known as the energy cut-off,  $E_{\text{cut}}$ , i.e.

$$E = \frac{\hbar^2}{2m} |\mathbf{k} + \mathbf{G}|^2 < E_{\text{cut}} . \quad (3.97)$$

with

$$E_{\text{cut}} = \frac{\hbar^2}{2m} G_{\text{cut}}^2 \quad (3.98)$$

Then the infinite sum reduces to:

$$\Psi_j(\mathbf{k}, \mathbf{r}) = \frac{1}{\sqrt{N_o \Omega}} + \sum_{|\mathbf{G} + \mathbf{k}| < G_{\text{cut}}} \mathbf{A}_j(\mathbf{k} + \mathbf{G}) \mathbf{e}^{(\mathbf{k} + \mathbf{G}) \cdot \mathbf{r}} . \quad (3.99)$$

The truncation of the plane wave basis set at a small  $E_{\text{cut}}$  might lead to an error when calculating the total energy of a system. However, such error can be reduced by increasing the  $E_{\text{cut}}$ . It is worth mentioning here that, all the  $E_{\text{cut}}$  used in this thesis to evaluate the physical properties of graphene based systems were chosen after convergence has been achieved with respect to the parameter.

### 3.4.2 Brillouin zone sampling

The evaluation of the physical properties of solids (such as the total energy, electron density of states, etc.), involves the integration of periodic functions of a Bloch wave vector over a whole Brillouin zone (BZ). There are a number of numerical techniques that have been reported for the BZ integration scheme such as Monkhorst and Pack [54], Baldereschi [55], Cunningham [56], Chadi and Cohen [57]. These integration schemes for generating special k-points within the irreducible Brillouin zone IBZ give a good approximation to the zone average of a generic periodic

function. An excellent review on the description of special k-points of the IBZ for crystals with different symmetries for use in the calculation of electronic structure and the physical properties of materials was reported by Evarestov and Smirnov [58]. In this thesis, all the calculations that are presented were done using the Monkhorst and Pack scheme. With this scheme, special k-points are presented in this form:

$$\mathbf{k}_p = \mathbf{u}_{p1}\mathbf{b}_1 + \mathbf{u}_{p2}\mathbf{b}_2 + \mathbf{u}_{p3}\mathbf{b}_3 + \mathbf{k}_0 . \quad (3.100)$$

where  $\mathbf{b}_i$  and  $\mathbf{k}_0$  are the reciprocal lattice vectors and an arbitrary vector, respectively. For a cubic system,  $u_{pi}$  is calculated as follows:

$$u_{pi} = \frac{2p_i - l - 1}{2l} . \quad (3.101)$$

where  $p_i=1, 2, 3 \dots l$  and  $i=1, 2, 3$ . The integer  $l$  is used to evaluate the number of special points in a given set. For a hexagonal BZ, the coefficient  $u_{pi}$  such that  $i=1, 2$  are expressed as:

$$u_{pi} = \frac{p_i - 1}{l} . \quad (3.102)$$

and for  $i=3$ ,  $u_{pi}$  is given as:

$$u_{pi} = \frac{2p_i - l - 1}{2l} . \quad (3.103)$$

Another important quantity that must be stated is known as the weight factor which is a factor associated with each special k-point. This factor can be expressed as follows:

$$\bar{f} = \sum_{i=1}^N \omega_i f(k_i) + \text{remainder} . \quad (3.104)$$

where  $f(\mathbf{k})$  is a periodic function and  $\bar{f}$  is the average;  $\omega_i$  is the weight factor such that  $\sum \omega_i = 1$ . In equation (3.104), the sum runs over  $N$  chosen  $k$ -points, and the smaller the ‘remainder’ term, the better the numerical integration technique. In this thesis,  $m \times m \times 1$  Monkhorst and Pack scheme was used to sample the BZ of all the graphitic systems studied. The right value of ‘ $m$ ’ was determined after a test of convergence of the total energy was done with respect to the parameter, ‘ $m$ ’.

### 3.4.3 Hellmann-Feynman forces

After the solutions of Kohn-Sham equations have been obtained self-consistently by the plane wave pseudopotential method, the total energy of the material and then the Hellmann-Feynman force on the atoms can be calculated. The total energy  $E_{\text{tot}}$  of a system can be expressed as the sum of the energies due to the electronic contribution  $E_{\text{ele}}$  (corresponding to the Hamiltonian  $H$  with an eigenstate  $|\psi\rangle$ ), and the ionic contribution  $E_{\text{ion}}$ :

$$\mathbf{E}_{\text{tot}} = \mathbf{E}_{\text{ele}} + \mathbf{E}_{\text{ion}} . \quad (3.105)$$

The derivative of the total energy with respect to the atomic positions  $\mathbf{R}_i$  gives rise to the force acting  $\mathbf{F}_i$  on the atoms of the system, i.e.:

$$\mathbf{F}_i = \frac{\delta \mathbf{E}_{\text{tot}}}{\delta \mathbf{R}_i} = \langle \Psi | \frac{\delta H}{\delta \mathbf{R}_i} | \Psi \rangle + \frac{\delta \mathbf{E}_{\text{ion}}}{\delta \mathbf{R}_i} . \quad (3.106)$$

If the basis set has ionic coordinates, equation (3.106) would have extra terms called the Pulay forces. However, with a non-local basis set, the Pulay forces can be removed. Geometry optimization calculations usually depend on the accurate evaluation of sum of the ionic forces. It is worth noting that such calculations exhibit excellent convergence when Pulay forces are included.

### 3.4.4 Self-Consistent iterative procedure

The trial plane-wave basis set defined in equation (3.99) along with the pseudopotential method described in **Error! Reference source not found.** could be used to solve Kohn-Sham equations. Although starting with a trial charge density, the solutions to the Kohn-Sham equations provide the initial ground state charge density which might not be the true ground state charge density of a given system. The true ground state charge density or a more reliable and stable result can be obtained by using the charge density calculated through iterating the solution of Kohn-Sham equations. This procedure is termed a self-consistent field (SCF) calculation, and it is outlined in the following algorithm:

- i) The trial electron density ( $n(\vec{r})$ ) is defined.
- ii) Kohn-Sham equations are solved with the trial electron density in step (i) to obtain a new single particle wave functions,  $\phi_i(\vec{r})$ .
- iii) A new electron density ( $n_{KS}(\vec{r})$ ) is calculated from the single particle wave functions  $\phi_i(\vec{r})$  obtained from step (ii).
- iv) The new density ( $n_{KS}(\vec{r})$ ) is then compared with the initial electron density ( $n(\vec{r})$ ) in step (i), if the two are equal, it is the ground state electron density and can be employed to calculate the total energy of the system. However, if the two electron densities are different, then the calculated electron density is updated in some way. After that is done, the process starts again from step (ii). However, this process might not lead to quick convergence. The reason being that due to the long-range nature of the Coulomb interaction, a slight change in the electron density input could lead to a larger change in the output electron density. Thus, a new charge density must be mixed with the previous output densities in a predetermined manner so as to attain ground state electron density

as quick as possible. Basically, there are two classes of electron charge densities mixing schemes, i.e, linear and non-linear schemes. An excellent review of these schemes can be found in Ref. [59]. In our calculations, one of the most attractive non-linear mixing methods for self-consistent field acceleration, also known as Broyden mixer, was adopted. Figure 3.2 gives the schematic flow chart of the self-consistent field calculation.

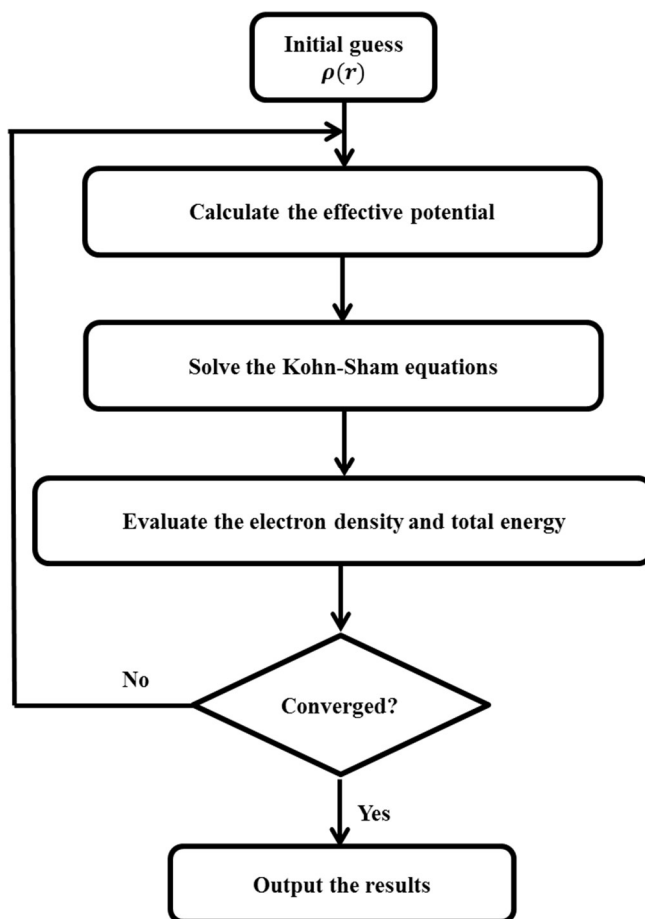


**Figure 3.2** A flow chart illustrating the self-consistent field (SCF) calculation of the DFT

### **3.5 Geometry optimization**

Before the physical properties of a periodic system is calculated within the framework of DFT, it is a good practice to check or ensure that the forces acting on the atoms within each unit cell are small as possible so as to render them insignificant. The process that brings about changes in the positions of the atoms, and in some cases the shape of the material, until the forces on the particles are insignificant, with a configuration that induces a minimum total energy, is called optimization. Optimization could be done by employing the total energy, Pulay forces as well as Hellmann-Feynman forces approaches. Mainly, there are two iterative corrections that determine the optimized geometry of any periodic system. In the first iterative correction, the Kohn-Sham equations are solved to attain a predetermined tolerance of self-consistency via the adjustment of the charge density. In the second iterative correction, the optimization of the geometry is done by changing the atomic positions in response to the prevailing forces. These iterative adjustments are done repeatedly until a fully relaxed geometry is achieved. Although there are different methods of geometry optimization [60], [61], in our study, Bendt-Zunger's conjugated gradient method [62] was adopted for the optimization. The reason for choosing this scheme is because the algorithm is robust and often works reasonably well even if the starting structural guess is quite different from the ground state structure.

### **3.6 Computational code**

The calculations in this thesis were performed with the Vienna Ab initio Simulation Package (VASP) code [63], [64]. The code was developed by Jürgen Furthmüller and Georg Kresse in some years back at the University of Vienna in Austria.

VASP code has been a huge success in implementing the DFT of Kohn-Sham. It has been used to predict the properties (such as the energies, forces, band structures, the density of states, charge densities, etc.) of materials. It computes the properties of periodic materials by first solving the Kohn-Sham equations self-consistently using plane-waves basis set and PAW as the pseudopotential. It also offers the level of accuracy of the all-electron approach while still has the advantages of a plane wave scheme.

The VASP 5.3, which was employed for this study, can be used to perform four types of calculations: single point energy, structure optimization, quasiparticle spectra (GW) and molecular dynamics. In this study, only the single point energy and the structural optimization have been performed to compute the properties of the graphene-based systems. As a result, only these two calculations types have been discussed herein.

If the flag of the single point energy is turned on, only the energy of the input structure is calculated without relaxing the geometry of the system. However, in most cases the single point energy calculation is done to compute the physical properties of materials after the structural optimization of the system in question has been achieved. This is because the single point energy converges very quickly, and usually leads to accurate ground state properties of the system if a well optimized input structure is used. However, in the case of the geometry optimization, if the flag is turned on, the cell parameters are relaxed with or without constraints depending on the specifications. There are three constraints that can be considered during geometry optimization of a system: i.e. relaxing atom positions; allowing cell volume and shape to change. If the geometry optimization is done with respect to the relaxation of the atom positions, the atoms are allowed to move until the Hellmann forces on them are just less than the convergence threshold. This type of constraint is used when a surface is to be relaxed; adsorption of a gas on a surface and the relaxation



of a structure around a defect or vacancy are to be considered. However, the cell volume option is allowed if the optimisation is to be done to take into account only isotropic changes of the supercell while keeping the angles and the ratios of the lattice parameters constant. This option is used when the effect of pressure on the physical properties of the systems of interest is of utmost importance. The last constraint, which is the cell shape option, allows the cell parameters, including the angles, to change. The three options described above can be allowed if full optimisation of the system is to be performed.

After geometry optimisation has been done within a prescribed convergence threshold, the physical properties (such as the ground state energy, charge density, band structure, the density of states, work function, optical characteristics, etc.) of the systems of interest can be computed. In this study, the focus is on the charge density, density of states, band structures, and optical characteristics. These properties are usually computed following two independent steps. The first step involves relaxing the structure, then reload the relaxed geometry as the input structure. Afterward, the desired properties of the system can be calculated using a single point energy calculation.

## References

- [1] D. S. Sholl and J. A. Steckel, "Density functional theory : a practical introduction," Wiley, vol. 49, no. 3, pp.485, Jan., 2009.
- [2] D. R. Hartree, "The Wave Mechanics of an Atom with a Non-Coulomb Central Field Part I Theory and Methods," *Math. Proc. Cambridge Philos. Soc.*, vol. 24, no. 1, pp. 89–110, Jan. 1928.
- [3] J. M. Leinaas and J. Myrheim, "On the theory of identical particles," *Nuovo Cim. B Ser. 11*, vol. 37, no. 1, pp. 1–23, Jan. 1977.
- [4] J. C. Slater, "The theory of complex spectra," *Phys. Rev.*, vol. 34, no. 10, pp. 1293–1322, Nov. 1929.
- [5] P. O. Lowdin, "Hartree-Fock Approximation," *Phys. Rev.*, vol. 24, no. 538, pp. 675–1474, 1928.
- [6] A. K. Rajagopal and J. Callaway, "Inhomogeneous electron gas," *Phys. Rev. B*, vol. 7, no. 5, pp. 1912–1919, 1973.
- [7] W. Kohn, "Thoughts about density functional theory in 1998," *J. Comput. Chem.*, vol. 20, no. 1, pp. 1–1, Jan. 1999.
- [8] L. H. Thomas, "The calculation of atomic fields," *Math. Proc. Cambridge Philos. Soc.*, vol. 23, no. 5, pp. 542–548, Jan. 1927.
- [9] E. Fermi, "Eine statistische Methode zur Bestimmung einiger Eigenschaften des Atoms und ihre Anwendung auf die Theorie des periodischen Systems der Elemente," *Zeitschrift für Phys.*, vol. 48, no. 1–2, pp. 73–79, Jan. 1928.
- [10] E. Fetil, Ş. Özkan, T. Ilknur, Y. Erdem, B. Lebe, and A. T. Güneş, "Multiple pilomatricoma with perforation," *Int. J. Dermatol.*, vol. 41, no. 12, pp. 892–893, 2002.
- [11] W. Kohn, A. D. Becke, and R. G. Parr, "Density functional theory of electronic structure," *J. Phys. Chem.*, vol. 100, no. 31, pp. 12974–12980, 1996.
- [12] W. Kohn and A. E. Mattsson, "Edge electron gas," *Phys. Rev. Lett.*, vol. 81, no. 16, pp. 3487–3490, Oct. 1998.
- [13] M. Probert, "Electronic Structure: Basic Theory and Practical Methods, by Richard M. Martin," *Contemp. Phys.*, vol. 52, no. 1, pp. 77–77, Jan. 2011.
- [14] M. Levy, "Electron densities in search of Hamiltonians," *Phys. Rev. A*, vol. 26, no. 3, pp. 1200–1208, Sep. 1982.
- [15] E. H. Lieb, "Density Functional for Coulomb systems," in *Int. J. Quant. Chem.*, vol. 24, Berlin, Heidelberg: Springer Berlin Heidelberg, 1983, p. 243.
- [16] M. E. Casida and M. Huix-Rotllant, "Progress in Time-Dependent Density-Functional Theory," *Annu. Rev. Phys. Chem.*, vol. 63, no. 1, pp. 287–323, May 2011.

- [17] P. O. Löwdin, “Quantum theory of many-particle systems. III. Extension of the Hartree-Fock scheme to include degenerate systems and correlation effects,” *Phys. Rev.*, vol. 97, no. 6, pp. 1509–1520, Mar. 1955.
- [18] J. P. Perdew, K. Burke, and M. Ernzerhof, “Generalized Gradient Approximation Made Simple,” *Phys. Rev. Lett.*, vol. 77, no. 18, pp. 3865–3868, Oct. 1996.
- [19] J. Hafner, “Ab-initio simulations of materials using VASP: Density-functional theory and beyond,” *J. Comput. Chem.*, vol. 29, no. 13, pp. 2044–2078, Oct. 2008.
- [20] J. P. Perdew *et al.*, “Restoring the Density-Gradient Expansion for Exchange in Solids and Surfaces,” *Phys. Rev. Lett.*, vol. 100, no. 13, p. 136406, Apr. 2008.
- [21] A. J. Cohen, P. Mori-Sánchez, and W. Yang, “Challenges for density functional theory,” *Chem. Rev.*, vol. 112, no. 1, pp. 289–320, Jan. 2012.
- [22] C. Lee, W. Yang, and R. G. Parr, “Development of the Colle-Salvetti correlation-energy formula into a functional of the electron density,” *Phys. Rev. B*, vol. 37, no. 2, pp. 785–789, Jan. 1988.
- [23] E. Igumbor, K. Obodo, W. Meyer, “Ab Initio Study of MgSe Self-Interstitial (Mgi and Sei),” *Trans Tech Publ.*, vol. 242, pp. 440-446, Oct. 2015.
- [24] J. P. Perdew and Y. Wang, “Accurate and simple analytic representation of the electron-gas correlation energy,” *Phys. Rev. B*, vol. 45, no. 23, pp. 13244–13249, Jun. 1992.
- [25] C. W. Murray, N. C. Handy, and R. D. Amos, “A study of O<sub>3</sub>, S<sub>3</sub>, CH<sub>2</sub>, and Be<sub>2</sub> using Kohn-Sham theory with accurate quadrature and large basis sets,” *J. Chem. Phys.*, vol. 98, no. 9, pp. 7145–7151, May 1993.
- [26] B. G. Johnson, P. M. W. Gill, and J. A. Pople, “The performance of a family of density functional methods,” *J. Chem. Phys.*, vol. 98, no. 7, pp. 5612–5626, Apr. 1993.
- [27] J. Muscat, A. Wander, and N. M. Harrison, “On the prediction of band gaps from hybrid functional theory,” *Chem. Phys. Lett.*, vol. 342, pp. 397–401, 2001.
- [28] P. Deák, B. Aradi, T. Frauenheim, E. Jánzén, and A. Gali, “Accurate defect levels obtained from the HSE06 range-separated hybrid functional,” *Phys. Rev. B - Condens. Matter Mater. Phys.*, vol. 81, no. 15, p. 153203, Apr. 2010.
- [29] S. Grimme, “Semiempirical GGA-type density functional constructed with a long-range dispersion correction,” *J. Comput. Chem.*, vol. 27, no. 15, pp. 1787–1799, Nov. 2006.
- [30] S. Kümmel and L. Kronik, “Orbital-dependent density functionals: Theory and applications,” *Rev. Mod. Phys.*, vol. 80, no. 1, pp. 3–60, 2008.
- [31] K. Kim and K. D. Jordan, “Comparison of density functional and MP2 calculations on the water monomer and dimer,” *J. Phys. Chem.*, vol. 98, no. 40, pp. 10089–10094, Oct. 1994.
- [32] F. J. Devlin, J. W. Finley, P. J. Stephens, and M. J. Frisch, “Ab-Initio Calculation of Vibrational Absorption and Circular-Dichroism Spectra Using Density-Functional Force-Fields - a Comparison of Local, Nonlocal, and Hybrid Density Functionals,” *J. Phys. Chem.*, vol. 99, no. 46, p. 16883, 1995.

- [33] J. P. Perdew, M. Ernzerhof, and K. Burke, “Rationale for mixing exact exchange with density functional approximations,” *J. Chem. Phys.*, vol. 105, no. 22, pp. 9982–9985, Dec., 1996.
- [34] C. Adamo and V. Barone, “Toward reliable density functional methods without adjustable parameters: The PBE0 model,” *J. Chem. Phys.*, vol. 110, no. 13, pp. 6158–6170, Apr. 1999.
- [35] J. Heyd, G. E. Scuseria, and M. Ernzerhof, “Hybrid functionals based on a screened Coulomb potential,” *J. Chem. Phys.*, vol. 118, no. 18, pp. 8207–8215, May 2003.
- [36] R. Baer, E. Livshits, and U. Salzner, “Tuned Range-Separated Hybrids in Density Functional Theory,” *Annu. Rev. Phys. Chem.*, vol. 61, no. 1, pp. 85–109, Mar. 2010.
- [37] J. Heyd and G. E. Scuseria, “Efficient hybrid density functional calculations in solids: Assessment of the Heyd-Scuseria-Ernzerhof screened Coulomb hybrid functional,” *J. Chem. Phys.*, vol. 121, no. 3, pp. 1187–1192, Jul. 2004.
- [38] A. V. Krukau, O. A. Vydrov, A. F. Izmaylov, and G. E. Scuseria, “Influence of the exchange screening parameter on the performance of screened hybrid functionals,” *J. Chem. Phys.*, vol. 125, no. 22, p. 224106, Dec. 2006.
- [39] F. Wetenschappen and D. Fysica, “First-principles study of defects in transparent conducting oxide materials First-principles studie van defecten in transparante geleidende oxide materialen,” 2014.
- [40] F. Drief, A. Tadjer, D. Mesri, and H. Aourag, “First principles study of structural, electronic, elastic and optical properties of MgS, MgSe and MgTe,” *Catal. Today*, vol. 89, no. 3, pp. 343–355, Mar., 2004.
- [41] D. J. Chadi and K. J. Chang, “Energetics of DX-center formation in GaAs and  $\text{Al}_x\text{Ga}_{1-x}\text{As}$  alloys.” *Phys. Rev. B - Condens. Matter Mater. Phys.*, vol. 39, no. 14, pp. 10063-10074, May. 1989.
- [42] P. Schwerdtfeger, “The pseudopotential approximation in electronic structure theory,” *ChemPhysChem*, vol. 12, no. 17, pp. 3143–3155, Dec. 2011.
- [43] M. T. Yin and M. L. Cohen, “Theory of ab initio pseudopotential calculations,” *Phys. Rev. B*, vol. 25, no. 12, pp. 7403–7412, Jun. 1982.
- [44] J. C. Phillips and L. Kleinman, “New method for calculating wave functions in crystals and molecules,” *Phys. Rev.*, vol. 116, no. 2, pp. 287–294, Oct. 1959.
- [45] E. Antoncik, “Approximate formulation of the orthogonalized plane-wave method,” *Journal of Phys. and Chem. of Solid*, vol. 10, no. 4, pp. 314-320, Aug., 1959.
- [46] K. Lejaeghere, V. Van Speybroeck, G. Van Oost, and S. Cottenier, “Error estimates for solid-state density-functional theory predictions: An overview by means of the ground-state elemental crystals,” *Crit. Rev. Solid State Mater. Sci.*, vol. 39, no. 1, pp. 1–24, Jan. 2014.
- [47] D. R. Hamann, “Generalized norm-conserving pseudopotentials,” *Phys. Rev. B*, vol. 40, no. 5, pp. 2980–2987, Nov. 1989.
- [48] D. Vanderbilt, “Optimally smooth norm-conserving pseudopotentials,” *Phys. Rev. B*, vol.

- 32, no. 12, pp. 8412–8415, Dec. 1985.
- [49] D. Vanderbilt, “Soft self-consistent pseudopotentials in a generalized eigenvalue formalism,” *Phys. Rev. B*, vol. 41, no. 11, pp. 7892–7895, Apr. 1990.
- [50] P. E. Blöchl, “Projector augmented-wave method,” *Phys. Rev. B*, vol. 50, no. 24, pp. 17953–17979, Dec. 1994.
- [51] G. Kresse and D. Joubert, “From ultrasoft pseudopotentials to the projector augmented-wave method,” *Phys. Rev. B*, vol. 59, no. 3, pp. 1758–1775, Jan. 1999.
- [52] D. Hobbs, G. Kresse, and J. Hafner, “Fully unconstrained noncollinear magnetism within the projector augmented-wave method,” *Phys. Rev. B - Condens. Matter Mater. Phys.*, vol. 62, no. 17, pp. 11556–11570, Nov. 2000.
- [53] J. R. Chelikowsky, N. Troullier, and Y. Saad, “Finite-difference-pseudopotential method: Electronic structure calculations without a basis,” *Phys. Rev. Lett.*, vol. 72, no. 8, pp. 1240–1243, Feb. 1994.
- [54] H. J. Monkhorst and J. D. Pack, “Special points for Brillouin-zone integrations,” *Phys. Rev. B - Condens. Matter Mater. Phys.*, vol. 13, no. 12, pp. 5188–5192, Jun. 1976.
- [55] A. Baldereschi, “Mean-value point in the Brillouin zone,” *Phys. Rev. B*, vol. 7, no. 12, pp. 5212–5215, Jun. 1973.
- [56] S. L. Cunningham, “Special points in the two-dimensional Brillouin zone,” *Phys. Rev. B*, vol. 10, no. 12, pp. 4988–4994, Dec. 1974.
- [57] D. J. Chadi and M. L. Cohen, “Special points in the Brillouin zone,” *Phys. Rev. B*, vol. 8, no. 12, pp. 5747–5753, Dec. 1973.
- [58] R. A. Evarestov and V. P. Smirnov, “Special points of the Brillouin zone and their use in the solid state theory,” *Phys. Status Solidi*, vol. 119, no. 1, pp. 9–40, Sep. 1983.
- [59] W. E. Pickett, “Pseudopotential methods in condensed matter applications,” *Comput. Phys. Reports*, vol. 9, no. 3, pp. 115–197, 1989.
- [60] R. Car and M. Parrinello, “Unified approach for molecular dynamics and density-functional theory,” *Phys. Rev. Lett.*, vol. 55, no. 22, pp. 2471–2474, Nov. 1985.
- [61] M. C. Payne, M. P. Teter, D. C. Allan, T. A. Arias, and J. D. Joannopoulos, “Iterative minimization techniques for ab initio total-energy calculations: Molecular dynamics and conjugate gradients,” *Rev. Mod. Phys.*, vol. 64, no. 4, pp. 1045–1097, Oct. 1992.
- [62] P. Bendt and A. Zunger, “New approach for solving the density-functional self-consistent-field problem,” *Phys. Rev. B*, vol. 26, no. 6, pp. 3114–3137, Sep. 1982.
- [63] G. Kresse, “Efficient iterative schemes for ab initio total-energy calculations using a plane-wave basis set,” *Phys. Rev. B*, vol. 54, no. 16, pp. 11169–11186, Oct. 1996.
- [64] G. Kresse and J. Furthmüller, “Efficiency of ab-initio total energy calculations for metals and semiconductors using a plane-wave basis set,” *Comput. Mater. Sci.*, vol. 6, no. 1, pp. 15–50, Jul. 1996.

## Chapter 4

### 4.1 Introduction

This chapter presents how the optimum values of Ecut and k-points that were used to get the results of this study were obtained. Moreover, the structural, lattice dynamic, electronic and optical properties of Be-S and Be-N co-doped graphene are also discussed.

In supercell calculations, some trade-offs between accuracy and computational costs are inevitable. These trade-offs include but are not exclusive to using an optimum number of k-points and kinetic energy cut-off (Ecut) to calculate the physical properties of materials with a decent level of accuracy. To this end, section 4.2.1 and 4.2.2 focus on the tests of convergence performed to get the optimum values that were required for the results of the calculations presented in the later sections. Section 4.2.3 presents the validation of the structural properties of graphene. The results, which are solely the author's findings, of this study are discussed in section 4.3, 4.4 and 4.5 using PBE-GGA and HSE06 functionals. Two of these results have already been published as articles in refereed journals while the result presented in section 4.5 has also been submitted to a reputable journal and currently under peer review.

In section 4.3, the results of an *ab initio* study of beryllium and sulphur (BeS) co-doped graphene were presented. Section 4.4 contains the report of the lattice dynamics, electronic and optical properties of beryllium and nitrogen (BeN) co-doped graphene. Section 4.5 addresses the optical properties of BeS co-doped graphene.

## 4.2 Test of convergence

Before employing DFT to calculate the physical properties of materials, it is important to perform tests of convergence of the total energy, first, with respect to the kinetic energy cut-off and, secondly, with respect to the number of k-points for the plane wave expansion of the wave function. These tests enable a balance to be struck between the computational cost and the accuracy of a given calculation.

### 4.2.1 Test of convergence with respect to cut-off energy ( $E_{\text{cut}}$ )

According to Bloch's theorem, the electronic wave function of a periodic system at each k-point can be expressed in terms of a discrete plane-wave basis set. In principle, an infinite number of plane waves are required for the plane wave basis set to be complete. The computational implementation of such an infinite basis set as an electronic wave function is not realistic for a practical DFT calculation. However, the plane waves with small kinetic energies contribute more to the total energy of the system than the plane waves with large kinetic energies. Consequently, the plane wave basis set can be truncated to comprise only plane waves with the kinetic energies smaller than some specific cut-off energy ( $E_{\text{cut}}$ ). Although the truncation of the basis set at a certain cut-off energy would lead to an error in the calculated total energy, the size of the error can be reduced systematically by increasing the value of the  $E_{\text{cut}}$  until the computed total energy converges just below the required tolerance or no longer changes appreciably. In this way, convergence can be said to have been achieved. Figure 4.1 **Error! Reference source not found.** shows the calculated total energy of 4X4 supercell of graphene with respect to  $E_{\text{cut}}$ . It can be observed from Figure 4.1, that the  $E_{\text{cut}}$  of 400 eV corresponds to the VASP total energy which is

very close to the converged value. As a result, Ecut of 400 eV was adopted for all the graphitic systems investigated in this study.

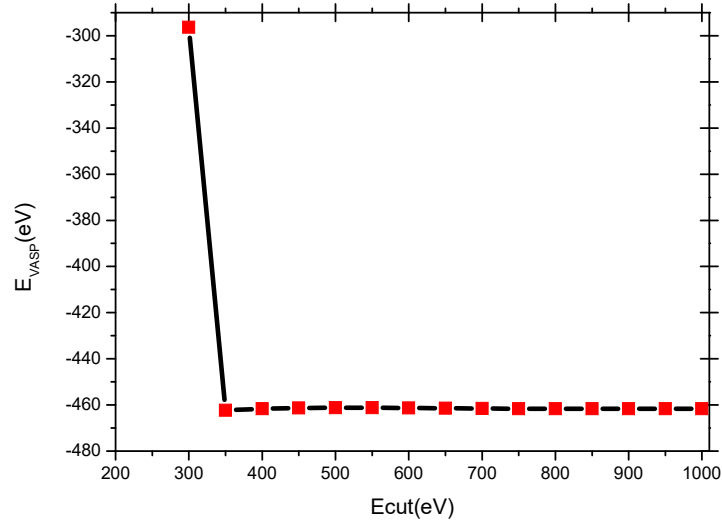


**Figure 4.1** The convergence of the calculated total energies of the unit cell of graphene against the cut-off energies.

The systems considered are pristine graphene, Be and S mono/co-doped; Be and N mono/co-doped graphene. Given a heteroatom doped graphene, since a cutoff energy only models the most rapidly varying core wave function of the constituent elements present in the material, the 400 eV determined for carbon would be an appropriate cutoff energy for any other monolayer graphene doped or co-doped with Be, S, or N. This is because carbon requires a very high energy cutoff to attain convergence compared to any of the aforementioned impurities in its most stable phase. The reason for such behaviour could be ascribed to the highly delocalized  $2p$  orbital which arises as a result of lack of  $p$ -core states in carbon. Besides finding the appropriate Ecut to use for the calculations, a test of convergence with respect to k-points is equally important and must be determined before any physical properties of a given system are computed.



#### **4.2.2 Test of convergence with respect to k-points mesh**

In order to compute the desired physical properties of pristine and co-doped graphene investigated in this study, three different supercell sizes were used i.e. 2x2, 3x3 and 4x4. It is known that for a given crystal, the number of k-points that is required to sample the BZ reduces with the increase in the size of the supercell. As a result of this, to determine the optimum number of k-points that would be required to sample the BZ of all the above-mentioned supercells; a test of k-points convergence (Figure 4.2) was done with respect to the smallest supercell (i.e. 2x2) of graphene using the Monkhorst-Pack scheme [1]. The convergence was done with respect to the 2x2 supercell since it is expected to have a higher density of k-points than the larger supercells (3x3 and 4x4). Running a supercell calculation with a higher number of k-points than the optimum value does not limit the accuracy of the result. Rather, it increases the accuracy and the cost of the computation. This computational cost is worth incurring compared to the higher amount of time that would be spent if we were to determine the required minimum value of k-points for each of the supercells (2x2, 3x3 and 4x4). Figure 4.2 shows that a minimum 5x5 k-points spacing would be required to sample the BZ of all the aforementioned supercells effectively.

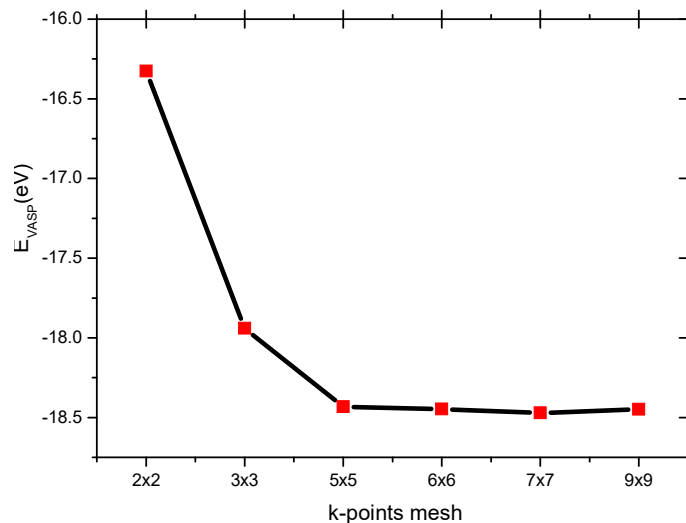


**Figure 4.2** The calculated total energy of 2x2 supercell of graphene as a function of k-points.

With  $E_{cut} = 400$  eV and k-point =  $7 \times 7 \times 1$ , the structural parameters of pristine graphene were calculated as follows:

### 4.2.3 Validation of the structural properties of graphene

The structural parameters of a unit cell of graphene were determined using the geometry optimization technique. This was done to ensure that the right parameters were used when calculating the physical properties of pristine and doped graphene considered in this study. To obtain the right lattice parameter, total energy calculations were done at different values of the lattice constant in the range of  $1.86 - 3.16$  Å, and the results are shown in Figure 4.3. In line with the standard convention, the results were fitted to the polynomial curve to determine the equilibrium lattice constant of graphene. The red arrow on the graph shows that  $2.46$  Å, which corresponds to the lowest energy value of the system, is the equilibrium lattice constant of graphene. After obtaining the energetically favourable lattice constant, the C–C bond length of the system was determined, and a value of  $1.42$  Å was found. These values are consistent with the

existing data [2], [3] on graphene. It is worth reiterating that graphene is a 2D material, as a result, in order to model the structure, a test of convergence with respect to interlayer spacing is required to isolate it from the interaction (via Van der Waals force) with other adjacent periodic layers. Van der Waals interaction is responsible for keeping the layers of graphene together. Figure 4.4 illustrates the results of the total energy calculations at different values of the interlayer spacing. It is observed that the total energy of the system converged at a minimum value of 4.0 Å. However, this value is significantly lower than the minimum value (8-14) used in most studies. The disparity between our result and the range of values commonly found in other reports is due to the neglect of Van der Waals interaction in the exchange-correlation functional that was used for this study. With respect to the literature, a minimum vacuum spacing of 8.0 Å is required to isolate monolayer graphene from the Van der Waals interaction of the adjacent periodic layers. Consequently, a vacuum spacing of 12 Å was adopted to model the pristine monolayer and the doped graphene in this study.

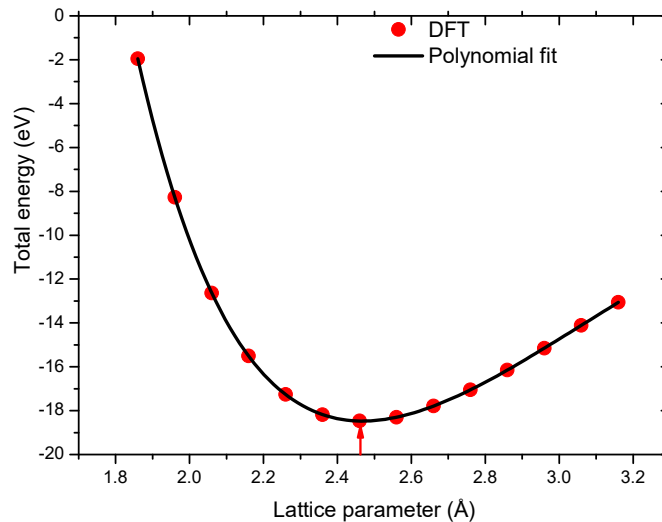


**Figure 4.3** The total energy vs lattice parameter of graphene. The red filled symbols show the numerically computed data points while the black curve shows a polynomial fit of the DFT data.

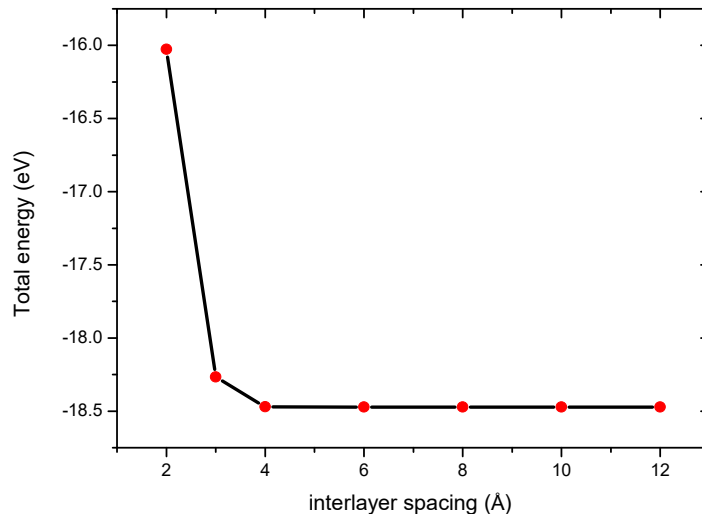


**Figure 4.4** The total energy vs interlayer spacing between two layers of graphene.

### 4.3 Exploring the stability and electronic structure of beryllium and sulphur co-doped graphene: a first principles study

#### 4.3.1 Introduction

Ever since the isolation from pyrolytic graphite by micromechanical cleavage in 2004 [4], graphene has attracted a lot of attention due to the remarkable properties (electronic, mechanical and thermal). Attributed to the linear dispersion relationship at the low energy region in the band structure, these properties have portrayed graphene as a strong contender to replace silicon for use in nanoelectronics and even in microelectronics. However, graphene has no band-gap magnitude (as explained in section 2.3.2) which renders it unsuitable for the proposed applications. In section 2.4, the different techniques that could be employed to induce a finite band-gap in graphene were discussed. Out of these techniques, heteroatom doping is the most effective method for creating and tailoring the band-gap magnitude in graphene to meet a device specification. Due to the

effectiveness of this technique, Denis *et al.*[5] investigated the effect of sulphur substitution on the electronic structure of graphene. They reported that the introduction of sulphur in graphene could change the electronic character of the system to either metallic or semiconducting depending on the impurity concentration. For example, at 2.0% of sulphur content in graphene, a band-gap of 0.3 eV was reported to be induced in the system while at a slightly higher impurity concentration the energy gap vanished and the material became metallic. The result of their study suggests doping graphene with sulphur might not always lead to the desired result except if the right amount of the impurity (which would be difficult to achieve within a normal experimental setup) is used.

In view of the challenges involved in transforming graphene to semiconductor using sulphur as the dopant, we investigated, from the first-principles within the framework of DFT, the isoelectronic co-doping of graphene with Be and S with a view that the heteroatom combination could be used to effectively induce and tailor the band-gap of graphene regardless of the impurity concentration. In the study, different doping patterns were considered to determine how the impurities preferred to co-exist in the matrix. The different isomers used in the study are shown in Figure 4.5. The cohesive energy and the electronic structure of each isomer were calculated to evaluate the stability and electronic character of the co-doped system. Bader charge analysis was performed to account for charges distribution in the system.

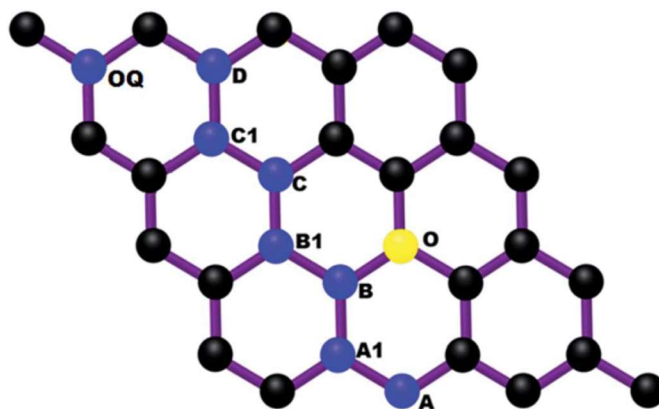


**Figure 4.5** The different doping configurations of Be-S co-doped mono layer graphene adopted in the study. Sites A1, B1, C2, etc. are the same sublattices occupied by Be-atom (blue colour) while site O is a fixed position occupied by S-atom (yellow colour). Only a pair of Be and S is considered at a time in each run.

### 4.3.2 Results and discussions

The details of the computation and the analysis of the results obtained using Be and S to co-dope graphene are presented in the published article below.

Cite this: *RSC Adv.*, 2016, 6, 88392

## Exploring the stability and electronic structure of beryllium and sulphur co-doped graphene: a first principles study†

O. Olaniyan, R. E. Mapasha, D. Y. Momodu, M. J. Madito, A. A. Kahleed, F. U. Ugbo, A. Bello, F. Barzegar, K. Oyedotun and N. Manyala\*

First principles density functional theory (DFT) calculations have been performed to explore the stability, structural and electronic properties of Be and S co-doped graphene sheets. The band-gap of graphene has been tuned by co-doping with beryllium and sulphur at different sites. The results show that by co-doping graphene with Be and S, the band-gap increases from zero up to 0.58 eV depending on the doping sites. The cohesive and formation energies of the systems were also determined. All the isomers formed by exploring different doping sites differ notably in stability, bond length and band-gap. Nevertheless, the planar structure of all the systems investigated was preserved even after geometry optimisation. The majority of the isomers that correspond to co-doping at non-equivalent sites favour higher band-gap opening, but lower stability, than the other set of isomers with equivalent doping sites. Bader charge analysis was adopted to account for charge distribution in the systems. As a result of the difference in electronegativity among carbon atoms and the impurities, it was observed that electron accumulation occurred more on the carbon atoms in the proximity of Be and S than at any other position in the graphitic systems investigated.

Received 10th July 2016  
Accepted 2nd September 2016

DOI: 10.1039/c6ra17640b

www.rsc.org/advances

### Introduction

Graphene is actively investigated as a possible replacement for silicon for use in micro, and even nanoelectronics. In silicon-based electronics, useful devices are made by doping with electropositive and electronegative elements. Similarly, doping will be needed to create useful devices in graphene-based electronics. This article uses DFT to investigate the atomic and electronic structure of one type of doping of graphene, namely substitution of carbon atoms by atoms of beryllium and sulphur.

Graphene is a two dimensional  $sp^2$  hybridized carbon atom material with a honey comb lattice and the unit cell has two carbon atoms in non-equivalent positions which form two interpenetrating triangular sublattices (see Fig. 1). It is known to be a fundamental and integral part of other forms of graphitic carbon such as fullerenes (bucky ball), carbon nanotubes and graphite.<sup>1–4</sup> While its existence was theoretically predicted by P. R. Wallace many years back,<sup>1</sup> it was not believed at that time to be physically attainable as a 2D crystalline material because it was adjudged to be thermodynamically unstable.<sup>5</sup> In 2004 however, Novoselov *et al.*<sup>6</sup> experimentally

isolated the graphene crystal through micromechanical exfoliation of pyrolytic graphite. Ever since, the material has drawn a lot of attention among researchers in the scientific community. More importantly, graphene has been lauded as a potential material in semiconductor nanoelectronics as a result of its stable hybrid structure, excellent electrical and optical properties and high charge carrier mobility.<sup>3,6–8</sup> In fact the charge carrier mobility, which is about  $10^6 \text{ cm}^2 \text{ V}^{-1} \text{ s}^{-1}$ , has been reported to be 2–3 times higher than that of conventional semiconductors.<sup>9</sup>

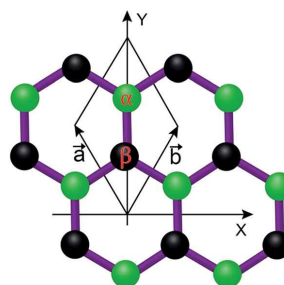


Fig. 1 Graphene has two carbon atoms in the unit cell. The two atoms are at non-equivalent sites denoted by  $\alpha$  and  $\beta$  where  $\vec{a}$  and  $\vec{b}$  symbolized the primitive unit vectors.

Department of Physics, Institute of Applied Materials, SARCHI Chair in Carbon Technology and Materials, University of Pretoria, Pretoria 0028, South Africa. E-mail: ncholu.manyala@up.ac.za; Fax: +27 12 420 2516; Tel: +27 12 420 3549

† Electronic supplementary information (ESI) available. See DOI: 10.1039/c6ra17640b

Pristine graphene however has zero band gap which makes it extremely difficult for direct electronic device applications. For instance in field-effect transistors (FETs) the role of a band gap in the drain material is crucial without which it would be difficult to switch off the device. To overcome this shortcoming, different techniques can be used to fabricate sizable band gaps in graphene sheets. Some of the techniques that could be employed to open up an energy gap in graphene are: superstructures fabrication, surface modification with atoms or polar molecules,<sup>19–24</sup> chemical doping,<sup>15–22</sup> application of electric field,<sup>23,24</sup> and deposition of graphene on epitaxial substrates.<sup>25–27</sup>

Superstructure fabrication like quantum-dot,<sup>28,29</sup> graphene nanoribbons<sup>30,31</sup> or nanomeshes<sup>32</sup> induce an energy gap in a material through quantum confinement. However, engineering of such structures dimensional-wise still poses a serious challenge. The design of such superstructures with uniform widths and edges below 10 nm is still quite tedious to attain with top-down techniques such as etching and lithography.<sup>33</sup> Although homogenous structures can be achieved easily with bottom-up approaches,<sup>34</sup> pulling off patterned ribbons still remains a contending procedure.

A facile approach to induce an energy gap in graphene is by depositing it on epitaxial substrates like SiC,<sup>35</sup> Al<sub>2</sub>O<sub>3</sub>,<sup>36</sup> etc. Apart from the difficulties involved in controlling the morphology and the surface energies of the material, the band gap induced by this technique is not tuneable.<sup>37</sup> However, for a tuneable band gap inducing technique, application of electric field could be a viable option.

The application of an external electric field ( $E$ ) perpendicular to the plane of AB stacked bilayer graphene can induce a band gap tuneable up to 0.25 eV through the breaking of the material inversion symmetry. The carrier mobility is not substantially affected in the process. Despite the robustness of this technique for AB stacked bilayer graphene, the electric field does not favour a band gap opening directly in monolayer graphene.<sup>37</sup> This is simply because the application of this field to monolayer graphene does not affect the inherent symmetry of the material sublattices.

Furthermore, unlike the electric field scheme which is applicable exclusively to few-layer graphene, chemical doping method *via* substitution of foreign atomic elements (heteroatoms) in place of the carbon atoms in graphene structure has been reported to be a suitable technique for creating sizeable and varying band gaps in monolayer graphene.<sup>38</sup> It involves using elements (like N and B) with comparable atomic radius (but different number of valence electrons) as carbon to replace the carbon atoms of graphene. The technique of substitution came into prominence shortly after the isolation of a single graphene layer in 2004, and ever since the method has widely been cited in different works in literature.<sup>39</sup>

In this study, we focused primarily on chemical doping as an avenue of modifying the electronic structure of graphene for band gap engineering, and the following are the highlights of the previous studies objectified by this technique. For examples, using *ab initio* calculations, Lee *et al.*<sup>40</sup> studied the adsorption of beryllium (Be) on fullerenes and their potential to store hydrogen molecules. They found that the clustering of Be on

pristine fullerenes is energetically stable but causes the dissociation of hydrogen molecules. Ferro *et al.*<sup>41</sup> carried out DFT studies of the absorption, diffusion of Be in graphite and the formation of Be<sub>2</sub>C. They reported that, in high quantity, the absorption of Be in graphite can result into formation of Be<sub>2</sub>C. Denis *et al.*<sup>42</sup> performed first principle studies of S and P-doped graphene. They found that below 0.5% impurity concentration, S-doped graphene has a band gap in the range of 0.1–0.2 eV while P-doped graphene has a higher gap between 0.3 and 0.4 eV. Recently, Ullah *et al.*<sup>33</sup> investigated structural and electronic properties of Be and Be/B dual doped graphene *via* density functional theory calculations, and remarked that with a rectangular doping configuration a maximum band gap of 1.44 eV can be obtained for Be-doped graphene at 12.5% impurity concentration. Moreover a maximum band gap of 0.99 eV can be attained for Be–B co-doped graphene at the same concentration. More recently, Huang *et al.*<sup>43</sup> reported electronic structure with optical properties of boron-doped, sulphur-doped and boron and sulphur dual doped graphene. They observed that doping modified the electronic and the optical properties of the doped graphene samples in question, and that the size of the energy gap depends on the impurities concentration in a doped graphene sample. Some other works relating to sulphur-doped graphene or SWCNTs can be found in ref. 44.

It is worth noting that in spite of the numerous previous studies, there has been none that addresses structural properties and electronic structure of Be and S co-doped graphene. Moreover, Be–S co-doping of graphene is expected to make a better semi-conducting material than either Be-doped or S-doped graphene. This is because doping of graphene with sulphur could lead to a material with metallic behaviour,<sup>15</sup> while doping with beryllium could form a material with Fermi-level lying within the valence band,<sup>33</sup> which to us might form a material with lower carrier mobility than Be–S co-doped graphene which has higher Fermi-level but lies within the energy-gap. In view of this, using first principle calculations within the frame work of density functional theory (DFT) we investigated structural properties and electronic structures of Be–S co-doped graphene. We have tried not only to accomplish band gap engineering and tuning in the sheet through Be and sulphur substitutional co-doping, but we have also explored the stability and the dependability of the energy gap on the doping sites across the sublattices in the graphene crystal. In addition, Bader charge analysis<sup>45–47</sup> has been adopted to account for charge distribution in the material under study.

## Methods

First-principles numerical non-spin polarised calculations were carried out using *ab initio* density functional theory as implemented in MedeA VASP software.<sup>48–51</sup> In the calculations, the projected augmented wave (PAW) was used to describe the system of electron–ion interactions, while the generalized gradient approximation (GGA) with PBE prescription<sup>52</sup> was utilized for exchange correlation. The kinetic energy cut-off for the wave function expansion was set to 400 eV with energy convergence criteria for all the systems considered set to 10<sup>–5</sup>



eV. Graphitic systems of 32 atoms with supercell model slab of  $4 \times 4$  were employed in all the calculations. To avoid interlayer interaction between two successive layers of graphene in the simulations, a vacuum spacing of  $14 \text{ \AA}$  was used in between the layers with applied periodic boundary condition along the graphitic plane. All the structures were geometrically relaxed until the Hellmann-Feynman forces converged below  $0.02 \text{ eV \AA}^{-1}$ . Based on the symmetry of the graphitic systems considered and in order to also actualise self-consistent field calculations, a  $\Gamma$ -centred grid of  $6 \times 6 \times 1$   $k$  mesh with Gaussian smearing was employed to sample the Brillouin zone. Moreover, a denser  $k$ -point grid of  $17 \times 17 \times 1$  was adopted when calculating the density of states (DOS). Cohesive energy,  $E_{\text{coh}}$  calculations were performed using the following formula:

$$E_{\text{coh}} = -\frac{[E_{\text{t}} - \sum n_x E_x]}{N}$$

here  $x$  represents C, Be or S;  $E_x$  and  $E_{\text{t}}$  stand for the atomic energies and electronic ground state energy of the whole system, respectively. The variable  $N$  stands for the total number of atoms in the system while  $n_x$  is the number of atoms of type  $x$ . The negative sign outside the bracket implies that all the stable structures should have positive cohesive energies, otherwise the system is unstable and the magnitude of the value is a measure of the bonding strength.

To calculate the atomic energies of the atoms, we created a  $10 \text{ \AA} \times 10 \text{ \AA} \times 10 \text{ \AA}$  super cell and centred an atom in the middle of the box. We set the  $K$ -integration to Gaussian and performed a single point spin polarised calculation with  $\Gamma$ - $k$  point. In this case spin polarised calculations was performed because carbon and sulphur atoms are both open shell systems.

Furthermore, we have calculated the difference between the formation energy (FE) of Be-S co-doped and the sum of the formation energies of Be-doped and S-doped graphene to check if this study is in agreement with the recent study by Denis *et al.*<sup>53</sup> who have shown that the FE of certain classes of dual doped graphene is less than the sum of the formation energies of the corresponding mono-doped graphene systems. To calculate the formation energy of co-doped and mono-doped graphene systems, we employed the following formula:

$$\text{FE}_{(\text{BeS})} = E_{\text{BeS}} + 2\mu_{\text{C}} - E_{\text{graphene}} - \mu_{\text{Be}} - \mu_{\text{S}}$$

$$\text{FE}_{(\text{Be})} = E_{\text{Be}} + 2\mu_{\text{C}} - E_{\text{graphene}} - \mu_{\text{Be}}$$

$$\text{FE}_{(\text{S})} = E_{\text{S}} + 2\mu_{\text{C}} - E_{\text{graphene}} - \mu_{\text{S}}$$

here  $E_{\text{BeS}}$ ,  $E_{\text{Be}}$  and  $E_{\text{S}}$  represent the electronic ground state energy of Be-S co-doped graphene, Be and S doped graphene respectively.  $E_{\text{graphene}}$  is the energy of pristine graphene. For the chemical potentials ( $\mu_{\text{C}}$ ,  $\mu_{\text{Be}}$  and  $\mu_{\text{S}}$ ), the atomic energies of carbon, beryllium and sulphur were used appropriately for the calculation of the formation energy of the systems. To this end, it is worth mentioning that the conclusion drawn from the analysis of the formation energy of dual doped graphene is independent of the sources of the chemical potentials used in the calculation.<sup>53</sup>

Note: having initially performed spin and non-spin polarised calculations for the geometry optimization of one of the configurations of Be and S co-doped graphene and realised that the energies of the two calculations are equal, along with zero net magnetic moment, we subsequently considered only non-spin polarised calculations for the rest of the configurations in order to save ample amount of time. Besides, Be and S are not the only dopants that preserve non-magnetic nature of graphene. Recently, Hussain *et al.*<sup>54</sup> also reported Be and N co-doped graphene to be non-magnetic.

## Results and discussion

First, a geometry optimization was carried out on a pure graphene sheet to allow all the carbon atoms to relax. After the optimization, the lattice constant of pristine graphene was found to be  $2.46 \text{ \AA}$ , while the C-C bond length measures as  $1.42 \text{ \AA}$ , as shown in Fig. 2a. These values are in excellent agreement with some reported theoretical<sup>55</sup> and experimental<sup>55</sup> results. The calculated band structure of the optimized pristine structure of graphene is presented in Fig. 2b which also corroborates previous findings in relations to zero band gap and linear dispersion crossing at the Dirac point.<sup>56</sup>

Subsequently, a pristine graphene sheet was co-doped with beryllium and sulphur atoms. Different configurations of the above mentioned impurities in the graphene sheet were considered in order to exploit the effect of doping sites on the electronic properties and stability of the co-doped graphene sheets.

In defining a configuration of a Be-S co-doped graphene (BeSG) system, we substituted two carbon atoms at equivalent sites (*i.e.* at O and C1) and non-equivalent sites (*i.e.* at O and C) of pristine graphene for beryllium (blue) and sulphur atom (yellow) as shown in Fig. 3. The co-doped structure with sulphur and beryllium now occupying O and C1 positions respectively is termed the OC1 configuration or simply the OC1 isomer while the OC isomer symbolizes another configuration with S and Be being substituted for two carbon atoms at the sites O and C of the pristine graphene.

Furthermore, in a similar manner to OC and OC1, other isomers of Be and S co-doped graphene (BeSG) system were also generated such that the relative positions of Be and S have been changed successively. Fig. 4 shows an overview of other configurations considered while exploring structural and electronic properties of Be and S co-doped graphene. Configurations OA1, OB1, OC1, OD1, *etc.* correspond to same sublattices or equivalent sites substitution of Be and S co-doping whereas, OA, OB, OC, or OD matches co-doping of monolayer graphene at different sublattices (or non-equivalent sites). It is worth noting that all the configurations were chosen with respect to the position of S atom at the lattice point, O in the systems.

Different isomers of Be-S co-doped graphene considered in this study yielded different electronic band structures and density of states. In the following discussion, for the sake of conciseness, we have considered in detail the cohesive energy and formation energy; charge transfer; structural and electronic

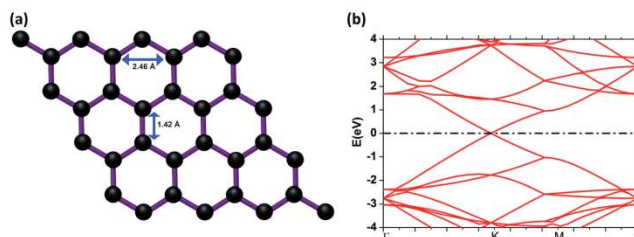


Fig. 2 (a) The optimised geometry of a  $4 \times 4$  supercell of pristine graphene sheet. (b) The calculated band structure of pristine graphene.

properties of OD, OB1 and OB isomers of Be-S co-doped graphene sheets.

#### OD isomer of BeSG

Two carbon atoms of graphene were replaced with Be and S atom as shown in Fig. 5a. This was followed by a geometry optimisation of the system until it reaches the level of the required accuracy. After the optimisation, it was observed that the planar structure of the system was preserved except for the palpable changes in the adjoining bond lengths. The adjoining bond lengths of S-C and Be-C expand to 1.62 Å and 1.55 Å respectively; this is as a result of the sizes of molecular covalent radii of Be (0.90 Å) and S (1.02 Å) which are larger than the covalent radius of the carbon atom (0.77 Å). Consequently, the C-C bond length nearest to sulphur reduces to 1.37–1.39 Å while that of beryllium reduces to 1.36–1.38 Å (see Fig. 5a). The sizes of the bond lengths of Be-C and C-C reported are in agreement with previous studies.<sup>33,54</sup> Besides, the cohesive energy which gives a measure of the respective stabilities of Be-S co-doped graphene systems was calculated and found to be equal to 7.32 eV per atom for this system with OD isomer. This value is less than 9.19 eV per atom that we calculated for  $4 \times 4$  pristine graphene. Meanwhile, the cohesive energy that we obtained for pristine graphene is in agreement with the previous reports by Ullah *et al.*<sup>33</sup> (9.21 eV per atom) and Rani and Jindal<sup>38</sup> (9.20 eV per atom). Note we have dropped the sign of the cohesive energy based on the model adopted as explained under Methods.

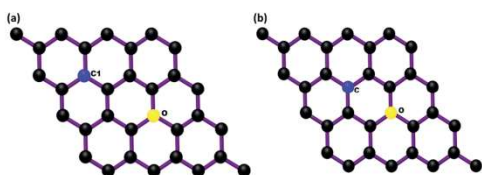


Fig. 3 (a) OC1 (which simply refers to as OC1 isomer) exemplifies a configuration with two carbon atoms at same sublattices (*i.e.* O and C1) substituted for Be and S. The blue colour in the diagram stands for Be while the yellow colour represents sulphur. (b) OC symbolises a configuration with two carbon atoms at different sublattices (*i.e.* O and C) substituted for Be and S.

Bader charge analysis was invoked to calculate the charge transfer among Be, S and Cs in the system. Due to the differing electronegativity among these three atoms, the valence charge of  $1.57e$  (Be) plus  $0.26e$  (S) is transferred to the carbon atoms in the system; the transferred charge is redistributed among the carbon atoms with the charges on each stretching from 3.81e to 4.47e. Moreover, as expected higher value of the charge is transferred to the carbon atoms in the neighbourhood of the impurities.

The calculations of density of states (DOS) and partial density of states (PDOS) were performed to study the effect of the co-doping on the system. The results are shown in Fig. 5 which shows that  $p_{xy}$  (*i.e.*  $2s$ ,  $2p_x$  and  $2p_y$  orbitals hybridization) orbitals of sulphur and beryllium hybridized sturdily with the  $p_{xy}$  of the carbon atoms of BeSG system. The stout overlapping between  $p_{xy}$  orbitals of carbon atoms and sulphur atom (in the range  $-8.0$  to  $-8.5$  eV in the valence region) partly leads to  $p$ - $\sigma$  bonds formation. Likewise,  $\pi$ -bond in the system could partly be attributed to the very weak overlapping of  $p_z$  orbitals of the carbon atoms and sulphur atom in the system. As for the beryllium atom, it contributed little to the DOS in the conduction band region. However, while the  $p_{xy}$  orbitals of Be hybridized strongly with  $p_{xy}$  orbitals of the carbon atoms around the Fermi level between 0 and 1.0 eV, the  $p_z$  orbital overlapped weakly with that of the carbon atoms contributing to  $\pi$ -bond formation of the system.

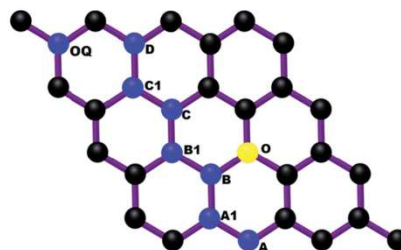


Fig. 4 Different isomers of Be-S co-doped graphene sheets. The relative position of Be has been updated through positions A, A1, B, B1, C, C1, etc. The sites A1, B1, C1, etc. denote Be atom position at the same sublattices with respect to S atom while other positions of Be atoms are non-equivalent with respect to S-atom. The blue colour represents Be-atom whereas yellow stands for sulphur atom.

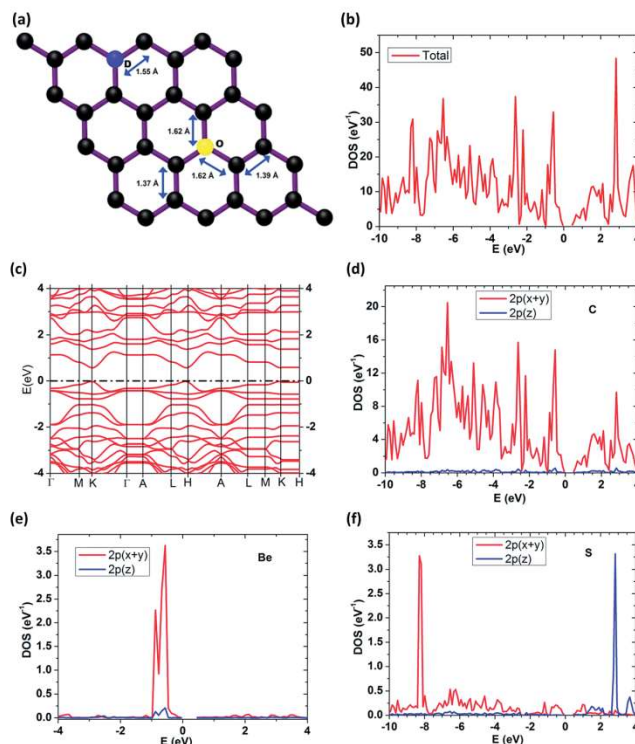
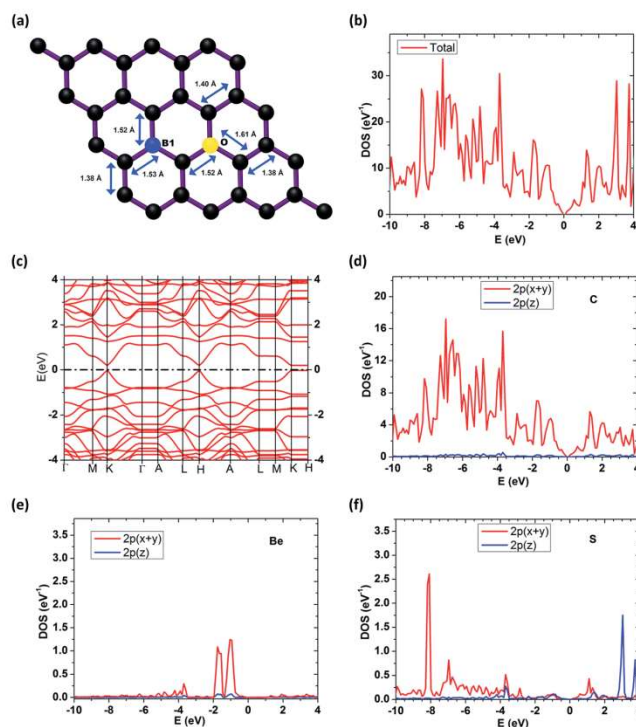


Fig. 5 (a) Optimized geometry of a Be–S co-doped graphene sheet. (b) Total DOS of BeSG with OD configuration. (c) The band structure of the optimised structure with OD configuration. (d) Projected DOS of carbon in BeSG with OD configuration. (e) Projected DOS of Be in BeSG with OD configuration. (f) Projected DOS of sulphur in BeSG with OD configuration.

The electronic band structure of the system was also calculated. A direct band-gap of 0.58 eV is induced around the Dirac point (see Fig. 5c). Here the position of the Fermi-level remains as it is in pristine graphene. This is as a result of isoelectronic nature of BeS co-doped graphene with respect to pristine graphene. That is, equal proportion of holes and electrons are introduced into carbon network simultaneously. S is electron rich and has two electrons more than C while Be is electron deficient and has two electrons less than C as such the net change in the number of electrons in the system is zero. Our results show that the band-gap induced by Be and S co-doped graphene with OD configuration is greater than those reported in the previous studies for single Be<sup>33</sup> or S<sup>43</sup> doping of graphene. Interestingly, a transistor with a graphene platform requires a minimum energy gap of 0.4 eV to operate suitably in on or off mode.<sup>57</sup> Thus the value (0.58 eV) from our calculation meets this specification. In addition, DFT usually underestimates band gaps hence the actual value for the band gap in this calculation might be greater than the value we reported. This significant result spurred us to perform further calculations on BeSG with different configurations.

#### OB1 isomer of BeSG

In the following case, S and Be are substituted accordingly for two carbons of graphene at O and B1 positions which are equivalent sites (see Fig. 6a). After the substitution, geometry optimisation was performed which still leads to the retention of the planar shape of the system but there were changes in the adjoining bond lengths of the structure. The optimised structure of the new system is presented in Fig. 6a. The bond length of S–C increases (relatively to C–C of pristine graphene) and falls within the range 1.54–1.62 Å while that of Be–C lies within the range 1.53–1.54 Å. Due to the large sizes of the covalent atomic radii of the aforementioned impurities relative to a carbon atom, the C–C bonds in the neighbourhood of S reduced to values within the range 1.36–1.40 Å whereas the values within the range of 1.36–1.38 Å (Fig. 6a) was observed for the bond lengths of C–C in the proximity of the Be impurity in the system under study. Unlike OD isomer, there is fluctuation in the bond lengths of S–C and Be–C of BeSG with OB1 isomer. For this system, the cohesive energy was calculated to be 7.35 eV per atom which is higher than that of OD isomer.



**Fig. 6** (a) The optimised structure of OB1 isomer of Be-S doped graphene. (b) The band structure of the optimised structure with OB1 configuration. Total DOS of Be-S with OB1 configuration. (c) The band structure of the optimised structure with OB1 configuration. (d) Projected DOS of carbon in Be-S with OB1 configuration. (e) Projected DOS of Be in Be-S with OB1 configuration. (f) Projected DOS of sulphur in Be-S with OB1 configuration.

Bader charge analysis reveals that the valence charge of  $1.57e$  (Be) along with  $0.48e$  from S is transferred to the carbon atoms in the system. It was noted that the size of the charge transferred from sulphur was greater than the corresponding transfer in the previous system with OD isomer. After the transfer of charges from the impurities to the system, charge reformation on carbon atoms occurs and stretches from  $3.80e$  to  $4.61e$ . In addition, we found as expected that more charges were transferred to the carbon atoms adjacent to the impurities in the graphene sheet.

To study the role of dopants in this system with this aforementioned configuration, the calculations of DOS and PDOS were performed. The results are displayed in Fig. 6. It is evident from the plots that the DOS contribution to the conduction band originated mainly from  $p_{xy}$  orbital of C atoms and little contribution from S. There is also minor contribution from  $p_z$  of S to these bands. For the valence bands, besides C, the population of this band is from  $p_{xy}$  orbitals of both S and Be.  $p_{xy}$  of C and Be strongly overlapped and form a  $\sigma$  bond which covers an energy range of  $-2.0$  to  $0.0$  eV. This wider range of energy of interaction between  $p_{xy}$  of C and Be over the corresponding

overlap in OD isomer might account for the slight increase in the cohesive energy of this system. Similarly,  $\sigma$  bond is also formed between  $p_{xy}$  orbitals of C and S. In this case the interaction covers an energy range from  $-8.5$  eV to  $-3.5$  eV, although it is more intense between  $-8.5$  eV to  $8.0$  eV.

The electronic band structure calculations show a band gap opening of  $0.22$  eV around the Fermi level of this system (see Fig. 6b). The gap opening around the Fermi level reflects the isoelectronic nature of Be-S co-doping. This value is less than the observed band gap of the previous structure with OD isomer. Thus the difference in the size of the band gaps can be ascribed to the configuration of the dopants in the given structures. This variation in the band gaps of the two isomers of the dual doped graphene due to the relative positions of the substituted dopants in them is consistent with the past studies<sup>38,58</sup> on B and N co-doped graphene.

#### OB isomer of Be-S co-doped graphene

When Be and S are substituted for two carbon atoms of graphene at two non-equivalent sites (*i.e.* at O and B) nearest to each other (see Fig. 7a), similar effects to the previously

discussed isomers are observed after the optimisation of the structure. The dopants interact with the other carbon atoms through  $sp^2$  hybridization. After optimisation of the structure, the bond lengths of Be–S, S–C and Be–C were found to be 1.69 Å, 1.62 Å and 1.50 Å respectively. These bond lengths are greater than the optimised C–C bond length of graphene. Consequently the immediate C–C bond lengths adjacent to the dopants are reduced leading to the distortion of some of the adjoining hexagonal carbon rings of the system. Though there were significant changes in the adjoining bond lengths of the atoms of the structure, the planar shape of the system is preserved.

For this isomer the cohesive energy of the system is equal to 7.41 eV per atom which is the highest value among the isomers of Be–S co-doped systems we considered, thus the most stable. Analogously, this configuration shows conformity with the most stable configuration of nitrogen and boron co-doped graphene as cited by Nath *et al.*<sup>59</sup> The detailed explanation of this favourable configuration has been provided in the immediate section.

Bader charge analysis confirms that the valence charge of 1.56e from Be along with 0.20e from S is transferred to the carbon atoms in the system. For this isomer, the size of the

charge transferred from sulphur is less than the corresponding transfer in the previous system with OB1 isomer. After the transfer of charges from the impurities to the system, charge redistribution on carbon atoms occurs which ranges from 3.75e to 4.52e. Moreover just like the previous cases, we observed that more charges were transferred to the carbon atoms adjacent to the impurities in the graphene sheet.

The results from the DOS and PDOS are presented in Fig. 7. The DOS contribution around the Dirac point comes mainly from  $p_{xy}$  of C, S and less from Be. There is also minor contribution from  $p_z$  orbital of S. The  $p_{xy}$  orbitals of Be does not only strongly hybridized with  $p_{xy}$  of C atoms over the range of –2.3 to 1.0 eV but also overlapped relatively softly over an interval of –4 to –9 eV and this leads to p– $\sigma$  bonds near the Fermi levels. Similarly, S and C which strappingly hybridized over a wide energy range (–14 to –1.0 eV) also forms p– $\sigma$  bond. The  $\pi$  bond between C and the dopants is very weak. This is illustrated by the slight overlapping between  $p_z$  of carbon and that of the impurities. As it can be seen from the band structures in Fig. 7c a gap opening of 0.28 eV which deviates slightly away from the Dirac point is observed. The deviation of the extremum of the

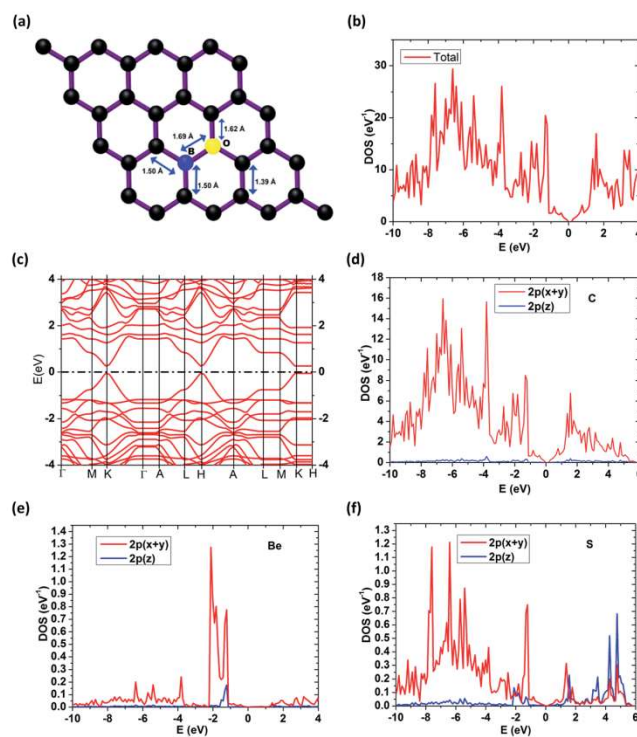


Fig. 7 (a) Optimized geometry of a Be–S co-doped graphene sheet. (b) Total DOS of BeSG with OB configuration. (c) The band structure of the optimised structure with OB configuration. (d) Projected DOS of carbon in BeSG with OB configuration. (e) Projected DOS of Be in BeSG with OB configuration. (f) Projected DOS of sulphur in BeSG with OB configuration.

gap of this system away from the Dirac point might be attributed to the loss of hexagonal symmetry of some of the carbon rings in the vicinity of the impurities in the system and as such the linear dispersion relationship at the Dirac point is lost. The non-uniformity in the hexagonal symmetry of the system in question is exemplified by the relative larger bond lengths of Be-S and S-C which have been uncovered in the preceding paragraphs under this isomer.

### Formation energies of BeS co-doped graphene

We have included this section to show that this work is in line with the recent study by Denis *et al.*<sup>52</sup> where it has been shown that certain classes of dual doped graphene have tendency to be more stable and easier to synthesise than their corresponding mono-doped graphene. For example, they pointed out that Al-X (where X = B, N, O) dual doped graphene are more stable than Al-doped graphene, and as such they would be easier to synthesise. In light of their report, we have calculated the formation energies of Be-S co-doped graphene involving all the isomers in this study and compared it with the formation energies of Be-doped and S-doped graphene. The result is presented in Table 1. We would like to reiterate once more that for the calculation of FE, atomic energies of the atoms were considered for the chemical potentials.

From Table 1, it can be seen that 0.61 eV which is associated with OB isomer has the least formation energy, followed by 2.39 eV that is shared by both the OA1 and the OB1 configuration. On the other hand, OC1 isomer has the highest FE which implies that is the least stable among the configurations considered in this study.

The above values show that Be and S atoms prefer to replace C-C bond of graphene since other configurations have higher FE. These favourable sites for Be-S co-doped graphene have also been echoed in recent studies<sup>54,60</sup> to be suitable sites for certain classes of dual doped graphene. So far, the only exception to this proposition is SiB along with GeB dual doped graphene. It is interesting to point out that the FE of BeS with OB1 isomer is lower than FE of Be or S-doped graphene. Similarly, OA, OA1, OB1 and OC have lower FE than S-doped graphene. Meanwhile, previous reports<sup>61,62</sup> showed S-doped graphene has been

successfully synthesised. Therefore we could generalise that it would be easier to synthesise Be-S co-doped graphene with these configuration than to synthesise S-doped graphene. In addition Table 1 reveals that the FE computed for different isomers of Be-S co-doped graphene is less than the FE resulting from the sum of Be and S-doped graphene. This shows that there is synergy between Be and S which lowered the FE significantly than the sum of FE of Be and S singly doped graphene.

### Summary

Band gap opening is important for developing electronic devices with graphene platforms. Nevertheless, it is not enough to create a finite band gap in graphene without a method of tuning energy gaps to suit different applications. Chemical doping of graphene at varying concentration *via* atomic substitution has constantly been reported as a good technique to actualise a band-gap tuning in graphene. However, doping of graphene with atomic impurities at increasing concentration leads to decrease in the cohesive energy of the material, and thus reduced stability. In order to overcome this shortcoming, the technique in this study which involves Be-S co-doping of graphene across the sublattices, is apparently a viable option of achieving band-gap tuning while keeping the impurities concentration in check, and thus the stability of the system. With this background, the plot of the variation of the cohesive energies of Be-S co-doped graphene with the different configurations is shown in Fig. 8a and supported with the Table 2 which includes the summary of all the results of the calculations.

It is evident from the plot that the pair of dopants, Be and S, substituted as nearest neighbour (OB isomer) in graphene is the most stable configuration since the cohesive energy is the highest while the formation energy the least among the configurations considered. This specific configuration (*i.e.* isomer OB) yields 7.41 eV per dopant whereas other isomers have cohesive energies that lie within 7.31–7.35 eV per dopant.

In addition, the band structures have been calculated for co-doped graphene systems *via* sampling route  $\Gamma \rightarrow M \rightarrow K \rightarrow \Gamma \rightarrow A \rightarrow L \rightarrow H \rightarrow A \rightarrow L \rightarrow M \rightarrow K \rightarrow H$  of the hexagonal Brillouin zone. Certain patterns of variations are observed in the electronic band structures and in the DOS of all the co-doped systems considered. It was found that pristine graphene exhibits a linear band at *k*-point of its hexagonal BZ with zero band-gap, whereas a finite band-gap has been observed in each of the aforementioned isomers of Be-S co-doped graphene systems investigated. Fig. 8b reveals the energy gaps values of all the doped graphene systems measured from the band structure calculations against different configurations.

It is evident from Fig. 8b that when the pair of Be and S have been substituted for two carbon atoms at different sublattices (non-equivalent) sites with varying relative distances in between the dopants, the electronic band-gaps of the resulting doped systems have been tuned from 0.42 eV through 0.58 eV aside from OB and OC isomer. However, an energy band-gap tuning within an interval of 0.17–0.34 eV has been achieved when the

**Table 1** Differences between the formation energies (FE) of  $4 \times 4$  BeS co-doped graphene and the sum of FE of  $4 \times 4$  Be and S singly doped graphene<sup>a</sup>

Configuration	$FE_{(BeS)}$ (eV)	$\sum(FE_{(Be)} + FE_{(S)})$ (eV)	$FE_{(BeS)} - \sum(FE_{(Be)} + FE_{(S)})$ (eV)
OA	2.45	5.19	-2.74
OA1	2.39	5.19	-2.80
OB	0.61	5.19	-4.58
OB1	2.39	5.19	-2.80
OC	2.45	5.19	-2.74
OC1	3.80	5.19	-1.39
OD	3.47	5.19	-1.72
OQ	3.47	5.19	-1.72

<sup>a</sup> Note:  $FE_{(Be)} = 2.09$  eV and  $FE_{(S)} = 3.10$  eV.

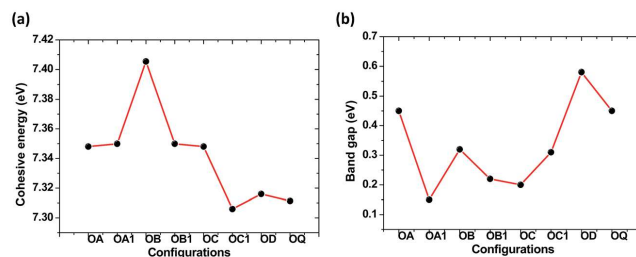


Fig. 8 (a) The variation of the cohesive energies of Be-S co-doped graphene with the different configurations. (b) The variation of the energy gaps of Be-S co-doped graphene with the different configurations.

Table 2 Summary of the configurations against the corresponding cohesive energies (coh), band-gaps and difference between formation energies (FE) of  $4 \times 4$  BeSG and the sum of FE of  $4 \times 4$  Be and S singly doped graphene<sup>a</sup>

Configuration	Cohesive energy (eV per atom)	$FE_{(BS)} - \sum(FE_{(Be)} + FE_{(S)})$ (eV)	Band gap (eV)
OA	7.35	-2.74	0.45
OA1	7.35	-2.80	0.18
OB	7.41	-4.58	0.28
OB1	7.35	-2.80	0.18
OC	7.35	-2.74	0.20
OC1	7.31	-1.39	0.31
OD	7.32	-1.72	0.58
OQ	7.32	-1.72	0.39

<sup>a</sup> Note:  $FE_{(Be)} = 2.09$  eV and  $FE_{(S)} = 3.10$  eV, coh of pristine graphene = 9.19 eV.

pair of Be and S has been substituted for a pair carbon atoms which are at varying distances apart but at the same sublattices of graphene. This results show that sublattices symmetry is subverted for co-doping at non-equivalent sites but tends to be preserved when is done at equivalent sublattice positions. Therefore Be-S co-doping of graphene creates a finite band-gap in the material. Moreover, the gap can be tuned if the effect of doping sites and dopant-dopant proximity is taken into consideration.

## Conclusions

The band-gap of graphene was tuned by co-doping it with Be and S. The sites occupied by the pair of Be and S in graphene were kept at varying distances from each other. The stability, structural and electronic properties of these systems for different lattice sites were determined. The electronic properties of graphene depend on the symmetry, and thus the sites of the impurities play an indispensable role in the modulation of the energy gap. The electronic character changes from semi-metal to semiconductor upon doping and, at the same time the flat structure of the graphene sheet was preserved. The isomers generated by choosing different doping sites differ notably in bond length, band gap and stability. Two set of

configurations were considered: one involves Be-S co-doping at equivalent positions while the other configuration deals with substitution of the impurities at non-equivalent sites of graphene sheets. Besides the OB and OC isomer, all the isomers that lent credence to the latter configuration enhanced a band-gap opening but are less stable than the isomers of the Be-S co-doped graphene sheets that shared the platform of the former configuration. As expected, the Fermi level of all the isomers of Be-S co-doped graphene considered in this study lied right in the middle of the band-gap. This shows that Be-S co-doped graphene has no metallic character as the case might be in sulphur (heavily) doped graphene. The result of cohesive and formation energies shows that when Be and S are substituted as nearest neighbour such a conformation gives the most stable configuration than any other one. Due to the differing electronegativity between a carbon atom and the impurities, electrons accumulation occurred on the carbon atoms closest to Be and S in all the doped systems investigated. Our result presents an avenue to tune the electronic band gaps of graphene from 0 eV through 0.58 eV so that the material can be used in electronic applications with operations within this energy range.

## Acknowledgements

The author would specifically like to acknowledge Mr Emmanuel Igumbor for his invaluable inputs made to this work. The author would also like to thank Prof. M. E. Casida, and Dr O. Akin-ojo for their suggestions after reading through the manuscript. This work is based on the research supported by the South African Research Chairs Initiative of the Department of Science and Technology and National Research Foundation (NRF) of South Africa (Grant No. 97994). O. Okikiola acknowledges the financial support from NRF and the University of Pretoria for his PhD studies.

## References

- 1 P. Wallace, *Phys. Rev.*, 1947, 71, 622–634.
- 2 R. Saito, G. Dresselhaus and M. Dresselhaus, *Physical properties of carbon nanotubes*, 1998.
- 3 A. K. Geim and K. S. Novoselov, *Nat. Mater.*, 2007, 6, 183–191.

- 4 A. H. Castro Neto, N. M. R. Peres, K. S. Novoselov, A. K. Geim, A. H. C. Neto, F. Guinea, N. M. R. Peres, K. S. Novoselov and A. K. Geim, *Rev. Mod. Phys.*, 2009, **81**, 109–162.
- 5 N. D. Mermin, *Phys. Rev.*, 1968, **176**, 250–254.
- 6 K. S. Novoselov, A. K. Geim, S. V. Morozov, D. Jiang, Y. Zhang, S. V. Dubonos, I. V. Grigorieva and A. A. Firsov, *Science*, 2004, **306**, 666–669.
- 7 K. S. A. Novoselov, A. K. Geim, S. V. Morozov, D. Jiang, M. I. K. I. V. Grigorieva, S. V. Dubonos, A. A. Firsov, M. I. Katsnelson and I. V. Grigorieva, *Nature*, 2005, **438**, 197–200.
- 8 A. K. Geim, *Science*, 2009, **324**, 1530–1534.
- 9 E. Castro, H. Ochoa, and M. Katsnelson, R. V. Gorbachev, D. C. Elias, K. S. Novoselov, A. K. Geim and F. Guinea, *Phys. Rev. Lett.*, 2010, **105**, 1008.2522.
- 10 P. A. Denis, *Chem. Phys. Lett.*, 2010, **492**, 251–257.
- 11 J. Zhou, M. Wu, X. Zhou and Q. Sun, *Appl. Phys. Lett.*, 2009, **95**, 103108.
- 12 X. Tian, J. Xu and X. Wang, *J. Phys. Chem. B*, 2010, **114**, 11377–11381.
- 13 R. Balog, B. Jørgensen, L. Nilsson, M. Andersen, E. Rienks, M. Bianchi, M. Fanetti, E. Lægsgaard, A. Baraldi, S. Lizzit, Z. Slijvančanin, F. Besenbacher, B. Hammer, T. G. Pedersen, P. Hofmann and L. Hornekær, *Nat. Mater.*, 2010, **9**, 315–319.
- 14 L. L. Zhang, X. Zhao, H. Ji, M. D. Stoller, L. Lai, S. Murali, S. McDonnell, B. Cleveger, R. M. Wallace and R. S. Ruoff, *Energy Environ. Sci.*, 2012, **5**, 9618.
- 15 P. A. Denis, R. Faccio and A. W. Mombru, *ChemPhysChem*, 2009, **10**, 715–722.
- 16 J. Dai, J. Yuan and P. Giannozzi, *Appl. Phys. Lett.*, 2009, **95**, 232105.
- 17 I. Zanella, S. Guerini, S. B. Fagan, J. Mendes Filho and A. G. Souza Filho, *Phys. Rev. B: Condens. Matter Mater. Phys.*, 2008, **77**, 073404.
- 18 P. Shinde and V. Kumar, *Phys. Rev. B: Condens. Matter Mater. Phys.*, 2011, **84**, 125401.
- 19 X. Deng, Y. Wu, J. Dai, D. Kang and D. Zhang, *Phys. Lett. A*, 2011, **375**, 3890–3894.
- 20 M. Escaño, T. Nguyen and H. Kasai, *Chem. Phys. Lett.*, 2011, **515**, 85–90.
- 21 H. Wang, Q. Wang, Y. Cheng, K. Li, Y. B. Yao, Q. Zhang, C. Z. Dong, P. Wang, U. Schwingenschlogl, W. Yang and X. X. Zhang, *Nano Lett.*, 2012, **12**, 141–144.
- 22 E. Cruz-Silva, Z. Barnett, B. Sumpter and V. Meunier, *Phys. Rev. B: Condens. Matter Mater. Phys.*, 2011, **83**, 1–9.
- 23 A. A. Avetisyan, B. Partoens and F. M. Peeters, *Phys. Rev. B: Condens. Matter Mater. Phys.*, 2009, **79**, 035421.
- 24 K. Mak, C. Lui, J. Shan and T. Heinz, *Phys. Rev. Lett.*, 2009, **102**, 256405.
- 25 P. Shemella and S. Nayak, *Appl. Phys. Lett.*, 2009, **94**, 2101.
- 26 X. Y. Peng and R. Ahuja, *Nano Lett.*, 2008, **8**, 4464–4468.
- 27 Y. H. Lu, P. M. He and Y. P. Feng, *J. Phys. Chem. C*, 2008, **112**, 12683–12686.
- 28 L. A. Ponomarenko, F. Schedin, M. I. Katsnelson, R. Yang, E. W. Hill, K. S. Novoselov and A. K. Geim, *Science*, 2008, **320**, 356–358.
- 29 B. Trauzettel, D. V. Bulaev, D. Loss and G. Burkard, *Nat. Phys.*, 2007, **3**, 192–196.
- 30 M. Han, B. Özyilmaz, Y. Zhang and P. Kim, *Phys. Rev. Lett.*, 2007, **98**, 206805.
- 31 X. Li, X. Wang, L. Zhang, S. Lee and H. Dai, *Science*, 2008, **319**, 1229–1232.
- 32 J. Bai, X. Zhong, S. Jiang, Y. Huang and X. Duan, *Nat. Nanotechnol.*, 2010, **5**, 190–194.
- 33 S. Ullah, A. Hussain, W. Syed, M. A. Saqlain, I. Ahmad, O. Leenaerts and A. Karim, *RSC Adv.*, 2015, **5**, 55762–55773.
- 34 J. Cai, P. Ruffieux, R. Jaafar, M. Bieri, T. Braun, S. Blankenburg, M. Muoth, A. P. Seitsonen, M. Saleh, X. Feng, K. Müllen and R. Fasel, *Nature*, 2010, **466**, 470–473.
- 35 S. Y. Zhou, G.-H. Gweon, A. V. Fedorov, P. N. First, W. A. de Heer, D.-H. Lee, F. Guinea, A. H. Castro Neto and A. Lanzara, *Nat. Mater.*, 2007, **6**, 770–775.
- 36 B. Huang, Q. Xu and S.-H. Wei, *Phys. Rev. B: Condens. Matter Mater. Phys.*, 2011, **84**, 155406.
- 37 R. Quhe, J. Zheng, G. Luo, Q. Liu, R. Qin, J. Zhou, D. Yu, S. Nagase, W.-N. Mei, Z. Gao and J. Lu, *NPG Asia Mater.*, 2012, **4**, e6.
- 38 P. Rani and V. K. Jindal, *RSC Adv.*, 2013, **3**, 802–812.
- 39 L. Ferrighi, M. Trioni and C. Di Valentin, *J. Phys. Chem. C*, 2015, **119**, 6056–6064.
- 40 H. Lee, B. Huang, W. Duan and J. Ihm, *J. Appl. Phys.*, 2010, **107**, 084304.
- 41 Y. Ferro, A. Allouche and C. Linsmeier, *J. Appl. Phys.*, 2013, **113**, 213514.
- 42 P. A. Denis, *Comput. Mater. Sci.*, 2013, **67**, 203–206.
- 43 C. Huang, L. Han, L. Wu, R. Su, J. Chen and P. Lu, *Eur. Phys. J. B*, 2015, **88**, 147.
- 44 G. K. Gueorguiev, Z. Czigány, A. Furlan, S. Stafström and L. Hultman, *Chem. Phys. Lett.*, 2011, **501**, 400–403.
- 45 W. Tang, E. Sanville and G. Henkelman, *J. Phys. Condens. Matter*, 2009, **21**, 084204.
- 46 E. Sanville, S. D. Kenny, R. Smith and G. Henkelman, *J. Comput. Chem.*, 2007, **28**, 899–908.
- 47 G. Henkelman, A. Arnaldsson and H. Jónsson, *Comput. Mater. Sci.*, 2006, **36**, 354–360.
- 48 G. Kresse and J. Hafner, *Phys. Rev. B: Condens. Matter Mater. Phys.*, 1993, **47**, 558–561.
- 49 G. Kresse and J. Hafner, *Phys. Rev. B: Condens. Matter Mater. Phys.*, 1994, **49**, 14251–14269.
- 50 G. Kresse and J. Furthmüller, *Comput. Mater. Sci.*, 1996, **6**, 15.
- 51 G. Kresse, *Phys. Rev. B: Condens. Matter Mater. Phys.*, 1996, **54**, 11169–11186.
- 52 J. P. Perdew, K. Burke and M. Ernzerhof, *Phys. Rev. Lett.*, 1996, **77**, 3865–3868.
- 53 P. A. Denis and C. P. Huelmo, *J. Phys. Chem. C*, 2016, **120**, 7103–7112.
- 54 A. Hussain, S. Ullah and M. Farhan, *RSC Adv.*, 2016, **6**, 55990–56003.
- 55 D. R. Cooper, B. D'Anjou, N. Ghattamaneni, B. Harack, M. Hilke, A. Horth, N. Majlis, M. Massicotte, L. Vandsburger, E. Whiteway and V. Yu, *ISRN Condens. Matter Phys.*, 2012, **2012**, 1–56.



- 56 S. M. Kozlov, F. Viñes and A. Görling, *Adv. Mater.*, 2011, **23**, 2638–2643.
- 57 F. Schwierz, *Nat. Nanotechnol.*, 2010, **5**, 487–496.
- 58 M. Hasegawa and K. Nishidate, *Phys. Rev. B: Condens. Matter Mater. Phys.*, 2004, **70**, 205431.
- 59 P. Nath, S. Chowdhury, D. Sanyal and D. Jana, *Carbon*, 2014, **73**, 275–282.
- 60 P. A. Denis, C. Huelmo and F. Iribarne, *Comput. Theor. Chem.*, 2014, **1049**, 13–19.
- 61 H. L. Poh, P. Šimek, Z. Sofer and M. Pumera, *ACS Nano*, 2013, **7**, 5262–5272.
- 62 S. Yang, L. Zhi, K. Tang, X. Feng, J. Maier and K. Müllen, *Adv. Funct. Mater.*, 2012, **22**, 3634–3640.

### 4.3.3 Concluding remarks

The result of the study shows that a finite gap is induced in graphene when it is co-doped with Be and S-atoms and the size can be tuned up to 0.5 eV depending on the doping sites. The cohesive energy calculation of the system shows that OB1 isomer, which is the configuration designated for Be and S atom occupying the positions of any two adjacent atoms of graphene, is the most stable. The origin of the stability of this configuration is attributed to the formation of ionic bonding between the impurities. This was further confirmed by Bader charge analysis which shows that there was charge transfer from Be to S-atom. OB1 configuration was observed to induce the minimum band-gap of 0.1 eV in graphene while a maximum band-gap of 0.58 eV was attained when the impurities occupied the sites that are two rings apart, designated as OD isomer in **Error! Reference source not found.** The difference in the band-gap between the isomers could be ascribed to charges redistribution in the system arising from different doping patterns.

#### Author contributions

O. Olaniyan designed the study and the main conceptual ideas. He worked out almost all of the technical details, and performed the numerical calculations for the suggested theory.

## References

- [1] H. J. Monkhorst and J. D. Pack, "Special points for Brillouin-zone integrations\*," vol. 13, no. 12, 1976.
- [2] S. Ullah *et al.*, "Band-gap tuning of graphene by Be doping and Be, B co-doping: a DFT study," *RSC Adv.*, vol. 5, no. 69, pp. 55762–55773, 2015.
- [3] D. S. L. Abergel, V. Apalkov, J. Berashevich, K. Ziegler, and T. Chakraborty, "Properties of graphene: A theoretical perspective," *Adv. Phys.*, vol. 59, no. 4, pp. 261–482, Jul. 2010.
- [4] K. S. Novoselov *et al.*, "Electric field effect in atomically thin carbon films.," *Science*, vol. 306, no. 5696, pp. 666–9, Oct. 2004.
- [5] P. A. Denis, R. Faccio, and A. W. Mombru, "Is it possible to dope single-walled carbon nanotubes and graphene with sulfur?," *ChemPhysChem*, vol. 10, no. 4, pp. 715–722, Mar. 2009.
- [6] C. W. Tang and S. A. VanSlyke, "Organic electroluminescent diodes," *Appl. Phys. Lett.*, vol. 51, no. 12, pp. 913–915, Sep. 1987.
- [7] M. A. Baldo *et al.*, "Highly efficient phosphorescent emission from organic electroluminescent devices," *Nature*, vol. 395, no. 6698, pp. 151–154, Sep. 1998.
- [8] B. H. Lee, I. G. Kim, S. W. Cho, and S. H. Lee, "Effect of process parameters on the characteristics of indium tin oxide thin film for flat panel display application," *Thin Solid Films*, vol. 302, no. 1–2, pp. 25–30, Jun. 1997.
- [9] U. Betz, M. Kharrazi Olsson, J. Marthy, M. F. Escolá, and F. Atamny, "Thin films engineering of indium tin oxide: Large area flat panel displays application," *Surf. Coatings Technol.*, vol. 200, no. 20–21, pp. 5751–5759, May 2006.
- [10] K. Rana, J. Singh, and J. H. Ahn, "A graphene-based transparent electrode for use in flexible optoelectronic devices," *J. Mater. Chem. C*, vol. 2, no. 15, pp. 2646–2656, 2014.
- [11] F. Bonaccorso, Z. Sun, T. Hasan, and A. C. Ferrari, "Graphene photonics and optoelectronics," *Nat. Photonics*, vol. 4, no. 9, pp. 611–622, 2010.
- [12] S. Bae *et al.*, "Roll-to-roll production of 30-inch graphene films for transparent electrodes," *Nat. Nanotechnol.*, vol. 5, no. 8, pp. 574–578, 2010.
- [13] A. K. Geim and K. S. Novoselov, "The rise of graphene," *Nat. Mater.*, vol. 6, no. 3, pp. 183–191, Mar. 2007.
- [14] S. Pang, Y. Hernandez, X. Feng, and K. Müllen, "Graphene as transparent electrode material for organic electronics," *Adv. Mater.*, vol. 23, no. 25, pp. 2779–2795, 2011.

## **4.4 A systematic study of the stability, electronic and optical properties of beryllium and nitrogen co-doped graphene**

### **4.4.1 Introduction**

Transparent conductors (TCs) are an important components in use today and are employed in a myriad of common applications that include but not exclusive to touch screens, solar cells, liquid crystal displays (LCDs), organic light emitting diode (OLED) [6], [7], smart phones, etc. Indium tin oxide is the most widely used TC[8], [9] in most device applications; this is because most of the required properties (such as high optical transparency, low sheet resistance, and stability[10]) of an ideal TC are unparalleled in the oxide. However, ITO has some limitations which suppress its use as a TC. Some of the limitations that the material exhibits are; brittleness, which limits its application in flexible devices; material cost, which is due to indium scarcity; and conductivity degradation if it is bent. As a result of these shortcomings an alternative material, which comprises all the essential qualities but also circumvents the limitations of ITO as a TC, is being sought after. Satisfying most of the important criteria earmarked for an ideal TC, graphene has been touted as a replacement for ITO due to its fascinating properties such as high flexibility, good transparency with a transmittance exceeding 97%, good mechanical, chemical and thermal stability[11]–[13]. Despite being characterised by these qualities, graphene is not a perfect TC material, because it has a higher sheet resistance and a lower electrical conductivity than ITO. The sheet resistance of the 2D material is between 1000 to 5000  $\Omega/\text{sq}$  while 10 to 30 $\Omega/\text{sq}$  [14] has been observed for ITO. Interestingly heteroatom doping has been widely reported as a useful approach to tailor the physical properties of graphene and could be applicable to tuning the sheet resistance.

In view of the above, a study aimed at finding the right dopants that could lower the sheet resistance of graphene without compromising the optical transparency is worth investigating. Recent study by Ullah *et al.*[2] suggests that the conductivity of graphene could be increased and transformed to p-type if it is doped with Be-atom. However, they did not study the lattice dynamics of Be-doped graphene to find out if the system is dynamically stable; probably the system is not stable and this could explain why the report on the experimental synthesis is scarce. Moreover, the optical properties of the system were also not investigated to know if it is transparent.

Following the study of Ullah *et al.*[2], we investigated from first-principles, within the frame work of DFT, the lattice dynamics, electronic and optical properties of Be-doped and, Be and N (Be-N) co-doped graphene. The effects of the impurities concentration on the aforementioned properties were also considered. As regards to the Be-N co-doped graphene, the system was studied along with the Be-doped graphene should in case the latter is not stable dynamically. The presence of the N-atom is expected to increase the stability of Be-N co-doped relative to the Be-doped graphene due to a possible ionic bonding between Be and N if they were to be placed adjacent to each other in a graphene matrix.

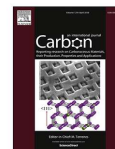
#### **4.4.2 Results and discussions**

The details of the computation and the analysis of the properties of Be and N singly doped and co-doped graphene are presented in the published article below.



Contents lists available at ScienceDirect

Carbon

journal homepage: [www.elsevier.com/locate/carbon](http://www.elsevier.com/locate/carbon)

## A systematic study of the stability, electronic and optical properties of beryllium and nitrogen co-doped graphene



O. Olaniyan, R.E. Maphasha, M.J. Madito, A.A. Khaleed, E. Igumbor, N. Manyala\*

Department of Physics, Institute of Applied Materials, SARCHI Chair in Carbon Technology and Materials, University of Pretoria, 0028, South Africa

### ARTICLE INFO

#### Article history:

Received 23 June 2017

Received in revised form

25 November 2017

Accepted 4 December 2017

Available online 6 December 2017

### ABSTRACT

*Ab-initio* calculations within the framework of density functional theory (DFT) have been performed to study the stability, electronic and optical properties of Be and N singly doped and co-doped graphene. The effect of the dopants concentration and isomerization on the electronic and the optical properties of these systems have been studied. It has been found that Be-N is more stable than Be-doped graphene. The transition from semi-metallicity as in the case of pristine graphene to semi-conducting of graphene doped separately with Be, N and pairs of Be-N has been observed. Both Be and Be-N co-doped graphene exhibit p-type character. Moreover, the size of the band-gap observed in these aforementioned systems increases with the impurity concentrations. All the systems investigated are transparent within the frequency interval of 7.0–10 eV for parallel electromagnetic polarization. In general, we observed that the optical properties of the doped systems studied, respond to doping concentration differently across the electromagnetic spectrum with respect to the polarization field vectors. The results of our study demonstrate Be-N co-doped graphene to be a more realistic p-type semiconductor than Be-doped graphene and the band-gap can be tailored to meet the requirements of specific applications in nano-electronic and optoelectronic devices.

© 2017 Elsevier Ltd. All rights reserved.

### 1. Introduction

Graphene, known to have a stable structure [1], high charge carrier mobility [2–6], high thermal conductivity [7], low Johnson noise [8], high surface area [6], unique electronic (e.g the linear energy dispersion at the Dirac points makes quasiparticles in the system to behave differently from the convectional semiconductors and metals) and optical characteristics (tunable surface plasmons, a behaviour that is not obtainable in metals), amongst other fascinating properties has triggered rising research interests. These properties have thus encouraged its potential applicability in various applications such as catalysis [9], field effect emission [10], energy storage [11,12], gas [13,14] and bio sensing [15–17]. Nevertheless, there is persistent inclination for its applicability range to be actively extended to the developing nanoelectronics field. However, graphene has a zero band-gap and this limits its direct application in electronic devices. A possible route employed by researchers to address the zero band-gap issue is by doping

techniques. Among different techniques [18–30] that have been reported, substitution doping of graphene with impurities is currently one of the preferred techniques to create a sizeable band-gap in the material leading to a new or improved physiochemical, optical and structural properties of the material. This is because impurities are frequently the prevailing scatterers that control the intrinsic electronic and transport properties of the system. In view of the necessity to expand its applicability, this present study employs density functional theory (DFT) to systematically investigate the electronic structure and optical properties of the substitutional type of doping of graphene, specifically, where the carbon atoms are replaced with beryllium and nitrogen atoms.

In an attempt to tailor the properties of graphene to meet specific applications demand, numerous theoretical and computational studies on heteroatom doped graphene have been reported, some of which have been found to agree with experimental findings. For example, Beheshti et al. [31] investigated a calcium-decorated and boron-doped graphene for high capacity hydrogen storage via a first-principles study, and realised that the substitutional boron doping of graphene eliminates the clustering of Ca atoms on graphene. In another study, Nath et al. [32] carried out some computational study on the electronic and optical properties

\* Corresponding author.

E-mail address: [ncholu.manyala@up.ac.za](mailto:ncholu.manyala@up.ac.za) (N. Manyala).<https://doi.org/10.1016/j.carbon.2017.12.014>

0008-6223/© 2017 Elsevier Ltd. All rights reserved.

of N and B-doped graphene, and found that the band-gap of the systems increases with an increase in doping concentration. Moreover, they observed, that the static dielectric constant of the systems, in the long wavelength limit for parallel polarization of the electric field, is modified with respect to impurity concentration. Rani et al. [33] also investigated the optical properties of pristine and doped graphene using DFT, and reported that N and B atoms can be used to tailor the optical properties of graphene in the visible region of electromagnetic (EM) spectrum. Recently, Jiang and co-workers [34] performed a first-principles study of nitrogen and boron doped graphene as potential catalysts in non-aqueous Li-O<sub>2</sub> batteries, and found that boron-doped graphene exhibits excellent performance as a catalyst for oxygen reduction reaction and the oxygen evolution reaction (OER) in non-aqueous Li-O<sub>2</sub> systems.

Theoretical predictions of B and N-doped graphene reported in the literature are now being supported by experimental findings involving the synthesis and characterization of these systems along with other heteroatoms doped graphene. For example, B-doped graphene with the impurity concentration of 4.3% has been successfully grown on copper foil at 1000 °C in an Ar atmosphere, employing polystyrene and boric acid as the sources of carbon and boron [35]. Similarly, B-doped graphene has been realised with the use of ethanol as the carbon source and boron powder as the B-precursor [36]. Ajayan et al. [37] reported the experimental synthesis of B and N co-doped graphene using methane (CH<sub>4</sub>) and ammonia borane (H<sub>3</sub>NBH<sub>2</sub>) as the carbon sources and boron-nitrogen sources respectively. Wang et al. [38] prepared N-doped graphene employing nitrogen plasma treatment of the graphene through a chemical method. Moreover, they observed that the as-prepared N-doped graphene exhibited a high electrocatalytic activity for the reduction of hydrogen peroxide and fast direct electron transfer kinetics for glucose oxidase. Despite the obvious choices of nitrogen and boron, heteroatoms with larger atomic radii have also been successfully substituted for the carbon atoms of graphene. For instance, Si-doped graphene has been theoretically demonstrated within the framework of DFT [21,39–41], and its experimental synthesis has also been successfully actualized [42] with its application as molecular sensors [40,43]. In the same way, other atoms such as Se [44,45], Ni [46,47], Mn [47], Fe [48] and Co [47] have all been substituted for the carbon atoms of the graphene system to obtain doped graphene systems. For further work on doped graphene and the potential applications, an interesting review has been given by Ruitao Lv and M. Terrones [49].

Properties of graphene can further be modified if dual doping is considered. Cruz-Silva et al. [50] revealed by first principle calculations that P-N dual doped graphene is a potential material for the fabrication of fast response and ultra-sensitive sensors. The laboratory synthesis of this nano-composite was recently demonstrated by Zhang et al. [51] in which the material was adopted as a catalyst for electrolytic hydrogen evolution [51] as well as an excellent anode material for lithium ion batteries [52]. Besides P-N dual doped graphene, the synthesis of sulphur (S) and nitrogen (N) dual doped graphene system has also been reported [53–61]. This system has been utilized as an electrocatalyst for oxygen reduction reactions (ORRs) and to improve the lithium storage capacity of sulphur-nitrogen-graphene (SNG) systems [54,55,59].

Meanwhile, using *ab-initio* calculations Lee et al. [62] studied the adsorption of beryllium (Be) on fullerenes and their capacity to store hydrogen molecules. They remarked that clustering of Be-atoms on fullerenes is energetically favourable but causes the dissociation of hydrogen molecules. Ferro et al. [63] performed a DFT study on the diffusion of Be in graphite. They stated that, in large quantities, the absorption of the Be in graphite could lead to the formation of Be<sub>2</sub>C. Recently, Ullah et al. [64] studied structural and electronic properties of Be and Be-B dual doped graphene

through DFT calculations and found that for an impurity concentration of 12.5%, the maximum band-gaps of 1.44 and 0.99 eV can be obtained for the Be-doped and Be-B dual doped graphene, respectively.

Bearing in mind the promising physical and electronic properties of Be-doped graphene as predicted through computational studies of the system, we wondered why the experimental synthesis of this nanostructure is yet to be reported in the literature. Based on this account, the present study seeks to explain why no experimental report of this aforementioned system exists till date by performing theoretical calculations related to the formation energies of Be-doped, N-doped and Be-N co-doped graphene (Be<sub>x</sub>N<sub>y</sub>G) systems within the framework of DFT. The effects of isomerization and impurities concentrations have also been taken into consideration.

From the calculation results, it was observed that the formation energy of Be-doped systems is very high in comparison to that of N-doped graphene (a system with a documented experimental synthesis) which might be why no report exist till to date on the experimental synthesis of the Be-doped graphene. On the account of the formation energy of the Be-doped system, it was observed that substitutional doping of graphene with Be-atom might be difficult to accomplish experimentally. Motivated by the necessity to reduce the formation energy of Be-doped graphene and still have the same p-type semiconducting material, co-doping of graphene with Be and N-atoms was done. Interestingly, it was seen from the results obtained that not only is there a significant reduction in the formation energy of Be-N co-doped graphene (Be<sub>x</sub>N<sub>y</sub>G, where x = 1, 2, 3 or 4 the number of Be or N-atoms in the system) as compared to that of Be-doped graphene, but also a similar electronic character exists between the two systems. Buoyed by this result, we subsequently attempted to tailor the properties of the system to meet the requirements of the specific application in nanoelectronics and optoelectronics by investigating the defect dependency of the electronic and optical properties of Be-N co-doped graphene. Lastly, the results will also be compared with that of single Be-doped and N-doped graphene.

## 2. Methods

The electronic and optical properties of the above mentioned graphitic systems have been calculated from first principles within the framework of *ab-initio* density functional theory as implemented in Vienna Ab-initio Simulation Package (VASP) [65]. In the calculations, while the electron-ion interactions were described by the Projected Augmented Wave (PAW) [66], the HSE06 hybrid functional with the Generalized Gradient Approximation as proposed by Perdew Burke Ernzerhof (PBE) [67] was employed for the exchange-correlation. For the expansion of Kohn-Sham orbitals in the plane wave basis set, a kinetic energy cut-off of 400 eV with energy convergence criteria of 10<sup>-5</sup> eV was utilized for all the calculations of the systems investigated. Each of the systems considered consists of 32 atoms with a periodic model slab of 4 × 4 supercell size.

In order, to avoid interlayer interaction between two successive layers of graphene, a test of energy convergence with respect to the interlayer spacing was performed and an interlayer gap spacing of 14 Å, found to give a converged result, has been used in between the layers with a periodic boundary condition applied along the graphitic plane. All the graphitic systems were geometrically relaxed until the Hellmann-Feynman forces converged just below 0.002 eV Å<sup>-1</sup>. In view of the symmetry of the graphitic systems employed and as a way of actualising self-consistent field calculations, Monkhorst-Pack gamma centered grid of 7 × 7 × 1 *k*-mesh with Gaussian smearing of 0.2 width was adopted to sample the

Brillouin zone.

Besides, when calculating the density of states, a denser  $k$ -point grid of  $17 \times 17 \times 1$   $k$  was employed for the calculations in order to reach a satisfactory coverage of the first Brillouin zone. Due to the breaking of graphene lattice symmetry as a result of doping of the system with impurities of larger molecular radii than carbon atom, the path in the reciprocal space along which the band structures are calculated is given via sampling route of  $\Gamma \rightarrow M \rightarrow K \rightarrow \Gamma \rightarrow M' \rightarrow K' \rightarrow \Gamma \rightarrow M'' \rightarrow K'' \rightarrow \Gamma$ .

To calculate the possibility of a substitutional defect to form and to contrast the energies of different defects in graphene, we have defined the formation energy of a defect to form as:

$$E_{form} = E_d - \sum_i n_i \mu_i \quad (1)$$

where  $E_d$  represents the total energy per unit cell of a graphene system with defects; 'i' is the summation index over all the atoms of given types; while the number of atoms of type 'i' is given by  $n_i$ ,  $\mu_i$  is the chemical potential of an atom of type  $i$ . For the chemical potential of carbon  $\mu_c$ , the energy of graphene per unit carbon atom was employed so that zero formation energy is obtained for defect-free graphene. To calculate the chemical potential of nitrogen  $\mu_N$ , we created a  $16 \times 17 \times 18$  Å supercell and placed nitrogen molecule in the middle of the box.  $K$ -integration was set to Gaussian and single point spin polarized calculation was performed. The minimum energy of a nitrogen molecule via the optimized geometry of the system as stipulated by spin polarized calculation was found to be the same as the result from a non-spin polarized calculation. This shows that a nitrogen molecule is a closed shell system. As a final step, the  $\mu_N$  of nitrogen was obtained as half of the energy of the molecule. Finally, Be chemical potential carbon  $\mu_{Be}$  was calculated using the energy per unit atom of crystalline Be in a simple hexagonal lattice with a space group of  $P6_3/mmc$ .

It should be noted that the spin and non-spin polarized calculations for the geometry optimization of a  $Be_xN_xG$  system were initially performed. The total energies of the two calculations were observed to be equal, along with net zero magnetic moments. As a result, the non-spin polarized calculation was subsequently considered for the rest of the calculations so as to save ample amount of time. Moreover, Be and N are not the only impurities that preserve the non-magnetic character of graphene. Recently, Be and S co-doped graphene have also been reported to be non-magnetic as elucidated in detail in our earlier work [68].

The ground state energy of a given crystal expressed as a function of atom positions  $r$  ( $\mathbf{R}_k$ ) could be expanded around the equilibrium positions using Taylor expansion:

$$E(\dots r(l, k) \dots r(l', k') \dots) = E_0 + \frac{1}{2} \sum_{l, k, l', k'} \varphi(l, k; l', k') U(l, k) U(l', k') + O(U^3) \quad (2)$$

Where  $\mathbf{k}$  is the position of an atom-in a unit cell  $\mathbf{l}$ -relative to another atom at  $\mathbf{k}'$ .  $E_0$  is the energy at the equilibrium while the displacement of any atom of the system is represented as  $U$ .

To calculate the phonon frequencies, the interatomic force constants  $\varphi_{\alpha\beta}$  is expressed as:

$$\varphi_{\alpha\beta}(\mathbf{l}k, \mathbf{l}'k') = \frac{\partial^2 E}{\partial r_\alpha(\mathbf{l}k) \partial r_\beta(\mathbf{l}'k')} \quad (3)$$

The Cartesian indices are represented as  $\alpha$  and  $\beta$  while  $\mathbf{r}$  is the position vector of any atom in the system. equation (3) could

further be expressed in terms of the forces on the atoms of a given system, i.e.

$$\varphi_{\alpha\beta}(\mathbf{l}k, \mathbf{l}'k') = \frac{F_\beta(\mathbf{l}'k') \Delta r_\alpha(\mathbf{l}k) - F_\beta(\mathbf{l}k) \Delta r_\alpha(\mathbf{l}'k')}{\Delta r_\alpha(\mathbf{l}k)} \quad (4)$$

In the above equation, the force experienced by an atom  $\mathbf{l}k$  in the direction of  $\beta$  is represented as  $F_\beta(\mathbf{l}k)$  whereas the finite displacement is denoted by  $\Delta \mathbf{r}_\alpha$ . With equation (4), the force constants  $\varphi_{\alpha\beta}$  and the dynamical matrices can be computed []. Thus, the phonon frequencies  $\omega_{q_i}$  of the system for a given wave vector  $\mathbf{q}$  and a mode  $i$  can be obtained by diagonalizing the dynamical matrix. All the required steps in the above equation (2) through (4) were automated with a phonon code interfaced with VASP Medea.

Generally, the optical properties of a system are calculated with the aid of a frequency dependent dielectric function  $\epsilon(\omega)$  (see equation (5)); where  $\epsilon_2$  is the imaginary component and is calculated using first-order time-dependent perturbation theory in the framework of simple dipole approximation.

$$\epsilon(\omega) = \epsilon_1(\omega) + i\epsilon_2(\omega) \quad (5)$$

In the limit of long wavelength,  $\epsilon_2$  could be expressed as:

$$\epsilon_2(q \rightarrow 0, \omega) = \frac{2e^2\pi}{V\epsilon_0} \sum_{c,v,k} \left\langle \psi_c^* | \vec{u} \cdot \vec{r} | \psi_v \right\rangle^2 \delta(E_c^c - E_v^v - \omega) \quad (6)$$

where  $V$ ,  $\epsilon_0$  and  $\omega$  (in eV) stand for the volume of the supercell, free space permittivity and a given radial frequency of the applied EM wave respectively. In turn,  $\vec{u}$  and  $\vec{r}$  represent the polarization vector of the incident EM field and the position vector. The eigenfunctions of the valence ( $v$ ) and conduction ( $c$ ) band of the systems at  $k$ -point are in that order denoted by  $\psi_v^v$  and  $\psi_c^c$  while the corresponding eigenvalues are given by  $E_v^v$  and  $E_c^c$ .

In the procedure, the calculations of the dipolar transition matrix elements between occupied and unoccupied single electrons orbitals are calculated and implemented in the VASP code within the formalism of Kohn-Sham [69,70].  $\epsilon_1$  which is the real part of the complex frequency dependent dielectric function is calculated from  $\epsilon_2$  using the Kramers-Kronig transformation:

$$\epsilon_1(\omega) = \text{Re} \left[ \epsilon(q \rightarrow 0, \omega) = 1 + \frac{2}{\pi} P \int_0^\infty \frac{d\omega' \epsilon_2(\omega') \omega'}{\omega'^2 - \omega^2 + i\eta} \right] \quad (7)$$

where  $P$  represents the Cauchy principal value.

The technique is well explained in Ref. [71] with both  $\epsilon_1$  and  $\epsilon_2$  having two independent components which are related to the two polarizations of the electric field in relation to the given systems. The two polarizations are termed parallel and perpendicular polarization in this study. Note that equation (6) does not include a Drude component. The Drude term describes intraband transitions which are prevalent at low energies.

VASP code uses equation (6) and (7) to compute the data of frequency dependent components of  $\epsilon(\omega)$ . With these data sets, the optical properties of the Be-doped graphene ( $Be_xG$ ), N-doped graphene ( $N_xG$ ) and Be-N co-doped graphene ( $Be_xN_xG$ ) (where  $x = 1, 2, 3, 4$  is the number of the atomic impurities in the graphene) systems have been calculated where  $x$  is defined as the number of impurity atoms introduced into the graphene crystal lattice. That is:



$$n(\omega) = \left( \frac{\sqrt{\epsilon_1^2 + \epsilon_2^2} + \epsilon_1}{2} \right)^{\frac{1}{2}} \quad (8)$$

$$k(\omega) = \left( \frac{\sqrt{\epsilon_1^2 + \epsilon_2^2} - \epsilon_1}{2} \right)^{\frac{1}{2}} \quad (9)$$

where  $n(\omega)$  and  $k(\omega)$  are in that order the real and imaginary parts of the complex refractive index  $\tilde{u}$ , and are related as  $\tilde{u} = n(\omega) + ik(\omega)$ . Through equation (8) and (9) the reflectivity  $R(\omega)$  (Equation (10)) of each system has been evaluated such that the incident polarized fields are normal to the samples.

$$R(\omega) = \frac{(n-1)^2 + k^2}{(n+1)^2 + k^2} = \left( \frac{1 - \sqrt{\epsilon(\omega)}}{1 + \sqrt{\epsilon(\omega)}} \right)^2 \quad (10)$$

The absorption coefficient  $\alpha(\omega)$  of each system given by equation (11) has been derived from equation (9)

$$\alpha(\omega) = \frac{2k\omega}{ch} = \frac{\epsilon_2\omega}{nch} \quad (11)$$

In equation (8),  $c$  stands for the speed of light in vacuum, while the other parameters maintain the same depictions as previously stated.

For a given system, the electron energy loss function (EELS)  $L(\omega)$  which is a measure of its collective excitation can be evaluated using equation (12). The function is derived from  $L(\omega) = \text{Im}(-1/\epsilon(q \rightarrow 0, \omega))$  and the magnitude increases as  $\epsilon_1 \rightarrow 0$  and  $\epsilon_2 < 1$  at plasma frequency. Plasmons play a significant role in dictating optical properties of semiconductors and metals. At Plasma frequency, electromagnetic waves of lower frequencies are reflected by a material because of the screening effect of the electrons in the material. However, light of higher frequencies above the plasma frequency are transmitted by the material as a result of the slower response of the electrons in the material in screening the field.

$$L(\omega) = \frac{\epsilon_2}{\epsilon_1^2 + \epsilon_2^2} \quad (12)$$

To calculate the optical properties of  $N_xG$ ,  $Be_xG$ ,  $Be_xN_xG$  and pristine graphene systems, quite a number of unoccupied bands have been taken into consideration in these present calculations. For DFT calculations, reasonable results are often obtained for the

dielectric properties of a system if the number of empty bands added above the Fermi-level is twice or three times the default value provided with respect to VASP. It is important to note that an appreciable number of empty bands are needed in DFT calculations to get fairly accurate results for the calculations of the density of states (DOS) and frequency dependent dielectric matrix. This is because in an iterative matrix-diagonalization scheme in VASP, eigenvectors near to the top of the computed number of vectors converge much slower than the lowest eigenvectors. This could result in substantial performance loss if enough empty bands are not utilized in the calculations. Also, a large number of empty bands are required to account for the high frequency electronic transition in the system. As a result of this, for the calculation of DOS or bandstructure, it is recommended to set the number of bands to be  $(\text{the number of valence electrons})/2 + (\text{the number of atoms})/2$ . Whereas, for the calculation of the optical properties, three folds of the default number of bands needed for the calculation of DOS is required. In this calculation, approximately 160 empty bands have been added to the default value in order to account for likely high-frequency interband transitions of the given systems.

### 3. Results and discussion

#### 3.1. Electronic properties

This section focuses on the electronic properties of the Be-doped, N-doped, and Be-N co-doped graphene systems, and the effect of the impurities (Be and N co-dopants) concentration on the band-gap of the system. In addition, in order to validate our results with previous reports from similar studies, and to draw a comparison between  $Be_xG$ ,  $N_xG$  and  $Be_xN_xG$  systems at different impurities concentrations, a systematic study of the electronic structures of these aforementioned systems and that of the pristine graphene was performed. Fig. 1 shows the optimized structure, electronic band structure and density of states (DOS) of pristine graphene. As indicated in Fig. 1 (left image), the lattice constant of the system after optimization was found to be 2.46 Å while the C–C bond length is equal to 1.42 Å. These values are in excellent agreement with previous studies [64,68]. The band structure along with the DOS of pristine graphene as illustrated in the right panel of Fig. 1 (right image), also agrees with the literature [32] with respect to the zero energy band-gap and linear dispersion crossing at Dirac point. Thus, these findings indicate the reliability of our computational methods.

Substitutional doping of pristine graphene with foreign atomic elements modifies the electronic properties of the material depending on the nature of the dopants, substitutional sites and the

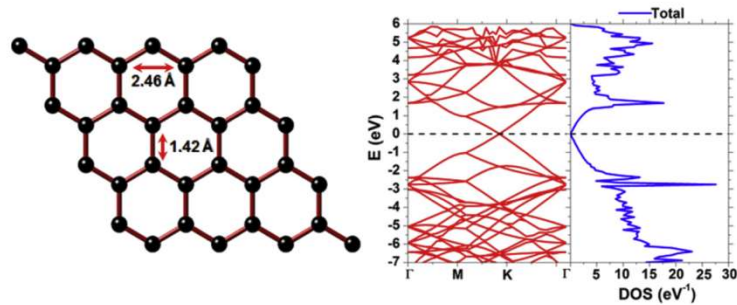


Fig. 1. The optimized structure and the calculated band structure with DOS of a  $4 \times 4$  supercell of a pristine graphene sheet.

concentration of the impurity [68]. With these in mind, in this work graphene was first doped singly with a set of N atoms, and then with Be atoms. Employing varieties of isomers at each impurity concentration, we varied independently the concentration of the two set of impurities in graphene from 3.13% through 12.50%. Although, a number of isomers at different impurity concentrations have been studied, for the sake of conciseness, we have presented here only the systems with stable configurations which also epitomise maximum electronic band-gap opening in the graphitic systems investigated are presented for conciseness.

Figs. 2 and 3 depict the optimized geometries and electronic structures of N-doped and Be-doped graphene at different impurity concentrations. From the results, it was found that at any impurity concentration, a maximum band-gap is induced in N-doped and Be-doped graphene if the dopants are substituted for the carbon atoms occupying the same sublattice sites of graphene (see Fig. 2(b)–(d) and Fig. 3(b)–(d)). This doping pattern which enhances maximum band-gap opening has been observed experimentally with a scanning tunneling microscopy (STM) by Ruitao Lv et al. [72] to be the preferred configuration for N-doped graphene while theoretical study by P. Rani and V.K. Jindal [73] equally confirms it to hold for boron doped graphene as well. Due to the size of the molecular radius of N, we also observed that the N atoms (red atoms in Fig. 2) could replace quite a number of carbon atoms in any hexagonal ring of graphene without deforming the ring. However, for an in-plane substitution of any two carbon atoms (especially the C–C) for a pair of Be atoms (blue atoms in Fig. 3) led to a significant distortion of the hexagonal ring of graphene and this is due to the longer molecular covalent radius of Be compared to carbon. A similar observation has also been reported by P. Rani et al. [73] for boron doped graphene. For this reason, we ensured that no two Be atoms were substituted for carbon atoms in the same hexagonal ring for all the doped graphene sheets considered so as not to alter severely the structural property of the system relative to pristine graphene.

The analysis of the electronic properties shows that the energy gap of the systems increases with increase in impurities concentrations. N-doped graphene was found to have a minimum band-gap of 0.21 eV at 3.13% and a maximum band-gap of 0.60 eV at 12.50% impurity concentration. Moreover, for this system due to the electron-rich trait of an N atom compared to the resident carbon atom, the Fermi level of the band structures moves noticeably above the Dirac point revealing the n-type semiconducting materials. However, for the Be-doped graphene, a minimum energy band-gap of 0.44 eV (0.54 eV at the level of HSE06) at 3.13% and a maximum band-gap of 1.41 eV (1.64 eV with HSE06) at 12.50% impurity concentration were observed. As a result of the electron deficiency in the Be in relation to carbon, the Fermi level of the system moves below the Dirac point showing that Be-doped graphene is a p-type semiconductor. For more detail about the trend of the results, the summary of the results is shown in Table 1. The result is consistent with previous similar studies as indicated in Table 1. However, we observed that Y. Fujimoto et al. [74] realised a significant lower  $E_{form}$  for N-doped graphene at an impurity concentration of 3.13%. The discrepancy between their result and ours' might be attributed to Local Density Approximation (LDA) that was employed in their calculation. LDA is known to over bind. The result of the formation energy ( $E_{form}$ ) of a doped system can be used to analyse the stability and viability for synthesis. We found that  $E_{form}$  of the doped graphene systems under investigation increases with increase in the impurity concentration of the systems. For example, N-doped graphene was found to have a minimum  $E_{form}$  of 0.86 eV at 3.13% and 4.39 eV as maximum  $E_{form}$  at 12.50%, while Be-doped graphene has minimum  $E_{form}$  of 5.79 eV at 3.13% and maximum  $E_{form}$  of 25.56 eV at 12.50% impurity concentration. A high value of

$E_{form}$  shows that the corresponding system is less favourable to be synthesised. Consequently, the high  $E_{form}$  of Be-doped graphene could be the reason why Be-doped graphene is yet to be synthesised. Whereas for N-doped graphene with a relatively low  $E_{form}$ , the synthesis has already been reported in the literature [75,76].

### 3.2. Beryllium and nitrogen co-doped graphene

Furthermore, the effect of Be-N co-doping on the electronic properties of graphene was studied. An increasing amount of equal proportion of Be and N impurities was substituted for the carbon atoms at different atomic sites within the graphene host system. As such, the following impurities concentrations of Be and N pairs in graphene were considered; i.e. 6.25% (a pair of Be-N), 12.5% (two pairs of Be-N), 18.75% (three pairs of Be-N) and 25% (four pairs of Be-N) in a  $4 \times 4$  pristine graphene supercell. At each impurity concentration, different configurations of the dopants in graphene were explored in order to obtain the energetically favourable system which shares closest lattice structure as pristine graphene. For the sake of brevity, only stable systems with impurities concentration dependent band-gap have been reported as illustrated in Fig. 4. Other configurations explored and their corresponding formation energy can be found in the supplementary information.

It was observed that for the Be-N co-doped graphene, N (red) and Be (blue) coexisting as the nearest neighbours (shown in Fig. 4), is energetically the most favourable configuration among other configurations considered in this study. The physical origin of the preferred configuration might be attributed to the formation of an ionic bonding between the co-dopants when they are placed adjacent to each other. This perhaps is responsible for the increase in the stability of the co-doped system.

The C–C preference as suitable sites for N and Be substitution in graphene has also been reported in recent studies [68,77] to be an ideal choice for certain classes of dual doped graphene. Thus far, the only concession to the proposed scheme is Si-B and Ge-B dual doped graphene. It is interesting to note that this pattern of co-doping of graphene with Be-N along with the optimized stability such that the band-gap of the system varies with the impurity concentration was not reported in previous studies done by Husain et al. [78] in which they stated that increasing the Be-N concentration in graphene resulted in a decrease in the band-gap of the system. However, it has been successfully demonstrated in the present study that based on the proposed nearest-neighbours configuration adopted, the band-gap of Be-N co-doped graphene increases with increase in impurities concentration. The as-obtained results provide an avenue to tailor the band-gap of the resulting nanostructure for a specific application. From the band structure as well as DOS calculations (also displayed in Fig. 4), a minimum energy gap of 0.54 eV (HSE) at 6.25% impurity concentration was realised while a maximum gap of 1.88 eV (HSE) at 25.0% impurity concentration was attained. Table 2 gives the summary of the result. Another significant observation is that, due to the electron-deficient trait of the Be-N pairs in graphene, the Fermi level of the resulting system crosses the valence bands. Inferably, this implies that the electronic character of Be-N co-doped graphene is p-type as against the semi-metallic trait exhibited by pristine graphene.

The analysis of the  $E_{form}$  of this system as seeing from Table 2 shows that it increases with the pairs of Be and N impurities concentration. For instance, the system has a minimum  $E_{form}$  of 3.05 eV at 6.25% concentration while 13.54 eV was the maximum  $E_{form}$  at 25.0%. The increasing value of the  $E_{form}$  of Be-N co-doped graphene with the impurities concentration shows the decreasing stability and tendency of synthesizing this system at a high concentration. Interestingly, we found that the  $E_{form}$  of  $\text{Be}_x\text{N}_x\text{G}$  at a

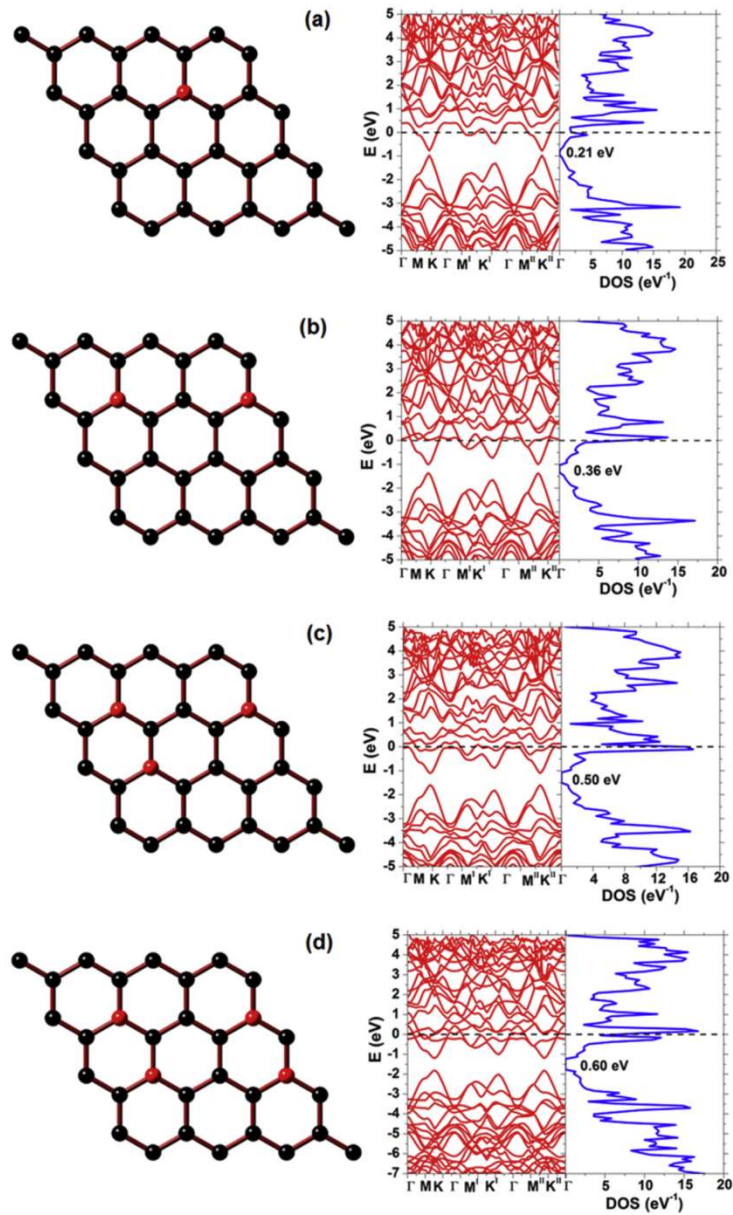


**Fig. 2.** The optimized geometry of N-doped graphene and the calculated band structure and DOS of N-doped graphene at different impurity concentrations: (a) 3.13% impurity concentration, (b) 6.25% impurity concentration, (c) 9.38% impurity concentration, and (d) 12.50% impurity concentration. The red spheres indicate N-atoms while the black spheres represent the C-atoms. (For interpretation of the references to colour in this figure legend, the reader is referred to the Web version of this article.)

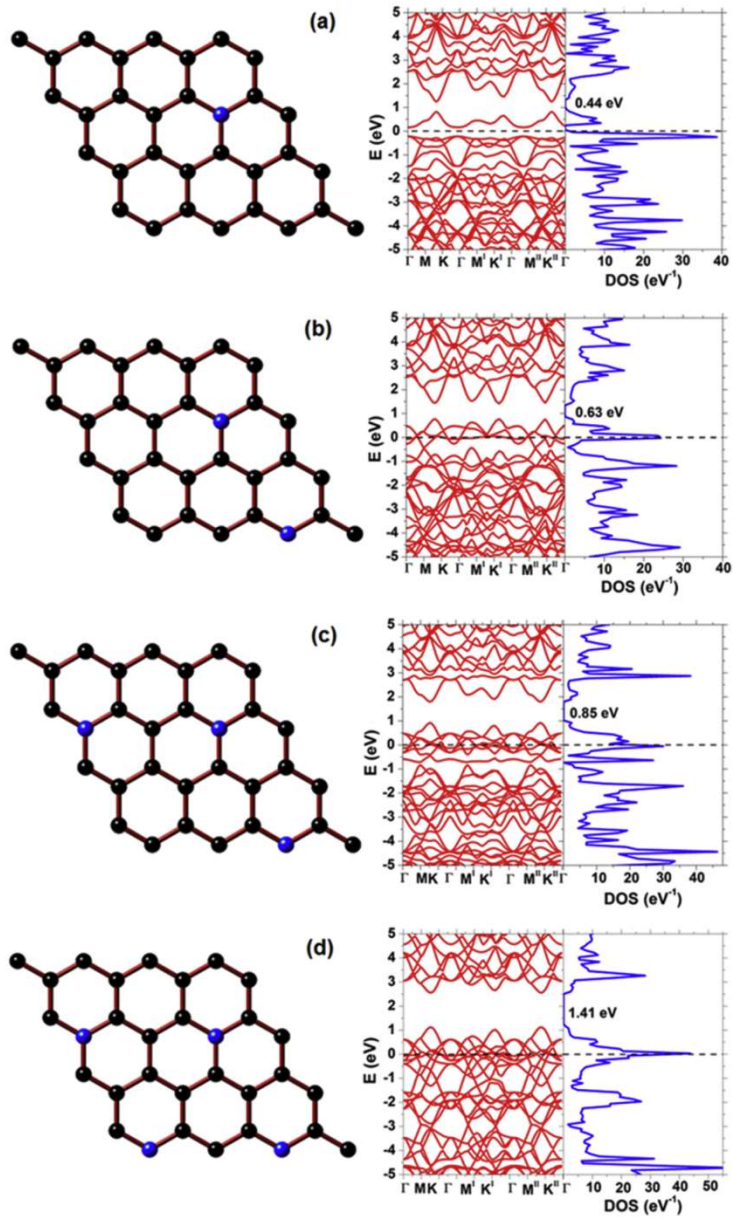


**Fig. 3.** The optimized geometry of Be-doped graphene isomers and the calculated band structure and DOS of Be-doped graphene at different impurities concentration: (a) 3.13% impurity concentration, (b) 6.25% impurity concentration, (c) 9.38% impurity concentration, and (d) 12.50% impurity concentration. The blue spheres indicate Be-atoms while the black spheres represent C-atoms. (For interpretation of the references to colour in this figure legend, the reader is referred to the Web version of this article.)

**Table 1**  
Formation energies and band-gaps of Be-doped and N-doped graphene with variable impurity concentration.

System	Impurity concentration (%)	Band-gap (eV) (GGA)	Reference	$E_{form}$ (eV)	
N-doped Graphene	3.13	0.21	Present work	0.86	
		-	[74]	0.32	
	6.25	0.21	[32]	-	
		0.36	Present work	1.94	
	9.34	0.37	[32]	-	
		0.50	Present work	3.18	
	12.50	0.49	[32]	-	
		0.60	Present work	4.39	
	Be-doped Graphene	3.13	0.61	[32]	-
			0.44	Present work	5.79
6.25		0.46	[64]	-	
		0.63	Present work	11.63	
9.34		0.60	[64]	-	
		0.85	Present work	18.10	
12.50		0.87	[64]	-	
		1.41	Present work	25.56	
		1.44	[64]	-	

given impurity concentration is lower than that of  $Be_xG$  at the same concentration. For example, the  $Be_xG$  system has  $E_{form}$  of 11.63 eV and 25.56 eV at 6.25% and 12.50% impurity concentration respectively, whereas formation energies of 3.05 eV and 6.25 eV were recorded at same concentrations for the  $Be_xN_xG$  system. Thus, these results of the  $E_{form}$  suggest that it is more viable to synthesise  $Be_xN_xG$  than to synthesise  $Be_xG$ . In other words, the results of this study suggest that it could be realistically easy to synthesise a p-type graphene semiconductor through Be-N co-doping than just Be-doping of the system.

Meanwhile, we would like to point out that all the doped systems investigated in this study are heavily doped. As a result, the Fermi level crosses the valence band for the cases of  $Be_xN_xG$  and  $Be_xG$  system, and conduction band in the case of  $N_xG$ . The position of the Fermi level shows that these systems also exhibit metallicity besides the semiconducting character. Thus, this class of materials is called the degenerate semiconductors. Indium tin oxide (ITO) and copper chalcogenides, known to be n-type and p-type respectively, are other examples of degenerate semiconductors.

Furthermore, the lower  $E_{form}$  of  $Be_xN_xG$  as compared to  $Be_xG$  at a given impurity concentration spurred us to investigate the lattice vibrational modes of the two systems to ascertain which one is stable under normal conditions. In this study, harmonic approximation—where all the oscillators in a given system vibrate with fixed frequencies—was considered. Before calculating the phonon dispersion curves of  $Be_xN_xG$  and  $Be_xG$  system, we first validated our computational method by trying to reproduce the phonon dispersion curve of graphene which has previously been reported through experimental [79] and computational study [80]. To calculate the phonon dispersion curve of graphene, a  $1 \times 1$  supercell with two carbon atoms which correspond to six phonon modes (i.e. three acoustic and three optical branches) was considered. The result of our calculation for a monolayer graphene is shown in Fig. 5

LO, TO and ZO at the upper part of Fig. 5 are called the longitudinal, transverse and optical branch while LA, TA and ZA are the corresponding acoustic branches. The phonon spectrum described above is in excellent agreement with the experimental study by Yanagisawa et al. [79] and the theoretical report by Mounet and Marzari [80] as demonstrated in Table 3. Thus, the agreement between the result of this study and the existing experiment data validates our computational method. Consequently, the method was extended to compute the phonon dispersion curves of  $Be_xN_xG$  and  $Be_xG$ . To investigate the stability of the two systems, two  $2 \times 2$  supercells of graphene which corresponds to 8 atoms per unit cell

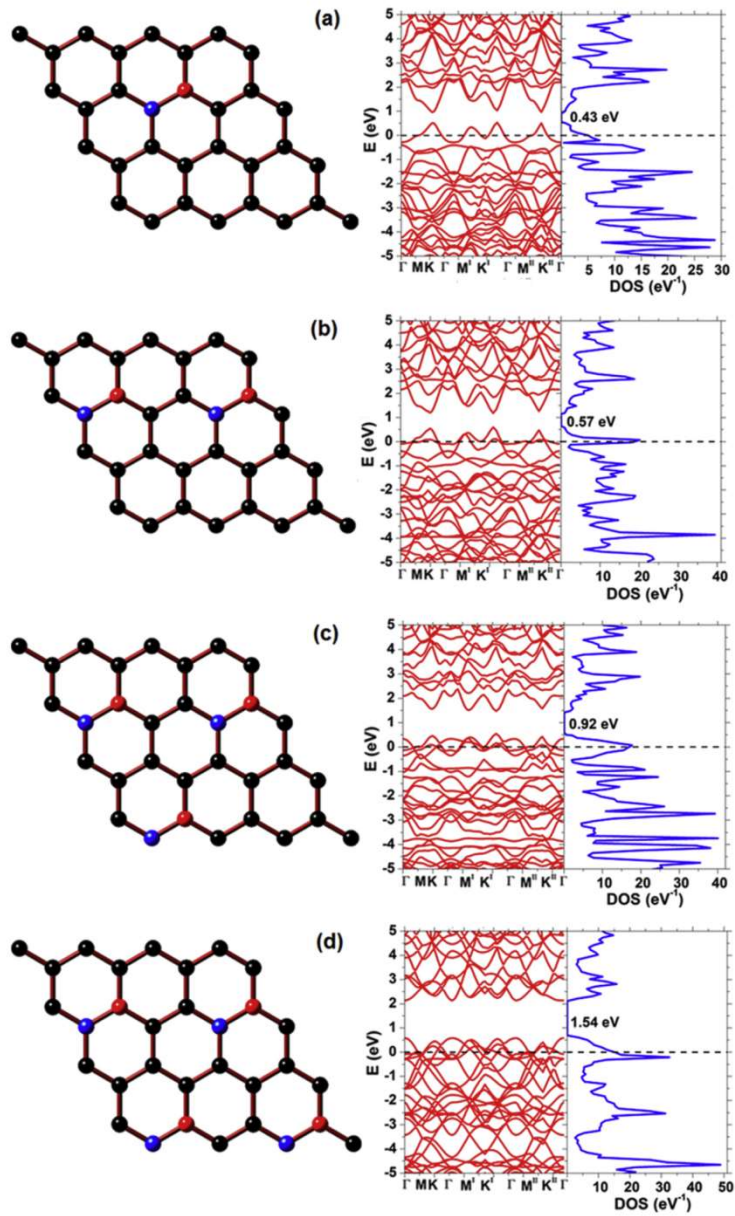
were considered. In the first supercell, two carbon atoms of graphene with C→C conformation were simultaneously substituted for Be and N-atom such that the resulting nanostructure forms Be-N co-doped graphene with 25% impurity concentration. However, in the second supercell, a carbon atom was replaced for a Be-atom to form a system with 12.5% impurity concentration. The two doped systems were geometrically relaxed until the Hellmann-Feynman forces on the atoms converged just below  $0.002 \text{ eV } \text{Å}^{-1}$ . Fig. 6 (a) and (b) show the corresponding dispersion curves of the two systems.

Fig. 6(a) is the phonon dispersion curves of  $Be_xN_xG$  with 25% impurity concentration. All the frequencies are positive; as a result,  $Be_xN_xG$  with 25% impurity concentration is stable. However, the dispersion curve of  $Be_xG$  with 12.5% impurity concentration has imaginary frequencies of (see Fig. 6(b)). This shows that the system is not stable at this concentration. The result confirms the reason why the system is yet to be synthesised at that concentration of impurity under normal conditions. It is quite necessary to point out that the results of the phonon spectral of the two systems are in agreement with their corresponding energy of formation. That is, the  $E_{form}$  of  $Be_xN_xG$  with 25% impurity concentration is significantly lower than that of  $Be_xG$  with 12.5% impurity concentration (see Table 2).

Interestingly, following the work of Zhou et al. [81] the stability of Be-doped graphene could also be established such that all the phonon frequencies of the system would be positive. Zhou and co-workers demonstrated that by applying appropriate tensile strain along with carriers doping, a doped graphene which original was unstable could be stabilized. Thus, in the next section it is assumed that  $Be_xG$  have been stabilized with an application of tensile strain and charges in accordance to Zhou et al. [81] As a result optical properties of  $Be_xG$ -up to 12.5% impurity concentration—can be discussed.

### 3.3. Optical properties

It has been exemplified from the electronic structure calculations that doping of graphene with Be, N or Be-N atomic pairs modifies the electronic properties. Consequently, the changes in the electronic properties of the resulting systems as a result of doping are expected to lead to the alteration of the optical properties of graphene. Fig. 7(a) illustrates the real ( $\epsilon_1$ ) and the imaginary part ( $\epsilon_2$ ) of the dielectric function of pristine graphene systems respectively, expressed in the long wavelength limit as a function of frequency under parallel ( $E_{||}$ ) and perpendicular ( $E_{\perp}$ )

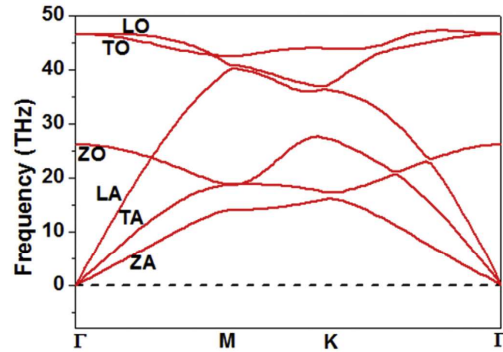


**Fig. 4.** The optimized geometry of Be-N (blue and red spheres) co-doped graphene and the calculated band structure and DOS of Be-N co-doped graphene at different impurities concentrations: (a) 6.25% impurity concentration, (b) 12.50% impurity concentration, (c) 18.75% impurity concentration, and (d) 25.0% impurity concentration. (For interpretation of the references to colour in this figure legend, the reader is referred to the Web version of this article.)

**Table 2**

Formation energies and band-gaps of Be-doped and BeN-doped graphene with variable impurity concentration. The band-gaps were estimated at the levels of GGA and HSE06.

System	Impurity conc.(%)	Band-gap (eV)		$E_{form}$ (eV)	System	Impurity conc.(%)	Band-gap (eV)		$E_{form}$ (eV)
		GGA	HSE06				GGA	HSE06	
Be <sub>x</sub> G	3.13	0.44	0.54	5.79	Be <sub>x</sub> N <sub>x</sub> G	6.25	0.43	0.54	3.05
	6.25	0.63	0.78	11.63		12.50	0.57	0.71	6.25
	9.34	6.25	1.00	18.10		18.75	0.92	1.19	9.71
	12.50	1.41	1.64	25.56		25.00	1.54	1.88	13.54

**Fig. 5.** Phonon dispersion curve of pristine graphene. ZA (ZO), TA (TO) and LA (LO) are in that order the out-of-plane acoustical, transversal and longitudinal (optical) branches.**Table 3**

Computed phonon frequencies at high symmetry points in the Brillouin zone

High symmetry point	This study	Computational	experimental
	GGA-PBE(THz)	Ref. 80 (THz)	Ref. 79 (THz)
$\Gamma_{ZO}$	26.14	26.41	26.02
$\Gamma_{LO}$	46.57	46.58	47.36
$\Gamma_{TO}$	46.57	46.58	47.36
$M_{ZA}$	13.78	14.12	13.52
$M_{TA}$	18.63	18.76	
$M_{LA}$	39.70	39.81	39.81
$M_{ZO}$	19.02	19.03	19.03
$M_{LO}$	40.80	40.17	39.66
$M_{TO}$	41.69	41.67	41.67
$K_{ZA}$	16.01	16.03	15.49
$K_{ZO}$	17.30	16.03	17.62
$K_{TA}$	29.77	29.88	
$K_{LA}$	36.32	36.36	36.36
$K_{LO}$	37.07	36.36	38.61
$K_{TO}$	41.32	38.61	38.61

polarization of electromagnetic waves. Moreover, the imaginary part of the dielectric function is related to the absorption spectrum of graphene (see equation (11)). It is worth reiterating that these theoretical curves do not incorporate the Drude term in the formulation. The Drude term is a phenomenological avenue to express intraband transition which is prevalent at low energies. Due to the lack of the Drude term in our theory, only the spectra peaks of Fig. 7(a) that correspond to a frequency energy of above 1.0 eV have been discussed. This is because, below this stated energy value, the Drude term applicability becomes relevant whereas above this value the intraband contribution is less significant. In view of the above approximation, the imaginary part  $\epsilon_2$  in Fig. 7(a) has two prominent peaks at 4.0 eV and 13.8 eV for  $E_{||}$  polarization.

These two peaks' positions, which are in good agreement with the results of Sedelnikova et al. [82] and M. Houmad et al. [41], are highlighted as X and Y. The origin of the peak X could be ascribed to  $\pi \rightarrow \pi^*$  transitions along the M–K direction in the neighbourhood of M in the  $\Gamma$ –M direction (see Fig. 1). The intense resonance at Y could be attributed to  $\sigma \rightarrow \sigma^*$  transitions around the M point in the direction of both  $\Gamma$ –M and M–K of the Brillouin zone. However, for the  $E_{\perp}$  polarization, the selection rules only sanction  $\pi \rightarrow \sigma^*$  and  $\sigma \rightarrow \pi^*$  transitions in graphene. Consequently, the observed peaks at 11.1 eV and 14.5 eV are due to  $\pi \rightarrow \sigma^*$  and  $\sigma \rightarrow \pi^*$  interband transition under  $E_{\perp}$  polarization.

Following the analysis of the optical property of pristine graphene, the change in the intensity and position of the imaginary part of the dielectric function,  $\epsilon_2$  of the doped systems around a particular energy frequency as a result of substitutional doping of graphene with impurities (Be, N and Be-N) have been investigated. The imaginary part of the dielectric function of Be<sub>x</sub>G, N<sub>x</sub>G and Be<sub>x</sub>N<sub>x</sub>G with respect to pristine graphene is plotted in Fig. 7(b)–(d). From the graphs, it is observed that the intensity of  $\epsilon_2$  of graphene responds to doping concentration differently across the EM spectrum with respect to the anisotropic signature of the system.

Under parallel polarization, for instance, it is found that the intensity of  $\epsilon_2$  of N<sub>x</sub>G, Be<sub>x</sub>G, and Be<sub>x</sub>N<sub>x</sub>G systems around 4.0 eV and 14.5 eV is lower than that of pristine graphene regardless of the impurities concentration of the doped systems (see Fig. 7(b)–(d)); it is independent of the impurities modulation within the interval of 6.0 eV–9.0 eV and approaches zero in that region of the EM spectrum. However, around 4.0 eV, it is well resolved with respect to the impurities concentration. That is, the intensity of  $\epsilon_2$  of the doped systems is observed to decrease with an increase in their corresponding impurity concentration in the neighbourhood of 4.0 eV whereas around 14.0 eV, it gets broadened as a function of the amount of the dopants in the graphene (see the red arrows in Fig. 7(b)–(d)).

Around 14.0 eV, at a high impurity concentration, the maximum peak of  $\epsilon_2$  is observed to be red-shifted relative to that of pristine graphene whereas around 4.0 eV it is blue-shifted. However, under  $E_{\perp}$  polarization, it is observed that doping does not have a significant effect on  $\epsilon_2$  of graphene (results not shown here). This is because, as rightly pointed by Marinopoulos et al. [83], under this polarization, the absorption spectrum of the system is not exclusively determined by the band structure but by the local field effects which are not taken into consideration in this calculation. With the understanding that other optical quantities like refractive index, reflectivity, absorption, and loss function of a system can be derived from the dielectric function, subsequent discussion is done to elucidate the effects of Be and N on the optical properties of graphene.

### 3.3.1. Refractive index $n(\omega)$ and reflectivity $R(\omega)$

For all the systems investigated in this study, the real  $n(\omega)$  and the imaginary  $k(\omega)$  part of the refractive index were calculated at normal incidence through equation (8) and (9). Fig. 8(a) illustrates typical  $n(\omega)$  spectra of the pristine graphene for parallel ( $E_{||}$ ) and

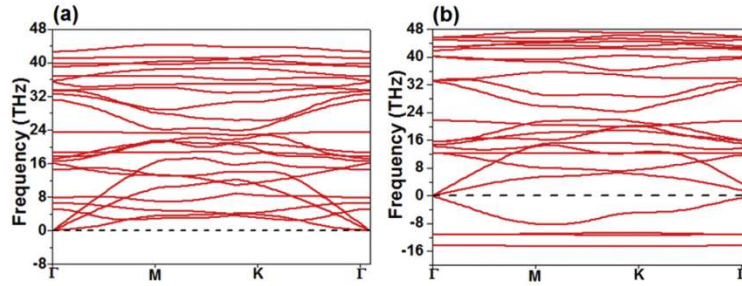


Fig. 6. Illustrates phonon dispersion of graphene doped with (a) Be and N at 25% impurity concentration and (b) Be at 12.5% impurity concentration respectively.

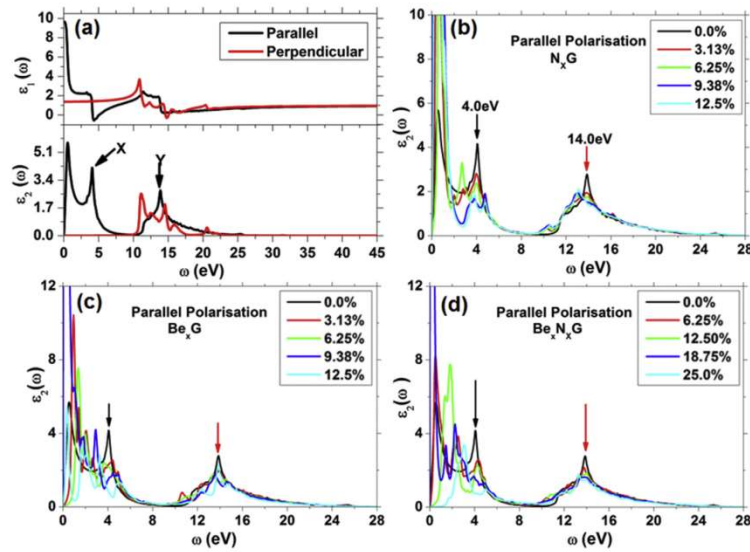


Fig. 7. (a) The real ( $\epsilon_1$ ) and the imaginary part ( $\epsilon_2$ ) of the dielectric function of pristine graphene for both  $E_{||}$  (black line) and  $E_{\perp}$  (red line) polarized field vector. The variation of  $\epsilon_2$  of (b) N<sub>x</sub>G, (c) Be<sub>x</sub>G, and (d) Be<sub>x</sub>N<sub>x</sub>G with impurity concentration for parallel polarization. In (b) and (c) the black, red, green, blue and cyan curves correspond to  $\epsilon_2$  spectra of pristine graphene, N-doped and Be-doped graphene at 3.13%, 6.25%, 9.38% and 12.5% impurity concentrations respectively. Whereas in (d) the black, red, green, blue and cyan curve correspond to  $\epsilon_2$  spectra of pristine graphene and Be-N co-doped graphene at 6.25%, 12.5%, 18.75% and 25.0% impurity concentrations respectively. For the arrows, the black and red colours indicate in turn the peak positions at 4.0 and 14.0 eV. (For interpretation of the references to colour in this figure legend, the reader is referred to the Web version of this article.)

perpendicular polarization ( $E_{\perp}$ ) of electromagnetic waves. With  $E_{||}$ ,  $n(\omega)$  spectra has two major peaks at 4.0 and 11.4 eV which correspond to the peak intensities of 1.7 and 1.6 respectively. However, for  $E_{\perp}$  polarization a value of 1.97 at a frequency of 10.89 eV was observed. The occurrence of peaks in the spectra is a strong indication of the maximum value of the refractive index at that optical frequency. The profile of these spectra with respect to the two polarizations agrees with the earlier report by P. Rani et al. [33]

As the impurities of the doped system increase, however, both the height of the peaks and their position changed slightly. The refractive index of each of the doped systems drops below 1.97 (associated with pristine graphene) for  $E_{\perp}$  polarization and their corresponding frequency falls within 10.59–11.40 eV spectrum region of EM (see Fig. 8(b)–(d)). Under  $E_{\perp}$  polarization, for the NG

and Be<sub>x</sub>N<sub>x</sub>G doped systems, a clear trend of the effect of the impurities concentration on  $n(\omega)$  was noticeable. That is, the magnitude of the maximum value of the refractive index ( $n_{\max}(\omega)$ ) of the N<sub>x</sub>G and Be<sub>x</sub>N<sub>x</sub>G systems decreases with increase in the impurities concentration, as shown in Fig. 8(e). Specifically, the  $n_{\max}(\omega)$  of the NG system was recorded as 1.76 at 3.13% while at 12.5% impurity concentration a value of 1.61 was obtained. Similarly, at 6.25%, the  $n_{\max}(\omega)$  of Be<sub>x</sub>N<sub>x</sub>G system has a value of 1.83 whereas at 25% impurity concentration a decreased value of 1.68 was realised (see Fig. 8(e)). For Be<sub>x</sub>G system, however, the response of the  $n_{\max}(\omega)$  to modulation in impurity concentration does follow decreasing-rising order. It decreased with an increased impurity concentration from 3.13% to 9.38% and then further increased at 12.5%. (Fig. 8(e)).



With regards to the  $E_{\parallel}$  polarization,  $n(\omega)$  spectra of the doped systems have two major peaks. As the impurity concentration increases, first set of peaks are redshifted relative to 4.0 eV while the second group of peaks are blueshifted with respect to (w.r.t) 11.4 eV (see Fig. 8 (b)→(d)). Within the starting frequencies window of 4.0 eV it can be seen from Fig. 8(f) that the  $n_{\max}(\omega)$  of the  $N_xG$  increases almost linearly with an increase in impurity concentration whereas the  $Be_xG$  and  $Be_xN_xG$ → apart from showing fluctuating trend with impurity concentration→ the systems have a unique maximum at 6.25% and 18.75% impurity concentration respectively. However, at a higher frequency of around 11.4 eV,  $n_{\max}(\omega)$  of the doped systems decrease with an increase in their corresponding impurity concentration, and show increasing tendency at a very high impurity concentration (see the second panel of Fig. 8(f)).

The reflectivity  $R(\omega)$  of all the systems investigated in this study were also calculated at normal incidence, in the long wavelength limit, using equation (10) with the values of the refractive indices of the systems within the frequency range of ~0–45 eV for both parallel and perpendicular polarization of the vector field. Fig. 9(a) graphically illustrates the reflection spectrum of pristine graphene. From the spectrum, with  $E_{\parallel}$  polarization (red spectra), the pristine graphene is seen to have a maximum reflectivity intensity,  $R_{\max}(\omega)$  of 0.28 around a frequency of 4.3 eV which is located in the UV regime. The peak position due to this polarization is in agreement with the result of M. Houmad et al. [41]. Having weaker intensity than the peak at 4.3 eV, there is also a weak intensity peak of the system at 14.0 eV due to the same polarization (Fig. 9(a)). Moreover, the coefficient values of 0.1 in the visible region of the EM spectrum and a nearly zero value in the interval of 7.5–10.0 eV have been observed in the reflectivity spectrum of the system with respect to the  $E_{\parallel}$  polarization. This observation is consistent with the report of P. Rani et al. [33]. However, with  $E_{\perp}$  polarization,  $R_{\max}(\omega)$  of the system is observed at 14.9 eV with an intensity value of 0.26. It is worth stating that similar vanishing reflectivity spectra within the window of 7.5–10.0 eV found in graphene has also been observed for the  $N_xG$ ,  $Be_xG$  and  $Be_xN_xG$  systems (see Fig. 9(b)–(d)).

As a result of the doping of graphene with impurities, specifically, N-atoms, the intensities and the positions of the reflectivity spectra peaks of graphene are noticeably modified with respect to the original peaks frequency energies at 4.3 eV and 14.0 eV. Fig. 9(b) depicts the reflectivity spectra of  $N_xG$  systems at different nitrogen atoms concentrations. From the figure, for  $E_{\parallel}$  polarization, it is observed that the reflectivity peaks of the systems near the frequency values of 4.3 eV and 14.0 eV (the positions of the most prominent peaks of graphene) decrease with an increase in the number of N atoms of  $N_xG$  systems (see Fig. 9(e)). However, at 12.5% N concentration, the peak of the system at some point close to 14.0 eV frequency shows an increasing tendency (Fig. 9(e)). It is fascinating to note that for most of  $N_xG$  systems investigated, the typical reflectivity peak observed near 4.3 eV is often blue-shifted relative to the typical position in the pristine graphene for the same polarization of the vector field. The only deviation from this above trend occurred when the proportion of N to C in graphene is 2:32. In that case, the reflectivity peak of the system near 4.3 eV is red-shifted with respect to that of pristine (Fig. 9(b)).

Fig. 9(c) illustrates the reflectivity spectra of  $Be_xG$  systems with different Be concentrations of 3.13, 6.25, 9.38, and 12.5% for parallel polarization of the vector field. The following description elucidates the effects of Be-doping around 4.3 eV and 14.0 eV, the reflectivity peak positions of graphene under  $E_{\parallel}$  polarization. Within the frequency interval of 7.5–10.0 eV, regardless of Be concentration in  $Be_xG$ , it is observed that the intensity of the reflectivity spectra of  $Be_xG$  systems approaches zero, and shows decreasing trend with the increase in the Be concentration at 4.3 eV except at 9.38% where

it exhibits a slightly increasing propensity. Moreover, at approximately 14.0 eV there is no significant change in the intensity of the peaks of the system due to the increase in Be concentration (see Fig. 9(c)). In general, the intensity of the reflectivity peak of  $Be_xG$  in the neighbourhood of 14.0 eV, regardless of the Be concentration, is less than that of pristine graphene for  $E_{\parallel}$  polarization.

For  $Be_xN_xG$  systems with  $E_{\parallel}$  polarization, while there are no substantial changes in the intensity of the reflectivity peaks near 14.0 eV (see the black arrow in Fig. 9(d)), it is found to diminish around 4.3 eV (see the red arrow in Fig. 9(d)), and slightly blue-shifted relative to the corresponding position in pristine graphene as the impurity concentration in the system increases.

Furthermore, with  $E_{\perp}$  polarization, the intensity of  $R_{\max}$  of  $N_xG$  in the neighbourhood of 11.0 eV remains almost unchanged with respect to that of pristine graphene, whereas at around 14.9 eV, it is observed to drop almost linearly with the increase in nitrogen concentration. (see Fig. 10(a) and (b)). As for the  $Be_xG$  systems, close to 12.4 eV, the intensity of the reflectivity peak spectra increases with increase in Be concentration whereas at 16.0 eV it decreases with the increase of the impurity concentrations (Fig. 10(c)). In addition, we found that the position of the  $Be_xG$  reflectivity peak at 16.0 eV is blue-shifted in relation to the corresponding position in pristine graphene for  $E_{\perp}$  polarization. For  $Be_xN_xG$  systems (Fig. 10(d)), it is observed that the reflectivity peaks at 11.1 eV and 16.3 eV decreases with increase in Be-N atomic concentration, while at 12.8 eV it increases with the impurities concentration. It is worth noting that a unique maximum of reflectivity coefficient is induced in the system at 11.1 eV when the pairs of Be and N concentration in the system is approximately 6.25%.

### 3.3.2. Electron Energy Loss Spectra (EELS) of the systems

To investigate the effect of impurities concentrations on plasmons oscillation in graphene, we have worked out the EELS of  $N_xG$ ,  $Be_xG$  and  $Be_xN_xG$  systems using equation (12) for both  $E_{\parallel}$  and  $E_{\perp}$  polarization. Fig. 11(a) shows EELS profile of pristine graphene. From the figure, two noticeable EELS peaks have been observed, one at 5.5 eV with the peak height of 1.40, the other one with a broader peak (though not smooth) lies within 15.7–17 eV and corresponds to a peak height of 1.3 for the  $E_{\parallel}$  polarization. However, for the  $E_{\perp}$  polarization, two dominant but very close peaks have been observed at 15.1 eV and 16.6 eV which in turn correspond to peak heights of 2.33 and 1.84 respectively. The occurrence of these peaks could be attributed to the  $\pi$  and  $(\pi+\sigma)$  plasmons for  $E_{\parallel}$  polarization, while out of plane plasmons peaks could be attributed to the transition between occupied  $\pi$  and unoccupied  $\pi^*$  bands. In general, the overall profile of this spectrum, i.e. the peak positions, the intensity as well as the line shape agree with the available experimental results [84,85] and previous all-electron calculations [83] where local-field-effect (LFE) was not taken into consideration. For monolayer graphene, the experimental peaks as observed by Eberlein et al. [84] were located at 4.7 eV and 14.6 eV. The inconsistency between the present simulation results and those from experiments is in the exact positions of the peaks for  $E_{\parallel}$  polarization. This discrepancy might be as a result of the neglect of the excitonic effect in our calculations.

Following the analysis of pristine graphene, the EELS of the doped graphene systems was investigated. With respect to all the singly doped and co-doped systems considered, it was found that the intensity of the EELS peaks of these systems at 16.6 eV decreases with the increase in the corresponding impurities concentration for the  $E_{\perp}$  polarization (see Fig. 11(b)). This observation is consistent with earlier reports by C. Huang et al. [86] and P. Nath et al. [32]. Fig. 11(b) illustrates the variation of the intensity of  $L(\omega)$  of the  $N_xG$ ,  $Be_xG$  and  $Be_xN_xG$  systems with the corresponding

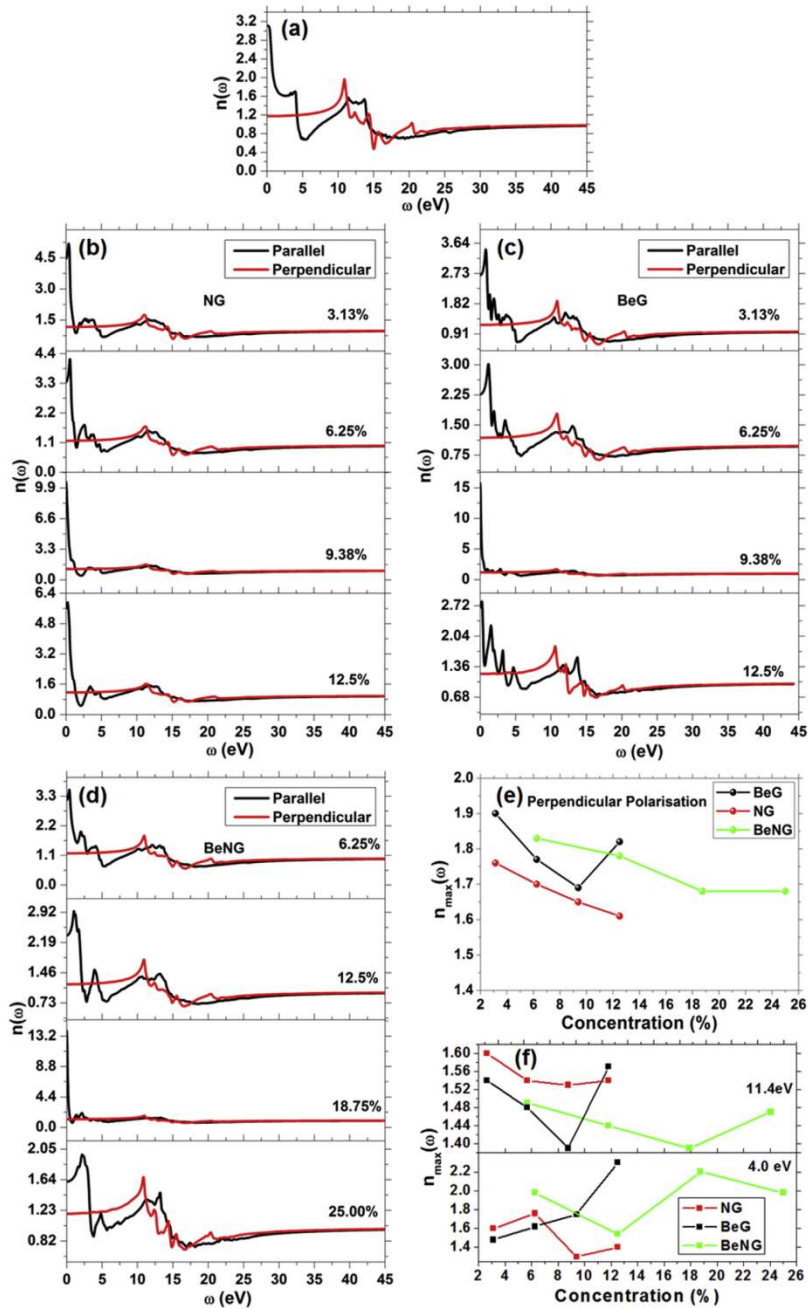


**Fig. 8.** Anisotropic optical properties of pure and doped graphene as a function of frequency for both  $E_{\parallel}$  (black line) and  $E_{\perp}$  (red line) polarized field vector. The real part of refractive index of (a) pristine graphene, (b)  $N_xG$ , (c)  $Be_xG$  and (d)  $Be_xN_xG$  at different impurity concentrations. The variation of  $n_{max}(\omega)$  with dopants concentration in  $N_xG$ ,  $Be_xG$  and  $Be_xN_xG$  with respect to (e)  $E_{\perp}$  and (f)  $E_{\parallel}$  polarization. (For interpretation of the references to colour in this figure legend, the reader is referred to the Web version of this article.)

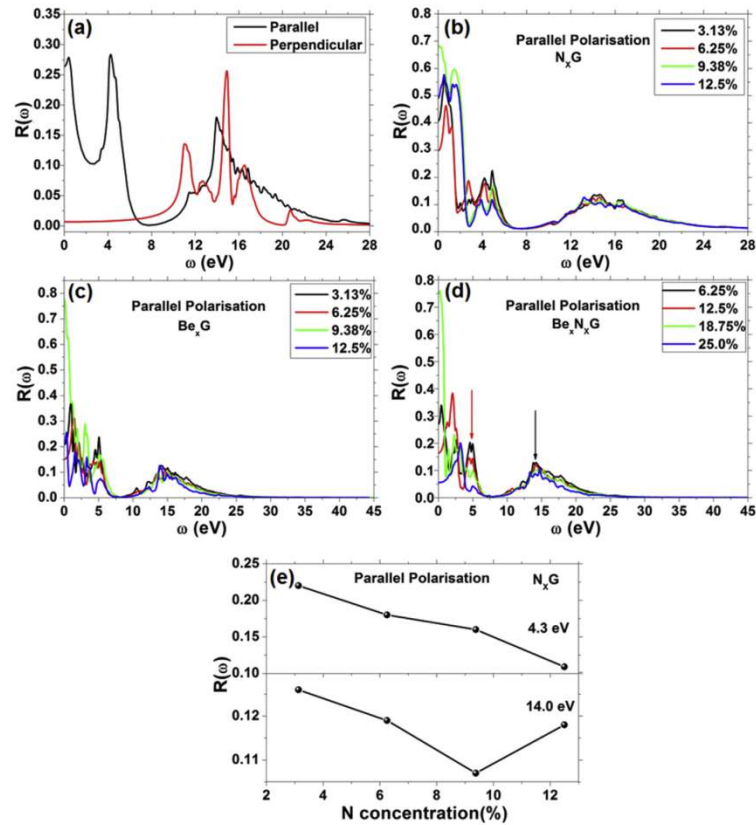


**Fig. 9.** (a) The reflectivity spectra of pristine graphene with  $E_{\perp}$  (red) and  $E_{\parallel}$  (black) polarization. The reflectivity spectra of (b)  $N_xG$ , (c)  $Be_xG$  and (d)  $Be_xN_xG$  systems at different impurity concentrations for  $E_{\parallel}$  polarization. (e) The variation of  $R(\omega)$  peaks of  $N_xG$  systems with N concentrations where 4.3 eV denotes the peaks position under  $E_{\parallel}$  polarization, 14.0 eV represents the second peak position under the same polarization. (For interpretation of the references to colour in this figure legend, the reader is referred to the Web version of this article.)

impurities concentrations. Interestingly, it was observed that the EELS profile of both  $Be_xN_xG$  and  $Be_xG$  systems are similar (see Fig. 11(c) and (d)). At a relatively low impurity concentration of 6.25%, the two systems have two prominent peaks at 15.1 and 16.6 eV which are similar to graphene peaks under  $E_{\perp}$  polarization. However, the peak of the systems at 16.6 eV has a higher intensity than the other at 15.1 eV. This is a case reversal of what is observed in pristine graphene under  $E_{\perp}$  polarization (Fig. 11(a)).

As the percentage of the impurity in  $Be_xG$  and  $Be_xN_xG$  system increases to 12% and 25% respectively, a new EELS peak at <14 eV is formed while the two other previously discussed peaks, which correspond to EELS peaks of graphene at 15.1 eV and 16.6 eV, approach the same intensity (Fig. 11(c) and (d)). Besides, the plasma frequencies of these p-type systems ( $Be_xG$  and  $Be_xN_xG$ ) are red-shifted relative to the 16.6 eV peak observed for pristine graphene, regardless of their impurity concentrations. In the case of  $N_xG$  system (Fig. 11(e)), regardless of the nitrogen concentration, the EELS spectra is similar to that of pristine graphene and the plasma frequency is blue-shifted in relation to the graphene peak at 16.6 eV for  $E_{\perp}$  polarization (Fig. 11(a)). For conciseness only  $N_xG$  at

12.5% N concentration has been shown in Fig. 11(f)). Thus, the as-explained results suggest that one could characterize a doped graphene system as either a p-type or n-type semiconductor if the peak of the EELS profile is red-shifted or blue-shifted relative to the EELS peak of pristine graphene at 16.6 eV under the influence of  $E_{\perp}$  polarization.

With  $E_{\parallel}$  polarization, it has been observed that a new EELS peak emerges around 1.56–2.36 eV when pristine graphene is doped with nitrogen and the intensity of the peak tends to increase with an increase in the impurity concentration (Fig. 12(a)). In Fig. 12(a), the newly formed peak is indicated with a red arrow. The emergence of the new peak is due to an in-plane low energy (1.56–2.36 eV) plasmon excitation which could be ascribed to the presence of extra  $\pi$  electron of nitrogen atoms within the system. The occurrence of an in-plane low energy plasmon excitation due to nitrogen atoms substitution in graphene has also been reported earlier by researchers in Ref. [32]. In the case of the  $Be_xG$  systems (Fig. 12(b)), the in-plane loss function could be analysed with respect to the two regions of the spectrum. The first region, which includes low-frequency region, starts from 0 eV and ends at 10 eV,

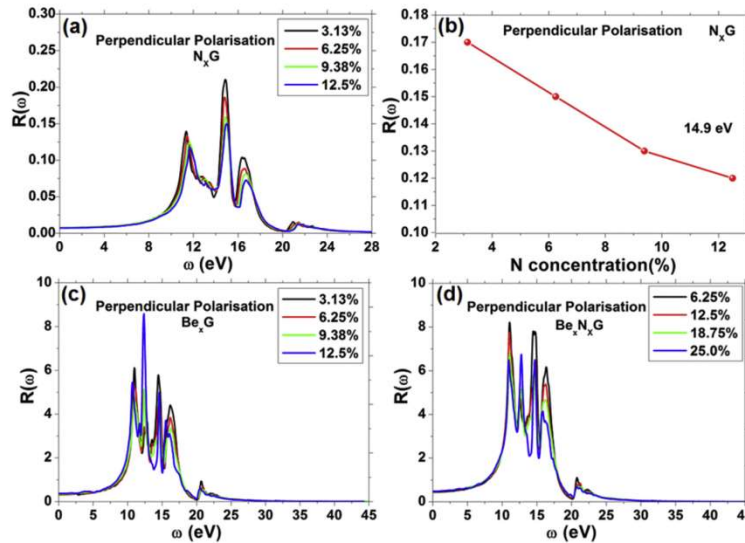


**Fig. 10.** (a) The reflectivity spectra of  $N_xG$  systems at different impurity concentrations for  $E_{\perp}$  polarization, and (b) the corresponding variation of  $R(\omega)$  peaks of  $N_xG$  systems with N concentration, where 14.9 eV is the position of  $R_{\max}(\omega)$  of the systems. The reflectivity spectra of (c)  $Be_xG$  and (d)  $Be_xN_xG$  systems at different impurity concentrations for  $E_{\perp}$  polarization.

while the second region extends beyond 10 eV and has a broader frequency than the first region. A very intense and sharp peak is formed at 5.62 eV, within the first region of the spectrum, when graphene is singly doped with beryllium. As Be concentration increases in the system, the number of distinct EELS peaks, within the first region of the spectrum, also increases (Fig. 12(b)).

It was interesting to observe that the number of the distinct peaks that is formed within the first interval of the spectrum commensurate with the number of Be atoms in  $Be_xG$  system (Fig. 12(b)). However, in the second region of the spectrum, only a single prominent peak is formed regardless of Be concentration in the doped system. The position of the EELS peak in the second region lies within 16.0–17.9 eV for all the  $Be_xG$  systems considered (Fig. 12(b)). Similarly, for  $Be_xN_xG$  systems, the in-plane loss function spectral is subjugated by two regions. The frequency range of each of the region corresponds to that of  $Be_xG$  systems. As the Be-N atomic pairs concentration in graphene increases, the EELS peak intensity in the first region of the spectrum decreases, while the corresponding frequency of the peak is blue-shifted relative to EELS peak of graphene at 5.5 eV for  $E_{\parallel}$  polarization (see Fig. 12(c)). Moreover, the peak of the system in the second region of the spectrum is not affected by the impurities concentration. Nevertheless, the intensity of the peak fluctuates within 1.12–1.36 as the amount of the pairs of Be-N atomic pairs increases in the system through substitution.

### 3.3.3. Absorption spectra of the systems

In Fig. 13(a), the absorption spectrum of pristine graphene has been illustrated, and restricted to the ultra-violet region. The optical absorption spectrum is related to the imaginary part of the dielectric function through equation (11). From the spectrum, it can be seen that pristine graphene has two distinct major peaks at the optical frequencies of 4.14 eV and 14.0 eV under  $E_{\parallel}$  polarization. The first peak at 4.14 eV has a higher intensity than the second peak.

Likewise, with  $E_{\perp}$  polarization, the system is characterized by two absorption peaks; having a wider range of frequency, one of the peaks has multiple spikes of which the dominant one occurs at 14.6 eV, while the second peak with weaker intensity is found at 20.6 eV. These two peaks' positions are in good agreement with the results of [33,86–88].

The change in the position and intensity of the most prominent peaks of graphene as a result of doping could be used to investigate the effect of impurity concentration on the absorption coefficient of the system with respect to  $E_{\parallel}$  and  $E_{\perp}$  polarizations. For example, from the  $N_xG$  spectra in Fig. 13(b), it is observed that the maximum value of the absorption peak  $\alpha_{\max}(\omega)$  decreases and blue-shifted (relative to the position of the most intense absorption peak of graphene, as shown in Fig. 13(b)) as the N-atom concentration increases with respect to the  $E_{\perp}$  polarization. Fig. 13(c) shows the variation of  $\alpha_{\max}(\omega)$  of  $N_xG$  with N-atoms concentration. Similarly, for the  $E_{\parallel}$  polarization, the intensity of the peak of the system also decreases with the increase in nitrogen concentration; however, it shows increasing tendency at a high impurity concentration (Fig. 13(b)). This result is in agreement with [87].

Regarding  $Be_xG$  system (where  $x = 1, 2, 3, 4$ ) there are two major absorption peaks which are similar to that of pristine graphene under  $E_{\perp}$  polarization. Having multiple spikes and a broader frequency (11.0–15.0 eV), the first peak has a higher intensity than the second peak which occurs at 20.5 eV. Following the analysis of the absorption peaks of the system, the effect of the Be concentrations on the prominent spikes of the  $Be_xG$  systems was investigated. At low Be concentration, the third spike emerges as the most prominent absorption peak followed by the first spike which occurs at a lower frequency. As the impurity concentration of the system increases the intensity of the third spike decreases, while that of the second spike intensifies. Fig. 14(a) illustrates changes in the intensities of the spikes of the absorption peaks of the systems with impurity concentration for  $E_{\perp}$  polarization. From the figure, the red

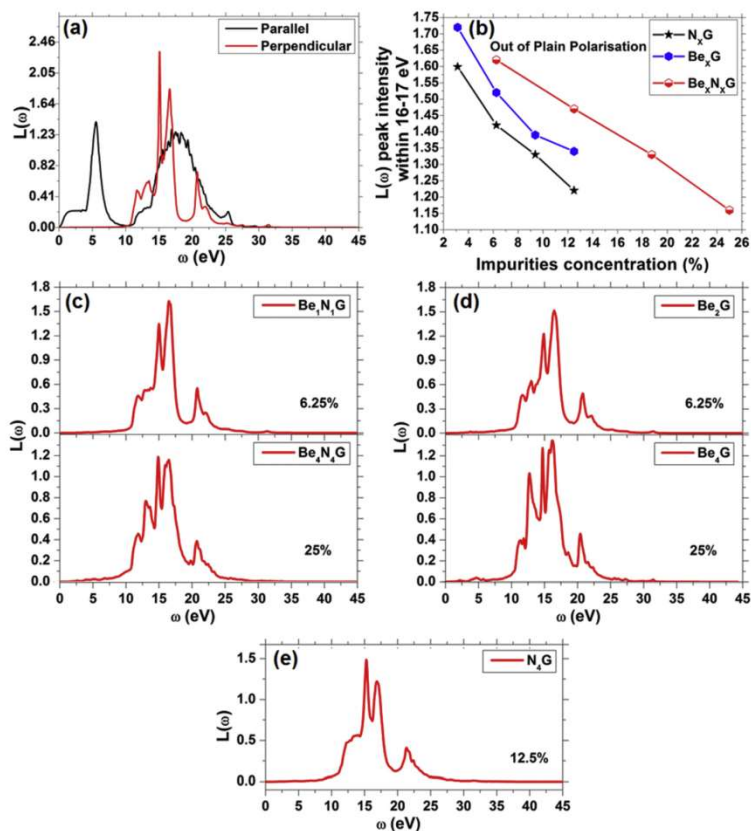


**Fig. 11.** (a) The EELS of pristine graphene with  $E_{\perp}$  (red) and  $E_{\parallel}$  (black) polarization. (b) The variation of EELS peak intensity, within 16.0–17 eV, with doping concentration of Be, N and Be-N pairs in  $N_xG$ ,  $Be_xG$  and  $Be_xN_xG$  systems respectively. (c) and (d) The EELS of both  $Be_xN_xG$  and  $Be_xG$  systems respectively, and (e) The EELS of  $N_xG$  due to perpendicular polarization of EM. (For interpretation of the references to colour in this figure legend, the reader is referred to the Web version of this article.)

and the black arrows comparatively highlight the intensities of the two spikes of the spectrum at different impurity concentrations. More importantly, it is worth mentioning that, at a relatively high Be concentration, the maximum value of the absorption peak of the  $Be_xG$  system is red-shifted with respect to the position of the peak at a low impurity concentration for the  $E_{\perp}$  polarization. However, with the  $E_{\parallel}$  polarization,  $\alpha_{\max}(\omega)$  of the  $Be_xG$  system varies with the impurity concentration in the same manner as does  $N_xG$  system with N-atom concentrations. That is, it decreases with increase in Be concentration although it shows increasing tendency when the impurity concentration is 9.38% (Fig. 14(a)).

For  $Be_xN_xG$  system, as the Be-N concentration increases, the  $\alpha_{\max}(\omega)$  decreases with respect to  $E_{\parallel}$ , whereas for  $E_{\perp}$  polarization it increases (see Fig. 14(b)). In spite of this immediate trend, a maximum unique value of  $\alpha_{\max}(\omega)$  of the system is attained at 6.25% impurities concentration.

It is worth noting that all the doped systems considered in this study, irrespective of the impurity concentrations, have a low value of  $\alpha(\omega)$  in the frequency range of 7.0–10.0 eV. Hence, the  $N_xG$ ,  $Be_xG$  and  $Be_xN_xG$  systems as well as the pristine graphene are

transparent in that frequency window. This is simply because the systems have low reflectivity and absorption coefficient in the frequency interval of 7.0–10.0 eV which falls within ultraviolet region (i.e. 150–175 nm).

#### 4. Proposed applications

Gadgets like smart phones, laptops, flat screen televisions and other household appliances are embedded with touch screens. Due to materials scarcity, raising costs, and together with market demand in the direction of flexible devices, the technological advancement of such devices looks bleak. Traditionally, indium tin oxide (ITO) is the most used transparent conducting materials (TCs). However due to its limited geographical availability (about 160 ppb), susceptibility to conductivity degradation, rising price-indium metal has attained a premium of \$900 per kilogram—there is a need for an ideal replacement for ITO. Despite such limitations, the required properties of TCs—such as low sheet resistance, high optical transparency, conductivity, and stability—found in ITO are difficult to match. Interestingly, graphene is seen as an ideal

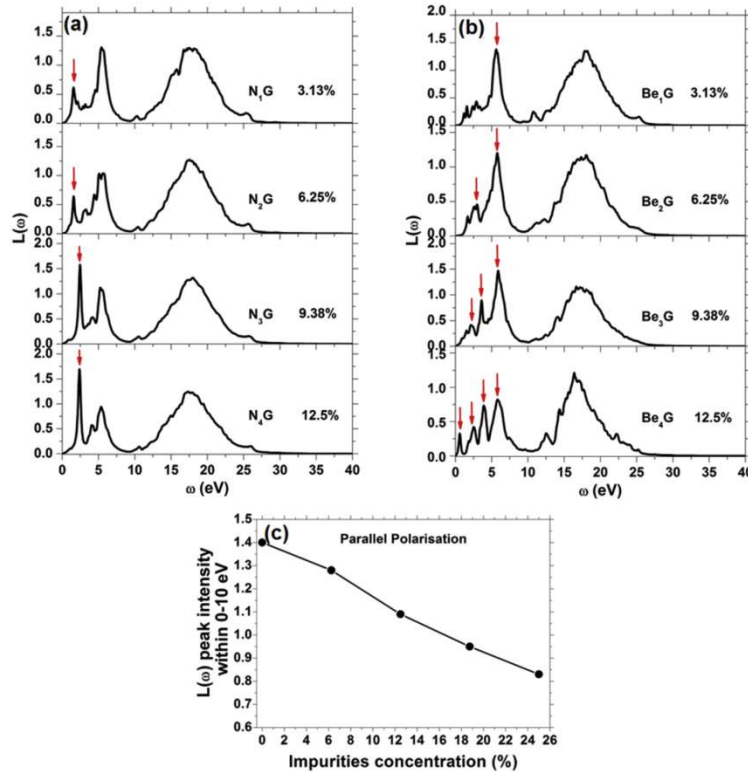


**Fig. 12.** The EELS profile of (a) nitrogen and (b) beryllium doped graphene systems, and the corresponding percentage of the impurity concentration is indicated in each panel. The red arrows point to the new EELS peaks and the number increases with increase in impurity concentration. (c) The variation of maximum EELS peak intensity, within 0–10 eV, with doping concentration of Be-N atomic pairs due to parallel polarization of EM. (For interpretation of the references to colour in this figure legend, the reader is referred to the Web version of this article.)

replacement for ITO because it shares many of the required properties of TCs such as high optical transparency, high tensile stress and flexibility. However, graphene has higher sheet resistance and lower conductivity compared to ITO. Usually, the sheet resistance in graphene is between 1000 and 5000 $\Omega$ /sq which is too high to be used as a TC. High sheet resistance leads to large dissipation of energy in the material, and thus reduced device performance. To make graphene useful as a TC it must be doped with an impurity to reduce the sheet resistance while increasing the conductivity and maintaining the high optical transparency. From this study, Be/BeN has been shown as a perfect impurity that could increase the conductivity of graphene while retaining the optical transparency of the material. For instance, the electronic structures of  $\text{Be}_x\text{N}_x\text{G}$  and of  $\text{Be}_x\text{G}$  show that they both exhibit metallic and semi-conducting character. The Fermi level in the bandstructures of the two materials crosses the valence bands, a feature that makes the materials metallic implying a higher conductivity, while the existence of a region of no electronic states indicates that the systems display semiconducting character. Moreover, the study of the optical properties of the two materials revealed that they are both transparent irrespective of the impurity concentration. Thus,  $\text{Be}_x\text{N}_x\text{G}$  and  $\text{Be}_x\text{G}$  could serve as ideal replacements for ITO.

Nevertheless, further research is needed to determine the work function of these materials to know if their application as TCs is imminent.

Another promising application of graphene is as a graphene based transistor. The excellent mobility of the material might not be the most fascinating feature in terms of a device application. Rather, it may be the tendency of making a miniaturised graphene field effect transistor without a performance restriction that is the most compelling feature of graphene over the existing devices. However, the major drawback in graphene based transistor is lack of a band-gap. A minimum energy gap of 0.4 eV is required for on/off ratio in a transistor with graphene platform [89]. Thus the value of the band-gaps we calculated for both  $\text{Be}_x\text{G}$  and  $\text{Be}_x\text{N}_x\text{G}$  with 3.13 and 6.25% impurity concentration respectively meets this specification.

## 5. Conclusions

First principles DFT techniques have been employed to systematically study the stability, electronic and optical properties of Be-N co-doped graphene in relation to pristine graphene. The analysis of the electronic structures of the systems reveal that both Be-doped and Be-N co-doped graphene share similar electronic

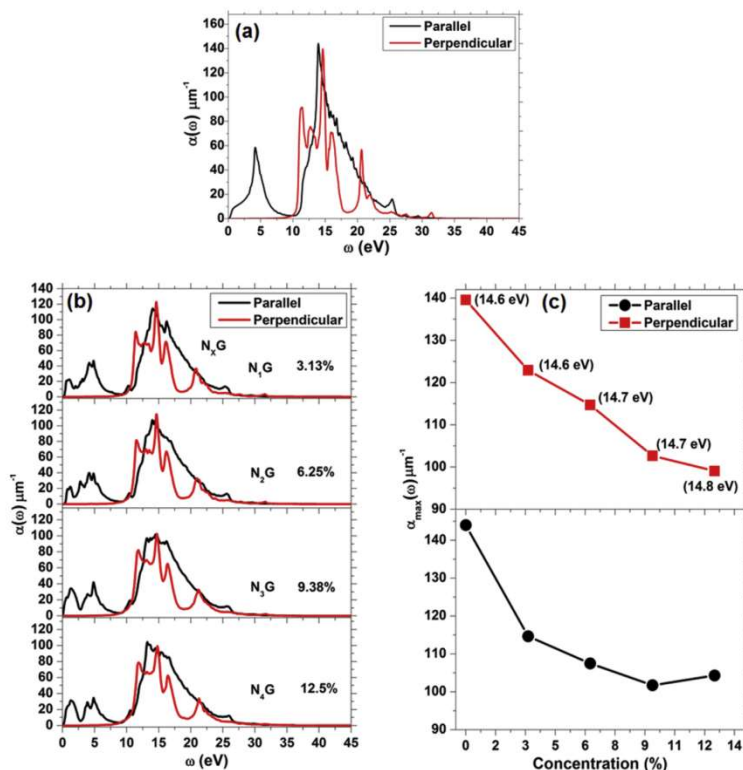


**Fig. 13.** (a) The absorption coefficient of pristine graphene with  $E_{\perp}$  (red) and  $E_{\parallel}$  (black) polarization. The absorption spectra of (b)  $N_xG$  systems with  $E_{\perp}$  (red) and  $E_{\parallel}$  (black) polarization. (c) The variation of  $\alpha_{\max}(\omega)$  of  $N_xG$  system with N concentration for both out-of-plane polarization and in-plane polarization. The numbers associated with the data points correspond to the frequencies in eV of the peaks positions. (For interpretation of the references to colour in this figure legend, the reader is referred to the Web version of this article.)

character i.e. p-type semiconductors while N-doped graphene has been verified to be n-type material. The effects of the isomerization and impurity concentration on the stability and energy gap of the systems show that Be- and N-atoms preferred to co-exist as the nearest neighbours to form an energetically stable Be-N co-doped graphene system ( $Be_xN_xG$ ). For the Be-doped graphene ( $Be_xG$ ) or N-doped graphene ( $N_xG$ ) systems, the impurity preferred to occupy the same sublattices within the host system; with this order of doping, it was observed that the band-gap of the doped systems increases with increase in impurity concentration. At an impurity concentration of 3.13%, a minimum band-gap of 0.44 eV and 0.21 eV was realised for the Be-doped and N-doped graphene respectively while at 12.5% impurity concentration, a corresponding maximum gap of 1.41 eV and 0.6 eV were observed. Besides, the Be-N co-doped graphene was found to have a minimum band-gap of 0.43 eV at 6.25% and a maximum gap of 1.54 eV at 25.0% impurities concentration.

Interestingly, it was observed that the Be-N co-doped graphene is much more stable than the Be-doped graphene due to its lower formation energy and thermodynamic stability. As such it is more appealing for synthesis experimentally than Be-doped graphene. Inferably, our study demonstrates the relative difficulties involved

in attempting to synthesis Be-doped over Be-N co-doped graphene and, perhaps this could be the reason why the material is yet to be synthesised experimentally. In view of this, Be-N co-doped graphene would be an alternative proposition for synthesis as a p-type semiconducting material rather than Be-doped graphene which might not be attainable experimentally.

The dielectric matrices of the doped systems were calculated with the help of first order time-dependent perturbation theory in the simple dipole approximation. It was found that all the systems investigated, irrespective of the impurity concentration, were transparent within the frequency interval of 7.0–10 eV for parallel EM polarization. This is simply because  $Be_xG$ ,  $Be_xN_xG$ ,  $N_xG$  systems as well as pristine graphene have low reflectivity and absorption coefficient in the energy range of 7.0–10.0 eV which falls within the ultraviolet spectrum (i.e. 150–175 nm).

The result of EELS analysis suggests that one could characterize a doped graphene system as either a p-type or n-type semiconductor if the peak of the EELS profile is red-shifted or blue-shifted relative to the EELS peak of pristine graphene at 16 eV under the influence of  $E_{\perp}$  polarization. In general, we observed that the optical properties of the doped systems investigated respond to doping concentration differently across the EM spectrum with respect to the

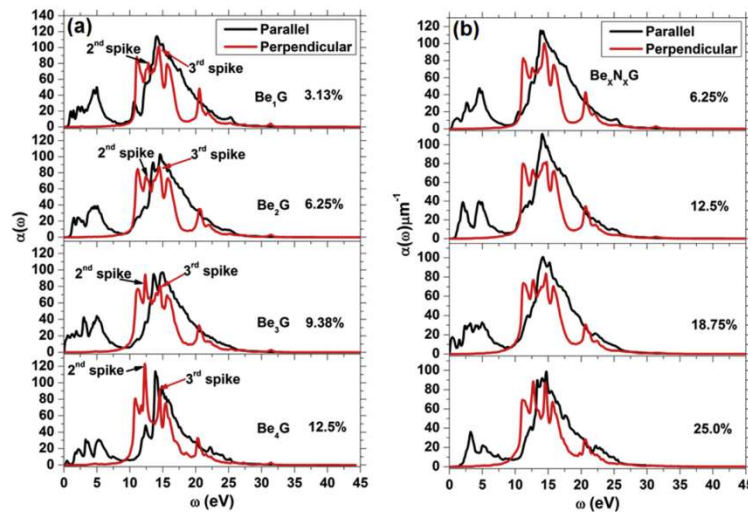


**Fig. 14.** (a) The absorption spectra of  $\text{Be}_x\text{G}$  systems with  $E_{\perp}$  (red curves) and  $E_{\parallel}$  (black curves) polarization. (b) The absorption spectra of  $\text{Be}_x\text{N}_x\text{G}$  systems with  $E_{\perp}$  (red curves) and  $E_{\parallel}$  (black curves) polarization. (For interpretation of the references to colour in this figure legend, the reader is referred to the Web version of this article.)

anisotropic signature of the host system.

The results of our study demonstrate that the band gap of graphene can be tailored to meet the requirements of specific applications in nanoelectronic and optoelectronic devices.

#### Acknowledgments

The authors would like to thank Prof. Mark E. Casida for his suggestions after reading through the manuscript. This work is based on the research supported by the South African Research Chairs Initiative (SARChI) of the Department of Science and Technology and National Research Foundation (NRF) of South African (Grant No. 61056). Any opinion, finding and conclusion expressed in paper is that of the authors and NRF does not accept any liability in this regard. O. Okikiola would like to acknowledge the financial support from NRF and University of Pretoria for his PhD studies.

#### Appendix A. Supplementary data

Supplementary data related to this article can be found at <https://doi.org/10.1016/j.carbon.2017.12.014>.

#### References

- [1] H.R. Soni, P.K. Jha, Vibrational and elastic properties of 2D carbon allotropes: a first principles study, *Solid State Commun.* 189 (2014) 58–62.
- [2] K.S. Novoselov, A.K. Geim, S.V. Morozov, D. Jiang, M.I. Katsnelson, I.V. Grigorieva, S.V. Dubonos, A.A. Firsov, Two-dimensional gas of massless Dirac fermions in graphene, *Nature* 438 (2005) 197–200.
- [3] J.-H. Chen, C. Jang, S. Xiao, M. Ishigami, M.S. Fuhrer, Intrinsic and extrinsic performance limits of graphene devices on  $\text{SiO}_2$ , *Nat. Nanotechnol.* 3 (2008) 206–209.
- [4] S.V. Morozov, K.S. Novoselov, M.I. Katsnelson, F. Schedin, D.C. Elias, J.A. Jaszczak, A.K. Geim, Giant intrinsic carrier mobilities in graphene and its bilayer, *Phys. Rev. Lett.* 100 (2008), 16602.
- [5] A.K. Geim, Graphene: status and prospects, *Science* 324 (2009) 1530–1534.
- [6] M.J. Allen, V.C. Tung, R.B. Kaner, Honeycomb carbon: a review of graphene, *Chem. Rev.* 110 (2010) 132–145.
- [7] A. Balandin, S. Ghosh, W. Bao, Superior thermal conductivity of single-layer graphene, *Nano Lett.* 83 (2008) 902–907.
- [8] C. Mukherjee, J.D. Aguirre-Morales, S. Fregonese, T. Zimmer, C. Maneux, H. Happy, W. Wei, Characterization and modeling of low-frequency noise in CVD-grown graphene FETs, in: *Eur. Solid-state Device Res. Conf., IEEE*, 2015, pp. 176–179.
- [9] B.F. Machado, P. Serp, Graphene-based materials for catalysis, *Catal. Sci. Technol.* 2 (2012) 54–75.
- [10] Z.-S. Wu, S. Pei, W. Ren, D. Tang, L. Gao, B. Liu, F. Li, C. Liu, H.-M. Cheng, Field emission of single-layer graphene films prepared by electrophoretic deposition, *Adv. Mater.* 21 (2009) 1756–1760.
- [11] M. Pumera, Graphene-based nanomaterials for energy storage, *Energy Environ. Sci.* 4 (2011) 668.
- [12] D.A.C. Brownson, D.K. Kampouris, C.E. Banks, An overview of graphene in energy production and storage applications, *J. Power Sources* 196 (2011) 4873–4885.
- [13] F. Schedin, A. Geim, S.V. Morozov, E.W. Hill, P. Blake, M.I. Katsnelson, K.S. Novoselov, Detection of individual gas molecules adsorbed on graphene, *Nat. Mater.* 6 (2007) 652–655.
- [14] J. Fowler, M. Allen, V. Tung, Y. Yang, R. Kaner, Practical chemical sensors from chemically derived graphene, *ACS Nano* 32 (2009) 301–306.
- [15] C. Shan, H. Yang, J. Song, D. Han, A. Ivaska, L. Niu, Direct electrochemistry of glucose oxidase and biosensing for glucose based on graphene, *Anal. Chem.* 81 (2009) 2378–2382.
- [16] S. Alwarappan, A. Erdem, C. Liu, C.-Z. Li, Probing the electrochemical properties of graphene nanosheets for biosensing applications, *J. Phys. Chem. C* 113 (2009) 8853–8857.
- [17] Y. Dan, Y. Lu, N.J. Kybert, Z. Luo, A.T.C. Johnson, Intrinsic response of graphene vapor sensors, *Nano Lett.* 9 (2009) 1472–1475.
- [18] Y.Y.-W. Son, M.M.L. Cohen, S.G.S. Louie, Energy gaps in graphene nanoribbons, *Phys. Rev. Lett.* 97 (2006), 216803.
- [19] L. Yang, C.-H. Park, Y.-W. Son, M.L. Cohen, S.G. Louie, Quasiparticle energies and band gaps in graphene nanoribbons, *Phys. Rev. Lett.* 99 (2007), 186801.
- [20] M. Han, B. Ozyilmaz, Y. Zhang, P. Kim, Energy band-gap engineering of graphene nanoribbons, *Phys. Rev. Lett.* 98 (2007), 206805.
- [21] P.A. Denis, Band gap opening of monolayer and bilayer graphene doped with aluminium, silicon, phosphorus, and sulfur, *Chem. Phys. Lett.* 492 (2010) 251–257.
- [22] J. Zhou, M. Wu, X. Zhou, Q. Sun, Tuning electronic and magnetic properties of graphene by surface modification, *Appl. Phys. Lett.* 95 (2009), 103108.
- [23] X. Tian, J. Xu, X. Wang, Band gap opening of bilayer graphene by F4-TCNQ molecular doping and externally applied electric field, *J. Phys. Chem. B* 114 (2010) 11377–11381.
- [24] R. Balog, B. Jørgensen, L. Nilsson, M. Andersen, E. Rienks, M. Bianchi, M. Fanetti, E. Laegsgaard, A. Baraldi, S. Lizzit, Z. Slijivancanin, F. Besenbacher, B. Hammer, T.G. Pedersen, P. Hofmann, L. Hornekaer, Bandgap opening in graphene induced by patterned hydrogen adsorption, *Nat. Mater.* 9 (2010) 315–319.
- [25] L.L. Zhang, X. Zhao, H. Ji, M.D. Stoller, L. Lai, S. Murali, S. McDonnell,



- B. Cleveger, R.M. Wallace, R.S. Ruoff, Nitrogen doping of graphene and its effect on quantum capacitance, and a new insight on the enhanced capacitance of N-doped carbon, *Energy Environ. Sci.* 5 (2012) 9618.
- [26] A.A. Avestisyan, B. Partoens, F.M. Peeters, Electric field tuning of the band gap in graphene multilayers, *Phys. Rev. B* 79 (2009) 35421.
- [27] K. Mak, C. Lui, J. Shan, T. Heinz, Observation of an electric-field-induced band gap in bilayer graphene by infrared spectroscopy, *Phys. Rev. Lett.* 102 (2009) 256405.
- [28] P. Shemella, S.K.S. Nayak, Electronic structure and band-gap modulation of graphene via substrate surface chemistry, *Appl. Phys. Lett.* 94 (2009) 32101.
- [29] X. Peng, R. Ahuja, Symmetry breaking induced bandgap in epitaxial graphene layers on SiC, *Nano Lett.* 8 (12) (2008) 4464–4468.
- [30] Y. Lu, P. He, Y. Feng, Asymmetric spin gap opening of graphene on cubic boron nitride (111) substrate, *J. Phys. Chem. C* 112 (2008) 12683–12686.
- [31] E. Beheshti, A. Nojeh, P. Servati, A first-principles study of calcium-decorated, boron-doped graphene for high capacity hydrogen storage, *Carbon N. Y.* 49 (2011) 1561–1567.
- [32] P. Nath, S. Chowdhury, D. Sanyal, D. Jana, Ab-initio calculation of electronic and optical properties of nitrogen and boron doped graphene nanosheet, *Carbon N. Y.* 73 (2014) 275–282.
- [33] P. Rani, G.S. Dubey, V.K. Jindal, DFT study of optical properties of pure and doped graphene, *Phys. E Low-Dimensional Syst. Nanostruct.* 62 (2014) 28–35.
- [34] H.R. Jiang, T.S. Zhao, L. Shi, P. Tan, L. An, First-principles study of nitrogen-, boron-doped graphene and Co-Doped graphene as the potential catalysts in nonaqueous Li–O<sub>2</sub> batteries, *J. Phys. Chem. C* 120 (2016) 6612–6618.
- [35] T. Wu, H. Shen, L. Sun, B. Cheng, B. Liu, J. Shen, Nitrogen and boron doped monolayer graphene by chemical vapor deposition using polystyrene, urea and boric acid, *New J. Chem.* 36 (2012) 1385.
- [36] X. Li, L. Fan, Z. Li, K. Wang, M. Zhong, Boron doping of graphene for graphene–silicon p–n junction solar cells, *Adv. Energy Mater.* 2 (2012) 425–429.
- [37] Atomic layers of hybridized boron nitride and graphene domains, *Nat. Mater.* 9 (2010) 430–435.
- [38] Y. Wang, Y. Shao, D.W. Matson, J. Li, Y. Lin, Nitrogen-doped graphene and its application in electrochemical biosensing, *ACS Nano* 4 (2010) 1790–1798.
- [39] P.A. Denis, When noncovalent interactions are stronger than covalent bonds: bilayer graphene doped with second row atoms, aluminum, silicon, phosphorus and sulfur, *Chem. Phys. Lett.* 508 (2011) 95–101.
- [40] Y. Zou, F. Li, Z.H. Zhu, M.W. Zhao, X.G. Xu, X.Y. Su, An ab initio study on gas sensing properties of graphene and Si-doped graphene, *Eur. Phys. J. B* 81 (2011) 475–479.
- [41] M. Houmad, H. Zaari, A. Benyoussef, A. El Kenz, H. Ez-Zahraoui, Optical conductivity enhancement and band gap opening with silicon doped graphene, *Carbon N. Y.* 94 (2015) 1021–1027.
- [42] W. Zhou, M.D. Kapetanakis, M.P. Prange, S.T. Pantelides, S.J. Pennycook, J.C. Idrobo, Direct determination of the chemical bonding of individual impurities in graphene, *Phys. Rev. Lett.* 109 (2012) 206803.
- [43] R. Lv, M.C. Dos Santos, C. Antonelli, S. Feng, K. Fujisawa, A. Berkdemir, A.L. Elias, N. Perea-Lopez, M. Terrones, R. Cruz-Silva, F. Lopez-Urias, H. Terrones, Large-area Si-doped graphene: controllable synthesis and enhanced molecular sensing, *Adv. Mater.* 26 (2014) 7593–7599.
- [44] Z. Jin, H. Nie, Z. Yang, J. Zhang, Z. Liu, X. Xu, S. Huang, E.J. Cairns, Y.G. Zhang, Z. Hu, Metal-free selenium doped carbon nanotube/graphene networks as a synergistically improved cathode catalyst for oxygen reduction reaction, *Nanoscale* 4 (2012) 6455.
- [45] P.A. Denis, Chemical reactivity and band-gap opening of graphene doped with gallium, germanium, arsenic, and selenium atoms, *ChemPhysChem* 15 (2014) 3994–4000.
- [46] E.J.G. Santos, A. Ayuela, S.B. Fagan, J. Mendes Filho, D.L. Azevedo, A.G. Souza Filho, D. Sanchez-Portal, Switching on magnetism in Ni-doped graphene: density functional calculations, *Phys. Rev. B* 78 (2008) 195420.
- [47] R.J. Toh, H.L. Poh, Z. Sofer, M. Pumera, Transition metal (Mn, Fe, Co, Ni)-Doped graphene hybrids for electrocatalysis, *Chem. - Asian J.* 8 (2013) 1295–1300.
- [48] A.W. Robertson, B. Montanari, K. He, J. Kim, C.S. Allen, Y.A. Wu, J. Olivier, J. Neethling, N. Harrison, A.I. Kirkland, J.H. Warner, Dynamics of single Fe atoms in graphene vacancies, *Nano Lett.* 13 (2013) 1468–1475.
- [49] R. Lv, M. Terrones, Towards new graphene materials: doped graphene sheets and nanoribbons, *Mater. Lett.* 78 (2012) 209–218.
- [50] E. Cruz-Silva, F. Lopez-Urias, E. Miño-Sandoval, B.G. Sumpter, H. Terrones, J.C. Charlier, V. Meunier, M. Terrones, Electronic transport and mechanical properties of phosphorus- and phosphorus-nitrogen-doped carbon nanotubes, *ACS Nano* 3 (2009) 1913–1921.
- [51] Y. Zheng, Y. Jiao, L.H. Li, T. Xing, Y. Chen, M. Jaroniec, S.Z. Qiao, Toward design of synergistically active carbon-based catalysts for electrocatalytic hydrogen evolution, *ACS Nano* 8 (2014) 5290–5296.
- [52] X. Ma, G. Ning, C. Qi, C. Xu, J. Gao, Phosphorus and nitrogen dual-doped few-layered porous graphene: a high-performance anode material for lithium-ion batteries, *ACS Appl. Mater. Interfaces* 6 (2014) 14415–14422.
- [53] J.P. Paraknowitsch, B. Wienert, Y. Zhang, A. Thomas, Intrinsically sulfur- and nitrogen-Co-doped carbons from thiazolium salts, *Chem. - A Eur. J.* 18 (2012) 15416–15423.
- [54] J. Liang, Y. Jiao, M. Jaroniec, S.Z. Qiao, Sulfur and nitrogen dual-doped mesoporous graphene electrocatalyst for oxygen reduction with synergistically enhanced performance, *Angew. Chem. Int. Ed.* 51 (2012) 11496–11500.
- [55] J. Xu, G. Dong, C. Jin, M. Huang, L. Guan, Sulfur and nitrogen Co-doped, few-layered graphene oxide as a highly efficient electrocatalyst for the oxygen-reduction reaction, *ChemSusChem* 6 (3) (2013) 493–499.
- [56] S.A. Wohlgemuth, F. Vilela, M.-M. Titirici, M. Antonietti, A one-pot hydrothermal synthesis of tunable dual heteroatom-doped carbon microspheres, *Green Chem.* 14 (2012) 741.
- [57] S.-A.A. Wohlgemuth, R.J. White, M.-G.G. Willinger, M.-M.M. Titirici, M. Antonietti, A one-pot hydrothermal synthesis of sulfur and nitrogen doped carbon aerogels with enhanced electrocatalytic activity in the oxygen reduction reaction, *Green Chem.* 14 (2012) 1515–1523.
- [58] B. Feng, J. Xie, C. Dong, S. Zhang, G. Cao, X. Zhao, From graphite oxide to nitrogen and sulfur co-doped few-layered graphene by a green reduction route via Chinese medicinal herbs, *RSC Adv.* 4 (2014) 17902–17907.
- [59] X. Ma, G. Ning, Y. Sun, Y. Pu, J. Gao, High capacity Li storage in sulfur and nitrogen dual-doped graphene networks, *Carbon N. Y.* 79 (2014) 310–320.
- [60] J.M. You, M.S. Ahmed, H.S. Han, J.E. Choe, Z. Üstündağ, S. Jeon, New approach of nitrogen and sulfur-doped graphene synthesis using dipyrrolemethane and their electrocatalytic activity for oxygen reduction in alkaline media, *J. Power Sources* 275 (2015) 73–79.
- [61] Y. Zhao, D. Truhlar, The M06 suite of density functionals for main group thermochemistry, thermochemical kinetics, noncovalent interactions, excited states, and transition elements: two new functionals and systematic testing of four M06-class functionals and 12 other functionals, *Theor. Chem. Acc. Theory* 120 (2008) 215–241.
- [62] H. Lee, B. Huang, W. Duan, J. Ihm, Ab initio study of beryllium-decorated fullerenes for hydrogen storage, *J. Appl. Phys.* 107 (2010) 84304.
- [63] Y. Ferro, A. Allouche, C. Linsmeier, Absorption and diffusion of beryllium in graphite, beryllium carbide formation investigated by density functional theory, *J. Appl. Phys.* 113 (2013) 213514.
- [64] S. Ullah, A. Hussain, W. Syed, M.A. Saqlain, I. Ahmad, O. Leenaerts, A. Karim, Band-gap tuning of graphene by Be doping and Be, B co-doping: a DFT study, *RSC Adv.* 5 (2015) 55762–55773.
- [65] G. Kresse, J. Furthmüller, Efficiency of ab-initio total energy calculations for metals and semiconductors using a plane-wave basis set, *Comput. Mater. Sci.* (1996).
- [66] P.E. Blöchl, Projector augmented-wave method, *Phys. Rev. B* 50 (1994) 17953–17979.
- [67] J.P. Perdew, K. Burke, M. Ernzerhof, Generalized gradient approximation made simple, *Phys. Rev. Lett.* 77 (1996) 3865–3868.
- [68] O. Olaniyan, R.E. Mapasha, D.Y. Momodu, M.J. Madito, A.A. Kahleed, F.U. Ugbo, A. Belle, F. Barzegar, K. Oyedotun, N. Manyala, Exploring the stability and electronic structure of beryllium and sulphur co-doped graphene: a first principles study, *RSC Adv.* 6 (2016) 88392–88402.
- [69] P. Ordejón, E. Artacho, J.M. Soler, Self-consistent order-*N* density-functional calculations for very large systems, *Phys. Rev. B* 53 (1996) R10441–R10444.
- [70] D. Sánchez-Portal, P. Ordejón, E. Artacho, J.M. Soler, Density-functional method for very large systems with LCAO basis sets, *Int. J. Quantum Chem.* 65 (1997) 453–461.
- [71] M. Gajdoš, K. Hummer, G. Kresse, J. Furthmüller, F. Bechstedt, Linear optical properties in the projector-augmented wave methodology, *Phys. Rev. B Condens. Matter Mater. Phys.* 73 (2006) 045112.
- [72] R. Lv, Q. Li, A.R. Botello-Mendez, T. Hayashi, B. Wang, A. Berkdemir, Q. Hao, A.L. Elias, R. Cruz-Silva, H.R. Gutiérrez, Y.A. Kim, H. Muramatsu, J. Zhu, M. Endo, H. Terrones, J.C. Charlier, M. Pan, M. Terrones, Nitrogen-doped graphene: beyond single substitution and enhanced molecular sensing, *Sci. Rep.* 2 (2012) 586.
- [73] P. Rani, V.K. Jindal, Designing band gap of graphene by B and N dopant atoms, *RSC Adv.* 3 (2013) 802–812.
- [74] Y. Fujimoto, S. Saito, Formation, stabilities, and electronic properties of nitrogen defects in graphene, *Phys. Rev. B - Condens. Matter Mater. Phys.* 84 (2011) 1–7.
- [75] Z. Lin, G. Waller, Y. Liu, M. Liu, C.-P. Wong, Facile synthesis of nitrogen-doped graphene via pyrolysis of graphene oxide and urea, and its electrocatalytic activity toward the oxygen-reduction reaction, *Adv. Energy Mater.* 2 (2012) 884–888.
- [76] D. Long, W. Li, L. Ling, J. Miyawaki, I. Mochida, S.H. Yoon, Preparation of nitrogen-doped graphene sheets by a combined chemical and hydrothermal reduction of graphene oxide, *Langmuir* 26 (2010) 16096–16102.
- [77] P.A. Denis, C.P. Huelmo, F. Iribarne, Theoretical characterization of sulfur and nitrogen dual-doped graphene, *Comput. Theor. Chem.* 1049 (2014) 13–19.
- [78] A. Hussain, S. Ullah, M. Farhan, Fine tuning of band-gap of graphene by atomic and molecular doping: a density functional theory study, *RSC Adv.* 6 (2016) 55990–56003.
- [79] H. Yanagisawa, T. Tanaka, Y. Ishida, M. Matsue, E. Rokuta, S. Otani, C. Oshima, Analysis of phonons in graphene sheets by means of HREELS measurement and ab initio calculation, *Surf. Interface Anal.* 37 (2005) 133–136.
- [80] N. Mounet, N. Marzari, First-principles determination of the structural, vibrational and thermodynamic properties of diamond, graphite, and derivatives, *Phys. Rev. B - Condens. Matter Mater. Phys.* 71 (2005) 1–14.
- [81] J. Zhou, Q. Sun, Q. Wang, P. Jena, High-temperature superconductivity in heavily N or B-doped graphene, *Phys. Rev. B - Condens. Matter Mater. Phys.* 92 (2015) 1–8.
- [82] O. V Sedelnikova, L.G. Bulusheva, A.V. Okotrub, Ab initio study of dielectric response of rippled graphene, *J. Chem. Phys.* 134 (2011), 244707.
- [83] A.G. Marinopoulos, L. Reining, A. Rubio, V. Olevano, Ab initio study of the optical absorption and wave-vector-dependent dielectric response of graphite, *Phys. Rev. B* 69 (2004), 245419.

- [84] T. Eberlein, U. Bangert, R.R. Nair, R. Jones, M. Gass, A.L. Bleloch, K.S. Novoselov, A. Geim, P.R. Briddon, Plasmon spectroscopy of free-standing graphene films, *Phys. Rev. B - Condens. Matter Mater. Phys.* 77 (2008) 1–4.
- [85] J.P. Reed, B. Uchoa, Y. Il Joe, Y. Gan, D. Casa, E. Fradkin, P. Abbamonte, The effective fine-structure constant of freestanding graphene measured in graphite, *Science* 330 (2010) 805–808.
- [86] C. Huang, L. Han, L. Wu, R. Su, J. Chen, P. Lu, Electronic structure and optical properties of boron-sulfur symmetric codoping in  $4 \times 4$  graphene systems, *Eur. Phys. J. B* 88 (2015) 1–7.
- [87] A. Laref, A. Ahmed, S. Bin-Omran, S.J. Luo, First-principle analysis of the electronic and optical properties of boron and nitrogen doped carbon monolayer graphenes, *Carbon N. Y.* 81 (2015) 179–192.
- [88] V.G. Kravets, A.N. Grigorenko, R.R. Nair, P. Blake, S. Anissimova, K.S. Novoselov, A.K. Geim, Spectroscopic ellipsometry of graphene and an exciton-shifted van Hove peak in absorption, *Phys. Rev. B - Condens. Matter Mater. Phys.* 81 (2010) 1–6.
- [89] F. Schwierz, Graphene transistors, *Nat. Nanotech.* 5 (2010) 487–496.

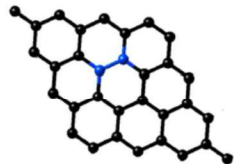
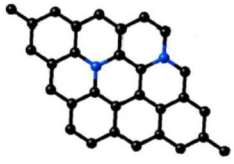
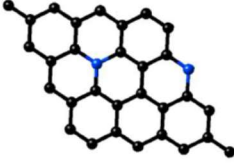
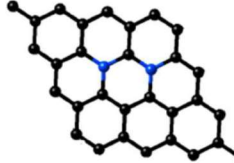
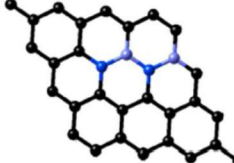
## Supplementary Information

### A systematic study of the stability, electronic and optical properties of beryllium and nitrogen co-doped graphene

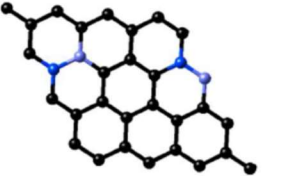
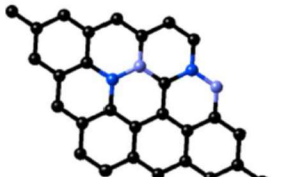
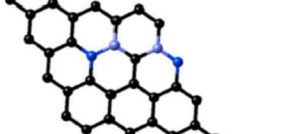
O.Olaniyan, R. E. Maphasha, M. J. Madito, A. A. Khaleed, E. Igumbor and N. Manyala\*

Department of Physics, Institute of Applied Materials, SARCHI chair in Carbon Technology and Materials, University of Pretoria, 0028, South Africa.

**Table S1:** Doping configurations of Be and BeN co-doped graphene with the corresponding formation energy ( $E_{form}$ )

System	Doping configuration	System description	$E_{form}$ (eV)
2Be		Different sublattices	11.96
2Be		Different sublattices	11.91
2Be		Same sublattices	11.63
2Be		Same sublattices	11.84
2Be2N		Same sublattices	6.27

\* Corresponding author. E-mail: [ncholu.manyala@up.ac.za](mailto:ncholu.manyala@up.ac.za) (Ncholu Manyala). Tel: +(27)12 420 3549. Fax: +(27)12 420 2516

2Be <sub>2</sub> N		Different sublattices	6.29
2Be <sub>2</sub> N		Different sublattices	6.28
2Be <sub>2</sub> N		Same sublattices	6.25

### **4.4.3 Concluding remarks**

The results of the lattice dynamics of the systems show that Be-N co-doped graphene is dynamically more stable than Be-doped graphene. The superior stability of Be-N co-doped to Be-doped graphene could be attributed to the formation of the ionic bonds between Be and N-atoms in the graphene matrix. The analysis of the electronic structures of the systems shows that both Be-doped and Be-N co-doped graphene have been transformed to p-type semiconductors with a metallic character. The presence of a metallic character in the Be-doped and Be-N co-doped graphene suggests that the systems have a higher conductivity than graphene. Optical properties of the systems reveal that the doped systems are transparent within the frequency interval of 7.0-10.0 eV for parallel electromagnetic polarization. Thus, the result of this study suggests that BeN-co-doped graphene is a viable candidate to replace ITO in optoelectronic devices.

### **Author contributions**

O. Olaniyan conceived the study, designed the model and the computational framework. He also analyzed the data.

## References

- [1] H. J. Monkhorst and J. D. Pack, "Special points for Brillouin-zone integrations\*," vol. 13, no. 12, 1976.
- [2] S. Ullah *et al.*, "Band-gap tuning of graphene by Be doping and Be, B co-doping: a DFT study," *RSC Adv.*, vol. 5, no. 69, pp. 55762–55773, 2015.
- [3] D. S. L. Abergel, V. Apalkov, J. Berashevich, K. Ziegler, and T. Chakraborty, "Properties of graphene: A theoretical perspective," *Adv. Phys.*, vol. 59, no. 4, pp. 261–482, Jul. 2010.
- [4] K. S. Novoselov *et al.*, "Electric field effect in atomically thin carbon films.," *Science*, vol. 306, no. 5696, pp. 666–9, Oct. 2004.
- [5] P. A. Denis, R. Faccio, and A. W. Mombru, "Is it possible to dope single-walled carbon nanotubes and graphene with sulfur?," *ChemPhysChem*, vol. 10, no. 4, pp. 715–722, Mar. 2009.
- [6] C. W. Tang and S. A. VanSlyke, "Organic electroluminescent diodes," *Appl. Phys. Lett.*, vol. 51, no. 12, pp. 913–915, Sep. 1987.
- [7] M. A. Baldo *et al.*, "Highly efficient phosphorescent emission from organic electroluminescent devices," *Nature*, vol. 395, no. 6698, pp. 151–154, Sep. 1998.
- [8] B. H. Lee, I. G. Kim, S. W. Cho, and S. H. Lee, "Effect of process parameters on the characteristics of indium tin oxide thin film for flat panel display application," *Thin Solid Films*, vol. 302, no. 1–2, pp. 25–30, Jun. 1997.
- [9] U. Betz, M. Kharrazi Olsson, J. Marthy, M. F. Escolá, and F. Atamny, "Thin films engineering of indium tin oxide: Large area flat panel displays application," *Surf. Coatings Technol.*, vol. 200, no. 20–21, pp. 5751–5759, May 2006.
- [10] K. Rana, J. Singh, and J. H. Ahn, "A graphene-based transparent electrode for use in flexible optoelectronic devices," *J. Mater. Chem. C*, vol. 2, no. 15, pp. 2646–2656, 2014.
- [11] F. Bonaccorso, Z. Sun, T. Hasan, and A. C. Ferrari, "Graphene photonics and optoelectronics," *Nat. Photonics*, vol. 4, no. 9, pp. 611–622, 2010.
- [12] S. Bae *et al.*, "Roll-to-roll production of 30-inch graphene films for transparent electrodes," *Nat. Nanotechnol.*, vol. 5, no. 8, pp. 574–578, 2010.
- [13] A. K. Geim and K. S. Novoselov, "The rise of graphene," *Nat. Mater.*, vol. 6, no. 3, pp. 183–191, Mar. 2007.
- [14] S. Pang, Y. Hernandez, X. Feng, and K. Müllen, "Graphene as transparent electrode material for organic electronics," *Adv. Mater.*, vol. 23, no. 25, pp. 2779–2795, 2011.

## **4.5 Ab-initio study of the optical properties of beryllium-sulphur co-doped graphene**

### **4.5.1 Introduction**

In **Error! Reference source not found.**the structural and the electronic properties of the in-plane Be and S co-doped graphene was discussed. The results of the calculations show that Be-S co-doped graphene has a finite direct band-gap, which depends on the configuration of the sites occupied by the impurities. It was further observed that the energetically favorable configuration, in which Be and S replaced the C–C adjacent atoms of graphene, was found to have the least band-gap while the maximum band-gap was induced by the least stable configuration among the set of isomers considered. However, in the study, the effect of the impurities concentration on the electronic and the optical properties of the graphene were not studied. While only in-plane substitution of Be and S in graphene was done, a conformation considering out-of-plane substitution of the impurities in graphene is worth investigating.

Herein, we investigated the effect of Be and S on the lattice dynamics and optical properties of graphene. In studying the aforementioned properties, the energy of formation of the in-plane and out-of-plane substitution of the defects in graphene were considered to determine the energetically favourable conformation. With the result of the formation energies, the energetically favourable configuration was subsequently employed to calculate the electronic and optical properties of the Be and S co-doped graphene systems.

### **4.5.2 Results and discussions**

The details of the computation and the analysis of the optical properties of Be and S co-doped graphene are presented in the following manuscript which is under review.

# Ab-initio study of the optical properties of beryllium-sulphur co-doped graphene

O.Olaniyan<sup>1</sup>, E.Igumbor<sup>1</sup>, A.A. Khaleed<sup>1</sup>, A.A. Mirghni<sup>1</sup> and N.Manyala<sup>1,a</sup>

1. Dept. of physics, institute of Applied Materials, SARCHI Chair in Carbon  
Technology and Materials, University of Pretoria, 0028, South Africa.

(Received 24 November 2018)

Graphene is a carbon material with excellent properties, which makes it applicable in a myriad of applications. However, the range of the applications of graphene can be extended to the developing field of nanoelectronics and optoelectronics by doping it with heteroatoms. In this study, Be and S atoms were used to co-dope graphene. The impurity concentration was varied by increasing the size of the supercell from 2x2 through 4x4. First-principles calculations were performed to determine the dynamic stability, band structure, and optical characteristics of the system. The results of the phonon dispersion of beryllium and sulphur co-doped graphene (Be-S) show the absence of imaginary modes, suggesting that Be-S is dynamically stable. The analysis of the band structure indicates that it has a tunable indirect band-gap which increases with the impurity concentration. Graphene has no band-gap. A band-gap magnitude is required in a graphene-based transistor. Thus, Be-S could be considered as a transistor material. As regards with the optical properties, it is observed that the optical transparency of the graphene in the ultraviolet region changes with the impurity concentration. The result shows that Be-S can be used to manipulate light waves for a device application.

## I. Introduction

Graphene is a single layer of  $sp^2$  hybridized carbon atoms packed in a honeycomb lattice. The outstanding properties (such as high carrier mobility,[1]–[4] exhibitions of ballistic transport,[5] high tensile strength,[6] high flexibility, high thermal conductivity,[7] and ambipolar field effect[8]) make it a promising material for use in nanoelectronic and optoelectronic devices. However, graphene has a zero band-gap,[8]–[10] high sheet resistance,[11]–[13] and these make it difficult for direct integration into nano-devices. The substitutional doping of graphene with heteroatoms has extensively been studied as an effective technique for creating a sizeable band-gap or tailoring the sheet resistance[14] of the material. In general, different heteroatom-doped graphene have been investigated either experimentally or theoretically. In the present study, we explored the potential application of graphene-based material in nano-devices by co-doping.

There are several reports on heteroatom-doped graphene and could be considered as the basis for the present study. Heteroatom-doping of graphene via substitution means an act of replacing a number of carbon atoms of graphene with the elements (other than carbon and hydrogen atom) in the periodic table. Nath et al.[15] performed a first-principles study to determine the electronic structures of boron (B), nitrogen (N), B and N co-doped graphene (B-N). They remarked that the induced direct band-gaps in the doped systems varied with the impurity concentration. Moreover, in the long wavelength limit, the optical parameters of the doped systems (with respect to the parallel polarisation of the field vector) were modified with the impurity concentration. However, they did not calculate the phonon dispersion of the systems to determine if the systems are dynamically stable. Similarly, but in a separate study, Rani et al.[16] employed density functional theory (DFT) investigated the frequency

---

<sup>a</sup> Corresponding author's email:ncholu.manyala@up.ac.za; Tel.: +(27)12 420 3548; Fax: +(27)12 420 2516



dependent optical characteristics of B, N doped graphene and B-N. They arrived at the same conclusion as Nath et al.[15]. In addition, they indicated that the absorption peaks of the B-N were red-shifted towards the visible regime as the impurity concentration increases. However, regardless of the impurities percentage in graphene, their results suggest that the B-N remain transparent in the UV region. In another study[17] pertaining to the electronic structure of the B-N, the size of the direct band-gap was observed to depend on the choice of the sublattice points that the co-dopants occupied in graphene. However, the report did not consider the effect of the sublattices occupied by the impurities on the optical properties of graphene. Recently, DFT was employed to study the effects of B, N concentration and the doping sites on the band-gap of graphene. [18] The results show that the energy gap of the doped system depends on the defects concentration and the doping pattern. However, the lattice dynamics study of the systems not was done to ascertain which pattern of doping is dynamically stable. More recently, Mann et al.[19] studied the thermodynamic properties of graphene doped separately with B and N. They remarked that the dynamic stability and the specific heat capacity of the system decreased with the impurity concentration.

Although N and B atoms are the ideal substitutes for carbon atoms of graphene, due to the size of their atomic radii which are almost the same as that of the carbon atom, other light elements like beryllium and sulphur have also been investigated. Beryllium's electronic configuration is  $1s^2 2s^2$ , which in the current form, appears not to favour the formation of covalent bonds with the carbon atoms of graphene. However, the electron in 2s could be partly promoted to 2p orbitals (since the energy interval between the two orbitals is small) leading to a substantial orbital mixing or hybridisation, and as a result seems to favour the formation of covalent bonding. Consequently, Ferro et al.[20] investigated the adsorption of Be atoms on monolayer and bilayer graphene, and realised that the dopants were more weakly bonded to a monolayer compared to the bilayer graphene. It was stated that  $Be_2$  could form magnetic or non-magnetic structures on graphene depending on the conformation of the adsorbates. However, the optical characteristics of the systems were not studied. Ullah et al.[21] reported on the geometric structure and the electronic characters of Be doped graphene, Be and B dual doped graphene (Be-B). They argued that, with a rectangular doping, a 12.5% impurity concentration would induce maxima band-gaps of 0.99 and 1.44 eV in Be-B and Be doped graphene, respectively. However, they did not report the effect of the impurities on the optical properties of the systems. Hussain et al.[22] studied the geometric structure and the electronic properties of Be and N co-doped, and Be-O molecule-doped graphene. They revealed that the increase in the impurity percentage in graphene does not always lead to a band-gap enhancement. However, they, likewise, did not report the optical properties of the systems or the dynamic stability to show that the systems investigated have no imaginary modes. In another study, Denis et al.[23] investigated the effects of sulphur substitution on single-walled carbon nanotubes and graphene from first principles. They remarked that, in the case of doped graphene, the defects could either induce a semiconducting or metallic character in graphene depending on the sulphur content. However, they did not investigate the effect of heteroatoms co-doping as an avenue to eliminate the metallic character of the system. Recently, we studied the geometric structure and electronic properties of the in-plane beryllium and sulphur co-doped graphene (Be-S) at a fixed impurity concentration. We observed that the band-gap of the Be-S depends on the relative positions between the impurities in the system.[24] However, in the study, the out-of-plane conformation of the defects in graphene was not taken into consideration to determine if it is more stable than the in-plane configuration. Moreover, the impurity concentration effect on the lattice dynamics, electronic and optical characteristics of the system were not studied as well.

Despite the numerous studies that have been done with ab-initio studies predicting the properties of heteroatom-doped graphene, synthesising such heavily doped (i.e. with the impurity concentration above 5%) nanostructures experimentally remain a contending issue. As a result, other heteroatoms doped graphene are being explored to determine if they would be amenable for synthesis experimentally at a higher impurity concentration. In view of the above, we report for the first time the effects of the atomic pairs of Be and S on the dynamic stability, electronic and optical properties of graphene. Moreover, in the study, the in-plane and out-plane substitution of the Be and S atoms in graphene were evaluated to determine how the impurities prefer to co-exist in graphene. It is expected that the result of this study would provide an insight into the realisation of graphene-based nano-devices.

## II. Methods

The electronic structures and optical characteristics of calculations Be-S were performed from first-principles within the scope of DFT as implemented in the Vienna Ab-initio Simulation Package (VASP).[25]–[28] In the simulations, the Projected Augmented Wave (PAW) was employed to model the system of the ion-electron interactions, while the Perdew Burke Ernzerhof (PBE) generalised gradient approximation (GGA)[29] was used as the exchange-correlation functional. To improve on the usual underestimation of energy band-gap by semi local functionals, we used HSE06.[30] The lattice symmetry of graphene can be broken if it is co-doped with dopants with larger molecular radii than carbon atom. Consequently, more high symmetry K-points in the Brillouin zone (BZ) (as shown in Fig. 1) must be sampled in order to obtain an accurate plot of the band structure of the co-doped system. Based on this, the path in the BZ via which the band structures of Be-S was calculated is given through  $\Gamma$ –M–K– $\Gamma$ –M'–K'– $\Gamma$ –M''–K''– $\Gamma$  sampling route. Kohn-Sham orbital expansions with the plane-wave basis set were done with the kinetic energy cutoff (Ecut) of 400 eV, and the convergence criterion of  $10^{-5}$  eV was used for the computations of all the systems that were studied. The systems that were studied consist of 8, 18 and 32 atoms corresponding to periodic slabs of 2x2, 3x3 and 4x4 supercell of graphene co-doped with an atomic pair of beryllium (Be) and sulphur (S). To avoid the interlayer interaction between a layer of graphene and the periodic image, a test of convergence with respect to vacuum spacing was done.

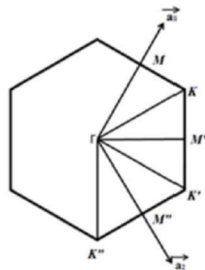


FIG. 1 The path between the high symmetry points in the BZ for the calculation of the band structure of Be-S.

A vacuum size of 14 Å along with the periodic boundary conditions was observed to give a converged result when applied between any two adjacent layers of graphene. Geometrical relaxation of all the systems was done such that the Hellmann-Feynman forces is less than a predetermined threshold value of 0.002 eV Å<sup>-1</sup>. For Brillouin zone (BZ) sampling, a  $\Gamma$ -centred grid of 13  $k \times 13 k \times 1k$ -mesh was used. For the integration scheme, Gaussian smearing with 0.2 eV width was used for the self-consistent field calculation (scf). The formation energy  $E_f$  requires for a defect to form in graphene was calculated as follows:

$$E_f = E_d - \sum_t n_t \mu_t . \quad (1)$$

where  $E_d$  denotes the energy per unit cell of graphene with impurities; the subscript 't' denotes the index of summation of the set of atoms of a particular type; whereas the number of a set of atoms of type 't' is represented as  $n_t$ , the chemical potential associated with atoms of type "t" is represented as  $\mu_t$ . Carbon chemical potential  $\mu_c$  was calculated as the total energy of graphene divided by the number of the carbon atom in the unit cell. So that the formation energy of defect-free graphene is equal to zero. To compute the sulphur (S) chemical potential  $\mu_S$ , the energy per unit atom obtained from the crystalline S with a face-centred orthorhombic lattice (space group of Fddd) was used. For Be, the hexagonal crystalline lattice was employed to compute the chemical potential  $\mu_{Be}$ .

It is worth mentioning that during the geometry optimization of Be-S, spin and unspin polarized calculations were performed. The results of the two computations have the same energy, with the resultant zero magnetic moments. Consequently, the unspin polarized calculations were applied to the remaining systems to save computational cost.

The optical characteristics of Be-S were calculated with the dielectric function  $\varepsilon(\omega)$  (equation 2); where the imaginary part  $\varepsilon_2$  was computed employing first-order time-dependent perturbation theory in the basis of simple dipole approximation. The changes in the periodic part of the potential, known as the local field effects, have been included within random phase approximation (RPA).

$$\varepsilon(\omega) = \varepsilon_1(\omega) + i\varepsilon_2(\omega) \quad (2)$$

In the long wavelength limit, the imaginary part of the complex dielectric function could be expressed as:

$$\varepsilon_2(q \rightarrow 0, \omega) = \frac{2e^2\pi}{V\varepsilon_0} \sum_{c,v,k} |\langle \psi_k^c | \vec{u} \cdot \vec{r} | \psi_k^v \rangle|^2 \delta(E_k^c - E_k^v - \omega) . \quad (3)$$

where ‘c’ and ‘v’ are the band indices corresponding to the conduction and valence bands;  $V$  and  $\epsilon_0$  represent the unit cell volume and the free space permittivity, respectively.  $\omega$  (expressed in eV) is a particular frequency of the incident electromagnetic (EM) wave. In this order,  $\vec{u}$  and  $\vec{r}$  denote the incident EM wave polarization vector and the position vector. At a k-point, the eigenfunctions corresponding to the valence and conduction bands of the given systems are represented by  $\psi_k^v$  and  $\psi_k^c$ , respectively. The  $E_k^c$  and  $E_k^v$  correspond to the eigenvalues.

The real component of the  $\epsilon(\omega)$ ,  $\epsilon_1$  is calculated from  $\epsilon_2$  employing the Kramers-Kronig transformation:

$$\epsilon_1(\omega) = \text{Re}[\epsilon(\omega \rightarrow 0)] = 1 + \frac{2}{\pi} P \int_0^\infty \frac{d\omega' \epsilon_2(\omega') \omega'}{\omega'^2 - \omega^2 + i\eta} \quad (4)$$

where  $P$  stands for the Cauchy principal value. The technique has been reported in Ref.[31]. It is worth noting that  $\epsilon_1$  and  $\epsilon_2$  have two independent parts which are the two polarizations of the EM field with respect to the plane of the materials. These two polarizations are called the parallel (the polarised vector is along the plane of the system) and the perpendicular (the polarised vector is out of the plane of the system) polarization in this study. It is worth mentioning that equation (3) has no Drude component. Drude term accounts for the intraband transition which is dominant at the low energy.

Given the data sets of  $\epsilon(\omega)$ , the optical characteristics of the graphene and Be-S were calculated using equation (5) through (9):

$$n(\omega) = \left( \frac{\sqrt{\epsilon_1^2 + \epsilon_2^2} + \epsilon_1}{2} \right)^{\frac{1}{2}} \quad (5)$$

$$k(\omega) = \left( \frac{\sqrt{\epsilon_1^2 + \epsilon_2^2} - \epsilon_1}{2} \right)^{\frac{1}{2}} \quad (6)$$

where  $n(\omega)$  is the real and  $k(\omega)$  is the imaginary part of the complex refractive index  $\tilde{n}$  with the relation,  $\tilde{n} = n(\omega) + ik(\omega)$ . The equations (5) and (6) were used to calculate the reflectivity  $R$  of the systems of study provided the incident polarized EM is perpendicular to the plane of the samples.

$$R(\omega) = \frac{(n-1)^2 + k^2}{(n+1)^2 + k^2} \quad (7)$$

The absorption coefficient  $\alpha(\omega)$  of the systems was computed with the equation (6) above

$$\alpha(\omega) = \frac{2k\omega}{c\hbar} \quad (8)$$

where the ‘c’ of equation. (8) represents the velocity of EM field in the vacuum. The remaining variables retain the same descriptions as earlier declared.

$$L(\omega) = \frac{\varepsilon_2}{\varepsilon_1^2 + \varepsilon_2^2} . \quad (9)$$

The measure of the collective excitation of a given system is expressed by the electron energy loss function  $L(\omega)$  and could be calculated by applying equation (9). The quantity can be derived from  $\text{Im}(-1/\varepsilon(q \rightarrow 0, \omega))$  and the magnitude of the value increases as  $\varepsilon_1 \rightarrow 0$  and  $\varepsilon_2 < 1$  at the plasma frequency. To evaluate the optical constants of the Be-S and the graphene, a considerable number of empty bands were applied in the calculations. Additional empty bands were included in our optical calculations to account for high-frequency interband transitions.

For the study of the lattice dynamics of the systems, the direct method[32] was used within the limit of the harmonic approximation.

### III. Results and Discussion

#### A. Formation energy

The formation energy per unit cell  $E_f$  of a solid could be employed to access the stability and the relative tendency of such system to be synthesized in the laboratory. As a result, in this study,  $E_f$  of pristine and Be-S was calculated with the equation (1). To calculate the  $E_f$  of pristine graphene, the system was first geometrically optimised. After the relaxation, 2.46, 1.42 Å (see Fig. 2a) and 0 eV were realised as the lattice constant, C-C bond length and  $E_f$  of the system respectively. The calculated values of the lattice parameters are in close agreement with the existing theoretical[21] and experimental[9], [33] reports. Therefore, the agreement between these results and the literatures validates the computational method adopted in this study. Meanwhile, as earlier stated, the  $E_f$  of the defect-free graphene is zero because the chemical potential of the carbon atom was calculated using pristine graphene (not graphite) as the reference. The advantage of zeroing the  $E_f$  of graphene is that the relative stability of a doped graphene system could easily be compared. This suggests that a doped graphene system with  $E_f > 0$  has lower stability than pristine graphene. Moreover, the converse of this statement also holds for  $E_f < 0$ .

Next, the  $E_f$  of Be-S was evaluated to determine how the defects prefer to co-exist in graphene. In our earlier report[24], it was demonstrated that Be and S atoms prefer to replace in-plane C-C of graphene. In the study, it is argued that the favourable predisposition of Be to S bonding in graphene is as a result of the formation of the ionic bonding between the defects. However, in the report, the out-of-plane substitution of the impurities was not taken into account in order to determine if it is energetically more favourable than the in-plane substitution. In the present study, the two conformations were accessed to determine which one is more favourable to be experimentally synthesised. The two conformations are shown in Fig. 2 [(b) and (c)] and they correspond to the in-plane and the out-of-plane substitution of Be and S for the carbon atoms in a 2x2 supercell of graphene, respectively. From the results of the formation energies, it is found that the out-of-plane substitution of Be and S atomic pair in graphene is energetically more favourable than the in-plane substitution of the defects. The lower value of the  $E_f$  of the Be-S co-doped graphene might be attributed to the fact that the atoms of the system have a tendency to be densely more packed in the out-of-plane than the in-plane arrangement thereby reducing the amount of stress experiences by the system. Consequently, in the rest of this study, the out-of-plane conformation was employed

whenever the atomic duo of Be and S were substituted for the carbon atoms of graphene. Fig. 2 [(d) and (e)] show a 3x3 and a 4x4 Be-S systems which correspond to 11.0 and 6.3% impurity concentrations respectively. The supercells of the systems were varied purposely to induce the

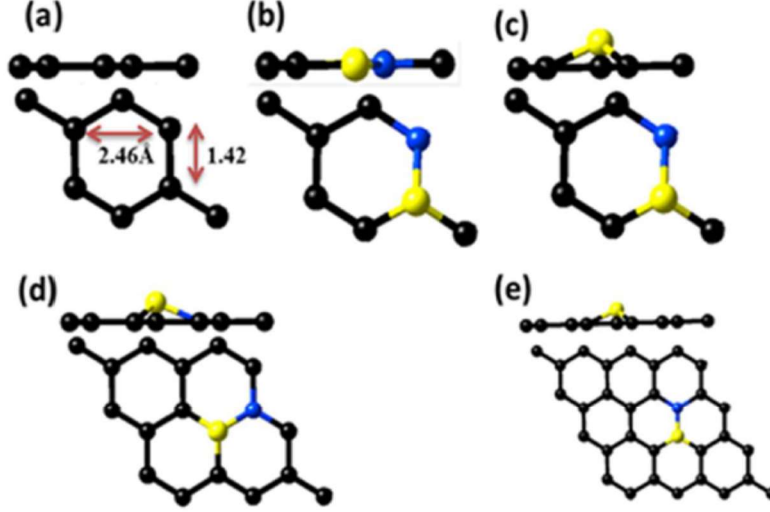


FIG. 2 The optimised geometry of Be-S with (a) 0% (b) 25% (in-plane) (c) 25% (out-of-plane) (d) 11% (e) 6.3% (out-of-plane).

different amount of the defects in graphene. Table I gives the summary of the different amount of the defects created in graphene and the corresponding  $E_f$ .

**Table 1** The relationship between the impurity concentration of Be-S and the  $E_f$ .

Impurity concentration (%)	Systems+Supercells	$E_f$ (eV)
0	Pristine graphene 2x2	0
6.3	Be-S 4x4	4.14
11.0	Be-S 3x3	4.22
25.0	Be-S 2x2	4.85

## B. Dynamic stability of Be-S

In order to establish the dynamical stability (lattice dynamics) of Be-S, due to the expensive nature of phonon calculations, only the lattice vibrational modes of the least stable Be-S (with 25 % impurity) were investigated using the harmonic approximation. If the least stable Be-S has no imaginary modes, thus the result should also be true for the other more stable structures. Table 1 shows that the  $E_f$  of the Be-S increases with the defects concentration. For instance, the pristine graphene is the most stable with 0 eV as the  $E_f$ , while 4.85 eV is for Be-S with the 25% impurity concentration. Due to the expensive nature of phonon calculations, in the present study, only the vibrational modes of the least stable structure of Be-S co-doped system along with that of pristine graphene were investigated.

The calculation of the phonon curve of pristine graphene was done with a 1x1 supercell which contained two carbon atoms. The result of the calculation is displayed in Fig. 3(a). Six phonon modes can be seen and they correspond to the three optical (LO, TO, ZO) and acoustic (LA, TA, ZA) branches. The LO, TO and ZO tags on the curve represent the longitudinal, transverse and optical

branches, respectively. The corresponding acoustic components are labelled as LA, TA, and ZA. Some of the key values of the curve at high symmetry points are tabulated in Table 2. According to Table 2, it is interesting to observe that the values are quite in agreement with the existing theoretical[34] and experimental[35] reports on the phonon dispersion curve of the pristine graphene. The close agreement between this result and the existing literature attests to the reliability of the computational method employed in this work.

Following the validation of the computation method, the technique was subsequently applied to calculate the phonon spectrum curve of Be-S with a 25% impurity concentration. The system was optimized until the forces on all the atoms were less than  $0.002 \text{ \AA}$ . Fig. 3(b) shows the phonon spectrum of Be-S with a 25% impurity concentration. It is worthwhile to note that the absence of imaginary modes on the curve is an indication that the system is dynamically stable, and as a result, it is amenable for synthesis in the laboratory if the necessary precursors are used.

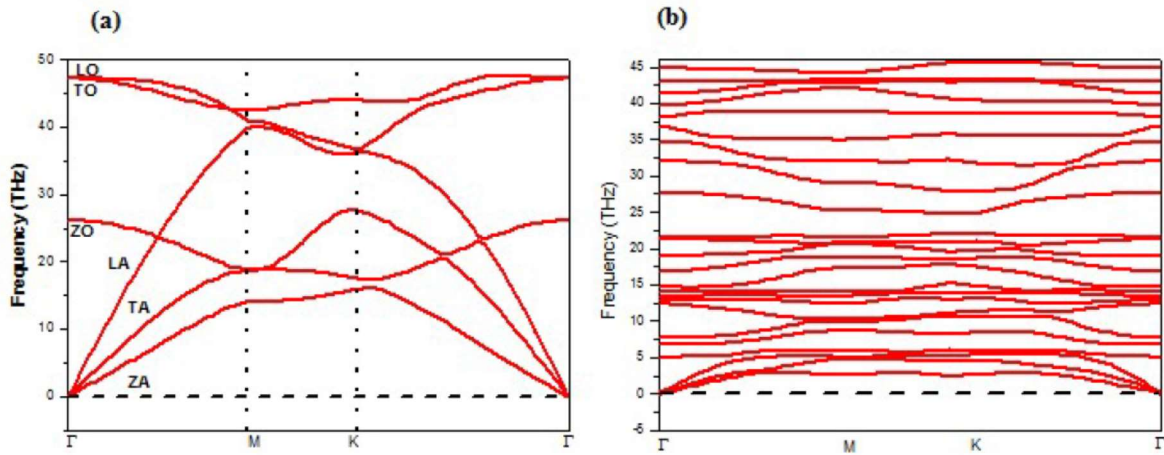


FIG. 3 Phonon dispersion curve of a (a) 1x1 supercell of pristine graphene (b) 2x2 supercell of Be-S with a 25% defect concentration. LO (LA), TO (TA), ZO (ZA) are the longitudinal, and transversal (optical) branches.

**Table 2** Computed phonon frequencies at  $\Gamma$ , M, K,  $\Gamma$  point in the BZ of graphene.

high-symmetry points	present study	theoretical	experimental
	GGA (PBE) (in THz)	ref.[34] (in THz)	ref.[35] (in THz)
$\Gamma_{ZO}$	26.14	26.41	26.02
$\Gamma_{LO}$	47.23	46.58	47.36
$\Gamma_{TO}$	47.23	46.58	47.36
$M_{ZA}$	13.78	14.12	13.52
$M_{LA}$	39.70	39.81	39.81
$M_{ZO}$	19.02	19.03	19.03
$M_{TO}$	41.69	41.67	41.67
$K_{ZA}$	15.68	16.03	15.49
$K_{ZO}$	17.30	16.03	17.62
$K_{LA}$	36.32	36.36	36.36
$K_{TO}$	38.26	38.61	38.61

### C. Band-gap tuning of graphene

The electronic band-gap of Be-S with different impurity concentration was studied and compared with that of the pristine graphene. It is shown in Fig 4 (a) that the pristine graphene is a gapless nanomaterial as a result of the touching of the minimum conduction and the maximum valence band at the K-point of the BZ. The  $\pi$  and  $\pi^*$  states form the valence and the conduction bands respectively. At the low energy region, the band has a linear relation and the band structure could be seen as two cones meeting at the Dirac point. The touching of the bands at the neutrality point indicates that graphene has no band-gap. The zero band-gap in graphene is as a result of the similar background of the two carbon atoms in the 1x1 unit cell of graphene. These basic features of the band structure of pristine graphene are in agreement with the earlier studies.[9], [10], [36]

However, a band-gap can be induced in graphene if the two atoms in the unit cell could be made to co-exist at a different potential. Doping of graphene with an impurity induces energy gap in the system. Moreover, with a certain doping pattern, the size of the gap often depends on the amount of the impurity concentration incorporated into graphene.[18] For example, the effect of the beryllium or sulphur concentration on the electronic structure of graphene has been done in separate studies.[21], [23] In the case of Be-doped graphene, it is stated that the band-gap could be tuned as a function of the impurity concentration. In our recent study,[36] we have undeniably confirmed this to be true.



However, at a high Be concentration, besides the material being dynamically unstable, we also found that the nanostructure formed a degenerate semiconductor. A degenerate semiconductor is a material with both metallic and semiconducting character. In another study, P.A. Denis *et al.*[23] have demonstrated that heavily S doped graphene exhibits a metallic character. Against this backdrop, in the present study, it is shown in Fig. 4 ((b)-(d)) that an atomic pair of Be and S could induce a tunable indirect gap of 0.72 eV (0.37 eV with GGA) in graphene. The system has a minimum indirect band-gap of 0.20 eV at 6.3 % while 0.72 eV is observed at 25 % impurity concentration. Table 3 shows the summary of the result. Moreover, Be-S could be touted as a nanostructure with no metallic character since the Fermi level is right within the band-gap irrespective of the impurity concentration. The key factor that keeps the Fermi level within the energy gap of the system could be attributed to the isoelectronic nature of Be and S with regard to the pristine graphene. It is worth mentioning that in microelectronics, the smallest band-gap of 0.4 eV is required for a transistor to work in ON/OFF mode. Thus, the calculated magnitude of the band-gap of Be-S satisfies this requirement.

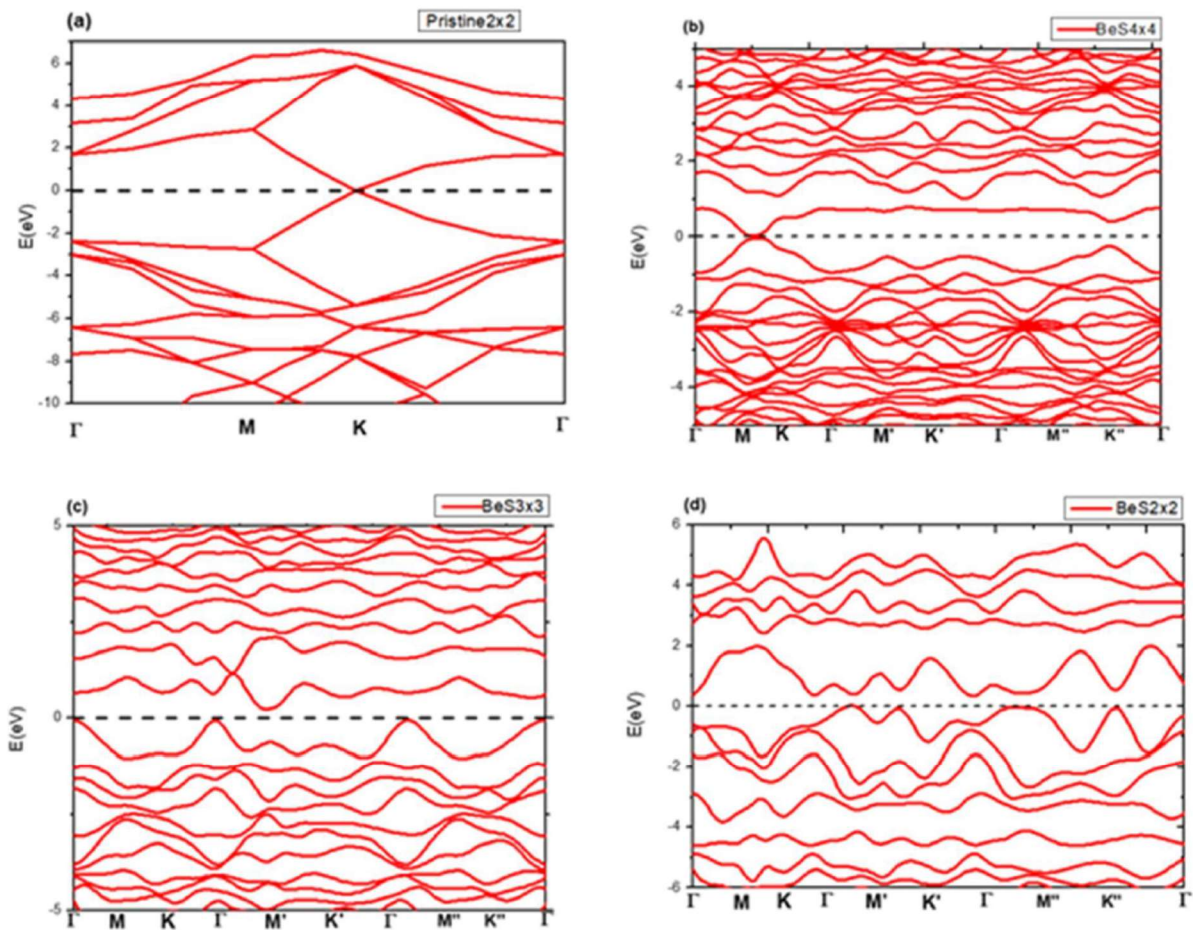


FIG. 4 Band structure of Be-S with a (a) 0 % (b) 6.3% (c) 11% and (d) 25 % impurity concentration.

**Table 3** The magnitude of the bandgap induced in graphene versus the impurity percentage.

System	defect conc.(%)	Band-gap (in eV)	
		GGA (PBE)	HSE06
Pristine graphene	0	0	0
Be-S co-doped graphene	6.3	0.08	0.2
	11.0	0.28	0.63
	25.0	0.37	0.72

#### D. Dielectric function

In the previous section, it was simply demonstrated that if graphene is co-doped with the atomic pair of Be and S atoms, the electronic band structure would be induced with the impurities dependent band-gap. Consequently, changes in the electronic structure of graphene are expected to result in the modification of the optical characteristics of the system. In this section, the effect of the impurity concentration of Be and S on the optical properties of pristine graphene has been studied. The discussion of the optical properties of the systems of interest is centred on the optical parameters like the dielectric function, refractive indices, reflectivity, absorptivity, and electron energy loss function (eels). Fig. 5 (a) and (b) show imaginary dielectric spectra of pristine (magenta colour), and co-doped graphene at different impurity concentrations (red, green and blue colour) with respect to the light polarisation vectors. The red spectrum is associated with a  $2 \times 2$  supercell of graphene doped, via substitution, with a pair of Be and S to forms a 25% impurity concentration.

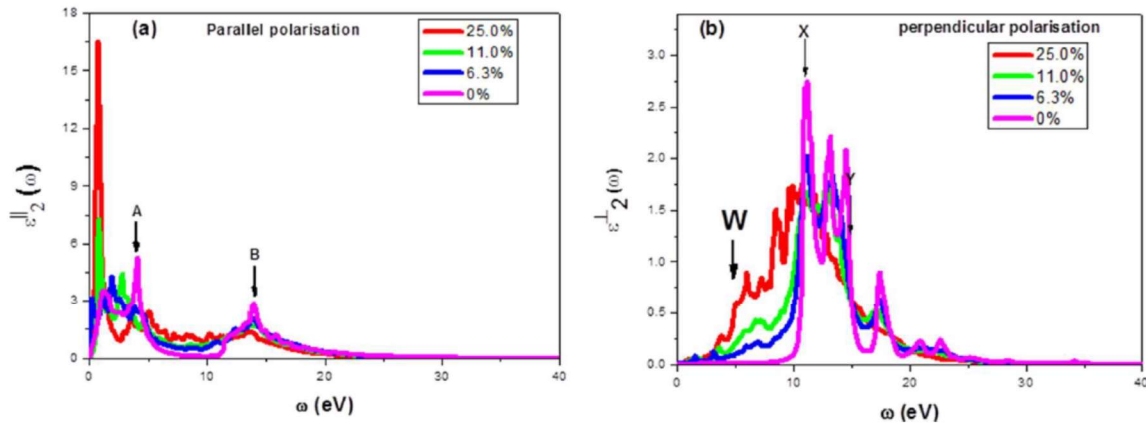


FIG. 5 The anisotropic imaginary dielectric spectra of graphene (magenta) and Be-S (blue, green, and red colour correspond to a 6.3, 11.0 and 25 % impurity concentration) for (a) parallel polarisation (b) perpendicular polarisation of the electric field vector.

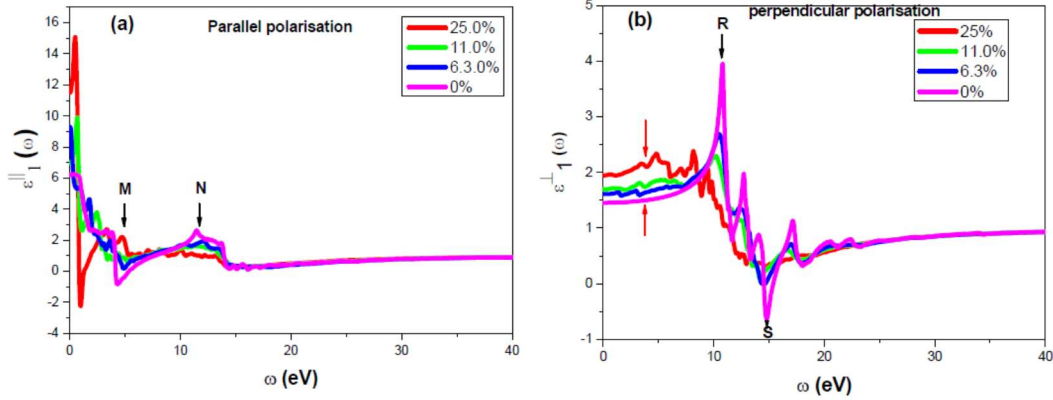


FIG. 6 The anisotropic real part of the dielectric spectra of graphene (magenta) and Be-S (blue, green, and red colour correspond to a 6.3, 11.0 and 25 % impurity concentration) for (c) parallel polarisation (d) perpendicular polarisation of the electric field vector.

The green spectrum is associated with a  $3 \times 3$  supercell of graphene doped with a pair of Be-S and corresponds to a 11.0% impurity concentration. The blue colour corresponds to  $4 \times 4$  supercell of graphene with a 6.3% impurity concentration. The dielectric function has two different components denoted as  $\epsilon_2^{\parallel}$  and  $\epsilon_2^{\perp}$  which correspond to the polarisation of EM field vectors relative to the plane of graphene and would be described as parallel and perpendicular polarisation. These notations have also been extended to other optical parameters in this study.

With respect to the parallel polarisation of the electric field vector ( $E_{\parallel}$ ), Fig.5 (a), the imaginary dielectric curve of graphene is characterised with two prominent peaks. The first one (**A**) covers low-frequency regime up to 5.0 eV arising from intraband and interband transition with an intense peak at 4.0 eV whereas the second peak (**B**) with a wider frequency range, as a result of mainly interband transition, has a pronounced peak at 14.0 eV. Sandwiched between the two peaks of the spectrum is a featureless region stretching between 7.5-10.6 eV and has nearly zero intensity. The corresponding frequency of the two peaks is in excellent agreement with previous studies[36]–[38]. Recent spectroscopic ellipsometry study of graphene grown on amorphous quartz shows a distinct absorbance peak at 4.6 eV.[39] The higher value obtained from the experiment as compared to the first peak of our study could be ascribed to the neglect of the interaction between the substrate and the graphene sheet in our calculation. The basis of the peak **A** is attributed to the  $\pi \rightarrow \pi^*$  transition on the line between M and K of the BZ (see Fig. 4 (a)) while the peak at **B** could be ascribed to  $\sigma \rightarrow \sigma^*$  transition on the symmetry line between  $\Gamma$  and M (see Fig. 4 (a)) and this arises mainly from interband transition. Next, the effect of the atomic pair of Be and S atoms on the optical spectrum of graphene was observed with respect to the same electric field polarisations. As the percentage of the impurities increases, the height of peak **B** was noticeably reduced, whereas the peaks at **A** are red-shifted towards lower energy photon (see Fig. 5 (a)).

For perpendicular polarisation of the electric field ( $E_{\perp}$ ), as shown in Fig. 5 (b), the  $\epsilon_2^{\perp}$  spectrum of graphene has two contrasting peaks at 11.2 and 17.4 eV which are indicated as **X** and **Y**, respectively. With respect to  $E_{\perp}$ , the dipole selection rule for the polarisation only allows the  $\pi \rightarrow \sigma^*$  and the  $\sigma \rightarrow \pi^*$  transitions. Thus, the basis of the peaks at **X** and **Y** in Fig. 5 (b) could be attributed to the  $\pi \rightarrow \sigma^*$  and the  $\sigma \rightarrow \pi^*$  interband transitions. Between 0 and 10 eV, we observed that the spectrum has zero intensity. This is because  $\pi \rightarrow \pi^*$  transition with low energy resonance is forbidden as prescribed by the

selection rule. Next, the effect of the impurity concentration on the graphene spectrum was considered. As the impurity concentration increases, it can be seen that the range of the energy frequency of the transition due to the peak **X** also increases while the intensity of the peak at **Y** decreases accordingly (see Fig. 5(b)). It is important to remark that while the  $\varepsilon_2^\perp$  spectrum of graphene has nearly zero intensity between 0 and 10 eV, that of the Be-S increases with the amount of the impurities within the given frequency interval. The change in the amplitude of  $\varepsilon_2^\perp$  spectra of Be-S, within 0-10.0 eV, as a result of the defect concentration is indicated with the black arrow and designated as **W** in Fig. 5 (b).

The  $\varepsilon_1$  of pristine and Be-S co-doped graphene was computed using Kramers-Kronig transformation (see Eq.4) for both  $E_{\parallel}$  and  $E_{\perp}$ . Fig 6 (a) and (b) depict the  $\varepsilon_1^{\parallel}$  and  $\varepsilon_1^{\perp}$  spectra respectively of the pristine along with Be-S co-doped graphene at different impurity concentration. With regard to  $\varepsilon_1^{\parallel}$  (Fig. 6 (a)), pristine graphene has a prominent peak in the region of 0-4 eV, a minimum near 5 eV and a broader peak with maximum intensity at 11.3 eV. The features of this spectrum and the exact position of the peaks are in good agreement with the existing theoretical and experimental reports. [15], [40] For Be-S, it is remarkable to note that the intensity of the spectrum of the system, within the region 1.0-15.0 eV, approaches that of pristine graphene as the percentage of the impurity decreases. For instance, in Fig. 6 (a) around **M** and **N** point, it can be observed that the intensity of the features of Be-S co-doped graphene tends to that of pristine as the impurity concentration decreases.

In the following discussion, the  $\varepsilon_1^\perp$  spectrum of pristine graphene is compared with that of Be-S at different impurity concentrations. (Fig. 6 (b)) shows the spectrum of graphene with a pronounced peak at 11.0 eV, a minimum at 15.0 eV and the features are highlighted as **R** and **S**. Next, the effect of the atomic pair of Be-S on the optical spectrum of graphene was studied. Between 0-11 eV it is observed that  $\varepsilon_1^\perp$  curve of Be-S approaches that of pristine graphene as the impurity percentage reduces from 25 % to 6.3%. A similar behaviour of the spectrum of Be-S in relation to graphene is noticeable at 15.0 eV.

### E. Absorptivity

Graphene is an outstanding system with excellent optical properties arising from its unique electronic structures. It can absorb light from the visible to infrared region of the electromagnetic spectrum. The absorption spectrum of the system arises from an intraband transition (at a low energy frequency within the far-infrared region) and an interband transition (at a higher energy frequency in the mid-infrared to the ultraviolet range).

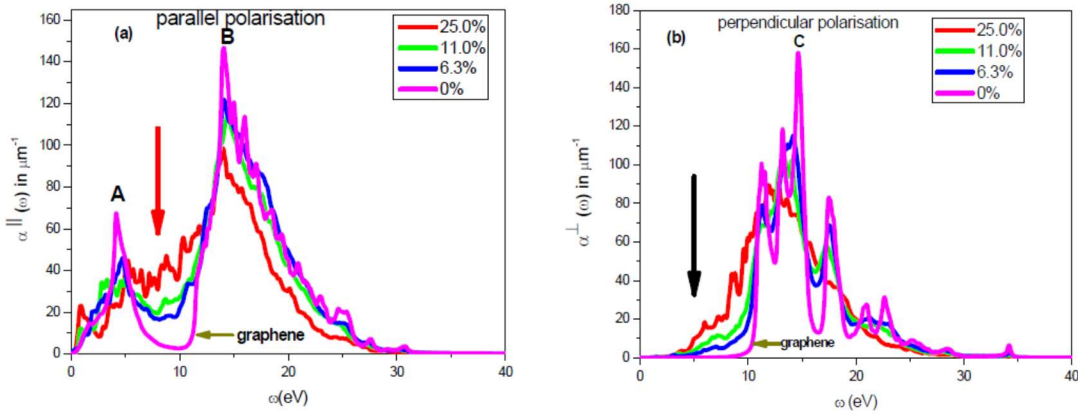


FIG. 7 The anisotropic absorption spectra of graphene (magenta) and Be-S (blue, green, and red colour correspond to a 6.3, 11.0 and 25 % impurity concentration) for (a) parallel polarisation and (b) perpendicular polarisation of the electric field vector.

Fig. 7 shows the absorption spectra of graphene and Be-S with the different impurity concentration in relation to  $E_{\parallel}$  and  $E_{\perp}$ . As regards to  $E_{\parallel}$  spectrum, pristine graphene has two pronounced peaks (see Fig. 7 (a)). The first peak is located at 4.2 eV and is due to the  $\pi \rightarrow \pi^*$  transition through M-K route in the Brillouin zone (see Fig. 4(a)). The transitions leading to the peaks are composed of the first valence band under the Fermi level to the first conduction band at the top of the Fermi level. However, the second peak occurs at 14.0 eV as a result of the  $\sigma \rightarrow \sigma^*$  transition which is dominated by the second valence state under the Fermi level to the second conduction state at the top of the Fermi level. In addition to this, the system has a featureless region (between A and B point) which exists within the interval of 7.0-10 eV where the absorption coefficient of pristine is almost equal to zero. It worth pointing out that the features of this spectrum are consistent with the existing reports [16], [36], [41] on the absorption of graphene. Next, the influence of the impurity concentration on the absorption spectrum of graphene was considered. As the impurity concentration increases, it is observed that the absorption coefficient of Be-S within 7.0-10.0 eV (see red arrow in Fig. 7 (a)) also increases while the intensity of A and B peaks not only decreases but slightly redshifted.

For  $E_{\perp}$  as shown in Fig. 7 (b), the graphene spectrum is characterised with one major peak at 14.6 eV, which is due to the  $\sigma \rightarrow \pi^*$  interband transition and a featureless region within the interval of 0-10.0 eV. The featureless region is designated with a black arrow, Fig. 7(b). This result with respect to  $E_{\perp}$  is in agreement recent reports on the absorption spectrum of pristine graphene.[16], [36], [39], [42], [43] Next, the effect of Be-S atomic pair on the absorption spectrum of graphene was investigated with respect to  $E_{\perp}$ . It is found that by increasing the impurity concentration of the Be-S, the absorption coefficient of the system within the interval of 7.0-10 eV (indicated with a black arrow in Fig. 7 (b)) also increases while the intensity of the peak at C decreases depending on the amount of the impurity. In summary, it is interesting to mention that under the two different polarisations of the electric field, the absorption coefficient of Be-S in the interval of 7.0-10 eV increases with the impurity concentration. However, the intensity of all the major peaks of the Be-S systems reduces with the increase of the impurity percentage, irrespective of the polarisation field vectors.

## F. Electron energy loss spectra (eels)

The eels of graphene and Be-S with different impurity percentage for the  $E_{\parallel}$  and  $E_{\perp}$  are shown in Fig. 8. The eels could be defined as the collective excitations of the electrons of a material and computed as the inverse of the dielectric tensors of the systems. In the case of pristine graphene, it has two prominent peaks with respect to  $E_{\parallel}$ , as shown in Fig. 8 (a). The two peak positions (highlighted as **A** and **B**) which are located at 5.7 and 15-17.0 eV are as a result of the  $\pi$  and the  $(\pi+\sigma)$  plasmons, respectively. For monolayer graphene, Eberlein *et al.*[44] reported experimental plasmon peaks due to  $\pi$  and  $(\pi+\sigma)$  as 4.7 and 14.6 eV, respectively. The slight difference between these values and our results might be attributed to the presence of the excitonic effects which is not considered in our computational method. Another interesting feature of the spectrum could be seen as the dip around the 10 eV where the intensity of the system is almost equal to zero (the black arrow in Fig. 8 (a)). As the impurity concentration increases, it could be seen that the intensity of the spectrum in the interval of 7.0-10 eV (indicated with a black arrow in Fig. 8 (a)) also increases. However, the graphene peak at **A** responds differently to the impurity variation. That is, it decreases with the increase in the impurity percentage. For the peak at **B**, it is important to add that there is no significant change that is observed as a result of the change in the impurity concentration.

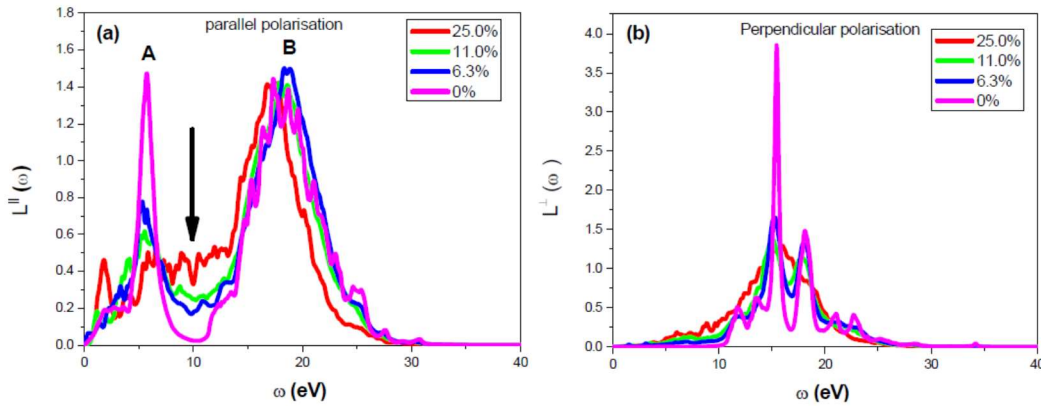


FIG. 8 The anisotropic electron energy loss spectra of graphene (magenta) and Be-S (blue, green, and red colour correspond to a 6.3, 11.0 and 25 % impurity concentration) for (a) parallel polarisation and (b) perpendicular polarisation of the electric field vector.

In the case of  $E_{\perp}$  (Fig. 8 (b)), a prominent resonance peak of graphene is observed at 15.4 eV and the occurrence is because of the transition between filled  $\pi$  and empty  $\pi^*$  bands. It could be seen that the spectrum also has a featureless region with almost zero amplitude within the window of 0-10 eV. It is important to point out that the position of the peak is in accordance with the previous experimental study by T. Eberlein *et al.*[44]. Following the analysed eels of graphene, the effect of Be and S atomic pair on the spectrum was investigated. It can be observed that all the amplitude of the peaks of Be-S at approximately 15.4 eV, irrespective of the impurity percentage, is smaller than that of the graphene (Fig. 8 (b)). It is worth mentioning that, as the impurity percentage increases, the behaviour of the spectra of Be-S with respect to  $E_{\perp}$ , within 5-10.0 eV, is similar to the ensued response of the material in relation to  $E_{\parallel}$ . That is, the intensity of Be-S spectra within the region of 5-10.0 eV decreases with the defect concentration.

### G. Refractive index (r.i)

Fig. 9 depicts the refractive index spectra of graphene and Be-S with different impurity concentrations with respect to the parallel and the perpendicular polarisation of the EM field. In this discussion, only part of the spectra slightly away from the low energy photons has been discussed. Because that region, which is also known as the Drude region, is dominated by the intraband transitions. It is worth reiterating that because of the lack of Drude component in the formulation of the refractive indices, there are inaccuracies in the features of the optical spectra in the low energy region. Based on this account, in relation to  $E_{\parallel}$ , in Fig. 9 (a), only the dip (black arrow direction) and peak (red arrow direction) of the spectra around 5.0 and 10.0 eV, respectively, have been compared in relation to that of the pristine graphene. As a result, it can be seen that as the impurity concentration increases, both the dip around 5 eV and the peaks at about 10.0 eV of the spectra decreases. However, for  $E_{\perp}$  (see Fig. 9 (b)) it is found that the pristine graphene has a maximum peak at 10.0 eV and a dip at 15 eV. As the impurity concentration increases, both peaks and the dips of the spectra of the doped systems reduce in comparison to that of the pristine graphene.

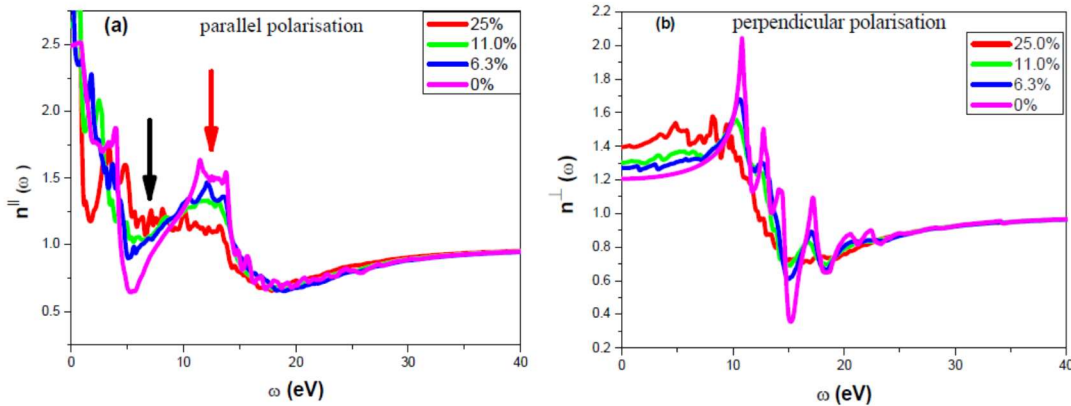


FIG. 9 The anisotropic refractive index spectra of graphene (magenta) and Be-S (blue, green, and red colour correspond to a 6.3, 11.0 and 25 % impurity concentration) for (a) parallel polarisation (b) perpendicular polarisation of the electric field vector.

### H. Reflectivity

Fig. 10 illustrates the reflectivity spectra of graphene and Be-S at different impurity concentrations with respect to (a) the parallel and (b) the perpendicular polarisation of the field vector. For  $E_{\parallel}$ , as shown in Fig. 10 (a), the pristine graphene is characterised with two major peaks. The maximum peak (indicated as **A**) occurs at 4.3 eV whereas the next peak highlighted as **B** is observed at 14.2 eV. Moreover, the spectrum of the system also has a featureless region of 7.0-10.0 eV which is marked with the arrow in Fig. 10 (a). The peak positions of this spectrum are in agreement with the recent theoretical studies[15], [36] on graphene. For Be-S, as the impurity percentage increases, it can be observed that the amplitude of the optical peak at **A** reduces as well; whereas for the peak at **B**, there is no substantial change in the amplitude. In the interval of 7.0-10 eV, Be-S also has a low value of reflectivity at a relatively small impurity concentration. However, the reflectivity of the system becomes significant as the impurity concentration increases.

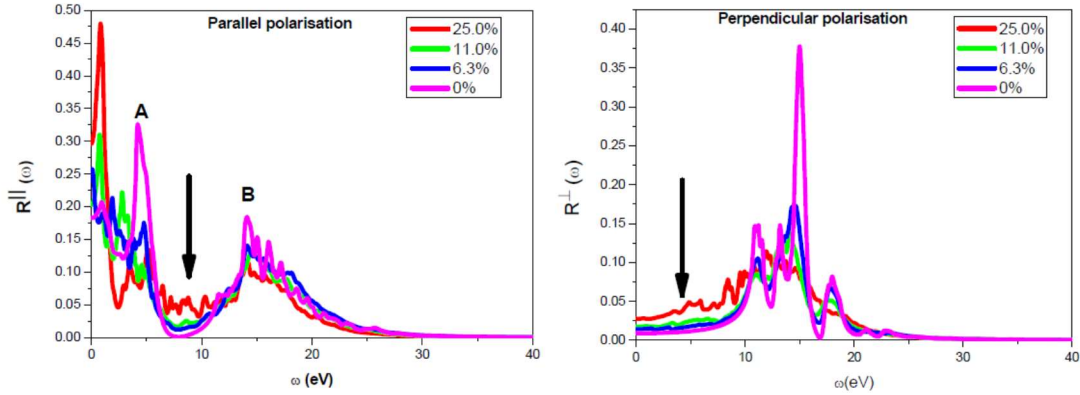


FIG. 10 shows anisotropic refractivity spectra of graphene (magenta) and Be-S (blue, green, and red colour correspond to a 6.3, 11.0 and 25 % impurity concentration) for (a) parallel polarisation (b) perpendicular polarisation of the electric field vector.

In the case of  $E_{\perp}$  (as shown in Fig. 10 (b)), a prominent graphene peak is observed at 15.0 eV while almost zero reflectivity coefficients (indicated with a black arrow) of the spectrum can be noticed within the interval of 0-10 eV. This finding agrees with earlier reports[15], [36] on the *ab-initio* investigation of the optical characteristics of graphene. Next, the effect of Be and S atomic pairs on the reflectivity spectrum of graphene was investigated. Within the interval of 0-10 eV (indicated with a black arrow in Fig. 10 (b)), it is noticeable that the amplitude of the Be-S spectra increases with the impurity concentration. However, for the peak around 15.0 eV, the amplitude decreases with the impurity percentage.

It is worth mentioning that for both  $E_{\parallel}$  and  $E_{\perp}$ , the pristine graphene has low values of reflectivity and absorption coefficients within the window of 7.0-10 eV. This implies that the system is transparent in that frequency interval which corresponds to the ultraviolet (UV) region of the electromagnetic spectrum. However, for the Be-S the two optical parameter values increase as the impurity percentage increases in the aforementioned photon energy interval. This response of the optical spectrum of graphene to Be and S co-doping shows that the optical properties of the system can be modulated with the impurity concentration.

#### IV. CONCLUSIONS

Ab-initio calculations, within the DFT, were employed to investigate the dynamic stability, band structure and optical characteristics of Be-S. The phonon spectrum of the system, due to the absence of imaginary mode, reveals that Be-S (with the impurity concentration of 25%) is dynamically stable. While Be and S preferred to co-exist in an out-of-plane conformation in graphene, the defect formation energy of the system demonstrates that the stability of the system decreases with the impurity concentration. The influence of the impurity concentration on the electronic structure of graphene reveals that it could open up a tunable indirect band-gap in the range of 0-0.72 eV as obtained from our hybrid calculations.

The optical parameters such as dielectric function; refractive index, eels, absorption, and reflectivity of the Be-S were also investigated and compared with that of graphene with respect to the two mutual light polarisation directions. For the pristine graphene, the calculated optical parameters were found to agree with the existing data from other reports. In the case of Be-S, the position of the spectra peaks mimic that of the pristine graphene especially at a small impurity percentage within the photon energy



window of 2.0-40.0 eV for both polarisation directions of the field vector. However, there are remarkable deviations at a relatively high impurity percentage. That is, the peaks of Be-S co-doped appeared to be redshifted relative to the corresponding peaks of the pristine graphene. Moreover, it is remarkable to notice that the amplitude of the dominant optical peaks of graphene decreases with the amount of the impurity present in the Be-S.

Graphene has vanishing absorption and reflectivity spectra within the interval of 7.0-10.0 eV, and this makes it a transparent material under ultraviolet radiation, irrespective of the orientation of the polarisation vector field to the sample. However, unlike in the case of the pristine graphene, within 7.0-10.0 eV, the coefficients of the two aforementioned optical parameters for Be-S have substantial values which tend to increase with the defect concentration. This reveals that the optical transparency of graphene can be tuned with the atomic pair of Be and S concentration. With the on-going trend of tailoring the optical characteristics of graphene with heteroatoms to satisfy certain applications in nanodevices, the result of this study provides an insight on the expected changes in the electronic and optical properties of graphene if it is co-doped with the atomic pair of the Be and S atom for use in nanoelectronic and optoelectronic devices.

#### ACKNOWLEDGEMENTS

This study is based on the research supported by the South Africa Research Chairs Initiative (SARChI) of the Department of Science and Technology, and National Research Foundation (NRF) of South African (Grant No. 61056). Any opinion, findings and conclusions stated in the article is that of the authors, and NRF does not accept any liability in this regard. The authors wish to thank Prof. Mark E. Casida and Dr. B. Mutuma for their invaluable suggestions after reading through the manuscript. O.Okikiola wishes to recognize the financial support from the University of Pretoria for his PhD study. The resources and supports from the Centre for High Performance Computing (CHPC), South Africa, are duly acknowledged.

- [1] K. S. Novoselov *et al.*, "Two-dimensional gas of massless Dirac fermions in graphene," *Nature*, vol. 438, no. 7065, pp. 197–200, Nov. 2005.
- [2] J.-H. Chen, C. Jang, S. Xiao, M. Ishigami, and M. S. Fuhrer, "Intrinsic and Extrinsic Performance Limits of Graphene Devices on SiO<sub>2</sub>," *Nat. Nanotechnol.*, vol. 3, no. 4, pp. 206–209, Apr. 2007.
- [3] S. V. Morozov *et al.*, "Giant intrinsic carrier mobilities in graphene and its bilayer," *Phys. Rev. Lett.*, vol. 100, no. 1, p. 016602, Jan. 2008.
- [4] D. A. Siegel *et al.*, "Many-body interactions in quasi-freestanding graphene," *Proc. Natl. Acad. Sci.*, vol. 108, no. 28, pp. 11365–11369, Jul. 2011.
- [5] B. Rosenstein, M. Lewkowicz, H. C. Kao, and Y. Korniyenko, "Ballistic transport in graphene beyond linear response," *Phys. Rev. B - Condens. Matter Mater. Phys.*, vol. 81, no. 4, pp. 1–4, 2010.
- [6] C. Lee, X. Wei, J. W. Kysar, and J. Hone, "Measurement of the elastic properties and intrinsic strength of monolayer graphene," *Science*, vol. 321, no. 5887, pp. 385–388, Jul. 2008.
- [7] A. A. A. Balandin *et al.*, "Superior thermal conductivity of single-layer graphene," *Nano Lett.*, vol. 8, no. 3, pp. 902–907, Mar. 2008.
- [8] K. S. Novoselov *et al.*, "Electric field in atomically thin carbon films," *Science*, vol. 306, no.

- 5696, pp. 666–669, Oct. 2004.
- [9] P. Avouris, “Graphene: Electronic and photonic properties and devices,” *Nano Lett.*, vol. 10, no. 11, pp. 4285–4294, 2010.
- [10] A. K. Geim and K. S. Novoselov, “The rise of graphene,” *Nat. Mater.*, vol. 6, no. 3, pp. 183–191, Mar. 2007.
- [11] K. S. K. S. Kim *et al.*, “Large-scale pattern growth of graphene films for stretchable transparent electrodes,” *Nature*, vol. 457, no. 7230, pp. 706–710, 2009.
- [12] A. Reina *et al.*, “Large area, few-layer graphene films on arbitrary substrates by chemical vapor deposition,” *Nano Lett.*, vol. 9, no. 1, pp. 30–35, Jan. 2009.
- [13] S. Bae *et al.*, “Roll-to-roll production of 30-inch graphene films for transparent electrodes,” *Nat. Nanotechnol.*, vol. 5, no. 8, pp. 574–578, 2010.
- [14] Z. Liu, J. Li, Z.-H. Sun, G. Tai, S.-P. Lau, and F. Yan, “The Application of Highly Doped Single-Layer Graphene as the Top Electrodes of Semitransparent Organic Solar Cells,” *ACS Nano*, vol. 6, no. 1, pp. 810–818, Jan. 2012.
- [15] P. Nath, S. Chowdhury, D. Sanyal, and D. Jana, “Ab-initio calculation of electronic and optical properties of nitrogen and boron doped graphene nanosheet,” *Carbon*, vol. 73, pp. 275–282, 2014.
- [16] P. Rani, G. S. Dubey, and V. K. Jindal, “DFT study of optical properties of pure and doped graphene,” *Phys. E: Low-dimensional Syst. Nanostructures*, vol. 62, pp. 28–35, 2014.
- [17] P. Nath, D. Sanyal, and D. Jana, “Semi-metallic to semiconducting transition in graphene nanosheet with site specific co-doping of boron and nitrogen,” *Phys. E: Low-Dimensional Syst. Nanostructures*, vol. 56, pp. 64–68, 2014.
- [18] P. Rani and V. K. Jindal, “Designing band gap of graphene by B and N dopant atoms,” *RSC Adv.*, vol. 3, no. 3, pp. 802–812, Dec. 2013.
- [19] S. Mann, P. Rani, R. Kumar, G. S. Dubey, and V. K. Jindal, “Thermodynamic properties of pure and doped (B, N) graphene,” *RSC Adv.*, vol. 6, no. 15, pp. 12158–12168, 2016.
- [20] Y. Ferro, N. Fernandez, A. Allouche, and C. Linsmeier, “Adsorption of beryllium atoms and clusters both on graphene and in a bilayer of graphite investigated by DFT,” *J. Phys. Condens. Matter*, vol. 25, no. 1, p. 015002, Jan. 2013.
- [21] S. Ullah *et al.*, “Band-gap tuning of graphene by Be doping and Be, B co-doping: a DFT study,” *RSC Adv.*, vol. 5, no. 69, pp. 55762–55773, 2015.
- [22] A. Hussain, S. Ullah, and M. Farhan, “Fine tuning of band-gap of graphene by atomic and molecular doping: A density functional theory study,” *RSC Adv.*, vol. 6, pp. 55990–56003, 2016.
- [23] P. A. Denis, R. Faccio, and A. W. Momburu, “Is it possible to dope single-walled carbon nanotubes and graphene with sulfur?,” *ChemPhysChem*, vol. 10, no. 4, pp. 715–722, Mar. 2009.
- [24] O. Olaniyan *et al.*, “Exploring the stability and electronic structure of beryllium and sulphur co-doped graphene: A first principles study,” *RSC Adv.*, vol. 6, no. 91, pp. 88392–88402, 2016.
- [25] G. Kresse and J. Hafner, “Ab initio molecular-dynamics simulation of the liquid-metal–

- amorphous-semiconductor transition in germanium,” *Phys. Rev. B*, vol. 49, no. 20, pp. 14251–14269, May 1994.
- [26] G. Kresse and J. Hafner, “Ab initio molecular dynamics for liquid metals,” *Phys. Rev. B*, vol. 47, no. 1, pp. 558–561, Jan. 1993.
- [27] G. Kresse and J. Furthmüller, “Efficiency of ab-initio total energy calculations for metals and semiconductors using a plane-wave basis set,” *Comput. Mater. Sci.*, vol. 6, no. 1, pp. 15–50, Jul. 1996.
- [28] G. Kresse, “Efficient iterative schemes for ab initio total-energy calculations using a plane-wave basis set,” *Phys. Rev. B*, vol. 54, no. 16, pp. 11169–11186, Oct. 1996.
- [29] J. P. Perdew, K. Burke, and M. Ernzerhof, “Generalized Gradient Approximation Made Simple,” *Phys. Rev. Lett.*, vol. 77, no. 18, pp. 3865–3868, Oct. 1996.
- [30] A. V. Krukau, O. A. Vydrov, A. F. Izmaylov, and G. E. Scuseria, “Influence of the exchange screening parameter on the performance of screened hybrid functionals,” *J. Chem. Phys.*, vol. 125, no. 22, p. 224106, Dec. 2006.
- [31] M. Gajdoš, K. Hummer, G. Kresse, J. Furthmüller, and F. Bechstedt, “Linear optical properties in the projector-augmented wave methodology,” *Phys. Rev. B*, vol. 73, no. 4, p. 045112, Published 17 Jan. 2006.
- [32] K. Parlinski, Z. Q. Li, and Y. Kawazoe, “First-principles determination of the soft mode in cubic ZrO<sub>2</sub>,” *Phys. Rev. Lett.*, vol. 78, no. 21, pp. 4063–4066, May 1997.
- [33] D. R. Cooper *et al.*, “Experimental review of graphene,” *ISRN Condens. Matter Phys.*, vol. 2012, pp. 1–56, 2011.
- [34] N. Mounet and N. Marzari, “First-principles determination of the structural, vibrational and thermodynamic properties of diamond, graphite, and derivatives,” *Phys. Rev. B - Condens. Matter Mater. Phys.*, vol. 71, no. 20, pp. 1–14, May 2005.
- [35] H. Yanagisawa *et al.*, “Analysis of phonons in graphene sheets by means of HREELS measurement and ab initio calculation,” *Surf. Interface Anal.*, vol. 37, no. 2, pp. 133–136, 2005.
- [36] O. Olaniyan, R. E. Maphasha, M. J. Madito, A. A. Khaleed, E. Igumbor, and N. Manyala, “A systematic study of the stability, electronic and optical properties of beryllium and nitrogen co-doped graphene,” *Carbon*, vol. 129, 2018.
- [37] O. V Sedelnikova, L. G. Bulusheva, and a V Okotrub, “Ab initio study of dielectric response of rippled graphene,” *J. Chem. Phys.*, vol. 134, no. 24, p. 244707, 2011.
- [38] M. Houmad, H. Zaari, A. Benyoussef, A. El Kenz, and H. Ez-zahraouy, “Optical conductivity enhancement and band gap opening with silicon doped graphene,” *Carbon*, vol. 94, pp. 1021–1027, 2015.
- [39] V. G. Kravets *et al.*, “Spectroscopic ellipsometry of graphene and an exciton-shifted van Hove peak in absorption,” *Phys. Rev. B - Condens. Matter Mater. Phys.*, vol. 81, no. 15, pp. 1–6, 2010.
- [40] A. G. Marinopoulos, L. Reining, A. Rubio, and V. Olevano, “Ab initio study of the optical absorption and wave-vector-dependent dielectric response of graphite,” *Phys. Rev. B*, vol. 69, no. 24, p. 245419, Jun. 2004.
- [41] L. Yang, J. Deslippe, C. Park, M. L. Cohen, and S. G. Louie, “Excitonic Effects on the Optical

Response of Graphene and Bilayer Graphene,” *Phys. Rev. Lett.*, vol. 103, no. 18, p. 186802, 2009.

- [42] C. Huang, L. Han, L. Wu, R. Su, J. Chen, and P. Lu, “Electronic structure and optical properties of boron-sulfur symmetric codoping in  $4 \times 4$  graphene systems,” *Eur. Phys. J. B*, vol. 88, no. 6, pp. 1–7, 2015.
- [43] A. Laref, A. Ahmed, S. Bin-Omran, and S. J. Luo, “First-principle analysis of the electronic and optical properties of boron and nitrogen doped carbon mono-layer graphenes,” *Carbon*, vol. 81, no. 1, pp. 179–192, 2015.
- [44] T. Eberlein *et al.*, “Plasmon spectroscopy of free-standing graphene films,” *Phys. Rev. B - Condens. Matter Mater. Phys.*, vol. 77, no. 23, pp. 1–4, 2008.

### **4.5.3 Concluding remarks**

DFT was used to study the dynamic stability, band structure and optical properties of Be-S co-doped graphene. The result of the phonon curves of the system shows that Be-S co-doped graphene with impurity concentration as high as 25% is dynamically stable, and the heteroatoms preferred to co-exist in an out-of plane conformation. The electronic and optical properties of the system also revealed interesting results. It is found that an indirect band-gap tuneable up to 0.72 eV (at level of HSE) is attained if graphene is co-doped with Be and S-atom at different concentration. The result of the optical properties reveal that the transparency of graphene could be tuned with Be and S-atom concentration. Specifically, the optical transparency of graphene was observed to decrease with the impurity concentration. The changes in the optical transparency of graphene demonstrate that Be-S co-doping could be used as an avenue for light manipulation in a device application.

### **Author contributions**

O. Olaniyan designed the study and the main conceptual ideas. He worked out almost all of the technical details, and performed the numerical calculations for the suggested theory.

# Chapter 5

## Concluding Remarks and Recommendations

Graphene is a semimetal with a higher sheet resistance than ITO. Heteroatom-doping is a facial approach for creating a sizeable band-gap in graphene and also for increasing the carrier concentration to lower the sheet resistance. However, not all heteroatom-doped graphene is dynamically stable or have a band-gap. For example, Be-doped graphene has been demonstrated to be dynamically unstable at 0 K while S-doped graphene could be a metal or semiconductor depending on the impurity concentration. Heteroatoms co-doping is an effective technique for addressing these challenges. This technique was used in this thesis to address the dynamic instability of Be-doped graphene, and the lack of a band-gap in S-doped graphene through Be-S co-doped and Be-N co-doped graphene. Furthermore, the optical properties of Be-S co-doped and Be-N co-doped graphene were investigated for a potential application in optoelectronics using the plane wave pseudopotential method, within the framework of density functional theory.

### 5.1 Conclusions

#### 5.1.1 Dynamic stability of Be, N, and S doped graphene

The lattice dynamics of the Be-doped, Be-N co-doped and Be-S co-doped graphene at 0 K was investigated using a finite displacement method within the harmonic approximation scheme. The results indicate that Be-N and Be-S (both with the impurity concentration tuned up to 25%) co-doped graphene are dynamically stable due to the absence of the imaginary modes in the calculated phonon dispersion curves of the systems. However, in the case of Be-doped graphene, with a relatively lower impurity concentration of 12.5%, the phonon curves of the system have imaginary modes. As a result, Be-doped graphene at 12.5% impurity concentration is not stable.

This result could explain the rarity of the experimentally synthesized Be-doped graphene in the literature.

The formation energy calculations for defects to form were performed for all the aforementioned systems. The results of the formation energies are in agreement with the result of the lattice dynamics of the systems. Be-N and Be-S co-doped graphene, in the energetically preferred configuration, were observed to have lower formation energies than Be-doped graphene. As a result, the two co-doped systems are more stable than Be-doped graphene. The existence of the ionic bonds between the co-dopants of the Be-N and Be-S co-doped graphene could be the reason why the co-doped systems are more stable than Be-doped graphene. An ionic bond involves the transfer of electrons from a metal to a non-metal, and usually stronger than the covalent bond. Be is a metal while N and S are non-metal. Consequently, an ionic bond is likely to form between Be and N or S if the pair of the impurities is used to replace any two adjacent atoms of graphene. However, in the case of the Be doped graphene, Be and C have a close electronegativity value, as such, prefer the formation of a covalent bond. The above reason was confirmed when Bader analysis was employed to analyze the charge distribution in Be-S co-doped graphene. The result revealed that charges are transferred from Be-atom to S-atom when the impurities were placed as adjacent atoms in the graphene matrix. The results in this section demonstrate that Be-N and Be-S co-doped graphene could be more realistic systems to synthesize experimentally than Be-doped graphene.

### **5.1.2 Electronic structure of Be, N, and S doped graphene**

The band structures and DOS calculations of the systems were carried out using GGA-PBE and HSE06 exchange-correlation functionals. All the doped systems exhibit semiconducting character. Be-S co-doped graphene has a direct band-gap (which changes with doping pattern) for

in-plane substitution of the defects. However, an indirect band-gap (which could be tailored with the impurity concentrations) magnitude was observed in the system when the substitution was done in out-of-plane conformation. In the case of Be-doped and Be-N co-doped graphene, while they both share p-type conductivity, the systems have a direct band-gap which increases with the impurity concentrations. Moreover, at a relatively high impurity concentration, the systems become degenerate semiconductors, exhibiting both metallic and semiconducting characters. The electronic structure of Be-N is similar to Be-doped graphene and could be considered as an alternative realistic p-type semiconductor to the latter since the former is more stable.

### **5.1.3 Optical properties of Be, N, and S doped graphene**

The optical properties of the Be-N and Be-S co-doped graphene were calculated using the first-order time-dependent perturbation theory. Regardless of the impurity concentration, due to the low value of the reflectivity and the absorption coefficient, it is found that BeN-co-doped and Be-doped graphene are transparent within the frequency window of 7.0–10 eV (UV region) for the parallel polarization field vector. However, for the Be-S co-doped graphene, the optical transparency of the system reduces with the increase in the impurity concentration. The out-of-plane substitution of Be and S in graphene disrupts the planar topology of the system (due to the molecular size of the impurities) and consequently the electronic property, which transforms from semi-metallic to semiconducting with an indirect band-gap. This is perhaps the reason why the Be-S co-doped is not transparent as compared to the pristine graphene.



#### **5.1.4 Applications**

The results of the electronic and optical properties of Be-S and Be-N co-doped graphene suggest that the systems could be used in device applications. For instance, Be-S co-doped has a band-gap tuneable up to 0.72 eV; consequently, the system could be used as a graphene-based transistor in microelectronics and nanoelectronics. A minimum band-gap of 0.4 eV is required for a graphene-based transistor to function in ON/OFF mode. Thus the band-gap of Be-S co-doped graphene could be tuned to such a specification. In the case of Be-N co-doped graphene, it is a degenerate semiconductor and could be used as an ITO in optoelectronics. This is because the material is transparent with both tuneable band-gap and metallic character. The system has a p-type conductivity which can be varied by changing the amount of the impurity in the system.

### **5.2 Recommendations**

#### **5.2.1 Methodology**

To calculate the optical properties of a material, an appropriate description of the many-body effects such as the electron-electron ( $e-e$ ) correlation and the excitonic effect ( $e-h$ ) are required. The independent particle approximation used in this thesis to study the optical properties of graphene is appropriate due to the fact that, in graphene, the self-energy correction and  $e-h$  correlation almost fortuitously cancel out [1]–[3]. However, since the self-energy correction and  $e-h$  correlation do not completely cancel out, a future study on doped graphene systems should be done using a higher level of theory such as Green function (GW) plus Bethe-Salpeter equation (BSE) which incorporates  $e-e$  and  $e-h$  effects.

### 5.2.2 Functionalization of graphene

There are a number of methods for tailoring the band-gap of graphene. Deposition of graphene on suitable substrates is one of the methods of opening a band-gap in the two-dimensional material. However, the band-gap induced by substrates in an experimental setup is still being contested[4]. Another method is by fabricating a finite size nanoribbon from graphene to create a band-gap in the system. But such a method is difficult to implement experimentally due to the difficulty involved in tuning to the size of the nanoribbons[5]. Because of these challenges, addition of molecules (such as  $H_2$ ,  $NH_2$ ,  $C_6H_5$ ,  $NH$ ,  $NC_6H_5$ ,  $NC_6H_4CH_3$ ,  $NC_2H_4OH$ , etc.) on graphene (known as functionalization) is another option of tailoring the properties of the graphitic material. Experimental investigations have revealed that the free standing[6] and supported[7] graphene functionalized with hydrogen have a band-gap. Thus, it would be interesting to investigate the electronic and optical properties of functionalized graphene using many-body perturbation theory.

### 5.2.3 Effect of Van der Waals on doped monolayer graphene

In this thesis, only the electronic and the optical properties of the heteroatoms doped monolayer graphene were studied. Given a multi-layered graphene in which one of the layers is doped with heteroatoms, a study of the layer-dependent electronic and the optical properties of the system would be worth investigating. It is important to note that to describe a layered system, such as graphite, both the local atom bonds and the weak Van der Waals forces must be considered. However, the exchange-correlation functionals employed in this thesis to describe the ground state properties of graphene are not suitable for the description of a multi-layered graphene due to the

absence of dispersion relation in the description. To overcome this shortcoming for a layered system, applying a fully nonlocal functional [8] is one way to proceed.

## References

- [1] L. Yang, J. Deslippe, C. Park, M. L. Cohen, and S. G. Louie, “Excitonic effects on the optical response of graphene and bilayer graphene,” *Phys. Rev. Lett.*, vol. 103, no. 18, p. 186802, 2009.
- [2] F. Karlický and M. Otyepka, “Band gaps and optical spectra of chlorographene, fluorographene and graphane from G0W0, GW0 and GW calculations on top of PBE and HSE06 orbitals,” *J. Chem. Theory Comput.*, vol. 9, no. 9, pp. 4155–4164, Sep. 2013.
- [3] K. F. Mak, J. Shan, and T. F. Heinz, “Seeing many-body effects in single- and few-layer graphene: observation of two-dimensional saddle-point excitons,” *Phys. Rev. Lett.*, vol. 106, no. 4, p. 046401, Jan. 2011.
- [4] S. Y. Zhou *et al.*, “Origin of the energy bandgap in epitaxial graphene,” *Nat. Mater.*, vol. 7, no. 4, pp. 259–260, 2008.
- [5] J. B. Neaton, M. S. Hybertsen, and S. G. Louie, “Renormalization of molecular electronic levels at metal-molecule interfaces,” *Phys. Rev. Lett.*, vol. 97, no. 21, p. 216405, Nov. 2006.
- [6] R. Balog *et al.*, “Atomic hydrogen adsorbate structures on graphene,” *J. Am. Chem. Soc.*, vol. 131, no. 25, pp. 8744–8745, Jul. 2009.
- [7] J. R. Votano, M. Parham, and L. Hall, “Control of graphene’s properties by reversible hydrogenation,” *Chemistry (Easton)*, no. January, pp. 610–613, 2004.
- [8] P. Hyldgaard *et al.*, “Van der Waals density functional for layered structures,” *Physical Review Letters*, vol. 91, no. 12. pp. 1–4, 2003.